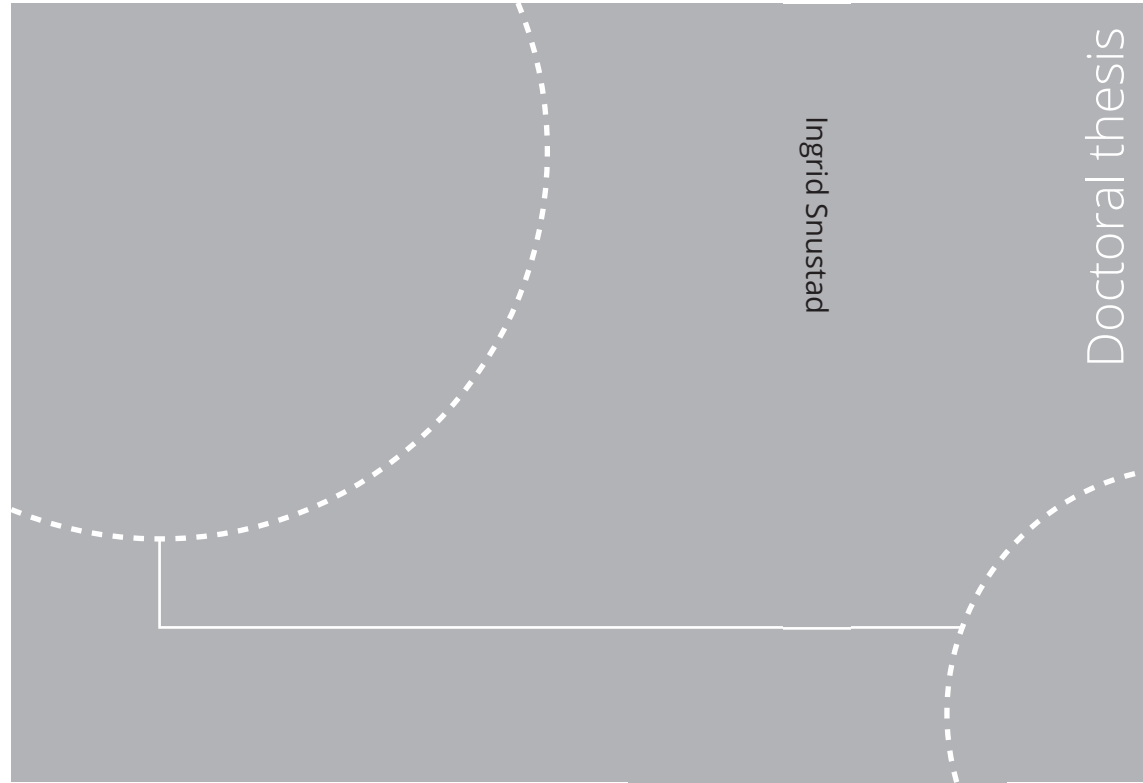


ISBN 978-82-326-5606-6 (printed ver.)
ISBN 978-82-326-6715-4 (electronic ver.)
ISSN 1503-8181 (printed ver.)
ISSN 2703-8084 (electronic ver.)



Doctoral theses at NTNU, 2020:236

Ingrid Snustad

Mechanisms and enhancement of CO₂ condensation heat transfer

Doctoral theses at NTNU, 2020:236

NTNU
Norwegian University of
Science and Technology
Thesis for the degree of
Philosophiae Doctor
Faculty of Engineering
Department of Structural Engineering

 **NTNU**
Norwegian University of
Science and Technology

 NTNU

 **NTNU**
Norwegian University of
Science and Technology

Ingrid Snustad

Mechanisms and enhancement of CO₂ condensation heat transfer

Thesis for the degree of Philosophiae Doctor

Trondheim, June 2021

Norwegian University of Science and Technology
Faculty of Engineering
Department of Structural Engineering



Norwegian University of
Science and Technology

NTNU

Norwegian University of Science and Technology

Thesis for the degree of Philosophiae Doctor

Faculty of Engineering
Department of Structural Engineering

© Ingrid Snustad

ISBN 978-82-326-5606-6 (printed ver.)
ISBN 978-82-326-6715-4 (electronic ver.)
ISSN 1503-8181 (printed ver.)
ISSN 2703-8084 (electronic ver.)

Doctoral theses at NTNU, 2020:236



Printed by Skipnes Kommunikasjon AS

NTNU

Mechanisms and enhancement of CO₂ condensation heat transfer

Ingrid Snustad

Supervisor: **Zhiliang Zhang**

Co-supervisors: **Jianying He, Åsmund Ervik and Amy
Brunsvold**

Preface

This doctoral thesis is submitted to the Norwegian University of Science and Technology (NTNU) in partial fulfillment of the requirements for the degree of philosophiae doctor (PhD).

The thesis consists of an introductory section, three published journal papers, and two conference papers.

The work presented in this thesis was conducted in the period between August 2016 and April 2021 at NTNU Nanomechanical Lab (NML), Department of Structural Engineering (KT), Faculty of Engineering (IV), NTNU, Trondheim, Norway and at SINTEF Energy Research, Trondheim, Norway. Two parental leaves of absence were taken in the periods April 2017-September 2017 and September 2018-April 2019.

Prof. Zhiliang Zhang (NTNU NML) has been my main supervisor during this work. Prof. Jianying He (NTNU NML), Senior Researcher PhD Amy Brunsvold (SINTEF Energy Research) and Researcher PhD Åsmund Ervik (SINTEF Energy Research) have been my co-supervisors.

I have conducted the experimental work in the laboratories at SINTEF Energy Research. Sample preparation and structural characterization was performed by master student Lene Hollund at NTNU NanoLab, the advanced clean room facilities at NTNU. During spring 2018 I stayed three weeks at Massachusetts Institute of Technology (MIT) visiting Prof. Evelyn Wang's research group. Prof. Evelyn Wang has been in the Advisory Board of this project.

The Research Council of Norway is acknowledged for support to the CLIMIT project no. 254813/E20 with the title: Superlyophobic surfaces for efficient separation and droplet condensation of CO₂ and also for supporting the Norwegian Micro- and Nano-Fabrication Facility, NorFab, project no. 245963/F50.

Ingrid Snustad
Trondheim, April 2021

Abstract

The aim of this thesis is to increase the understanding of the mechanisms governing Carbon Dioxide (CO_2) condensation, and in that way finding a pathway towards a higher condensation efficiency. Liquefaction of CO_2 occurs e.g. in industrial processes such as in heat exchangers for thermal management. Compact geometries have become increasingly important in thermal management following the decrease in size of electronic equipment. CO_2 is a suitable solution as a refrigerant in such heat exchangers due to its thermophysical properties. It is also a viable substitute as a refrigerant in conventional heat transfer equipment in the quest for eliminating fluorine based refrigerants, due to their negative environmental impact. Liquefaction of CO_2 also occurs when processing the gas prior to ship transportation of CO_2 being captured from e.g. power plant exhaust. Reduction of the anthropogenic emissions of CO_2 is required for reducing the global warming and achieving the 2-degree scenario set forth by the International Panel of Climate Change.

The main reason for resistance to heat transfer during condensation is the restricted conduction through the condensate film that is formed on the condenser surface. The research on more efficient condensation currently focuses on suppressing the formation of this condensate film and in stead achieving dropwise condensation. An introduction of droplets on the surface will reduce the heat transfer resistance and a more efficient condensation process emerges. The condensation heat transfer coefficient could be increased by up to an order of magnitude. For CO_2 this alternative has not yet been considered and the research on CO_2 condensation has hitherto focused on understanding how the flow properties affects the heat transfer in flow condensation inside tubes and channels. These are relevant geometries for heat exchangers and the flow in microchannels must be deciphered to gain control of the condensation in compact equipment. The condensation of CO_2 on flat and structured surfaces has, however, not yet been studied, and the models for predicting the behavior do not include the influence of condenser material or surface structures on the heat transfer. We have through this work tried to answer if condensation of CO_2 could be achieved in the dropwise mode, and if not, how the efficiency of CO_2 condensation otherwise can be increased. We have also explored how the condenser material and/or surface structures influence the heat transfer during condensation.

For solving these issues we have designed a methodology and built an experimental facility for measuring the CO_2 condensation heat transfer coefficient on various sur-

faces. By achieving elevated pressures and low temperatures CO₂ has been liquefied on vertical surfaces and the heat transfer has been measured.

We have in this work established a first set of experimental data for CO₂ condensation on vertical walls. We have found that surface properties such as roughness and surface energy affect the condensation heat transfer. With surface roughness, the material's thermal conductivity also comes into play, as the uniformity of the temperature within the liquid will be influenced by the conductivity of the peaks of the material when the liquid film is thin. We have also found that structuring the surface with micro- and nanosized features will alter the heat transfer efficiency. A combination of micro- and nanostructures could result in a thinner liquid film on the surface, consequently reducing the heat transfer resistance through the condensate. On the other hand, the structures could also cause significant liquid retention and therefore a thicker liquid film. The results indicate that a careful design and fabrication of a combination of micro- and nanostructures will enhance the condensation heat transfer by increasing the surface area, reducing liquid retention and increasing the effective thermal conductivity of the composite surface of liquid and nanostructures similar to wicking condensation.

The results in this thesis show that there are pathways to increasing condensation heat transfer of CO₂, which will lead to reduced costs and energy demands of the liquefaction process. Two main parameters have been identified: 1) roughness control and 2) optimization potentials for structured surfaces. This will result in e.g. lower CO₂ transport costs during carbon capture and storage, and in improved thermal management of small electronic devices.

Popular science summary

CO₂ emission is a large contributor to global warming. To reach the 2-degree scenario set forth by the UN we need to remove CO₂ from e.g. fossil fuel powered industry, car exhaust and possibly the air itself. Mitigation of CO₂ emissions could be done through Carbon Capture and Storage (CCS). During this process, liquefaction is sometimes a necessary step, e.g. for ship transportation of CO₂ to the storage location. In addition to being an unwanted compound due to global warming, CO₂ is actually an environmentally friendly alternative as a refrigerant in process equipment, for example for cooling a motor vehicle engine, or in the refrigerators in grocery stores. A thorough understanding of the condensation process is crucial for accurate modelling and design of these applications. For both CCS and industrial process with CO₂ as refrigerant, enhanced liquefaction efficiency means less energy consumption and lower costs.

In light of this, we initiated a project for enhancing the efficiency of CO₂ condensation. Initially, the project goal was to achieve a way of condensation called dropwise condensation. This mode occurs on specially tailored surfaces and can result in heat transfer efficiencies ten times that of the conventional filmwise condensation. However, after conducting a literature survey of the potential surfaces for achieving dropwise condensation, it became clear that our initial goal was not achievable for the period of this project. We then shifted the focus towards enhancing condensation efficiency on micro- and nanostructured surfaces in the filmwise condensation mode. However, experimental data for heat transfer on different unstructured materials had not yet been published, hence the baseline for determining if a structured surface increased the condensation efficiency or not, did not exist. The reason for lack of data could be that the Nusselt model for predicting condensation on flat surfaces has been widely accepted and used in process design for a century. The model does not include the influence of the surface properties, and it will therefore not result in different heat transfer coefficients (HTC) on e.g. smooth copper (Cu) and rough aluminum (Al). In our study of Cu, Al and stainless steel (316), we found that the roughness and surface energy affected the condensation HTC. The HTC is highest on smooth Cu and lowest on Al and steel, caused by the different roughness and surface energy. Following the work with flat surfaces, we conducted a study on CO₂ condensation on micro- and nanostructured Cu. The results indicate that properly designed hierarchical surface structures (structures on both micro- and nanoscale on the same surface) promote higher condensation efficiency.

With continued research on micro- and nanostructured surfaces we believe that it is possible to enhance CO₂ condensation efficiency even more, and thereby reducing the energy demand during condensation. A smaller energy consumption will reduce the costs of CO₂ condensation and may ultimately contribute to the large scale implementation of CCS and CO₂ as an environmentally friendly refrigerant in industrial processes.

Generelt sammendrag

CO₂-utslipp er en viktig årsak til global oppvarming. For å nå FNs togradersmål må vi fjerne CO₂ fra for eksempel industri, bileksos og fra lufta. Vi kan blant annet fjerne CO₂-utslipp ved hjelp av karbonfangst og -lagring (CCS). I denne prosessen er det iblant nødvendig å gjøre CO₂ flytende, for eksempel når fanget CO₂ skal transporteres på skip til lagringsstedet. Samtidig som CO₂ er en drivhusgass som øker global oppvarming, er det også et miljøvennlig alternativ som kjølemiddel i prosessutstyr, for eksempel i kjøling av bilmotorer eller i kjøleskap og fryserer i matvarebutikker. Det helt avgjørende å ha god kunnskap om kondenseringprosessen for å nøyaktig modellere og designe prosesser for disse formålene. En økt effektivitet vil bety mindre energiforbruk og lavere kostnader for både CCS og industrielle prosesser med CO₂ som kjølemedium.

I lys av dette initierte vi et prosjekt for å øke effektiviteten av CO₂-kondensasjon. Initielt var det ønskelig å oppnå dråpekondensering av CO₂, en prosess som kan føre til ti ganger så høy varmetransport som i tradisjonell filmkondensering. Etter en nøye litteraturgjennomgang med fokus på potensielle overflater for å oppnå dråpekondensering av CO₂, viste det seg imidlertid å være svært vanskelig å realisere dette på en skalerbar måte i løpet av dette prosjektets tidsramme. Vi skiftet derfor fokus mot å oppnå effektiv kondensering av CO₂ på mikro- og nanostrukturerte overflater, fortsatt ved hjelp av filmkondensering. Vi oppdaget derimot fort at det ikke fantes data for kondensering på ubehandlede overflater, så sammenlikningsgrunlaget for å si noe om strukturering kunne øke kondensasjonseffektiviteten var for dårlig. Dette er nok forårsaket av at kondensering på flate overflater med vekslende hell har blitt beregnet ved hjelp av Nusselt-modellen som ble utviklet tidlig på 1900-tallet. Denne modellen inkluderer ikke effekten av overflaten eller materialet det kondenseres på, så den vil ikke resultere i forskjellige varmetransportkoeffisienter (VTK) på for eksempel kobber og aluminium. I vår studie av kobber, aluminium og stål har vi sett at et ruheten på overflaten påvirker effektiviteten av kondensasjonen. VTK er høyest på kobber og lavest på aluminium og stål, noe som følger disse prøvenes ruhet og materialenes overflateenergi. Etter studien på flate overflater fortsatte vi med å se på effekten av mikro- og nanostrukturer på kondensasjonen. Vi lagde og studerte to typer mikro- og nanostrukturerte kobberoverflater. Resultatene er noe sprikende og en enkel konklusjon var ikke å finne etter dette ene studiet. Resultatene indikerte likevel at en hierarkisk struktur (overflatestrukturer på både mikro- og nanoskala samtidig) vil øke varmetransporten ved CO₂-kondensasjon.

Ved å fortsette forskningen på mikro- og nanostrukturerte overflater for effektiv varmetransport i kondensasjonsprosessen mener vi det er mulig å effektivisere CO₂-kondensasjonen og dermed redusere energiforbruket. Dette vil igjen føre til reduserte kostnader forbundet med kondensasjon og følgelig muliggjøre storskala implementering av CCS og av CO₂ som et miljøvennlig kjølemedium i industrielle prosesser.

List of contributions

Journal papers

Paper I: A Review on Wetting and Water Condensation - Perspectives for CO₂ Condensation

Ingrid Snustad, Ingeborg Treu Røe, Amy Brunsvold, Åsmund Ervik, Jianying He and Zhiliang Zhang. *Advances in Colloid and Interface Science* **256**: 291-304 (2018) [1]

Liquefaction of vapor is a necessary, but energy intensive step in several important process industries. This review identifies possible materials and surface structures for promoting dropwise condensation, known to increase efficiency of condensation heat transfer. Research on superhydrophobic and superomniphobic surfaces promoting dropwise condensation constitutes the basis of the review. In extension of this, knowledge is extrapolated to condensation of CO₂. Global emissions of CO₂ need to be minimized in order to reduce global warming, and liquefaction of CO₂ is a necessary step in some carbon capture, transport and storage (CCS) technologies. The review is divided into three main parts: 1) An overview of recent research on superhydrophobicity and promotion of dropwise condensation of water, 2) An overview of recent research on superomniphobicity and dropwise condensation of low surface tension substances, and 3) Suggested materials and surface structures for dropwise CO₂ condensation based on the two first parts.

Co-author contributions: Ingeborg was a master student with a summer internship in SINTEF Energy Research. She conducted the initial literature search in her internship and wrote a first draft of the paper, under the supervision of Amy and Åsmund. I continued the work Ingeborg started, included additional papers and extended the review. Zhiliang and Jianying contributed in the revision and discussions of the paper.

Paper II: Heat transfer characteristics of CO₂ condensation on common heat exchanger materials: Method development and experimental results

Ingrid Snustad, Åsmund Ervik, Anders Austegard, Amy Brunsvold, Jianying He and Zhiliang Zhang. *Experimental Thermal and Fluid Science* **129**: 110440 (2021) [2]

Understanding condensation of CO₂ is essential for e.g. designing compact heat exchangers or processes involved in Carbon Capture and Storage. However, a consistent experimental campaign for condensation of CO₂ on common materials is lacking. In this work, we present an experimental method and an associated laboratory setup for measuring the heat transfer properties of CO₂ condensation on materials commonly used in heat exchangers for the liquefaction of CO₂. We have investigated the heat transfer during CO₂ condensation on copper, aluminum, stainless steel (316) to reveal the heat transfer dependency on surface properties. The experiments are conducted at three saturation pressures, 10, 15, and 20 bar and at substrate subcooling between 0 and 5 K. The results show that the heat transfer coefficients decrease with increasing surface subcooling. Also, increasing the saturation pressure increases the heat transfer coefficient. The results indicate that surface roughness and surface energy affect the condensation heat transfer coefficient, and an increased roughness results in reduced heat transfer coefficients. The highest heat transfer coefficient is found for condensation on copper, for which the lowest surface roughness has been measured.

Co-author contributions: Åsmund, Anders, Amy and I started the work with developing the methodology and designing the experimental setup. The method and setup was revised several times especially after I visited MIT during spring of 2018. I conducted the heat transfer experiments. The results were discussed with Anders, Åsmund and Zhiliang. I wrote the first draft of the paper, while all authors contributed equally to the revision and discussion of the final paper.

Paper III: Condensation heat transfer of CO₂ on Cu based hierarchical and nanostructured surfaces

Ingrid Snustad, Lene Hollund, Åsmund Ervik, Anders Austegard, Amy Brunsvold, Jianying He and Zhiliang Zhang. International Journal of Heat and Mass Transfer **175**: 121367 (2021) [3]

Phase-change processes such as condensation are efficient means of heat transfer. However, condensation is also an energy-intensive process and extensive research is conducted to increase the heat transfer efficiency. Increasing the effective heat transfer area in terms of surface structures on macro or microscale is one such technique of heat transfer enhancement. In this work, we have studied micro- and nanostructured surfaces for their potentials in increasing heat transfer during condensation of CO₂. Three Cu-based surfaces on which CuO nanoneedles have been grown, have been investigated. We hypothesize three competing mechanisms govern the overall heat transfer on structured surfaces: 1) increased heat transfer area, 2) lower thermal conductivity of oxides, and 3) condensate flooding of the structures. Our study has shown that in some cases, the effect of these mechanisms can be neutralized. More importantly, the results show that superior heat transfer can be achieved by optimizing the surface structure. The best of the structured surfaces resulted in a heat transfer coefficient 66 % higher than that of the unstructured surface.

Co-author contributions: Lene was a master student who first started with a summer internship in SINTEF Energy Research, where she helped conditioning and testing the experimental setup. She continued with a Project and finally a Master thesis in which she fabricated and characterized the hierarchical and nanostructured substrates in NTNU Nanolab. The explanation of the fabrication processes and some of the characterization results are based on her Master work. I supervised Lene in her work, conducted all heat transfer experiments and wrote the first draft of the paper. All authors contributed equally to the revision and discussion of the final paper.

Co-authored publications

Paper IV: Contact Angle and Condensation of a CO₂ Droplet on a Solid Surface

Jianyang Wu, Åsmund Ervik, Ingrid Snustad, Senbo Xiao, Amy Brunsvold, Jianying He and Zhiliang Zhang. *The Journal of Physical Chemistry C* **123**: 443-451 (2019) [4]

Paper V: CO₂ wetting on pillar-nanostructured substrates

Jianyang Wu, Ingrid Snustad, Åsmund Ervik, Amy Brunsvold, Jianying He and Zhiliang Zhang. *Nanotechnology* **31**: 245403 (2020) [5]

Conference presentations

Ingrid Snustad, Åsmund Ervik, Anders Austegard, Gunhild Reigstad, Jianying He, Zhiliang Zhang, Amy Brunsvold. Poster presentation: "Efficient Liquefaction of Carbon Dioxide on Superlyophobic Surfaces" Greenhouse Gas Control Technologies GHGT-14, 21st-25th October 2018, Melbourne, Australia.

Ingrid Snustad, Lene Hollund, Amy Brunsvold, Åsmund Ervik, Anders Austegard, Jianying He, Zhiliang Zhang. Poster presentation: "Nanostructured surfaces for efficient liquefaction of CO₂" Trondheim CCS Conference TCCS-10, 17th-19th June 2019, Trondheim, Norway.

Ingrid Snustad, Åsmund Ervik, Anders Austegard, Jianying He, Zhiliang Zhang, Amy Brunsvold. Poster presentation: "CO₂ liquefaction: an experimental method for determining the heat transfer coefficient of various materials" Greenhouse Gas Control Technologies GHGT-15, 15th-18th March 2021, Virtual Conference to be hosted in Khalifa University, Abu Dhabi, United Arab Emirates.

Acknowledgements

There are several persons that I could not have been without when conducting my PhD work. First of all, I would like to thank my main supervisor Professor Zhiliang Zhang for your keen interest in my work and all the encouragements you have given me the last 4.5 years. Your knowledge is widespread and your way of finding significance and importance in all small and large questions I have set forth for you have been invaluable for my motivation and learning. Secondly, I would like to thank my co-supervisor Professor Jianying He for the interesting discussions and meetings we have had, and your well founded comments on my written work. Especially during Zhiliang's sabbatical, you were very important for my PhD progress. I would also like to thank my co-supervisor, and the project manager, Dr. Amy Brunsvold. Our discussions have been of both personal and intellectual character and your guidance and, most importantly, your friendship has been very important to me. Also, I would like to thank my third co-supervisor Dr. Åsmund Ervik who stepped in as my co-supervisor in the middle of the PhD period. The long discussions with you, always starting with "do you have 5 minutes?", but ending up with hours of discussions, have been of the outermost importance for me. You have helped me see interesting outcomes of my research when I could not see it myself, and I always end up being more motivated to go on with my work after having talked with you. More than I think you know, you have helped me on my way to becoming a PhD and a better researcher. In addition I would like to thank Dr. Anders Austegard for all the interesting discussions on the experimental setup, and on the results. Your eye for details has been very important for the quality of my work. To all my colleagues at the Nanomechanical lab, especially Susanne, Sigrid, Merete and Sandra, thank you for your friendship and nice lunch talks the last few years. Also thank you all for the comments and interest you have shown to my work during our weekly group meetings. To my mom and dad, thank you for your support and for always believing in me. Thank you for letting me be myself and for your interest in all small and large projects that I set out to do. I know that you are always there backing me up and cheering me on. Thank you also to my beautiful children, Edvin and Fride. You help me put everything into perspective and help me realize that there are, luckily, more important things to life than heat transfer. You help me see that life has meaning, even on the hardest and most meaningless days. And last, but absolutely not least, thank you so much for all your support and for always being there for me, my beloved Hanne. I know it is not always easy to live with a PhD candidate, but

nevertheless, you have pushed me forward and made an exceptional effort at home so that I could concentrate on getting this thesis ready. Without your patience and generosity I would never have finished on time – or even at all. I love you!

List of Figures

1.1	The Hampson-Linde refrigeration cycle was the first cycle to use regenerative cooling in a condensation process. The feed gas is compressed and the compressed gas is fed through a cooler. The cold pressurized gas flows through a heat exchanger before expansion in a Joule-Thomson expansion valve. The gas is now at its coldest and at low pressure, and in a separator the liquid is condensed and drained. The un-condensed cold gas is fed back into the counterflow heat exchanger to work as a coolant for the incoming compressed gas and finally being fed back into the cycle.	2
1.2	A work flow diagram showing the stages of the work in this thesis. Included is also a scenario of where this work could lead, namely to design the optimum surface for CO ₂ condensation.	8
2.1	Schematic drawing of dropwise and filmwise condensation. The contact angle θ is an important parameter for determining the condensation mode.	12
2.2	Condensation on a vertical plate with the necessary parameters for deriving the Nusselt model.	13
2.3	The wetting state of a surface is characterized by the contact angle in the three phase line between solid, liquid and gas, θ . The contact angle is above 90° for non-wetting surfaces, below 90°, but finite, for wetting surfaces, and equal to 0° for complete wetting surfaces.	17
2.4	(a) A liquid droplet at rest on a solid surface. The contact angle, θ , is given by the interfacial tensions, γ , through Young's equation, Equation (2.1.26). (b) The receding (θ_{rec}) and advancing (θ_{adv}) contact angle on an inclined surface. The contact angle hysteresis is defined as the difference between the advancing and receding contact angles.	18

2.5	A droplet on a rough surface will either be in the Wenzel state (a) where the liquid fills the gaps in the rough surface, or in the Cassie state (b) where air pockets are trapped underneath the droplet. Intermediate states between the two extremes also exist.	19
2.6	An example of a cascade refrigeration cycle with CO ₂ as the low-temperature side refrigerant. The high-temperature side refrigerant could be a natural refrigerant such as NH ₃	21
3.1	Photo of the high-speed camera and the pressure chamber.	24
3.2	Piping and Instrumentation Diagram of the experimental setup. Pure CO ₂ flows into the pressure chamber with the Alicat PCD as the pressure controller. Liquid CO ₂ is fed to the cooling element with the Alicat PC3 as a back pressure regulator, accurately controlling the pressure which results in a uniform temperature in the cooling element.	25
3.3	(a) The interior of the cooling element consists of narrow channels in which the two-phase CO ₂ flows. (b) The assembled cooling element with an inlet and outlet for the two-phase flow, an insulated Cu block and a rotation disc, which can be mounted on the rotation motor. The cooling element is insulated with teflon on top and insulation foam on the sides.	27
3.4	(a) Interior of the pressure chamber with the cooling element attached to the rotational stage. Two PT100 elements for measuring the gas temperature are visible below and above the cooling element. The lid of the chamber is removed for convenience. (b) Water droplet on a structured surface photographed by the high-speed camera. The depth of field is narrow and the contact angle can be measured.	28
3.5	Sketch of the experimental setup showing the pressure chamber, the inlet and outlet of the cooling element, the Cu cylinder with embedded thermocouples, the investigated substrate and the camera viewing through a see glass within the lid of the chamber.	29
3.6	Temperatures in the four thermocouples in the cylinder and the calculated (extrapolated) surface temperature shown as a green star.	31
3.7	Temperature measurements in the Cu cylinder during CO ₂ condensation. (a) shows the measured temperatures at the initiation of condensation, including the transition zone between two stable temperature levels. (b) shows the temperatures during an entire experimental series on flat Cu at 15 bar. Figure is also found in Paper III.	32
3.8	Ice bath calibration of the thermocouples embedded in the Cu cylinder, while the thermocouples are coupled to the circuit as they are during experiments.	33

- 3.9 Liquid CO₂ spreading on a Cu surface. The images are recorded at two different levels of subcooling, with the lowest level in (a) and the highest level in (b). The liquid front will gradually cover the entire surface at sufficient subcooling, higher than shown here 33
- 3.10 CO₂ condensation on Al at three levels of subcooling: (a) 1.2 K, (b) 1.6 K and (c) 2.1 K. The saturation pressure is 10 bar in all cases. The condensate film retention at the bottom of the surface increases with increased subcooling, as the film thickness and condensation rate increase with subcooling. 34
- 3.11 Theoretical and experimental heat flux data for CO₂ condensation on the bare Cu cylinder and on the Cu sample while attached to the cylinder with the TIM. All experimental data lies within the values of uncertainty, and within a 15 % deviation from the Nusselt model. The figure is also shown in Paper II. 37
- 3.12 Results of finite element analysis of the temperature distribution on (a) Cu, (b) Al, and (c) Steel. The samples are attached to the Cu cylinder with 1.5 mm thick Thermal Interface Material (TIM). The heat flux is set to 10 kW m⁻². The perimeter if the cylinder is isolated (zero heat flux), while the samples are not (heat flux set to 10 kW m⁻² in the radial direction). 39
- 3.13 Fabrication of the hierarchical structures consists of three steps: 1) Photolithography, 2) Chemically Assisted Ion Beam Etch and 3) Solution Immersion. 40
- 3.14 Scanning Electron Microscope images of CuO nanostructures on a Cu substrate fabricated by solution immersion. 42
- 3.15 Scanning electron microscopy images of the two hierarchical surfaces fabricated and studied in this work. For both surfaces the length of the nanoneedles are approximately 10 μm. (a) and (b) show the surface of the S17 substrate. The nanoneedle density is not uniform and the nanoneedles have preferentially grown on the sides of the micropillars. (c) and (d) show the surface of the S19 substrate at two different magnifications. The nanoneedles have grown around the sides of the micropillars, and in all directions. 43
- 4.1 Phase diagram of CO₂ showing the triple point and the critical point. 45
- 5.1 (a) The geometry of a micropillared surface. a is the pillars width, b is the spacing between the pillars and c is the height. (b) The results of a thermodynamic analyses simulating the contact angle of a static water droplet on the micropillars as a function of the pillar spacing to pillar height (b/a) [122]. The figure is also found in Paper I. 50

5.2	Condensation heat flux of CO ₂ on Cu, Al and Steel at 10, 15 and 20 bar saturation pressure, along with the Nusselt model for each pressure. The error bars represent the propagated errors of each measured quantity. These results are also shown in in Paper II.	52
5.3	Condensation HTC of CO ₂ on Cu, Al and Steel at saturation pressures of 10, 15 and 20 bar, and the Nusselt model for each pressure. These results are also shown in Paper II.	53
5.4	Condensation HTC for Cu, S17, S19 and NS at saturation pressures of 10, 15 and 20 bar. The figure is also found in Paper III.	55
5.5	Schematic representation of the proposed condensation mechanism. The volume flow rate, \dot{V}_{liq} , is directed downward in the sketch. (a) The condensation is initiated with nucleation and growth at the untreated Cu surface between the micropillars. The drainage of the condensate is increased due to the nanoneedles, and the condensate film is thinner than on a flat surface. (b) The thermal conductivity of the composite layer, k_{eff} , is higher than the thermal conductivity of the pure condensate, k_{CO_2} . The composite layer is the combination of the condensate and the nanoneedles.	56

List of Tables

3.1	Table with the estimated uncertainties used for calculating the overall uncertainties in heat flux and subcooling.	36
3.2	Theoretical effect of variation in surface temperature on the condensation HTC. The numbers are representative results from the finite element analysis shown in Figure 3.12. T_m is the average temperature, T_0 is the temperature in the center of the sample, and Δh_{Nu} is the percentage error in HTC caused by averaging the surface temperature.	38
4.1	Relevant thermophysical properties of CO ₂ at the two-phase line . . .	46
4.2	MA and RMS roughness of the investigated surfaces, along with typical values for the surface energies and thermal conductivities. The surface energy for the aluminum sample is given for Al ₂ O ₃ as an Al surface in atmospheric environment will be oxidized.	47
4.3	Geometry and dimensions of the fabricated micro- and nanostructured surfaces: S17, S19 and NS.	47

List of abbreviations

Al Aluminum.

CAIBE Chemically Assisted Ion Beam Etch.

CCS Carbon Capture, Transport and Storage.

CO₂ Carbon Dioxide.

Cu Copper.

CuO Copper Oxide.

DWC Dropwise Condensation.

FWC Filmwise Condensation.

HTC Heat Transfer Coefficient.

LIS Lubricant Infused Surface.

MD Molecular Dynamics.

NN Nano Needles.

NS Nanostructured Surface.

P&ID Piping and Instrumentation Diagram.

PR Photo Resist.

RIE Reactive Ion Etch.

SLIPS Slippery Lubricant Infused Porous Surface.

TIM Thermal Interface Material.

Contents

Preface	i
Abstract	iii
General summary	v
Generelt sammendrag	vii
List of contributions	ix
Acknowledgements	xv
List of figures	xvii
List of tables	xix
List of abbreviations	xxi
1 Introduction	1
1.1 Motivation	1
1.2 Liquefaction of CO ₂ - research needs	4
1.3 Objectives	7
1.4 My contribution to the field	8

2	Background	11
2.1	Condensation heat transfer	11
2.1.1	Filmwise condensation (FWC)	12
2.1.2	Dropwise condensation (DWC)	16
2.2	Liquefaction of CO ₂	19
2.2.1	Liquefaction in Carbon Capture, Transport and Storage	19
2.2.2	CO ₂ as a refrigerant	20
2.2.3	Enhanced condensation of CO ₂	21
3	Methodology	23
3.1	Achieving steady state condensation of CO ₂	23
3.2	Observing the condensation process	27
3.3	Heat transfer measurements	28
3.3.1	From cylinder heat flux to condensation heat transfer coefficient	29
3.3.2	Data acquisition	31
3.3.3	Observing filmwise condensation	32
3.3.4	Uncertainty analysis of the heat transfer experiments	34
3.4	Validation of the experimental method and setup	36
3.5	Fabrication of micro- and nanostructured surfaces	40
3.5.1	Photolithography	40
3.5.2	Chemically Assisted Ion Beam Etch	41
3.5.3	Nanoneedles grown by Solution Immersion	41
3.5.4	Hierarchical structures	42
4	Chemicals and materials	45
4.1	Thermophysical properties of CO ₂	45
4.2	Investigated materials	46

5	Main results	49
5.1	Condensation mechanisms - knowledge from dropwise condensation of water extracted for CO ₂	49
5.2	Novel experimental methodology and measurements of heat transfer characteristics of CO ₂ condensation on common heat exchanger materials	51
5.3	Enhanced CO ₂ condensation heat transfer on Cu based micro- and nanostructured surfaces	54
5.4	Application of the results in paper II and III	57
6	Conclusions and further work	59
6.1	Summary and conclusions	59
6.2	Suggestions for further work	61
	References	65
A	Papers	76
A.1	Paper I	76
A.2	Paper II	91
A.3	Paper III	111
B	Publication list	125

Introduction

Condensation heat transfer is a complex process that has been studied extensively the previous decades. We know how to take advantage of the superior heat transfer in the phase change process, but still there is a lot of unexploited potential. Through the work with this thesis, we have moved one step closer to understanding the complex nature of the condensation process, and especially that of CO₂.

This PhD thesis is divided into five chapters. In Chapter 1 (Introduction) the main motivation of the research is presented. I have stated what has been studied previously, and which research questions remain. The objectives of the work and how I have tackled the research questions are also a part of the introduction. In Chapter 2 (Background) the theoretical background of the work is given. In this chapter the fundamental theories that have been applied in the work, and how other research groups have adapted the theories is presented. In Chapter 3 (Methodology) the research methods that have been applied in this thesis are thoroughly described. The methods are chosen to solve the research tasks set forth in Chapter 1 in the most appropriate way. The answers to the research questions are summarized in Chapter 4 (Main results), which is written as a summary of the three papers that constitutes this thesis. Finally, the conclusions of the research work, the significance of the results and suggestions for how the research should be continued in future work is presented in Chapter 5 (Conclusions and further work).

As an appendix, the three papers resulting from this PhD work are included. The first paper is published in *Advances in Colloid and Surface Technology*, the second is under review in *Experimental Thermal and Fluid Science*, while the third is published in *International Journal of Heat and Mass Transfer*.

1.1 Motivation

Condensation of vapor is a phase change process that occurs in numerous applications, both in household equipment such as refrigerators and heat pumps, and in

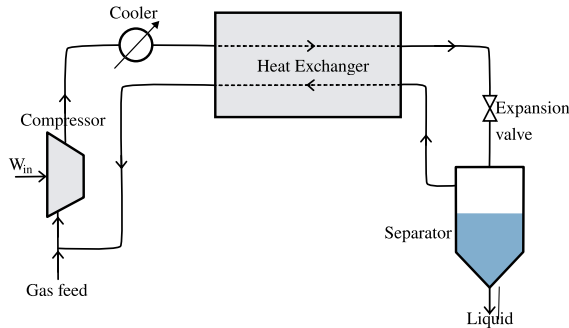


Figure (1.1): *The Hampson-Linde refrigeration cycle was the first cycle to use regenerative cooling in a condensation process. The feed gas is compressed and the compressed gas is fed through a cooler. The cold pressurized gas flows through a heat exchanger before expansion in a Joule-Thomson expansion valve. The gas is now at its coldest and at low pressure, and in a separator the liquid is condensed and drained. The un-condensed cold gas is fed back into the counterflow heat exchanger to work as a coolant for the incoming compressed gas and finally being fed back into the cycle.*

industrial processes for e.g. thermal management. Also in the power industry, pressurized gas is converted to liquid in a condenser as a part of the power generation. Hampson and Linde were the first two to file for a patent on a regenerative cooling cycle in the late 19th century [6, 7]. The cycle is today called the Hampson-Linde cycle and the steps are shown in Figure 1.1. Even though this is a fairly simple cycle, the most important equipment of a refrigerant cycle are included: the compressor, the cooler, the heat exchanger and the separator. The condensation occurs in the latter two. Increasing the heat transfer of the inner surfaces of the heat exchanger channels and the separator walls, e.g. by augmenting the surfaces, will increase the process efficiency. Independent of the scale of the system, the mechanisms governing the condensation process are important to unravel and to control. Condensation heat transfer is generally much more efficient than heat transfer without phase change as the release of latent heat in the gas is a part of the process. During the condensation, the latent heat is transferred to the condenser solid surface, which results in large heat transfer coefficients even for small temperature differences.

Condensation occurs in one of two modes, or a combination, namely the conventional Filmwise Condensation (FWC) and the generally more efficient Dropwise Condensation (DWC). FWC on flat vertical surfaces was thoroughly examined in the early 1900's and especially the work by Nusselt has drawn a lot of attention. The Nusselt model has been the standard way of modelling FWC heat transfer the last 100 years [8, 9]. For DWC, the pioneering work of Schmidt et al. laid the foundation of a large research field [10], further developed by Le Fevre and Rose during the 1960's [11–13]. The development of techniques for fabrication of structures on the nanoscale has increased the interest and research focus on DWC during the 1990's and 2000's [14].

The work with understanding and modelling the condensation heat transfer process started over a decade ago, and in the first half of the 1900's, several studies on the topic were reported [8, 15–18]. Still, fluids with properties far from that of water, such as liquid metals and condensates with very low surface tension, have proven hard to predict with the Nusselt model. Bromley stated already in 1952 that the heat capacity has the opposite influence on the heat transfer coefficient as predicted by the Nusselt model [15], while Rohsenow claimed that a modified expression for the latent heat, including the influence of the change in heat capacity with subcooling, will result in a more accurate Nusselt model [16].

Even though condensation heat transfer is already an efficient way of transporting heat due to the release of latent heat in the phase change process, there are a variety of solutions to enhance the heat transfer efficiency further. With a more efficient condensation process the energy demand will be lower, or we can, with the same energy input, achieve increased heat transfer or additional amount of condensate. Even more, increased condensation efficiency can aid in reducing the size of cooling equipment such as heat pipes for small electronics [19] or enabling a better thermal management in high-power systems [20]. As stated previously, DWC is the most efficient mode of condensation. DWC requires a non-wetting surface towards the condensate, and can typically be achieved by coating a surface with a low-surface energy chemical and/or structuring a surface with micro- and nanosized features [21–27]. Also, the combination of nanostructuring a surface followed by infusion of a chemical with low surface energy, could result in DWC [28–34]. This is called a Lubricant Infused Surface (LIS) or Slippery Lubricant Infused Porous Surface (SLIPS). The LIS/SLIPS provide an atomically flat liquid-liquid interface towards the condensate, and as long as the chemical and the condensate are immiscible (along with a few other criteria [35]) the condensing liquid will form highly mobile droplets on the surface. Even some low surface tension fluids have been reported to condense in the dropwise mode on SLIPS [36, 37]. However, the requirement for immiscibility between the lubricant and the condensate has proven hard to achieve, and as the lubricant and the condensate are mixed and removed from the surface, lubricant depletion leads to a rapid deterioration of the DWC [37]. In addition, the lubricants suitable for low surface tension fluids are often highly volatile and will evaporate within minutes or even seconds if not continuously applied to the LIS [38].

As a consequence of the challenges connected to DWC of low surface tension fluids, an enhancement of the FWC heat transfer has been pursued. The main cause of the lower heat transfer for FWC is the heat transfer resistance through the liquid film. A reduction in the thickness of the film is thus a viable solution for increasing the heat transfer by conduction through the film. Jin et al. [39] studied paraffin coated Copper (Cu) surfaces for enhanced condensation heat transfer of a low surface tension refrigerant. The paraffin coating resulted in a 10% enhancement of the Heat Transfer Coefficient (HTC) compared with a bare Cu surface. This was attributed to a thinner condensate film caused by increased drainage, which again was caused by the low surface energy of the coated Cu. Aili et al. [40] also studied the condensation of a low surface tension refrigerant. They investigated the heat transfer enhancement of FWC on a microporous Aluminum (Al) surface. However, they showed no change in the heat transfer on microstructures, with a hydrophobic coating or on an oil infused microporous surface, i.e. a SLIPS.

Surface roughness may play an important role in condensation [41], and an alteration of the HTC with micro- and nanostructures have been widely investigated [1, 42–44]. However, whether the role of the roughness is to enhance or decrease heat transfer efficiency is still under debate. Soontarapiromsook et al. [45] concluded that roughness increases the condensation HTC, while the opposite was the case in the study by Yun et al. [46]. A reduction of HTC was also the case in the report from Budakli et al., who studied water condensation on structured Cu surfaces [47]. They actually reported a 30% reduction in the HTC on a microstructured surface. Induced roughness through growth of nanowires has, however, shown to increase the phase-change heat transfer [48, 49], both for condensation, boiling and evaporation. These are all important phase-change processes for thermal management of e.g. electronic equipment. The results are highly dependent on the choice of material, the fabrication of the structures and on the different length scales of the structures. Consequently, more studies on various types of micro- and/or nanostructured surfaces are necessary for closing the knowledge gaps relating to roughness and phase-change heat transfer.

Preston et al. [50] showed that wicking condensation is a solution for increasing condensation efficiency. This mode of condensation is especially interesting for low surface tension fluids for which DWC is not a viable solution, and for enhancing durability of the structured surfaces. The latter has been a recurring problem for many of the surfaces exhibiting large enhancements in heat transfer [51, 52]. Either nanostructures are distorted by the condensation process, or lubricants for use in LIS/SLIPS are gradually drained from the surface. Some of the surfaces show poorer heat transfer after such failure, compared with conventional, unstructured surfaces. Cu foam wicks can, on the other hand, withstand mechanical abrasion and are robust and durable [53]. In the work by Preston et al., the wicking condensation HTC of pentane increased 3 or 4 times depending on the width of the Cu wicks, at low levels of subcooling. Their model result in a maximum increase of 8 times the FWC values (compared with the Nusselt model) for the highest possible subcooling before the wick is flooded with condensate and the enhancement effect diminishes. The wicking condensation mode has a large potential and should be examined for other low surface tension fluids, such as CO₂, as well.

1.2 Liquefaction of CO₂ - research needs

Anthropogenic emissions of CO₂ are increasing at a rate too high for a sustainable future. According to the International Panel of Climate Change, Carbon Capture, Transport and Storage (CCS) will play a key role for reducing these emissions [54, 55]. Two major obstacles to implementing CCS technology at all sources of CO₂ emission are the costs and the energy consumption [56]. For adsorption based technology, which is the capture technology mainly implemented today, the energy consumption of the capture process alone could be 20% of the power generated from a power plant [57, 58]. Increased capture efficiency in terms of costs, energy demand and footprint of equipment is therefore highly necessary in order to reach full-scale deployment of CCS. As CO₂ condensation is a part of some of the CCS

chains, a reduction of CO₂ condensation energy demand will reduce the costs of the CCS systems, which again will result in an increase in the number of CCS projects globally [59].

Condensation of CO₂ in heat exchangers and separators occurs in processes where a gaseous, CO₂-rich stream is liquefied, for example in order to purify the gas to ensure that it satisfies transport specifications. This solution for purification is commonly selected in the Gas Processing Unit of an oxyfuel power plant [60, 61]. CO₂ capture by separation through phase change, i.e. separation by condensation, is also proposed as an efficient route for mitigating the CO₂ emissions [62, 63]. In some cases, it could be the most cost-efficient solution [64]. Purification by condensation and separation could also be applied as a last step after novel post-combustion capture technologies such as Vacuum Pressure Swing Adsorption and membrane separation [65]. High capture rates may be obtained in the adsorption process alone, but at a high energy penalty due to the needed vacuum pressure [58]. A single stage membrane typically yields a gaseous flow with a CO₂ concentration in the range of 60 % - 70 % [65]. Hence, for both technologies, purification by condensation and separation may be competitive. A combined membrane-liquefaction CO₂ capture technology has also been proposed, overcoming some of the challenges with a one-step process [66]. Another strategy to combine existing technologies is to use solar power to integrate power generation, CO₂ capture and production of liquefied CO₂ [67].

Following capture, CO₂ must be transported in a safe and cost-efficient way to the storage location. Traditionally, CO₂ has been transported via pipeline in a compressed state. Transporting captured CO₂ by ship in the liquefied state will, at certain conditions, be the cost efficient solution, compared to pipeline transport [68–72]. Transportation of liquid CO₂ has the advantage of high density and high capacity utilization. CO₂ transportation by ship also provides flexibility compared to the establishment of pipeline infrastructure [69, 70, 73]. Ship transportation is particularly advantageous for long-distance transport of limited quantities of CO₂, which is typical for many CO₂ point sources in the Nordic countries. In the Nordic CCS Roadmap, ship transportation was evaluated as the most cost efficient solution for 45 out of 55 potential Nordic CCS chains [74]. However, liquefaction of CO₂ is in itself an energy intensive process, and enhancing the heat transfer efficiency, thus decreasing the energy demand, will reduce the costs of CO₂ transport. To enable ship transport of CO₂ captured in gaseous phase e.g. through adsorption, a downstream liquefaction step is needed. For this reason, the implementation of efficient heat exchangers and separators will contribute to reduced costs regardless of capture technology.

Despite the focus on mitigating CO₂ emissions, CO₂ is not only regarded as a problematic greenhouse gas, but a useful fluid for heat exchanger technology [75]. In several refrigeration systems such as heat pumps, air-conditioners, vending machines and water heaters, the refrigerant has traditionally been fluorine based chemicals with a large negative environmental impact [76]. The motivation for finding alternative refrigerants is therefore high, and one solution is to use CO₂. The thermo-physical properties of CO₂ are beneficial for efficient refrigeration and heat transfer, along with its relatively low global warming potential compared with traditional

refrigerants [77, 78]. Especially, CO₂ is a suitable refrigerant for compact heat exchangers, e.g. for motor-vehicle air conditioning and residential air-conditioning, or in systems where the requirement for uniformity and control is very high, such as in applications in space [75, 79–81]. Since CO₂ is a promising refrigerant, the research on CO₂ condensation has been focused on CO₂ behavior during two-phase flow in channels and tubes and on flow condensation heat transfer in macro- and microchannels. Especially flow patterns and HTC dependency on mass flux and vapor quality has been under intensive study [80, 82–91]. Modelling condensation heat transfer of CO₂ in a tube or microchannel has proven to be difficult, which the large discrepancies in existing studies prove [89]. Huai and Koyama [82] indicated that the mass velocity of CO₂ had a large impact on the condensation HTC data, but the scattering in the results is too large to conclude. The study also showed large discrepancies when comparing to existing models. The discrepancies are attributed to the large variation in CO₂ properties in the near-critical region, and that the models are developed for other refrigerants without this variation in properties. Park and Hrnjak [83] investigated the flow condensation HTC at saturation temperatures of -15 and -25 °C. The results were compared with two well-known models for heat transfer in channels and it was again shown that the flow pattern and the HTC were strongly correlated. The direct relation between the thermophysical properties and HTC is, however, not apparent and modelling flow condensation HTC based on thermophysical properties for various fluids has not yet been successful. Kang et al. [85] investigated the flow condensation of CO₂ in a horizontal smooth tube with varying mass flux and condensation temperature. The study concluded that the influence by mass flux on the HTC was minor. The variation in the data is, however, striking. A comparison with previous studies is not consistent, without any apparent reason. Li and Norris [90] developed a model for CO₂ flowing in a tube at low temperatures. Previous flow condensation heat transfer models overpredict the condensation rate of CO₂, e.g. the Thome et al. model [92]. Li and Norris underlined the importance of the special thermophysical properties of CO₂ compared to traditional refrigerants. At relevant saturation temperatures, the enthalpy of vaporization, the thermal conductivity and the specific heat are significantly higher than for the conventional refrigerants. The high enthalpy of vaporization of CO₂ results in a high conductive heat flux through the condensate during FWC. These studies show that the condensation of CO₂ is not yet fully understood.

The literature mentioned above consists of studies on CO₂ condensation at low temperatures with the application of CO₂ as a refrigerant in mind. However, there have also been some reports on the investigation of CO₂ condensation at near-critical or supercritical temperatures and pressures, as these are relevant for pipe transport during CCS. Baik and Yun [93] studied the in-tube condensation of CO₂ and CO₂+ N₂ between 20 and 30 °C. The CO₂+ N₂ mixture is commonly found as the product after CO₂ capture, especially for CO₂ capture by chemical adsorption. Since the thermophysical properties of CO₂+ N₂ mixtures deviates from pure CO₂ [94], studies on mixture flow pattern and heat transfer are important. Lee and Yun [95] extended the number of mixtures to include CO₂+ CH₄ and CO₂+ Ar, which they investigated in a tube under supercritical conditions.

Despite all the effort on flow condensation of CO₂ in tubes and macro- and microchannels, the effect of the condenser's surface properties on condensation heat

transfer has not been investigated. The relevant models to compare the experimental data with do not include surface properties, and if flat surfaces are considered it is the Nusselt model yet again that is used for comparison. The previous studies on CO₂ do not focus on enhanced CO₂ condensation efficiency either, but focus on understanding the mechanisms governing the condensation. There is therefore a need for a method and equipment to investigate different types of materials and surfaces and how these influence the condensation heat transfer. This is exactly what is presented in this thesis. We have conducted studies to better understand the influence of material and surface properties and the surface structures on the heat transfer. To eliminate the effect of flow conditions and pressure drop in channels, the investigations have been conducted with a stagnant saturated vapor on a vertical surface and compared with the traditional Nusselt model.

1.3 Objectives

The main aim of this thesis has been to understand the mechanisms governing heat transfer during condensation, and to develop surfaces with increased heat transfer efficiency. Specifically, we wanted to reveal how the condenser surface influences the heat transfer, answering to the challenges set forth in the previous section. Thereby, one objective on the way was to establish an experimental methodology and laboratory setup to measure heat transfer during condensation, and to observe the condensation process. We wanted to develop a method that was versatile, enabling the investigation of several materials, but also a variation of gases for additional applications of the methodology. The equipment should be designed in such a way that the investigated surface can easily be replaced. Another objective has been to fabricate micro- and/or nanostructured surfaces on Cu in a repeatable manner. The liquefaction process equipment are potentially large, so we aimed for finding fabrication techniques that balance cost and scalability, and at the same time, enhance heat transfer.

To summarize, the main objective in this work is:

- to find the optimum surface structure for efficient CO₂ condensation heat transfer by
 - drawing knowledge from increased heat transfer of liquefaction of water to CO₂ condensation
 - developing a methodology for measurement of heat transfer, where the solid surface can easily be switched between different materials, included micro-and nanostructured ones
 - gaining understanding of the CO₂ condensation process
 - studying the effect of surface structures on the condensation heat transfer and revealing the optimal condensation surface

The objectives are summarized in the work flow diagram shown in Figure 1.2. Here,

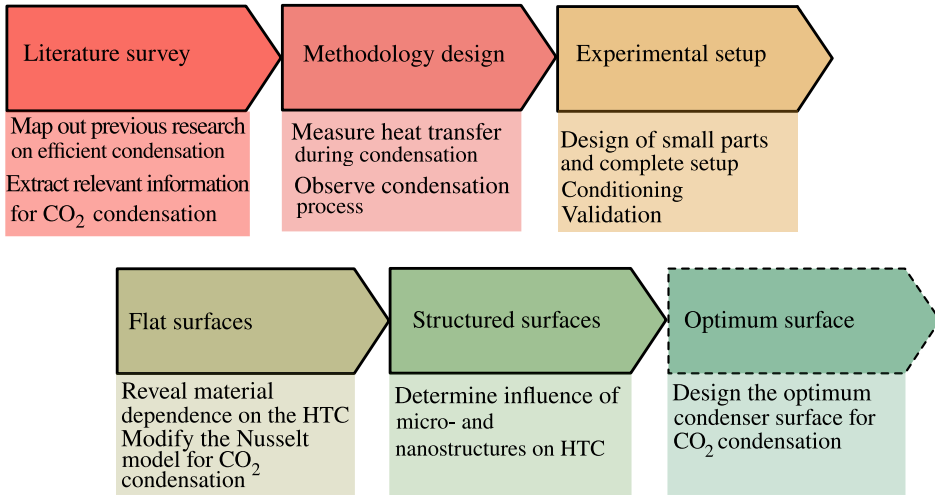


Figure (1.2): A work flow diagram showing the stages of the work in this thesis. Included is also a scenario of where this work could lead, namely to design the optimum surface for CO₂ condensation.

I have included a possible continuation of the work into the design of the optimum condenser surface for efficient CO₂ condensation.

1.4 My contribution to the field

During the work with this PhD thesis, I have developed knowledge that is important for condensation heat transfer in general and for CO₂ liquefaction in particular.

Firstly, I have conducted a literature survey of relevant research on condensation heat transfer, especially focusing on DWC. The literature review goes through the most important concepts for understanding hydrophobicity, such as contact angle, contact angle hysteresis and how they are altered by surface roughness and modification. The review is informative for a reader who is getting into the field of wetting and surface modification, and gives an overview of the recent development in the field. Surface design models for fabricating superhydrophobic surfaces are reviewed, with focus on the geometric specifications necessary for obtaining stable non-wetting surfaces. Importantly, the review also gives a novel view on how to extend the research on superhydrophobic surfaces to superomniphobic surfaces, and especially with focus on low surface tension fluids such as CO₂.

Secondly, I have developed a methodology and working principles for experimentally determining the HTC during condensation. With the method it is possible to examine several factors influencing the heat transfer, such as the choice of material and surface structures. An experimental laboratory facility is designed, built and commissioned and is readily available for studying CO₂ condensation in detail. The

setup is built in such a way that other gases can be examined at a later stage, which is important for building a general knowledge database for condensation heat transfer on different materials. The well-known Nusselt model does not include surface properties of the condenser material, and systematic studies of the effect of surface structures on heat transfer will result in more accurate models for engineering applications.

Finally, I have laid the foundation for further investigation of the influence of micro- and nanostructures on the condensation efficiency. The direct investigation of structures fabricated in NTNU Nanolab in the heat transfer setup in SINTEF Energy had not been done previously, and important steps have been taken towards fabricating an optimal surface for CO₂ condensation. In my study I have found that a balance in the relative size of the structured and the un-structured areas of the surface is beneficial for the heat transfer. The nanostructures increase the surface area, and therefore the heat transfer. I do not believe that the optimum surface has been fabricated yet, but we have reported important indications on what design parameters to pursue in future work.

No studies on detailed investigation of CO₂ condensation on flat and structured surfaces are previously reported in literature. My work has therefore initiated a promising new line of investigation regarding condensation, and when continued, will help in designing even more efficient liquefaction processes and equipment.

Background

2.1 Condensation heat transfer

Condensation is the phase change process between gas and liquid, in which latent heat in the gas is transferred to the surface on which the condensation occurs. The initiation of condensation starts with liquid nuclei forming and growing on a surface. The nuclei typically form on impurities or non-uniformities on the surface, such as spikes, where the surface energy is higher than the average. In conventional condensation, the droplets grow as more gas releases latent heat and condense into the nuclei, or as droplets coalesce, until the coalescence is complete and a liquid film covers the surface. Subsequently, the condensation occurs directly into the liquid film and the latent heat is conducted through the film to the condenser surface. This is the FWC mode of condensation and occurs on flat unmodified surfaces when the surface energy is higher than the liquid surface energy. If the energy difference is the opposite, most often caused by surface modification, the droplets will not coalesce into a film. They will, however, be removed from the surface by gravity, due to the weak interactions between the surface and the droplet. This is the DWC mode of condensation and was first recognized by Schmidt et al. in 1930 [10]. A schematic presentation of the condensation modes is shown in Figure 2.1.

The key parameters when measuring condensation heat transfer are the surface temperature, the saturated vapor temperature and vapor pressure. Through measuring these parameters, calculations will give the heat flux and the HTC in terms of sub-cooling or other factors. Broadly speaking, there are three methods for measuring the heat rate in the condensation process, \dot{Q} :

1. Controlling the mass flow rate, \dot{m} , and measuring the temperature change in the refrigerant, ΔT_{ref} :

$$\dot{Q} = \dot{m}c_p\Delta T_{ref}$$

2. By collecting the condensate and measure the condensate mass flux:

$$\dot{Q} = \dot{m}h_{fg}$$

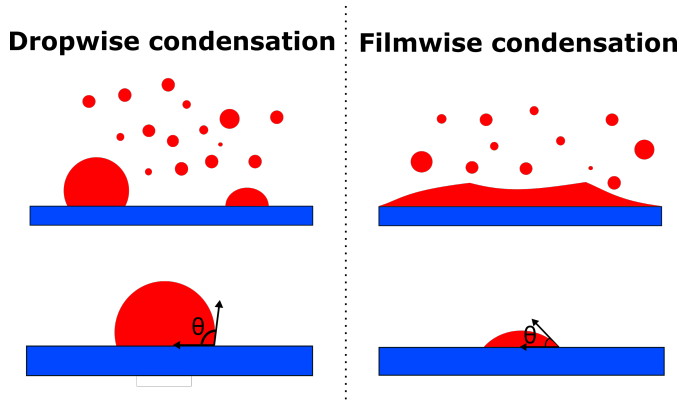


Figure (2.1): Schematic drawing of dropwise and filmwise condensation. The contact angle θ is an important parameter for determining the condensation mode.

3. Embedding thermocouples in the measurement block on which the condensation occurs on the end, and calculating the heat flux through the block

$$\dot{Q} = -kA\nabla T$$

Here, c_p is the specific heat capacity, h_{fg} is the latent heat, k is the thermal conductivity of the measurement block with surface area A and ∇T is the temperature gradient through the block. In this thesis, we have used method 3 with four thermocouples embedded in a Cu cylinder. Similar methods are e.g. used by Kim et al. [96], Preston et al. [50], and Ho et al. [97]. The adapted methodology is described in Chapter 3.

2.1.1 Filmwise condensation (FWC)

When a condenser's surface energy and the condensate surface tension is such that the condensate spreads on the surface, the condensation will occur in the filmwise mode. This is the case for conventional metals and condensates in industrial processes. After initial nucleation and growth, the condensate will spread across the surface as a continuous film. The condensate film then serves as a resistance to further heat transfer. A theoretical description of FWC on a vertical surface was developed by Nusselt in the early 20th century [8, 9], and has been, and is still, used as the reference in condensation studies. The theory describes condensation on a vertical flat surface with laminar downward flow of the condensate, i.e. when the Reynolds number is less than 30. The condensing gas is assumed to be pure, quiescent and saturated. Figure 2.2 shows the setup used for developing the analytical Nusselt model.

The condensate is assumed to be in equilibrium with the saturated gas, and the interfacial thermal resistance between the vapor and the liquid is neglected. Consequently, the temperature of the gas-liquid interface is the same as the saturation

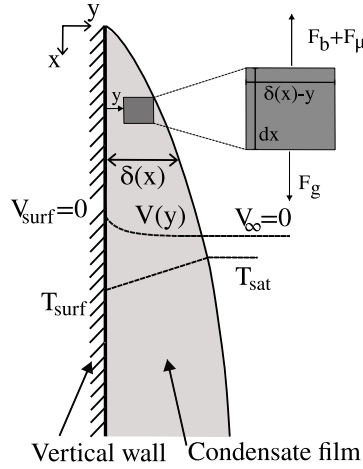


Figure (2.2): *Condensation on a vertical plate with the necessary parameters for deriving the Nusselt model.*

temperature at the given pressure, T_{sat} . The liquid is static at the condensate-solid interface, i.e. $V_{surf} = 0$, following the non-slip condition. The velocity of the liquid increases in the y -direction (coordinate system in Figure 2.2). In addition it is assumed that there is no drag force at the liquid-gas interface, and as the condensate flows downward, there will be no shear force on the liquid surface. The velocity of the liquid is assumed to be very small, resulting in negligible convective effects.

The condensate properties are evaluated at the film temperature, calculated as the average between the condenser surface temperature and the saturation temperature, $T_{film} = \frac{T_{surf} + T_{sat}}{2}$. The condensate properties are assumed constant within the film. The temperature profile in the film is assumed linear between the wall and the gas. All of T_{film} , T_{sat} and T_{surf} are therefore independent of x and y .

The Nusselt model is derived by performing a force, heat and mass balance on a differential element of liquid with height dx , width $\delta(x) - y$ and depth b , as shown in Figure 2.2. The forces on the element are the buoyancy force, F_b , given by Equation (2.1.1), viscous shear force in the liquid, F_μ , given by Equation (2.1.2), and gravity, F_g , given by Equation (2.1.3).

$$F_b = \rho_v V g = \rho_v (b dx (\delta(x) - y)) g \quad (2.1.1)$$

$$F_\mu = \mu_l \frac{du}{dy} (b dx) \quad (2.1.2)$$

$$F_g = m g = \rho_l b dx (\delta(x) - y) g \quad (2.1.3)$$

Here, ρ_v is the density of the vapor, $V = b dx (\delta(x) - y)$ is the volume of the differ-

ential element, μ_l is the viscosity of the liquid, m is the mass of the liquid in the differential element and g is the gravitational acceleration constant. The forces on the differential element is balanced, since momentum effects are neglected in the model development. The force balance gives that: $F_g = F_b + F_\mu$, or

$$\rho_l b dx (\delta(x) - y) g = \rho_v (b dx (\delta(x) - y)) g + \mu_l \frac{du}{dy} (b dx). \quad (2.1.4)$$

Solving for $\frac{du}{dy}$ we get

$$\frac{du}{dy} = \frac{(\rho_l - \rho_v)(\delta(x) - y)g}{\mu_l}. \quad (2.1.5)$$

Integrating with respect to u between 0 and $u(y)$ and y between 0 and y , yields:

$$\int_0^{u(y)} du = \frac{(\rho_l - \rho_v)g}{\mu_l} \int_0^y (\delta(x) - y) dy \quad (2.1.6)$$

$$u(y) = \frac{(\rho_l - \rho_v)g}{\mu_l} \left(\delta(x)y - \frac{1}{2}y^2 \right) \quad (2.1.7)$$

The mass flux through the condensate film at a point x is found by integrating density times the velocity profile in Equation (2.1.7) over the cross sectional area of the control volume, $A = bdy$,

$$\dot{m}(x) = \int_A \rho_l u(y) dA = b \int_y \rho_l u(y) dy \quad (2.1.8)$$

$$= \frac{b\rho_l(\rho_l - \rho_v)g}{\mu_l} \int_0^{\delta(x)} \delta(x)y - \frac{1}{2}y^2 dy \quad (2.1.9)$$

$$= \frac{b\rho_l(\rho_l - \rho_v)g}{\mu_l} \frac{\delta(x)^3}{3} \quad (2.1.10)$$

The derivative of the mass flux, needed below, is

$$\frac{d\dot{m}}{dx} = \frac{b\rho_l(\rho_l - \rho_v)g}{\mu_l} \delta(x)^2 \quad (2.1.11)$$

The heat transfer at the liquid-wall boundary is given by

$$\frac{k_l \Delta T b dx}{\delta(x)}, \quad (2.1.12)$$

where $\Delta T = T_{sat} - T_{surf}$. The heat transfer at the vapor-liquid interface is caused by transfer of latent heat of condensation, h_{fg} , and is given by

$$h_{fg}d\dot{m}, \quad (2.1.13)$$

where $d\dot{m}$ is the mass flux entering the control volume. To balance the heat transfer, we equate Equation (2.1.13) and Equation (2.1.12) and we get an expression for the derivative of the mass flux:

$$h_{fg}d\dot{m} = \frac{k_l\Delta T b dx}{\delta(x)} \quad (2.1.14)$$

$$\frac{d\dot{m}}{dx} = \frac{k_l b \Delta T}{h_{fg} \delta(x)} \quad (2.1.15)$$

Inserting the derivative of the mass flux from Equation (2.1.11), we get

$$\frac{b\rho_l(\rho_l - \rho_v)g\delta^2}{\mu_l} \frac{d\delta}{dx} = \frac{k_l b \Delta T}{h_{fg} \delta(x)} \quad (2.1.16)$$

$$\delta(x)^3 \frac{d\delta}{dx} = \frac{k_l \mu_l \Delta T}{h_{fg} \rho_l (\rho_l - \rho_v) g} \quad (2.1.17)$$

To get an expression for the film thickness at a given point x , we integrate Equation (2.1.17) between $\delta(0) = 0$ and $\delta(x) = \delta$ for δ and between 0 and x for x :

$$\int_0^\delta \delta(x)^3 d\delta = \int_0^x \frac{k_l \mu_l \Delta T}{h_{fg} \rho_l (\rho_l - \rho_v) g} dx \quad (2.1.18)$$

$$\frac{1}{4} \delta(x)^4 = \frac{k_l \mu_l \Delta T x}{h_{fg} \rho_l (\rho_l - \rho_v) g} \quad (2.1.19)$$

$$\Rightarrow \delta(x) = \left(\frac{4k_l \mu_l \Delta T x}{h_{fg} \rho_l (\rho_l - \rho_v) g} \right)^{1/4} \quad (2.1.20)$$

The local HTC, $h(x)$, in the liquid film equals the thermal conductivity of the liquid divided by the thickness of the film at the point in x . This is a result of the assumption that the liquid velocity is low and, consequently, that heat transfer in the film is by conduction only. The heat flux is therefore given by Newtons law and Fouriers law, and they can be equated:

$$q(x) = h(x)\Delta T = k_l \frac{\Delta T}{\delta(x)} \Rightarrow h(x) = \frac{k_l}{\delta(x)} \quad (2.1.21)$$

By inserting Equation (2.1.20) for $\delta(x)$ we get the following expression for the local HTC

$$h(x) = \left(\frac{\rho_l(\rho_l - \rho_v)k_l^3 h_{fg} g}{4\mu_l \Delta T x} \right)^{1/4} \quad (2.1.22)$$

The Nusselt model has been the subject of many studies, and is used as is for many applications. However, a modification of the latent heat to account for advective effects is recommended by Rohsenow and widely accepted [16]. The latent heat used in this work is therefore

$$h'_{fg} = h_{fg} + 0.68c_{p,l}\Delta T \quad (2.1.23)$$

Finally, the average HTC is found by integrating the local HTC over the height of the vertical wall, L .

$$\bar{h} = \frac{1}{L} \int_0^L \left(\frac{\rho_l(\rho_l - \rho_v)h'_{fg} g}{4k_l^3 \mu_l \Delta T x} \right)^{1/4} dx \quad (2.1.24)$$

$$= \frac{4}{3} \left(\frac{\rho_l(\rho_l - \rho_v)k_l^3 h'_{fg} g}{4\mu_l \Delta T L} \right)^{1/4} \quad (2.1.25)$$

Equation (2.1.25) is the Nusselt model for condensation on a vertical plate.

2.1.2 Dropwise condensation (DWC)

When a condenser surface is non-wetting towards the condensate, i.e. that the surface energy of the condenser material is lower than the surface tension of the liquid, the condensate will form discrete droplets on the surface. Due to the non-wetting nature of the surface, the droplets easily roll off an inclined surface, and the condenser surface is available for new droplet nucleation and growth. The absence of the liquid film substantially reduces the heat transfer resistance and thereby increases the HTC. The process of DWC is initiated with droplet nuclei forming on a surface. The gaseous phase is saturated at this point, with pressure at or above the saturation pressure corresponding to the temperature on the condenser surface. The drops grow with continued condensation into the drop, and with coalescence with neighboring drops. Drop removal occurs either by gravity when the size is large enough for gravity to overcome the adhesion to the surface or by sweeping by already falling drops. The condenser surface is then free for new nucleation, growth and removal, resulting in a cyclic process on the surface.

The wetting nature of a surface is characterized by the contact angle between the solid surface and the liquid droplet (or film, for which the contact angle is zero), as

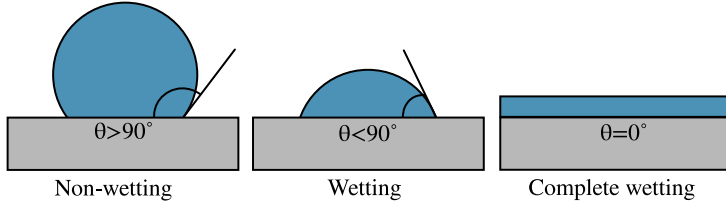


Figure (2.3): The wetting state of a surface is characterized by the contact angle in the three phase line between solid, liquid and gas, θ . The contact angle is above 90° for non-wetting surfaces, below 90° , but finite, for wetting surfaces, and equal to 0° for complete wetting surfaces.

shown in Figure 2.3. The contact angle, θ , was first described by Thomas Young in 1805 and is given by the Young's equation, Equation (2.1.26) [98].

$$\cos(\theta) = \frac{\gamma_{sv} - \gamma_{sl}}{\gamma_{lv}} \quad (2.1.26)$$

Here, γ_{sv} is the surface tension of the solid, γ_{sl} is the interfacial tension between the solid and the liquid and γ_{lv} is the surface tension of the liquid. A schematic drawing showing the relevant parameters is shown in Figure 2.4(a). There is always work consumed when constructing a surface, and the work is proportional to the added surface area. The interfacial, or surface tension is the proportionality constant between the work added and the surface area created. Surface tension depends on temperature, composition of the liquid or solid, and pressure, but is independent of the surface area. The surface is said to be wetting towards the liquid, if the contact angle is smaller than 90° . This is the case when the interfacial tension of the solid-liquid interface is smaller than the solid-vapor. The liquid will then spread across the surface, either totally to a liquid film, or towards a finite, but small value of the contact angle. In the opposite case, the surface is called non-wetting, and the terms hydrophobic (in the case when the liquid is water) and omniphobic (the more general term, especially used for low surface tension fluids) are commonly used. On an inclined surface, the droplet cap will no longer be spherical, and the contact angle on the advancing and the receding sides of the droplet will be unequal, depending on the surface structure and the interfacial tensions, as shown in Figure 2.4(b). The difference between advancing and receding contact angles is the definition of the contact angle hysteresis. If the contact angle is above 150° , and the contact angle hysteresis is below 10° , the surface is called superhydrophobic/superomniphobic. Such a surface is yet to be found on flat surfaces in nature, where the highest observed contact angle towards water is 120° [99].

The non-wetting nature of a surface can be enhanced by introducing roughness on a periodic or random manner [98, 100]. The apparent contact angle, θ_{app} , on such a surface depends on the roughness and is given by the Wenzel equation, $\cos(\theta_{app}) = r \cos(\theta)$. The roughness factor r is the ratio between the actual contact area (including the roughness) and the projected surface area, and will always be

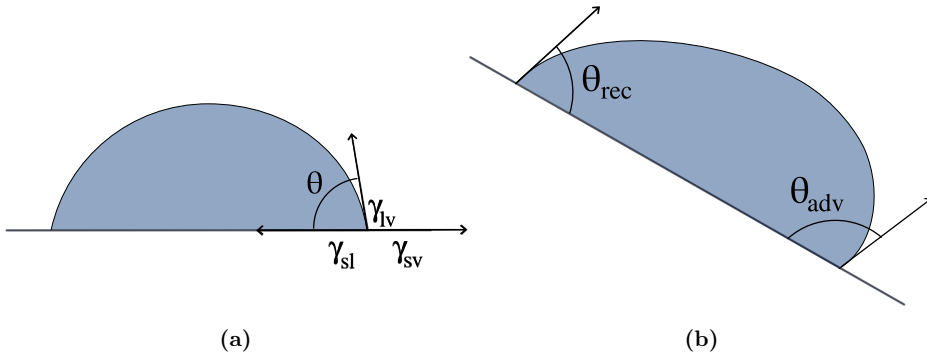


Figure (2.4): (a) A liquid droplet at rest on a solid surface. The contact angle, θ , is given by the interfacial tensions, γ , through Young's equation, Equation (2.1.26). (b) The receding (θ_{rec}) and advancing (θ_{adv}) contact angle on an inclined surface. The contact angle hysteresis is defined as the difference between the advancing and receding contact angles.

equal to or larger than 1. The result is that a surface that is wetting towards a liquid will become more wetting with roughness, while a non-wetting surface will become more non-wetting and the contact angle increases. In this manner, it is possible to structure a surface to become superomniphobic. However, a droplet in the Wenzel state will in most cases be pinned to the surface, and the contact angle hysteresis will be high. In the Wenzel state the liquid penetrates the rough structure, as shown in Figure 2.5(a). For increased droplet removal, which is imperative for efficient DWC, a droplet must therefore be in the Cassie-Baxter state, see Figure 2.5(b). In this case, air pockets are trapped underneath the droplets and the contact angle hysteresis will be significantly lower than in the Wenzel state [101, 102].

Apart from the influence of solid-liquid interactions (in terms of contact angle) on the condensation mode, there are properties of the liquid itself determining if the condensation will be DWC or FWC. A high surface tension will reduce the probability of coalescence, and thereby promote DWC. The same goes for high density and high viscosity. These factors can be combined into *coalescence time*, which were first modelled by Rose in 1967 [13]. His results suggest that the coalescence time will decrease with heat flux and that a transition from DWC to FWC will occur if the heat flux becomes large enough (i.e. coalescence time is small enough).

The mechanisms of heat transfer during DWC has been, and is still, under some debate. But, undisputably, one important factor is the condensate drop size distribution. Initially, the nucleated droplets are on nanometer scale, while several micrometer sized drops are present on the surface before departure, depending on pressure, surface energy and surface structures, among others. Already in 1973, both Graham and Griffith [103] and Rose and Glicksman [104] suggested a model for the drop size distribution, and gave a description of the heat transfer mechanism in the different drop size regimes. For the smallest droplets, the heat transfer is largely influenced by the surface curvature of the droplet and direct condensation

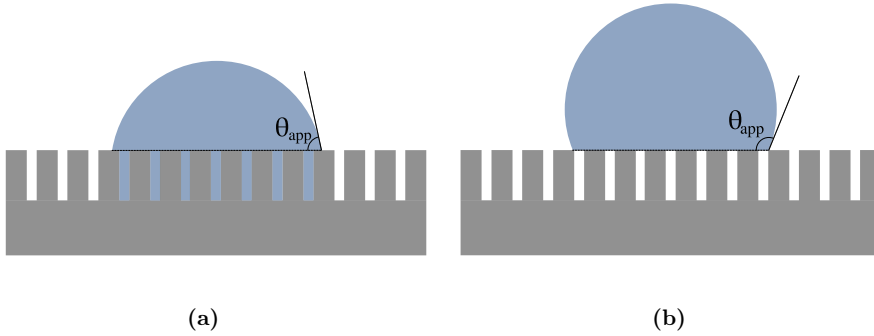


Figure (2.5): A droplet on a rough surface will either be in the Wenzel state (a) where the liquid fills the gaps in the rough surface, or in the Cassie state (b) where air pockets are trapped underneath the droplet. Intermediate states between the two extremes also exist.

into the droplet. For larger droplets, conduction through the droplet is the limiting and determining mechanism. It is therefore agreed that if the departure of small droplets is promoted, the condensation heat transfer will increase.

There are, in other words, many mechanisms that govern if the condensation on a surface will occur in the FWC mode or the DWC mode, and also affecting how efficient DWC is. The main focus of this work has been the condensation of CO₂ with its low surface tension. In the following, a background on the research on liquefaction of CO₂ is presented.

2.2 Liquefaction of CO₂

The liquefaction of CO₂ occurs to a large degree in two fields: either as a part of the CCS chain, or in a cooling cycle as a refrigerant. The two cases are elaborated in the following sections.

2.2.1 Liquefaction in Carbon Capture, Transport and Storage

In the CCS chain, the liquefaction of CO₂ occurs in the post-processing step after capture, or as a part of the capture process itself. The latter occurs in the oxy-fuel combustion process with CCS. Oxy-fuel combustion is the process of power generation by burning fossil fuels in an environment of pure oxygen. The resulting flue gas will mainly consist of CO₂ and water, as opposed to conventional power generation flue gas which is a mixture of CO₂ and e.g. N₂ or O₂, depending on the combustion process. The composition of the oxy-fuel flue gas makes it suitable for separation by condensation, leaving a highly concentrated CO₂ stream that can

directly be transported by ship, or compressed prior to pipeline transportation. This is also the case for the product resulting from CO₂ capture by a combination of membranes and liquefaction [65, 105]. The liquefaction of CO₂ is most efficient if there is a high degree of CO₂ in the gas. This is often not the case for flue gases and for example the exhaust from cement production consists of O₂, H₂O, CO₂ and N₂. In such cases the hybrid membrane/liquefaction capture technology has been shown to be a suitable solution in terms of techno-economical considerations [106].

If CO₂ is captured by more conventional capture techniques, such as amine adsorption, liquefaction is necessary to reduce the volume prior to shipping to the permanent storage locations e.g. underground in the North Sea [107]. Several CO₂ liquefaction cycles exist, based on either one refrigerant or a cascade system with multiple refrigerants. The latter consists of multiple steps with different refrigerants [68]. Common for all is the requirement of elevated pressures and low temperatures. The triple point occurs at 5.2 bar and 216.6 K = -56.6 °C. Studies have shown that transporting the CO₂ at around 7-9 bar is the most techno-economical solution [69].

An example of a proposed process for liquefaction of CO₂ prior to ship transportation is given by Lee et al. [108]. They proposed a direct condensation process using liquid natural gas (LNG) as a source for cooling energy. In most applications, the LNG must be evaporated prior to usage, and this evaporation could be the energy source for the CO₂ liquefaction. The results show that condensation around 145 to 165 K is most economic for direct condensation of CO₂.

2.2.2 CO₂ as a refrigerant

CO₂ has been proposed as an environmentally friendly and efficient alternative as a refrigerant. Li and Norris [90] underlined the importance of the special thermophysical properties of CO₂ compared to traditional refrigerants. At relevant saturation temperatures, the enthalpy of vaporization, the thermal conductivity and the specific heat are significantly higher than for conventional refrigerants. The high enthalpy of vaporization of CO₂ results in a high conductive heat flux through the condensate during FWC. This is also the case for a high thermal conductivity. The high specific heat of CO₂ could lead to one of the important assumptions of the Nusselt model to be invalid, namely the neglect of convective heat transfer.

Due to the special thermophysical properties of CO₂, it is especially suitable as a refrigerant in the the low-temperature circuit of a cascade system. Many such configurations have been proposed, with various refrigerants in the high-temperature cycle. A sketch of such a cascade system is shown in Figure 2.6. The choice of the high-temperature side refrigerant has been studied by many and a comprehensive comparison is made by Bellos and Tzivanidis [109]. As for all other refrigeration cycles, the important process equipment are the heat exchanger, the evaporator and the condenser.

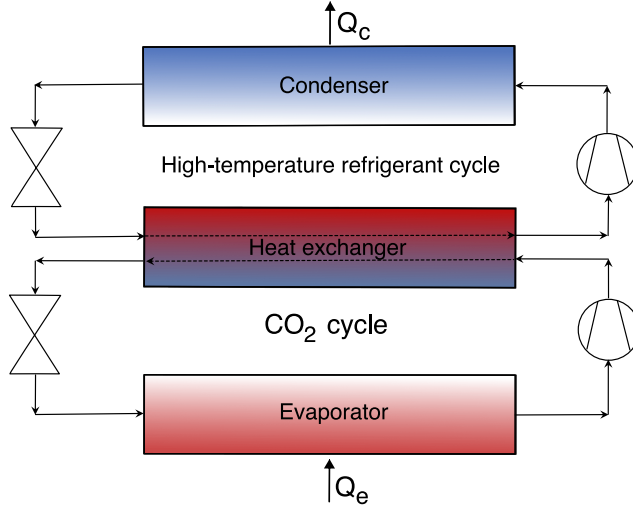


Figure (2.6): An example of a cascade refrigeration cycle with CO₂ as the low-temperature side refrigerant. The high-temperature side refrigerant could be a natural refrigerant such as NH₃.

2.2.3 Enhanced condensation of CO₂

As stated previously, research on condensation enhancement has to a large degree focused on achieving DWC. Research on DWC of CO₂ is, however, almost non-existing, with two exemptions by Wu et al. [4, 5]. Here, we have investigated DWC of CO₂ using classical Molecular Dynamics (MD) simulations. In the first study, the surface energy of a Cu-like surface was exactly tuned to reproduce CO₂ droplets with contact angles varying between 0° (perfectly CO₂-philic) to 180° (perfectly CO₂-phobic) [4]. It was found that an interfacial surface energy of 10 mJ m⁻² between the CO₂ liquid and the Cu-like solid yields a liquid droplet contact angle of 90°, and hence mark the transition between CO₂-philic and CO₂-phobic. For comparison, a typical Cu condenser surface has a surface energy of 1650 mJ m⁻², over two orders of magnitude larger than the transition surface energy of the investigated Cu-like surface. On the other hand, Rykaczewski et al. [36] fabricated a silicon surface functionalized with a fluorosilane coating with a surface energy as low as 10.1 mJ m⁻². On this surface DWC of pentane (surface tension of 15 mN m⁻¹) was achieved. By comparison, CO₂ has a surface tension of 16.54 mN m⁻¹ at -52.2 °C, which decreases with increasing temperature [110].

Surface structuring has been shown to promote DWC and enhance condensation heat transfer, if the structures are carefully designed and fabricated and the surface energy is low enough. In some cases a low energy chemical, such as a fluorine based chemical, is necessary. The second study by Wu et al. showed that a surface covered with square pillars promoted DWC if the surface energy is low enough [5]. The contact angle of a CO₂ droplet on a pillar structure is generally higher than on a smooth surface, for the same surface energy. However, also for the structured surfaces the surface energy must be lower than 10 mJ m⁻² to obtain efficient DWC. The contact

angle for this surface energy is higher than 90° , but the droplets penetrate the pillars and are in the Wenzel state. This state results in a high contact angle hysteresis and therefore reduces droplet removal and, consequently, the condensation heat transfer is decreased. When reducing the surface energy to 9 mJ m^{-2} the droplets on the surface are suspended in the Cassie-Baxter state, resulting in easy droplet removal by gravity and increased heat transfer. The Cassie-Baxter state is also obtained if the pillar width and spacing are reduced, i.e. the surface roughness is increased. The transition point between the Cassie-Baxter and the Wenzel states on a Cu-like surface with 9 mJ m^{-2} is in this study found to be with pillar width and spacing of approximately 3 nm.

The two MD studies on DWC of CO_2 show that it is possible to obtain droplets of CO_2 on a surface with low surface energy. However, the requirements on the surface energy and/or on the topography of a structured surface are so strict that a practical method of fabricating such surfaces does not exist today. DWC of butane, with its extremely low surface tension, is on the other hand proven, but the experimental conditions were far away from practical or from the pressure or temperature levels that are required for CO_2 condensation [38]. In addition, hexafluoroisopropanol was used as a coating chemical, which is highly toxic and volatile and requires constant refilling for sustained DWC.

The combination of the mentioned studies on DWC of CO_2 and research for DWC for other low surface tension fluids led to the search for alternative pathways to enhance condensation heat transfer of CO_2 . This PhD work is, by our knowledge, the first attempt to enhance condensation heat transfer of CO_2 by filmwise condensation, and the first to compare the condensation heat transfer on different materials commonly found in process equipment, namely Cu, Al and 316 Stainless Steel (henceforth named Steel). It was therefore necessary to develop a methodology for the specific purpose, which is described in the following chapter.

Methodology

During the work with this PhD the methodology has been adjusted several times. The project started with the goal of achieving and visualizing DWC of CO₂. After leaving this path, we wanted to achieve FWC of CO₂ on various surfaces and measuring condensation heat transfer. Eventually, the objective of the work was to increase heat transfer by micro- and nanostructured surfaces, and the methodology included fabrication of such structures and heat transfer measurements. The development of the methodology, some pitfalls on the way, and the design of the experimental setup is described in this chapter, beginning with the work done to achieve CO₂ condensation on a surface, how we wanted to observe and measure relevant parameters for DWC, and ending with the experimental method and setup for measuring the condensation heat transfer on different materials and surface structures. The methods for fabricating the investigated surfaces are also described, along with a summary of the relevant physical properties of the materials.

3.1 Achieving steady state condensation of CO₂

An important first milestone when developing the experimental method and designing and building the equipment, was to achieve CO₂ condensation on a surface while we accurately controlled the saturation pressure and the subcooling between the condenser surface and the saturated gas. The first and most important parts of the original design of the setup were therefore a pressure chamber, a gas supply system and a cooling element.

The experimental setup consists of two separate gas supply circuits, one for filling a pressure chamber with pure CO₂ with an accurate control of the pressure, and one for circulating two-phase CO₂ through the cooling element for achieving the desired temperature at the cooling element surface, and hence on the investigated surface. The Piping and Instrumentation Diagram (P&ID) of the setup is shown in Figure 3.2. Details of the important features in the P&ID are described in the following. The pure CO₂ is fed to the pressure chamber through a series of tubes and valves

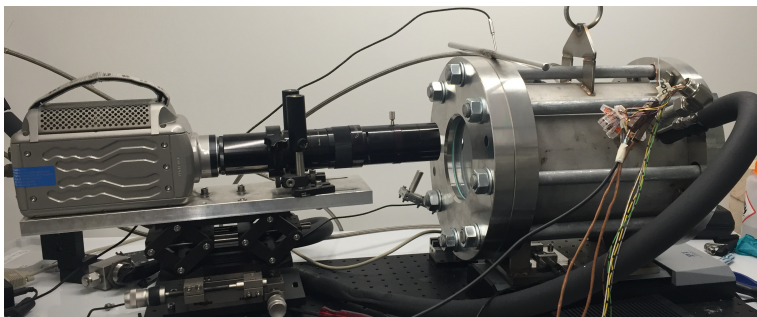


Figure (3.1): *Photo of the high-speed camera and the pressure chamber.*

to provide accuracy and control, and to perform pressure release to exhaust when necessary. The inlets and outlets to the pressure chamber are 1/8" tubes that are welded into holes of the walls. The transitions to the surrounding tubes are secured by Swagelok couplings. The pressure chamber is a 30 cm long steel pipe, 20 cm in diameter, with lids on each side, see Figure 3.1. Both lids are circular flanges and they are kept in place with 8 large bolts. O-rings are placed in trenches that are carved into the steel at both ends of the pipe. By tightening the bolts, the o-rings are pressed between the flanges and the steel pipe ends. This results in a pressure tight chamber. The pressure in the chamber is regulated with an Alicat Dual Valve Absolute Pressure Controller (PCD) with an accuracy of 0.25% of full range. The working pressure can be varied between 6 and 20 bar, and the pressure is tested for leakage up to 25 bar. However, the high pressure is not attainable at very high condensation rates due to high subcooling of the surface. The achievable mass flow through the PCD is too low to maintain a steady state vapor-liquid equilibrium in the pressure chamber, and the pressure drops as the gas condenses and the relative volume of the liquid phase increases. This limits the range of subcooling that is tested in this work. Switching to a pressure regulator with a higher maximum mass flow will be a solution to this problem, and in a future version of the experimental setup another type of regulator should be considered.

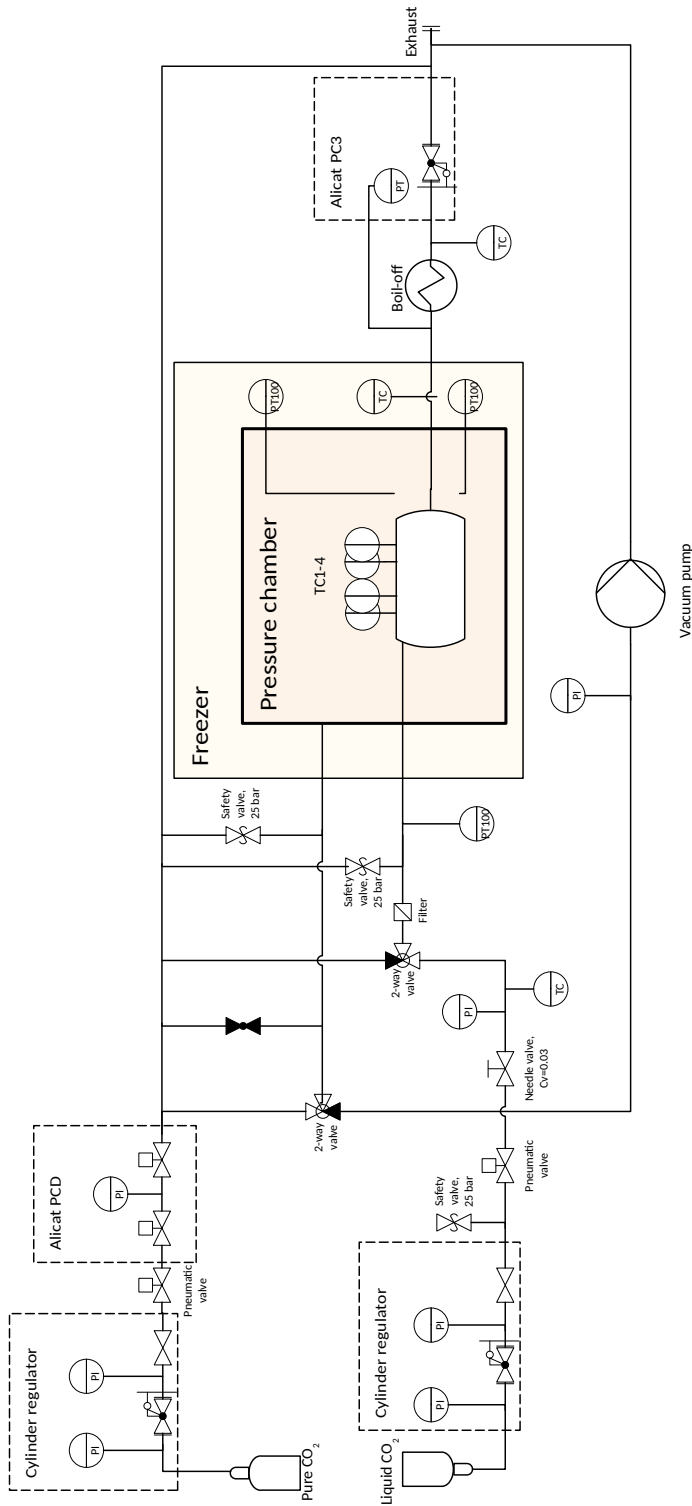


Figure (3.2): Piping and Instrumentation Diagram of the experimental setup. Pure CO₂ flows into the pressure chamber with the Alicat PCD as the pressure controller. Liquid CO₂ is fed to the cooling element with the Alicat PC3 as a back pressure regulator, accurately controlling the pressure which results in a uniform temperature in the cooling element.

The second gas circuit is the cooling circuit and consists of a gas cylinder, 1/8" tubes, controlling valves and regulators and the cooling element. The main purpose of the cooling element is to cool the backside of the investigated substrate to a temperature such that CO₂ condensation can occur on the surface. In order to obtain valuable heat transfer results, two main requirements must be fulfilled: 1) the temperature on the cooling element surface must be uniform and 2) the temperature must be tunable and accurately controlled. For requirement 1) we chose to use two-phase CO₂ as the refrigerant. Liquid CO₂ is provided by a gas cylinder with a dip tube. The liquid evaporates in the tubes and by ensuring a sufficiently large flow rate, the two-phase front will gradually move down the circuit and eventually be situated at the downstream side of the cooling element. CO₂ kept exactly at the vapor-liquid two-phase transition point will have a constant temperature as long as the pressure is kept constant and the mass flow is large enough to ensure that the liquid phase is not completely evaporated in the element. Calculations of the two-phase flow at pressures between 6 and 20 bar resulted in the design parameters of the cooling element: a Cu block with 25 narrow channels with a width of 0.5 mm. The interior of the cooling element is shown in Figure 3.3 (a), with the lid flipped to show the narrow channels. For ensuring requirement 2) an adjustable and accurate temperature, a back pressure regulator (Alicat, PC3 series) was inserted in the gas circuit upstream the cooling element, with the control point downstream the cooling element. Two thermocouples (type K, Omega Engineering) were inserted upstream and downstream the element to monitor that two-phase CO₂ was present at both locations of the circuit. The temperatures will, in that case, be equal to each other and equal to the desired saturation temperature. The back pressure regulator is damaged by liquid or two-phase flow, so a heat exchanger (5 m 1/8" tube for direct heat exchange with the surroundings) was inserted after the second thermocouple in which the two-phase CO₂ could completely evaporate. A needle valve was inserted upstream the cooling element to regulate the mass flow such that the two phase front was situated within the long heat exchanger, and not within the cooling element (too low mass flow) or within the back pressure regulator (too high mass flow). A third thermocouple was inserted before the pressure regulator to monitor the temperature. This must at all times be higher than the saturation temperature at the given pressure to ensure that there is only gas present. The described equipment is shown in the P&ID in Figure 3.2.

Both electrical and thermocouple wires had to be fed through the pressure chamber wall. Commercial feed-throughs of cables do exist, but none that included both enough and the correct type of thermocouple wires and electrical cables, and that would be tight over a 25 bar pressure difference. We therefore designed and fabricated a custom made feed-through. It consisted of a tube with 16 mm outer diameter and a Swagelok coupling closing the transition between this tube and a tube with 16" inner diameter that was welded into the pressure chamber side wall. Five thermocouple wires and three electrical cables intended for LED lights were inserted into the tube. A two-component epoxy was injected into the tube around the cables at an elevated temperature in two rounds, 24 hours apart. In addition, the insulation around the cables were removed 2 cm from the end and a small amount of epoxy was placed at the insulation cut-off to ensure that no gas leakage occurred between the wires and the insulation. The feed through was tested with 25 bar

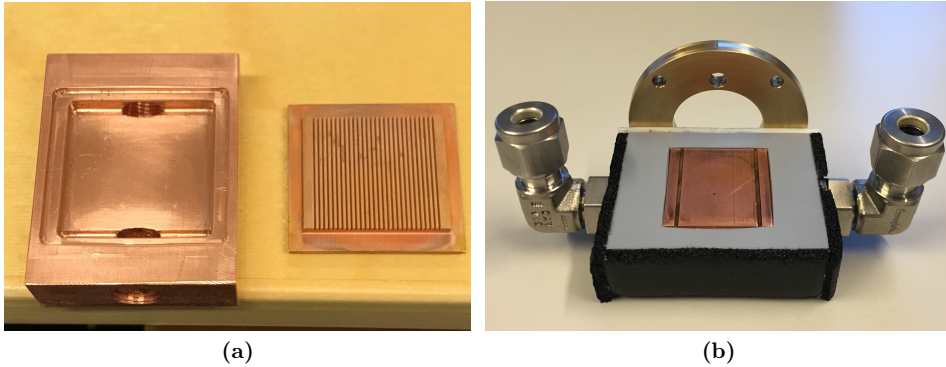


Figure (3.3): (a) The interior of the cooling element consists of narrow channels in which the two-phase CO_2 flows. (b) The assembled cooling element with an inlet and outlet for the two-phase flow, an insulated Cu block and a rotation disc, which can be mounted on the rotation motor. The cooling element is insulated with teflon on top and insulation foam on the sides.

helium, and no leakage was detected.

To measure the surface temperature of the investigated substrates, two narrow slits were carved into the cooling element surface, see Figure 3.3 (b). In these slits thin thermocouple wires, welded at the tip, could be inserted. At a later stage of the method development, the surface temperature was not measured in this way, while for the initial tries to achieve DWC the thermocouples were successfully embedded into the slits and used for measuring the surface temperature.

3.2 Observing the condensation process

To observe the condensation mode, and the droplets in the case of DWC, a sight glass was embedded in one of the flanges closing off the pressure chamber. A high-speed camera (Phantom 9.1) was used to monitor the condensation process through the sight glass. The camera and the sight glass are shown in Figure 3.1. The high-speed camera can capture up to 150000 frames per second (fps) at full speed or 1000 fps at full resolution (1632 x 1200). The high-speed camera was chosen to enable the observation of nucleation, growth, coalescence and roll-off of droplets in the DWC process. Three LED lights were placed in the top and at the two sides of the roof of the pressure chamber and coupled to a voltage source. As a result, the investigated substrate could be illuminated from the top and/or from one or both of the two sides. It was, hence, possible to see various droplets on the surface depending on their relative position, and to illuminate in such a way that the contact angle could be measured. In Figure 3.4(b) an image of a water droplet on a structured surface is shown. The droplet is illuminated from the top and recorded by the high-speed camera.

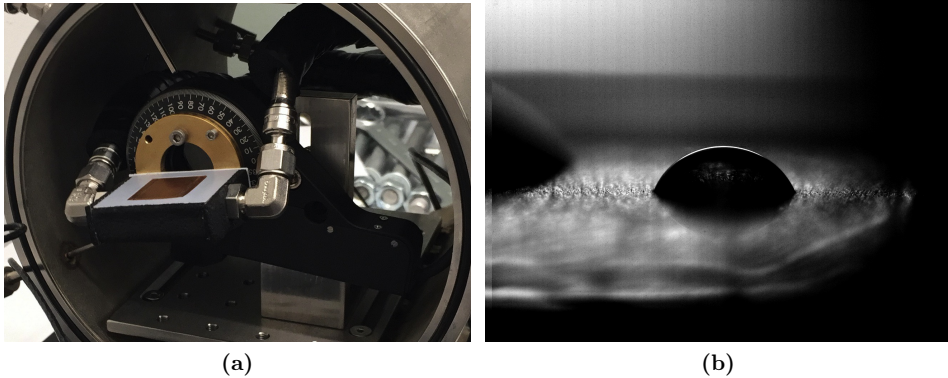


Figure (3.4): (a) Interior of the pressure chamber with the cooling element attached to the rotational stage. Two PT100 elements for measuring the gas temperature are visible below and above the cooling element. The lid of the chamber is removed for convenience. (b) Water droplet on a structured surface photographed by the high-speed camera. The depth of field is narrow and the contact angle can be measured.

The substrate and cooling element were mounted to a rotational stage to enable the observation of advancing and receding contact angle, as well as tilt angle for initiation of droplet movement. All the observed properties are measures of the adhesion forces between droplet and substrate. These forces are important to minimize for increasing heat transfer efficiency. The rotational stage and the interior of the pressure chamber as they were assembled for observation of DWC are shown in Figure 3.4(a).

3.3 Heat transfer measurements

The heat transfer measurements were conducted with an experimental method especially developed to investigate the condensation of CO_2 on a variety of substrates. The substrates are easily interchangeable to enable systematic studies of the effect of the material on condensation heat transfer. The experimental setup for observing DWC was redesigned and the interior of the pressure chamber was rebuilt to achieve condensation on a vertical wall and to measure the heat transfer. The goal was to develop a database for CO_2 condensation heat transfer on common heat exchanger materials and to further find methods for enhancing heat transfer, by e.g. micro- and nanostructures on the surfaces. Surface modifications, such as coatings and structuring or a combination, have been reported to enhance condensation of water and low surface tension fluids, and we wanted to extend this knowledge to CO_2 .

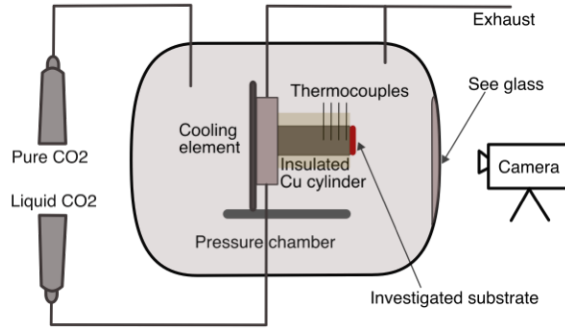


Figure (3.5): Sketch of the experimental setup showing the pressure chamber, the inlet and outlet of the cooling element, the Cu cylinder with embedded thermocouples, the investigated substrate and the camera viewing through a see glass within the lid of the chamber.

3.3.1 From cylinder heat flux to condensation heat transfer coefficient

For studying the condensation heat transfer on various materials, a Cu cylinder is attached to the cooling element and the investigated material is attached to the cylinder with a TIM (Aldrich Chemistry, Silver Conductive paste 735825). A sketch of the setup is shown in Figure 3.5. The Cu cylinder is insulated with a teflon cylinder with a hollow core, exposing only the circular ends of the Cu. There are four thermocouples, type K, embedded in the core of the cylinder, situated 2.2, 5.3, 11.4 and 14.5 mm from the cylinder end. The temperature variation throughout the cylinder is measured with the four thermocouples. The heat flux through the cylinder is directed from the gas to the cooling element, and the temperature profile through the cylinder is linear due to the teflon insulation. The calculations showing the linear temperature profile are included in the Supplementary Information of paper II [2]. The total heat flux through the cylinder can therefore be calculated with the one dimensional Fourier equation, Equation 3.3.1.

$$q_x = -k \frac{dT}{dx} \quad (3.3.1)$$

Here, k is the thermal conductivity of Cu and $\frac{dT}{dx}$ is the temperature gradient within the Cu cylinder, which is measured with the four thermocouples in the cylinder center. Even though the insulation is thick enough to obtain a linear heat transfer, some heat will be lost in the radial direction. The heat loss through the insulation depends on the inner and outer radii of the hollow teflon cylinder, r_i and r_o , the thermal conductivity of the insulation, k_{teflon} , and the temperature difference across the insulation, ΔT , as [9]:

$$q_{ins} = \frac{2\pi k_{teflon} L \Delta T}{\log r_o/r_i}. \quad (3.3.2)$$

The temperature difference across the insulation is equal to the difference between the temperature in the gas and the core temperature of the Cu cylinder. The latter is measured by the innermost thermocouple embedded in the cylinder and the gas temperature is measured by a PT100 element that is inserted through the wall of the pressure chamber and situated directly above the insulation cylinder. In the data reduction, one average value of q_{ins} is used for each saturation pressure. The values are averaged over several hundred measurement points. Consequently, the heat flux actually flowing through the investigated surface is $q_x - q_{ins}$. We are interested in the heat flux involved in the condensation, and have therefore quantified the relative portion of the heat that is used for cooling the surrounding gas before it reaches the saturation temperature and the latent heat of evaporation is released, q_{gas} :

$$q_{gas} = A c_p T_{gas} M m \Delta T \quad (3.3.3)$$

$$\Delta T = T_{gas} - T_{sat}. \quad (3.3.4)$$

Here, ΔT is the temperature difference between the average gas temperature and the saturation temperature at the given pressure, A is the investigated surface area, c_p is the molar heat capacity of the gas and Mm is the molecular mass of the gas. Finally, the condensation heat flux is calculated with Equation (3.3.5) and the condensation HTC is calculated with Equation (3.3.6). The HTC is here defined for uniform surface temperature, T_{surf} , being the boundary condition of the liquid side HTC.

$$q_{cond} = q_x - q_{ins} - q_{gas} \quad (3.3.5)$$

$$h_{cond} = \frac{q_{cond}}{T_{sat} - T_{surf}} \quad (3.3.6)$$

The pressure chamber is filled with pure CO₂ (Aga 5.0 Scientific grade) and regulated with a back pressure regulator, as described previously. The condensation heat transfer is investigated at saturation pressures of 10, 15 and 20 bar, corresponding to saturation temperatures of -40.1°C , -28.5°C and -19.5°C , respectively.

The surface temperature, T_{surf} , used in the calculations above is determined by extrapolating the linear temperature profile in the cylinder, first to the cylinder surface, through the TIM and finally through the investigated substrate. Through all the layers, the heat flux is equal to the heat flux in the cylinder ($q_x - q_{ins}$) and by using the Fourier equation, Equation (3.3.1), the temperature gradient through the TIM and the substrate is found, and the surface temperature is calculated. In these calculations, the thermal conductivity of the TIM and the investigated material (Cu, Al or Steel) is used. An example of a plot of the data necessary for acquiring the

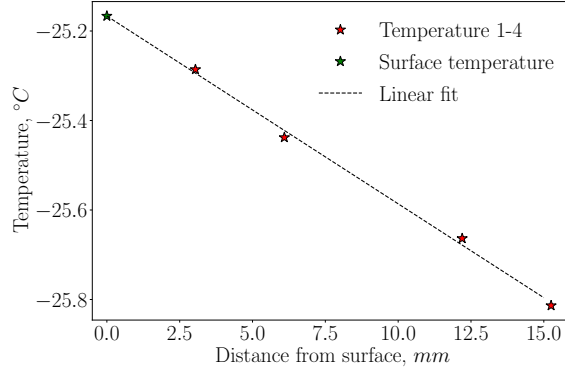


Figure (3.6): *Temperatures in the four thermocouples in the cylinder and the calculated (extrapolated) surface temperature shown as a green star.*

temperature gradient and the surface temperature is shown in Figure 3.6. In this example, the investigated surface is Cu, so there is no jump in temperature caused by a change in material.

3.3.2 Data acquisition

Figure 3.7 shows the temperature measurements in the Cu cylinder. Thermocouple T1 is closest to the cylinder and the investigated surface, and T4 is closest to the cooling element. Figure 3.7(a) shows typical temperature measurements at the initiation of condensation. The data in this figure is acquired during condensation on flat Cu at 16 bar. There is no condensate on the surface for the first 100 seconds. At $t = 100$ s, the temperature set point in the cooling element is reduced, followed by approximately 100 s where the temperatures first drop, then increase, and finally drops to a new stable level. During this period the condensation is initiated and the condensate film forms on the surface. The condensation reaches steady state at about 200 s and the temperatures are stable until the cooling element set point is altered, yet again (not included in the Figure). The temperature gradient through the cylinder, i.e. the spread between the four thermocouples, is significantly higher when there is condensate present at the surface, which is seen in Figure 3.7(b). Here, the temperature measurements are recorded for one experimental series for 15 bar saturation pressure. The jump in time is the necessary time for stabilizing a new temperature set point. Temperatures are generally not recorded during this stabilizing period, but the available data display similar behavior to the transition zone in Figure 3.7(a). Each temperature is kept stable for 3 minutes, and the resulting temperature gradient, and hence heat flux, is an average over the 300 data points recorded during this time. The increase in temperature gradient with decreasing temperatures is caused by the latent heat that is released in the phase change process, and the improved heat transfer between liquid and solid, compared with gas and solid. The initial increase in gradient is used to validate that the required temperature is reached on the substrate surface and that the condensation has been initiated.

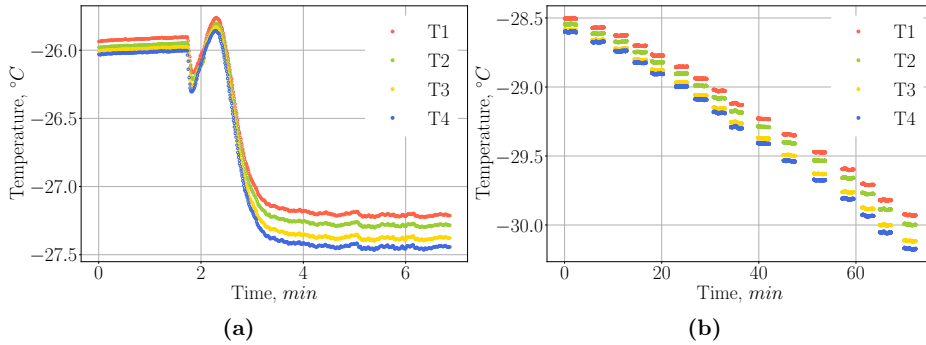


Figure (3.7): Temperature measurements in the Cu cylinder during CO₂ condensation. (a) shows the measured temperatures at the initiation of condensation, including the transition zone between two stable temperature levels. (b) shows the temperatures during an entire experimental series on flat Cu at 15 bar. Figure is also found in Paper III.

The thermocouples in the cylinder, and the wires connecting them to the voltage meter, were from the same supplier and comes from the same batch. This is critical to ensure temperature measurements with a high degree of accuracy. From the supplier, the thermocouples' uncertainty is stated to be ± 1 K. This value is too high for accurate measurements of the heat flux. Additional calibration of the thermocouples is therefore needed for measuring temperature differences of less than 0.5 K. Due to the operational properties of thermocouples, the calibration is only valid and trustworthy when it is conducted with the exact same conditions as the experiments, and with the same connections. To reduce uncertainty, one of the thermocouples' wire junctions are submerged in a water cooling bath at 4.5°C controlled by a refrigerated circulator (Julabo). This procedure is called cold junction compensation and reduces the scattering in the results. The thermocouples are, in addition, calibrated in an ice bath while situated in the Cu cylinder and with the wires coupled in the same manner as for the experiments. The cylinder is submerged in an ice bath, shown in Figure 3.8, and the temperatures are measured 6 times. The average value of the four thermocouples are used for calibration, and the uncertainty is assumed to be equal to the standard deviation of the measurements in the ice bath calibration, which was 0.02 K.

3.3.3 Observing filmwise condensation

During the condensation experiments the high-speed camera records the process and the surface is continuously observed. The onset of the condensation is visible as either a darker or brighter spot on the surface that gradually spreads when the surface temperature is decreased. The onset of condensation is also verified by a jump in the temperature gradient in the cylinder, as described previously. Figure 3.9 shows the onset of the condensation at a Cu surface. The liquid front, observed as a brighter area in the Figure, gradually spreads across the surface as the subcooling



Figure (3.8): Ice bath calibration of the thermocouples embedded in the Cu cylinder, while the thermocouples are coupled to the circuit as they are during experiments.

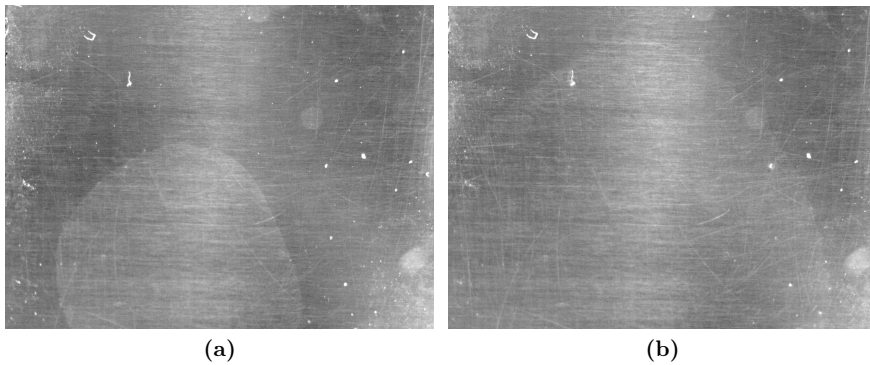


Figure (3.9): Liquid CO_2 spreading on a Cu surface. The images are recorded at two different levels of subcooling, with the lowest level in (a) and the highest level in (b). The liquid front will gradually cover the entire surface at sufficient subcooling, higher than shown here

is increased.

At some of the surfaces, and especially visible on the Al surface, a retention of the condensate can be observed at the bottom of the vertical surface. This retention is caused by a roughness around the circumference of the circular surfaces and the surface tension of the fluid. The development of the condensate retention can be seen in Figure 3.10.

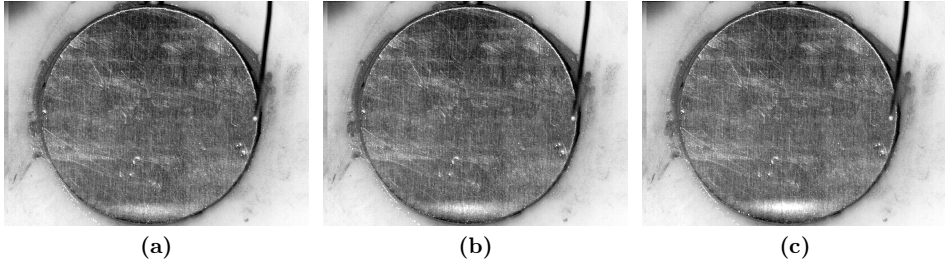


Figure (3.10): CO_2 condensation on Al at three levels of subcooling: (a) 1.2 K, (b) 1.6 K and (c) 2.1 K. The saturation pressure is 10 bar in all cases. The condensate film retention at the bottom of the surface increases with increased subcooling, as the film thickness and condensation rate increase with subcooling.

3.3.4 Uncertainty analysis of the heat transfer experiments

The experimental investigation of heat transfer during condensation of CO_2 has been performed in the newly developed experimental apparatus described above. All experimental results are subject to uncertainties, which in this work is related to the intrinsic uncertainties of the temperature and pressure measurements. One way to quantify the combined uncertainty of the experimental results is to use Gaussian propagation of uncertainty. The method is based on propagating each uncertainty by their first partial derivatives. The propagated error in the heat flux, E_q , is derived with use of the one-dimensional Fourier law, Equation (3.3.7), with k being the thermal conductivity of Cu and d_{1-4} being the distance between thermocouple 1, T_1 , and thermocouple 4, T_4 , in the cylinder.

$$q = -k_{Cu} \frac{T_4 - T_1}{d_{1-4}} \quad (3.3.7)$$

The expression for the total error in heat flux, E_q , is found using the variance formula which results in Equation (3.3.8).

$$E_q = \sqrt{\left(\frac{T_4 - T_1}{d_{1-4}}\right)^2 E_{k_{Cu}}^2 + 2 \left(\frac{k_{Cu}}{d_{1-4}}\right)^2 E_T^2 + \left(\frac{T_4 - T_1}{d_{1-4}^2}\right)^2 E_{d_{1-4}}^2} \quad (3.3.8)$$

Here, E_k is the estimated error in Cu thermal conductivity, E_T is the error in the temperature measurements, and E_d is the error in the measured distance between the thermocouples.

We have estimated the temperature dependent thermal conductivity of Cu from the correlation presented by Abu-Eishah [111] which is given with an absolute relative error of 0.013%. The error in temperature measurements, E_T , is based on the icebath calibration of the thermocouples, using the standard deviation of the estimated calibration value as a constant error in the measurements. The placement of the

thermocouples inside the Cu cylinder has been measured with a caliper and the error is therefore assumed to be within 0.02 mm, relating to the smallest measurable values with a caliper.

The error in subcooling is also derived with the Gaussian error distribution and the resulting formula is

$$E_{\Delta T} = \sqrt{E_{T_{sat}}^2 + E_{T_{surf}}^2} \quad (3.3.9)$$

Here, the error in the saturation temperature, $E_{T_{sat}}$, is based on the given uncertainty of the pressure controller used to control the pressure in the chamber, P_{sat} . The error in the surface temperature, $E_{T_{surf}}$, is calculated through a series of dependent uncertainties following the derivation below.

First, the uncertainty in the estimated cylinder surface temperature, T_{cyl} , is derived as follows:

$$T_{cyl} = \frac{x_1}{d_{1-4}}(T_1 - T_4) + T_1 \quad (3.3.10)$$

$$E_{T_{cyl}}^2 = \left(\frac{T_1 - T_4}{d_{1-4}}\right)^2 \left(E_{x_1}^2 + \left(\frac{x_1}{d_{1-4}}\right)^2 E_{d_{1-4}}^2\right) + E_T^2 \left(1 + 2\left(\frac{x_1}{d_{1-4}}\right)^2\right) \quad (3.3.11)$$

Here, x_1 and E_{x_1} are the placement of the outermost thermocouple in the cylinder and the corresponding uncertainty, as measured with a caliper. Second, an expression for the temperature in the interface between the TIM and the sample, T_{TIM} , and the corresponding error function, $E_{T_{TIM}}$, are calculated and shown in Equation (3.3.13). Calculations have showed that changing k_{TIM} with $\pm 50\%$, changed the surface temperature by 0.15 K. We can therefore safely assume that an error in k_{TIM} has negligible effect on the total uncertainty and set $E_{k_{TIM}}$ to be zero.

$$T_{TIM} = \frac{k_{Cu} t_{TIM}}{k_{TIM} x_1} (T_{cyl} - T_1) + T_{cyl} \quad (3.3.12)$$

$$E_{T_{TIM}}^2 = \left(\frac{1}{k_{TIM} x_1}\right)^2 \left((t_{TIM}^2 E_{k_{Cu}}^2 + k_{Cu}^2 E_{t_{TIM}}^2) (T_{cyl} - T_1)^2 + \left(\frac{k_{Cu}}{x_1}\right)^2 E_{x_1}^2 (T_{cyl} - T_1)^2 + k_{Cu}^2 (E_{T_{cyl}}^2 + E_T^2) \right) + E_{T_{cyl}}^2 \quad (3.3.13)$$

Finally, the calculation of T_{surf} follows Equation (3.3.14), and the corresponding uncertainty is calculated with Equation (3.3.15). The values of each uncertainty needed for the calculations are given in Table 3.1.

$$T_{surf} = \frac{k_{TIM} t_{mat}}{t_{TIM} k_{mat}} \left(T_{TIM} - T_1 - \frac{x_1}{d_{1-4}} (T_1 - T_4) \right) + T_{TIM} \quad (3.3.14)$$

$$E_{T_{surf}}^2 = \left(\frac{k_{TIM} t_{mat}}{t_{TIM} k_{mat}} \right)^2 \left[\left(\left(\frac{E_{t_{TIM}}}{t_{TIM}} \right)^2 + \left(\frac{E_{k_{mat}}}{k_{mat}} \right)^2 \right) \left(T_{TIM} - T_1 - \frac{x_1}{d_{1-4}} (T_1 - T_4) \right)^2 + \left(E_{T_{TIM}}^2 + E_T^2 \left(1 + 2 \left(\frac{x_1}{d_{1-4}} \right)^2 \right) \right) \right] + E_{T_{TIM}}^2 \quad (3.3.15)$$

Table (3.1): Table with the estimated uncertainties used for calculating the overall uncertainties in heat flux and subcooling.

Parameter	Uncertainty name	Uncertainty value
T_1, T_2, T_3, T_4	E_T	± 0.0337 K
P_{sat}	n/a	± 0.0875 bar
T_{sat}	$E_{T_{sat}}$	± 0.2 K
t_{TIM}	$E_{t_{TIM}}$	± 0.05 mm
k_{Cu}	$E_{k_{Cu}}$	$\pm 0.013\%$ [111]
k_{mat}	$E_{k_{mat}}$	$\pm 0.5\%$
$x_4 - x_1 = d_{1-4}$	$E_{d_{14}}$	± 0.04 mm
x_1	E_{x_1}	$E_{d_{14}}/2$

3.4 Validation of the experimental method and setup

As a validation procedure of the experimental setup, an experimental campaign where CO₂ was condensed on the Cu cylinder without any attached substrate was conducted. The resulting condensation heat fluxes are shown in Figure 3.11 together with the results from condensation on the untreated Cu (the same results as shown in Figure 5.2). The data are overlapping for all three saturation pressures and the difference is within the calculated uncertainty range. The errors in subcooling for the Cu cylinder data are caused by the estimated error in saturation pressure. These results verify a proper repeatability of the experimental setup and that the method of attaching the investigated substrates do not deteriorate the validity of the results. In the figure, theoretical heat flux calculated with the Nusselt model is also plotted. We see that the experimental data lies within a 15% deviation from the theoretical values, which validates the experimental setup. The deviation from the theoretical values is expected as the Nusselt model is idealized and does not consider surface properties of the material, vapor drag, or non-laminar flow.

When calculating the HTC we set uniform surface temperature as the boundary condition. Consequently, a validation of the uniformity of the surface temperature

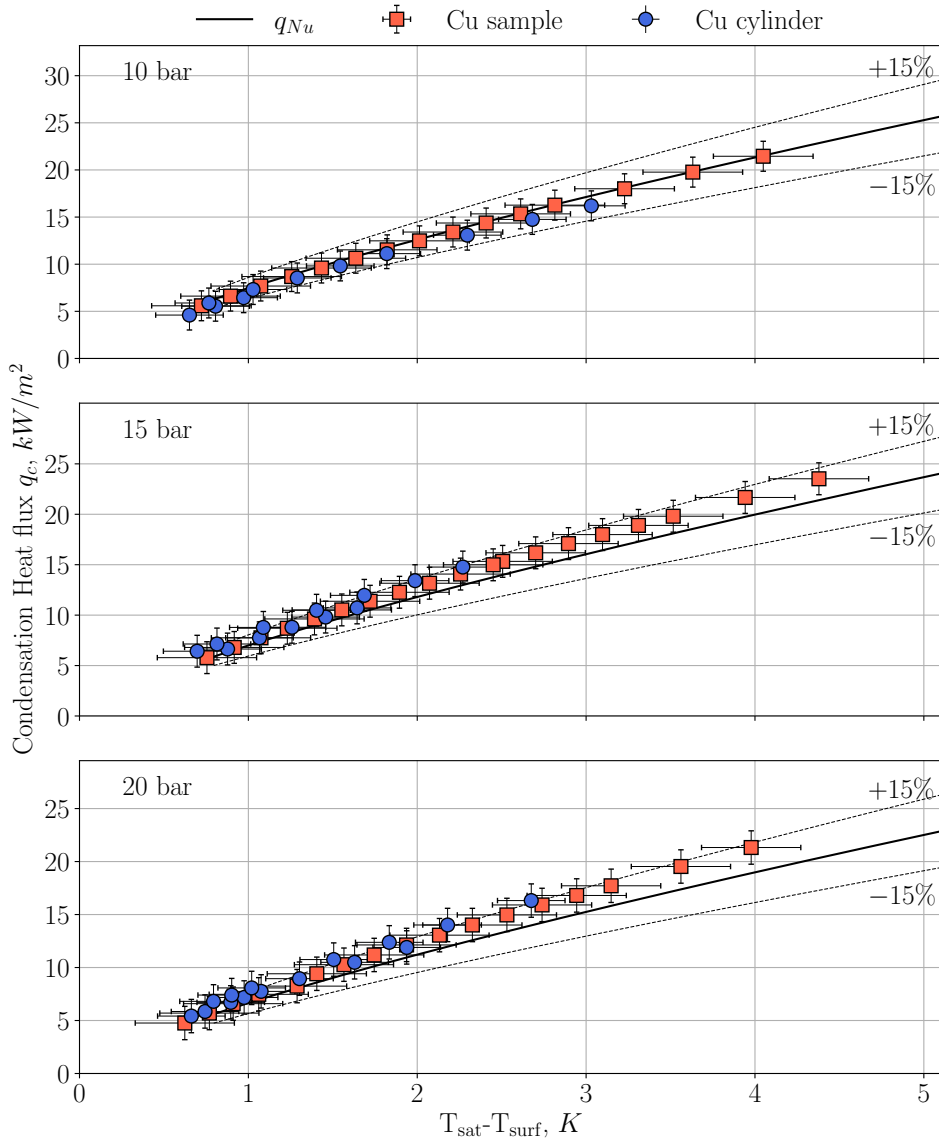


Figure (3.11): Theoretical and experimental heat flux data for CO_2 condensation on the bare Cu cylinder and on the Cu sample while attached to the cylinder with the TIM. All experimental data lies within the values of uncertainty, and within a 15% deviation from the Nusselt model. The figure is also shown in Paper II.

Table (3.2): Theoretical effect of variation in surface temperature on the condensation HTC. The numbers are representative results from the finite element analysis shown in Figure 3.12. T_m is the average temperature, T_0 is the temperature in the center of the sample, and Δh_{Nu} is the percentage error in HTC caused by averaging the surface temperature.

	T_m (°C)	T_0 (°C)	$T_m - T_0$ (10^{-3} °C)	Δh_{Nu}
Cu	-33.137	-33.138	0.9	0.02 %
Al	-33.124	-33.126	1.6	0.04 %
steel	-32.780	-32.798	18.8	0.44 %

will strengthen the validity of the experimental results. A finite element analysis has therefore been conducted to show the surface temperature distribution for the different samples. In the analysis we have set a constant heat flux through the Cu cylinder of 10 kW m^{-2} , and the back side temperature is constant at 240 K. The cylinder is perfectly isolated around the perimeter, i.e. $q = 0$ in the radial direction. The sample is not isolated and the heat flux out of the sides of the sample is also set to 10 kW m^{-2} . We have included a test on how different TIM thicknesses will influence the temperature distribution, and found that the differences between 0.1, 0.15, and 0.2 mm is not significant. In Figure 3.12 snapshots of the predicted temperature distribution on (a) Cu, (b) Al and (c) steel are shown. The TIM is 0.15 mm thick in this case, which is measured to be a representative thickness. The temperature in the center is different at the three samples. This is caused by the different thermal conductivity of the materials and hence that the temperature gradient within the sample will be different at equal heat flux. As seen in the images, the temperature is uniform on a large portion of the surface area. The differences in temperature between center and edge are approximately 0.01 K for Cu, 0.02 K for Al and 0.25 K for steel. The temperature difference for steel is much higher than for Al and Cu, due to steel's low thermal conductivity. However, the change in temperature occurs only the outer circle of the sample, as seen in Figure 3.12(c), and the HTC is therefore affected only 0.44 %. The deviation between the average temperatures and the center temperatures are 0.9 mK for Cu, 1.6 mK for Al, and 18.8 mK for steel. We have calculated how large the effect of these deviations will be on the calculated HTC in the case of Cu, Al, and steel, and the results are summarized in Table 3.2. In the example case, we used the theoretical HTC from the Nusselt model with a subcooling of 1 K and a saturation pressure of 15 bar. At larger subcooling, the error caused by averaging the surface temperature is even smaller. From this we conclude that the variation in surface temperature is not significant.

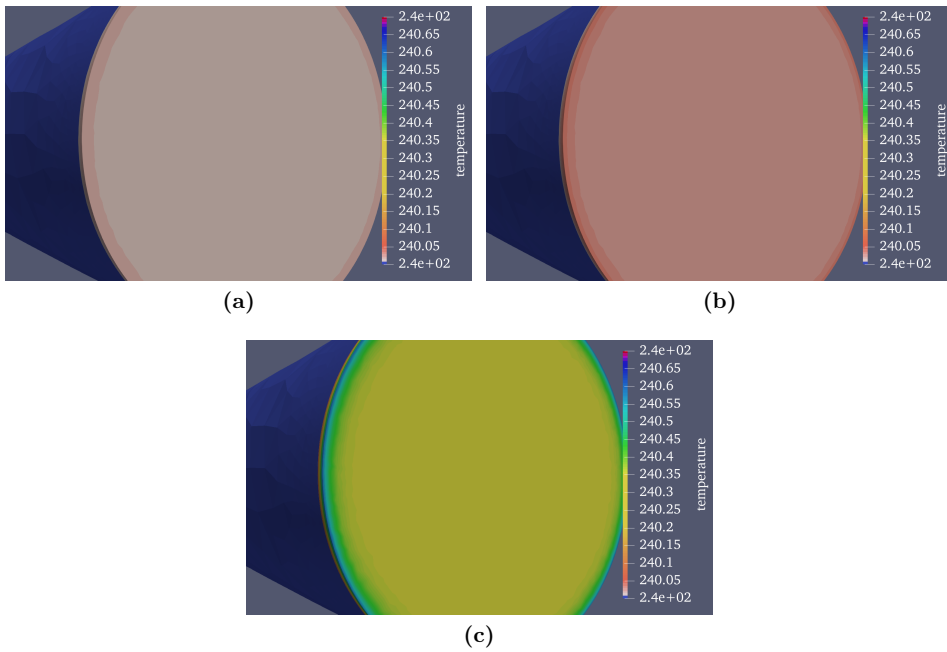


Figure (3.12): Results of finite element analysis of the temperature distribution on (a) Cu, (b) Al, and (c) Steel. The samples are attached to the Cu cylinder with 1.5 mm thick TIM. The heat flux is set to 10 kW m^{-2} . The perimeter of the cylinder is isolated (zero heat flux), while the samples are not (heat flux set to 10 kW m^{-2} in the radial direction).

3.5 Fabrication of micro- and nanostructured surfaces

Two types of micro- and nanostructured surfaces have been investigated in this work: (1) CuO Nano Needles (NN) grown on Cu substrate and (2) hierarchical surfaces with CuO NN grown on microsized Cu pillars on a Cu substrate. For the latter, two different surfaces were fabricated and tested. Figure 3.13 shows the fabrication steps towards the hierarchical structures, starting with Photolithography, followed by Chemically Assisted Ion Beam Etch (CAIBE) and finalized with Solution Immersion. By skipping the first two steps, the result is the pure nanostructured surface. The following sections describe the fabrication techniques.

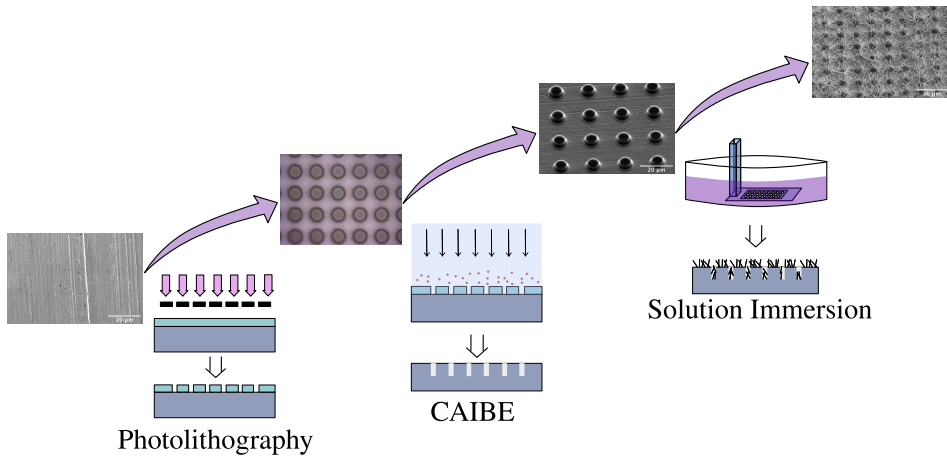


Figure (3.13): Fabrication of the hierarchical structures consists of three steps: 1) Photolithography, 2) Chemically Assisted Ion Beam Etch and 3) Solution Immersion.

3.5.1 Photolithography

Photolithography is a process to create microsized features on a surface with a predefined pattern [112]. The pattern is transferred from a mask onto the substrate with the aid of a Photo Resist (PR) and an optical source. The source could either be a UV lamp or a focused laser beam. In the case of a UV lamp, the mask is a physical mask on a glass plate (typically quartz) that is aligned with and in contact with the substrate. If the optical source is a laser, a digital mask is created and the laser is scanned across the surface according to the mask. Prior to the light exposure, the substrate is coated with a photosensitive chemical called a PR, typically with a thickness around $4\ \mu\text{m}$. The PR is either initially soft and hardens when exposed to the optical source (negative PR) or initially hard and softens with exposure (positive PR). Following exposure, the soft part (determined by the mask) is removed by another chemical called a developer. The result of such a process is a

microsized pattern in the PR, which will work as a physical mask on the substrate for consecutive treatment, such as physical or chemical etch or deposition of additional material. At the end of the process, the remaining PR on the surface is dissolved, leaving a microsized pattern in the underlying solid substrate.

In this thesis, a negative PR (ma-N440, Micro Resist Technology) is spin coated onto the substrate and the resulting PR thickness is $4.60 \pm 0.3 \mu\text{m}$. The PR is soft baked at 95°C to cure the exposed PR before submerged in a developer (ma-D332/S, Micro Resist Technology). The optical exposure was done in a Maskless Aligner (MLA150, Heidelberg Instruments) using a digital mask and a 405 nm wavelength laser. The exposure doses used were 1700 mJ m^{-2} and 1900 mJ m^{-2} , resulting in two different hierarchical structures, described in Section 3.5.4.

3.5.2 Chemically Assisted Ion Beam Etch

Following the photolithography process, features such as cylinders, pillars or holes in the microsized range could be etched into a solid surface by a high-energy ion beam. This is called dry etch, in contrast to wet etch with a liquid chemical, and one such method is called CAIBE. The CAIBE process relies on a high-energy ion beam, e.g. Ar^+ , along with a directed spray of a reactive chemical, e.g. chlorine ions. It is a subprocess of the general Reactive Ion Etch (RIE) process, for which the etch is done in vacuum. Common for the etch processes is that a high-energy ion beam is focused onto the surface and parts of the solid material is removed by sputtering. In the case where a PR mask is already fabricated on the surface, the pattern is transferred to the substrate itself. By controlling the energy of the beam along with the etch time, an accurate control of the depth and profile of the features can be obtained. In the CAIBE process a reactive chemical is placed close to the surface, such that both chemical and physical etch can occur at the same time. The reactive chemical can enhance etch rates and selectivity towards the mask material, such that a more clean etch of the substrate material is obtained. Finding the optimum ratio between the inert ion source and the reactive chemical will result in an accurate control of the sidewall of the etched features. In the present work an Ar^+ beam was used as the ion source and oxygen ions were used as the reactive chemical.

3.5.3 Nanoneedles grown by Solution Immersion

Solution immersion is the process of submerging a substrate into a chemically reactive solution in order to spontaneously grow e.g. nanostructures on the surface. On Cu, a variety of nanostructures can be fabricated by this process, depending on what chemical is used in the solution. Wang et al. [113] showed the formation of flowerlike structures on Cu with the use of n-tetradecanoic acid. He et al. [114, 115] fabricated CuO NN on a Cu substrate with a solution of ammonium persulfate $((\text{NH}_4)_2\text{S}_2\text{O}_8)$ and sodium hydroxide (NaOH). In this work, CuO NN are fabricated on a Cu substrate with an adapted version of the solution immersion technique developed by He et al., and is henceforth called Nanostructured Surface (NS).

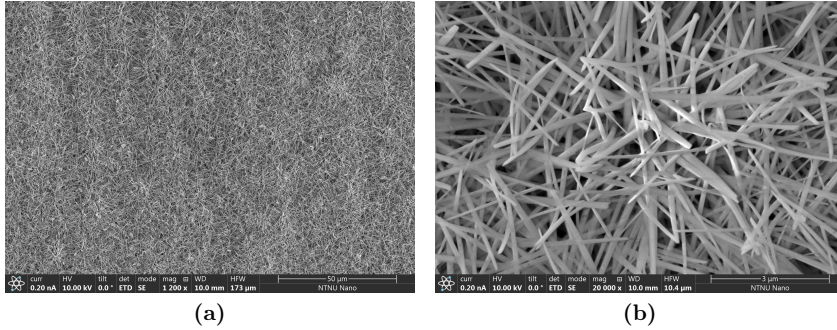
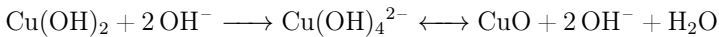
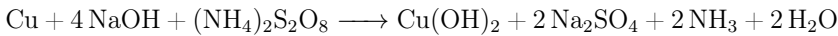


Figure (3.14): Scanning Electron Microscope images of CuO nanostructures on a Cu substrate fabricated by solution immersion.

Initially, the Cu substrate is cleaned with ethanol, isopropanol and acetone. Then, the substrate is immersed into the highly oxidizing solution of 0.1 M $(\text{NH}_4)_2\text{S}_2\text{O}_8$ and 2.5 M NaOH for 3 min. The Cu is oxidized according to the following mechanism:



The reaction results in the growth of $\text{Cu}(\text{OH})_2$ NN on the substrate surface. Subsequently, the surface is dried at 120°C to fully dehydrate the structures, i.e. removing the OH-groups, resulting in a surface with stable CuO NN. A Cu surface covered in a high density of randomly oriented CuO NN is shown in Figure 3.14. The width of the NN is on average 175 nm and the average length is $3\mu\text{m}$. The NN initially grow at preferential nucleation sites with high surface energy such as trenches and spikes on the surface. Therefore, the original surface structure of the Cu surface is seen as lines with higher density of NN, or alternatively as a somewhat wavy pattern.

3.5.4 Hierarchical structures

By combining the fabrication techniques described so far, a hierarchical structure can be fabricated. A hierarchical structure has features on different length scales, in this case both on micro and nano scale. By firstly conducting photolithography and CAIBE and secondly conducting solution immersion, surfaces with Cu micropillars covered with CuO NN were fabricated. An overview of the surfaces is shown in Figure 3.15(a) and (c). The difference in the fabrication of these two surfaces is the laser dose used in the photolithography step. For the surface in Figure 3.15(a) the dose was 1700mJ cm^{-2} , and this surface is henceforth named S17. For the surface in Figure 3.15(c) the laser energy flux was 1900mJ cm^{-2} , and the surface is henceforth named S19. Two obvious differences between S17 and S19 are the density and uniformity of the NN. On S17 the long NN grow mainly from the base of the micropillars and in the horizontal direction, and there are shorter NN found everywhere on the surface. On S19 the long NN also grow from the base of the

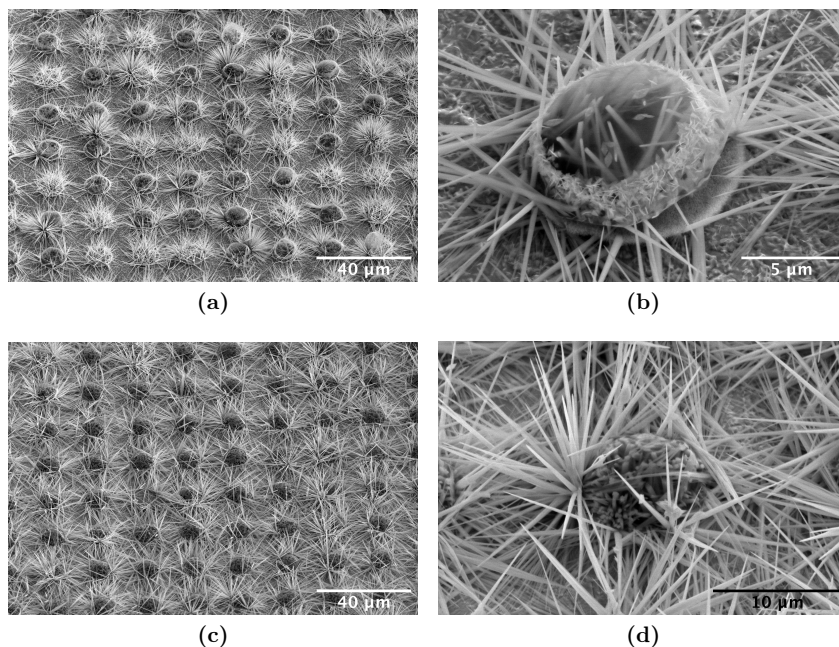


Figure (3.15): Scanning electron microscopy images of the two hierarchical surfaces fabricated and studied in this work. For both surfaces the length of the nanoneedles are approximately $10\ \mu\text{m}$. (a) and (b) show the surface of the S17 substrate. The nanoneedle density is not uniform and the nanoneedles have preferentially grown on the sides of the micropillars. (c) and (d) show the surface of the S19 substrate at two different magnifications. The nanoneedles have grown around the sides of the micropillars, and in all directions.

micropillars, but they are more densely packed and grow in all directions, covering the Cu substrate. On some of the micropillars on S17 the NN also grow in all directions and appear as clusters around the pillars, but the occurrence of these clusters is much lower on the S19 surface. In addition, the Cu surface between the micropillars are covered with a network of horizontally aligned NN on S19. In summary, the appearance of the micropillars and the growth of the NN are more uniform on the S19 than the S17 surface.

Chemicals and materials

4.1 Thermophysical properties of CO₂

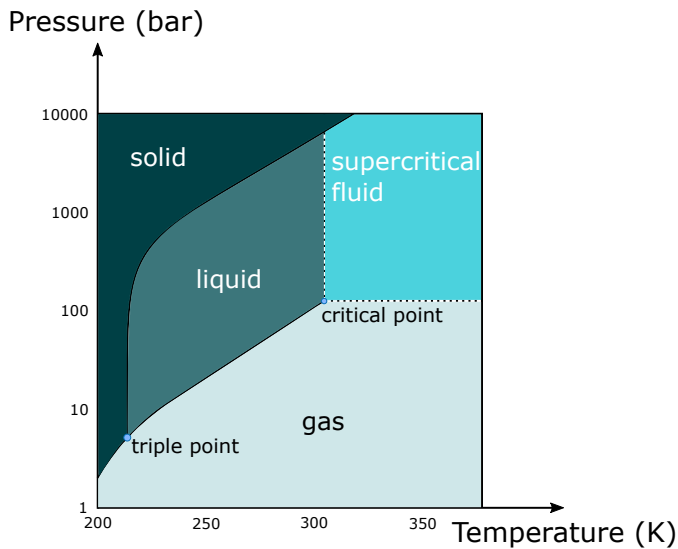


Figure (4.1): Phase diagram of CO₂ showing the triple point and the critical point.

This PhD work focuses on revealing the mechanisms of CO₂ condensation and how to, if possible, increase the heat transfer efficiency. In Figure 4.1 the phase diagram of CO₂ is shown. Condensation of CO₂ occurs at pressures above 5.2 bar, as seen in the phase diagram. Below this pressure a direct sublimation to dry ice would occur if the temperature is decreased from a gas phase temperature. Compared to other refrigerants CO₂ has a relatively low critical temperature ($T=31\text{ }^{\circ}\text{C}$). Refrigeration cycles with CO₂ as a refrigerant is therefore often designed for transcritical operation, where a decrease in temperature, e.g. in the gas cooler, does not cause a phase

Table (4.1): *Relevant thermophysical properties of CO₂ at the two-phase line*

Pressure	10 bar	15 bar	20 bar
Saturation temperature (at set pressure)	−40.1 °C	−28.5 °C	−19.5 °C
Liquid density, ρ_l (kg m ^{−3})	1121.8	1074.2	1034.0
Vapor density, ρ_v (kg m ^{−3})	26.2	39.2	52.8
Density difference, $\rho_l - \rho_v$ (kg m ^{−3})	1095.6	1035.0	981.2
Viscosity, μ_l (mPa s)	2.0	1.7	1.4
Latent heat, h_{fg} (kJ kg ^{−1})	320.8	300.0	281.6
Thermal conductivity, k_l (mW m ^{−1} K ^{−1})	159.8	145.4	134.3
Surface tension, λ (mN m ^{−1})	13.15	10.47	8.48

change. In the present work, the starting point of investigation was condensation for CO₂ transport in the CCS cycle and the focus is therefore on the two-phase line between liquid and gas. Relevant thermophysical properties of CO₂ at the two-phase line for the three investigated saturation pressures are summarized in Table 4.1. The thermodynamic properties are calculated with Span-Wagner Equation of State [116] and the thermophysical properties are calculated with correlations by Vesovic et. al [117]. All calculations are performed with the library *CO2lib* developed at NTNU/SINTEF Energy Research.

4.2 Investigated materials

During the work with this thesis, three materials have been the basis for the investigation of heat transfer properties during CO₂ condensation: Cu, Al and stainless steel (316). The materials were chosen based on their wide usage in process equipment where condensation occurs. In addition, Copper Oxide (CuO) nanostructures have been grown on Cu substrates, as described in Chapter 3.5. When the material was chosen, the intent was to achieve DWC on the nanostructured surfaces. In the dropwise mode, thermal conductivity of the condenser material is an important factor [118], and we chose Cu as the base material for its superior thermal conductivity. The substrates investigated in the first experimental study (paper II) were circular discs, 2 cm in diameter, which were cut from rolled plates. The thickness of the Cu and steel discs were 0.5 mm, while the Al disc was 0.7 mm thick. The surface roughness of the substrates has been measured for all surfaces with a Veeco Dektak 150 Profilometer. Ten line scans, each 5 μ m in length, was performed for each surface, and the resulting averages are presented in Table 4.2. The Al surface has the highest roughness, while the Cu surface is least rough, in terms of arithmetic mean average (MA) roughness and root mean square (RMS) roughness. The investigated substrates were cleaned with acetone, isopropanol and ethanol, and subsequently dried with pressurized dry air prior to heat transfer experiments. The micro- and nanostructured surfaces investigated in paper III were fabricated from 2.5x2.5 cm Cu squares, also cut from rolled plates. The handling and fabrication steps of these substrates are described in Chapter 3.5.

Table (4.2): MA and RMS roughness of the investigated surfaces, along with typical values for the surface energies and thermal conductivities. The surface energy for the aluminum sample is given for Al_2O_3 as an Al surface in atmospheric environment will be oxidized.

Material	MA Roughness (nm)	RMS Roughness (nm)	Peak-to-valley Roughness (nm)	Surface Energy (mJ/m ²)	Thermal Conductivity (W/m-K)
Copper	73.3	93.4	250	1650 [119]	410
Aluminium	513.1	722.6	2000	169 [120]	205
Stainless steel	243.5	312.3	1000	53 [121]	14.2
Copper Oxide	n/a	n/a	n/a	n/a	33

Table (4.3): Geometry and dimensions of the fabricated micro- and nanostructured surfaces: S17, S19 and NS.

	Nanoneedle length (μm)	Nanoneedle base diameter (nm)	Composition		
			Cu (wt%)	O ₂ (wt%)	std. dev.
S17	10	300			
S19	10	200			
NS	4	175	69.7	30.3	0.2

For heat transfer experiments, the substrates were attached to the Cu cylinder with a TIM. The TIM was applied in a thin uniform layer covering the entire cylinder end surface. The investigated substrates were pressed onto the surface resulting in a uniform layer of TIM between the substrate and the Cu cylinder. The thickness of the TIM has been measured to be around 0.15 mm with an estimated error of ± 0.05 mm. The thickness was measured with a caliper by applying a layer of TIM on a detached circular disc with the same application technique as in the experiments. The relevant material properties are summarized in Table 4.2.

The micro- and nanostructured surfaces have been characterized in terms of dimensions of the nanoneedles and composition of the surface. The dimensions were measured by investigating the SEM images of the surfaces in the software ImageJ and the compositions were found by using EDX (Electron Diffraction Spectroscopy), which is a feature of the SEM. The EDX analysis was performed only for the purely nanostructured surface (NS), and we assume that the nanoneedle composition is the same on the hierarchical surfaces.

Main results

The work with this thesis has resulted in a path from the idea of DWC via a literature review on wetting and surface design, to the work with heat transfer on flat surfaces and finally to the attempt to enhance condensation efficiency on micro- and nanostructured surfaces. The main findings along the way are described in this chapter.

5.1 Condensation mechanisms - knowledge from dropwise condensation of water extracted for CO₂

For a surface to be classified as either hydrophobic or hydrophilic, the value of the contact angle must be determined. With a contact angle above 90° the surface is said to be hydrophobic and a contact angle below 90° is related to a hydrophilic surface. For a surface to be superhydrophobic, which is the desired state for DWC to occur, there are two requirements: a) the contact angle must be above 150°, and b) the contact angle hysteresis must be less than 10°.

To achieve stable droplets on a structured surface, there are strict requirements for the geometry relating to width vs height of ordered structures and the liquid's surface tension. Design criteria have been proposed and thermodynamic calculations show that careful consideration of height, width and spacing of micropillars will result in contact angles above 120° [122], see Figure 5.1. Surface tension is a very important property when it comes to DWC, and since water has quite high surface tension due to the hydrogen bondings between the water molecules, achieving DWC of water is not a large challenge today. When considering low surface tension fluids, such as organic fluids (e.g. ethanol, hexane and hexadecane), the requirements on the surface structures are, however, much stricter. It is in this case not enough to fabricate nanopillars or hierarchical structures to obtain DWC. Wu et al. [123] has shown that T-shaped surface structures will promote floating static droplets of hexadecane, even

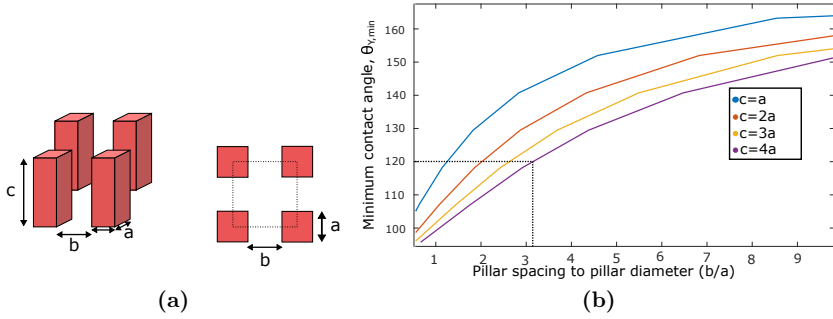


Figure (5.1): (a) The geometry of a micropillared surface. a is the pillars width, b is the spacing between the pillars and c is the height. (b) The results of a thermodynamic analyses simulating the contact angle of a static water droplet on the micropillars as a function of the pillar spacing to pillar height (b/a) [122]. The figure is also found in Paper I.

though no DWC was shown. On the other hand, Rykaczewski et al. [36] was able to obtain DWC of pentane, which has a surface tension comparable to CO_2 , on both a smooth oleophobic (non-wetting towards oily substances) and SLIPS. The SLIPS was impregnated with Krytox oil and the advancing contact angle was as low as 50.3° . In the case of SLIPS it is crucial that the lubricant exhibits good adhesion to the surface and that it is immiscible and repellent towards the condensing liquid. It is also important that the vapor pressure of the lubricant is low enough to maintain in the liquid state at the condensation pressure and temperature.

The latter requirement is the main challenge when trying to design a SLIPS for DWC of CO_2 . CO_2 has a surface tension of 16.5 mN m^{-1} . Lubricants with very low surface tension, such as hexafluoro-2-propanol (HFIP), has a high vapor pressure and is likely to evaporate within minutes at the pressures required for CO_2 condensation. By using the model set forth by Preston et al. [35] it is found that HFIP is a candidate for dropwise CO_2 condensation, but the model does not consider vapor pressure or, more importantly, environmental impact of the lubricant. Fluorinated compounds are hazardous for the environment, and these chemicals have been banned in several countries. This finding is important and it contributed to change the focus of the PhD from achieving DWC to understanding and enhancing FWC heat transfer.

5.2 Novel experimental methodology and measurements of heat transfer characteristics of CO₂ condensation on common heat exchanger materials

As a part of my PhD work I have developed an experimental methodology to determine the heat flux and the heat transfer coefficient during condensation of CO₂. The method and the experimental setup were developed for investigating the condensation behavior on different materials and eventually, different surface structures. The main parts of the experimental setup is the pressure chamber which has a design pressure of 25 bar and a cooling element that is designed for cooling the sample down to -55°C . The method is described in Chapter 3, Methodology.

As a baseline for further studies on the potential of enhancing condensation heat transfer on modified surfaces, we conducted a study on the heat transfer characteristics of CO₂ condensation on Cu, Al and steel. The commonly known and well-used Nusselt model does not include any influence of the substrate or surface properties, and is developed for a flat surface without structure or modification of any kind. In industrial applications, condensation surfaces are far from ideal, and we saw the need for investigating flat surfaces as they are used, with intrinsic roughness from the fabrication process.

CO₂ condensation was studied at three different saturation pressures, 10 bar, 15 bar and 20 bar, corresponding to saturation temperatures of -40.1°C , -28.5°C and -19.5°C , respectively. The condensation heat flux data are shown in Figure 5.2, together with the Nusselt model at the same pressures. The condensation HTC are shown in Figure 5.3, along with the Nusselt model at the same saturation pressures. The deviation from the theoretical values is larger for HTC than for heat flux, as the calculations include the term $(1/(T_{sat} - T_{surf}))^{(1/4)}$, which will be very large when the difference between surface and saturation temperatures becomes small. The heat flux increases with subcooling, as expected, since heat flux is proportional to the temperature gradient. The heat flux also increases for increasing saturation pressure. The condensation HTC is highest for Cu and lowest for Al and steel. For the latter two, the experimental heat flux results lie within the estimated uncertainty range, and we can not distinguish between these results.

Below subcooling of 1 K, the HTC on Cu at 20 bar and steel at 10 bar do not follow the Nusselt model. Generally, the data at low subcooling is hard to determine. One reason for this is the coupling between the surface roughness and the thickness of the condensate film. At saturation pressure of 10 bar and subcooling of 2 K, the Nusselt model predicts that the film is $34.1\ \mu\text{m}$ thick. The film is therefore thicker than the substrates' roughnesses at this point, which is $0.7\ \mu\text{m}$ RMS at the highest (Al). When the subcooling is close to zero, the film thickness also decreases to zero. At some point, the relative influence of roughness will increase and cause retention of the condensate. The liquid will not flow as freely as it would on an atomically flat surface and the liquid could be trapped in the grooves or between small spikes on the surface, thereby increasing film thickness and reducing the local HTC. This is

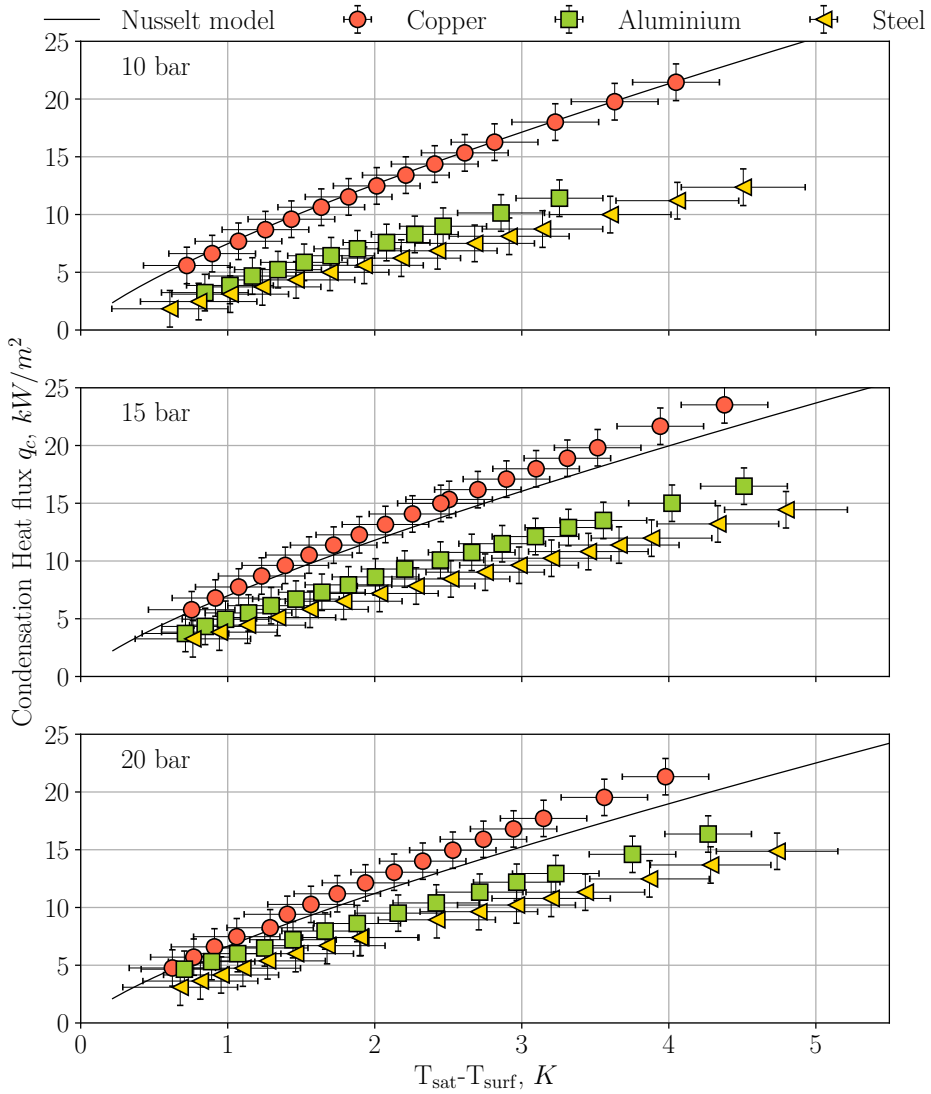


Figure (5.2): Condensation heat flux of CO_2 on Cu, Al and Steel at 10, 15 and 20 bar saturation pressure, along with the Nusselt model for each pressure. The error bars represent the propagated errors of each measured quantity. These results are also shown in in Paper II.

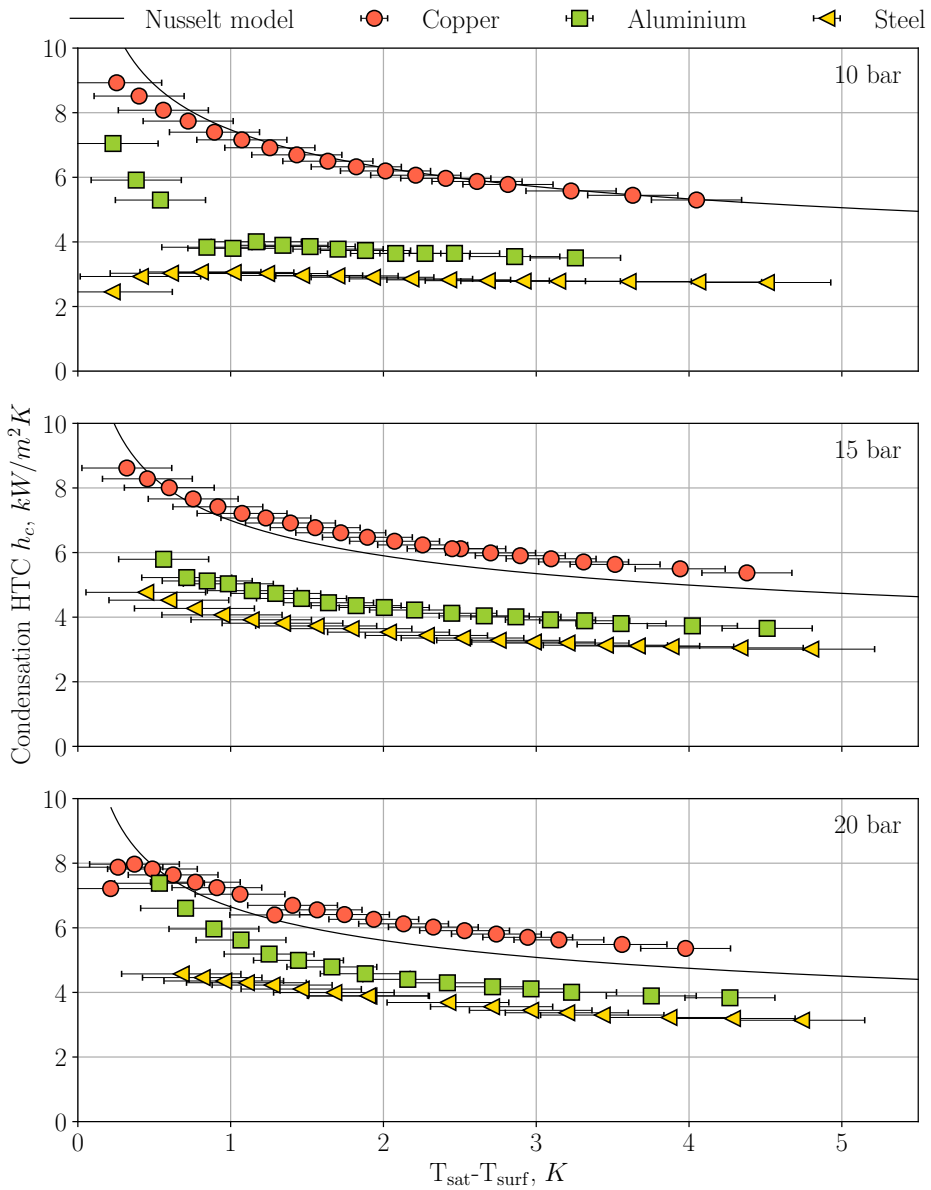


Figure (5.3): Condensation HTC of CO₂ on Cu, Al and Steel at saturation pressures of 10, 15 and 20 bar, and the Nusselt model for each pressure. These results are also shown in Paper II.

more pronounced at low film thicknesses, hence at low subcooling. It is here we see that the HTC deviates the most from the Nusselt model. At a sufficiently low level of subcooling the film will be discontinuous. The surface temperature will not be uniform in this case, which is another cause for the model-experiments discrepancy.

5.3 Enhanced CO₂ condensation heat transfer on Cu based micro- and nanostructured surfaces

For investigating the influence of surface structures on CO₂ condensation heat transfer, three Cu-based surfaces were fabricated. The first surface is a purely nanostructured surface fabricated where NN were grown by solution immersion. The second and third are hierarchical surfaces with microstructures constructed by photolithography, CAIBE, and nanoneedles grown by solution immersion.

The condensation HTCs on the structured surfaces and the Cu reference surface are shown in Figure 5.4. The saturation pressure has been varied between 10, 15, and 20 bar. The HTCs are nearly independent of subcooling, $T_{sat} - T_{surf}$, for the investigated surfaces. For the three surfaces unstructured Cu, S19, and NS, the condensation HTCs are within the uncertainty range of each other for all pressures and subcooling, and the heat transfer is therefore indistinguishable. We propose that this is caused by three competing effects: 1) increase in surface area due to the nanostructures, 2) lower thermal conductivity of the CuO NN compared with Cu, and 3) flooding of the NN. The first mechanism increases the HTC, while the two others reduce the heat transfer. For the S19 and the NS surfaces, the three effects balance each other. It is apparent that the high density of NN on the S19 surface diminishes the effect of the underlying microstructure, and the effective topography of the S19 and the NS are similar enough for the heat transfer behavior to be equal. The thermal conductivity of metallic oxides is generally lower than of the pure metal, and for CuO it is over ten times lower than for Cu. However, if thermal conductivity was the determining factor, as in the work by Hoenig et al. [118], the heat transfer would have been lower on S19 and NS than on unstructured Cu. The effect of increased surface area must therefore be dominating. An increase in HTC by increased surface area has been observed for other augmented surfaces as well, such as fins [124] and pin-fins [125] on tubes in e.g. shell-and-tube condensers. However, if the distance between the surface structures becomes too small, mechanism 3) comes into play; flooding of the nanostructures. Since the NN density is high on both S19 and NS, the structures are likely flooded by the condensate. Flooding will cause an increased condensate film thickness due to liquid retention in the structures, which again increases the thermal resistance through the film. Consequently, the increase in HTC by augmented area is balanced by low thermal conductivity and surface flooding, and the resulting condensation HTCs on S19, NS and unstructured Cu become equal.

On the S17 surface, the condensation HTC is significantly higher compared with the three other surfaces. At most, the HTC is 66 % higher for the S17 substrate than the Cu substrate. This occurs at 1 K subcooling and 20 bar saturation pressure.

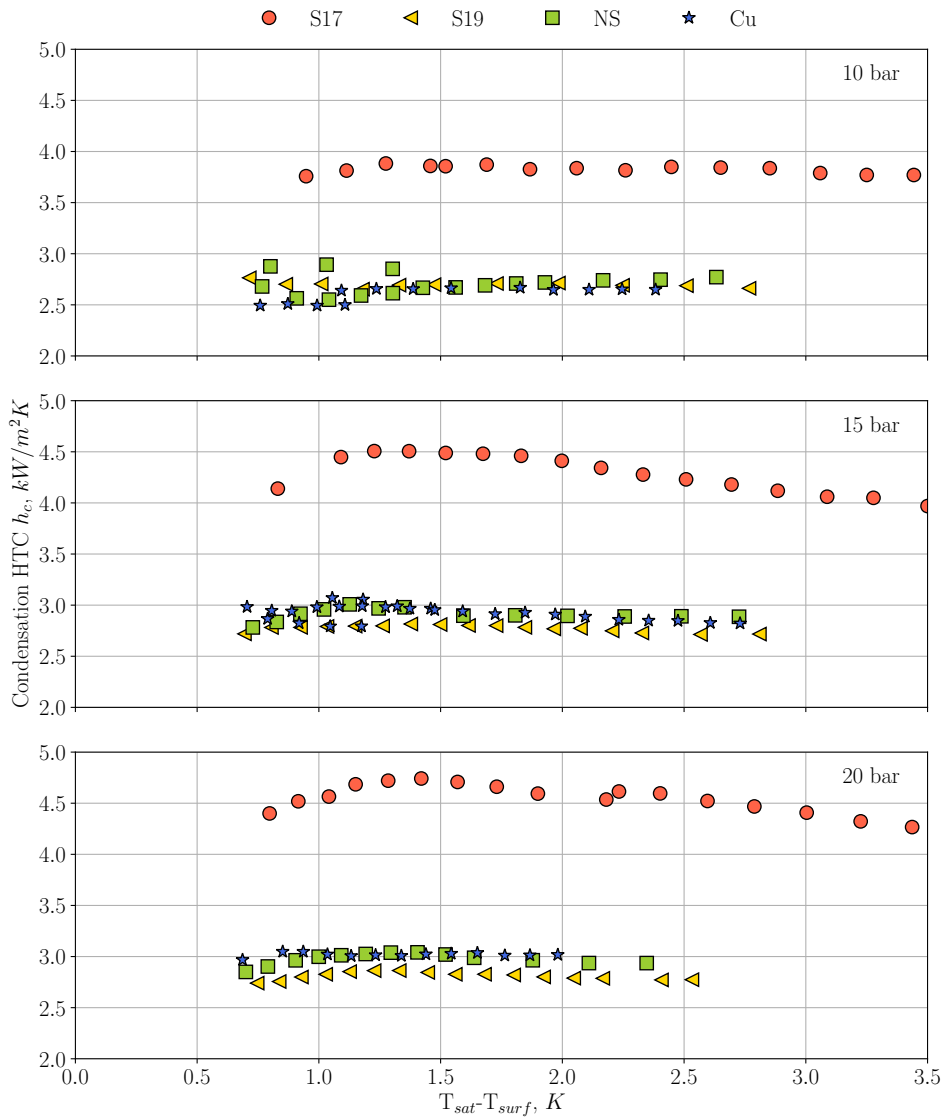


Figure (5.4): Condensation HTC for Cu, S17, S19 and NS at saturation pressures of 10, 15 and 20 bar. The figure is also found in Paper III.

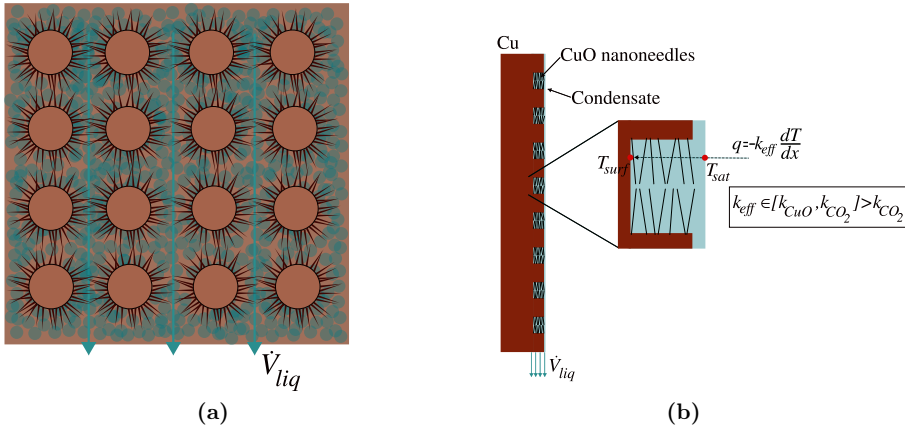


Figure (5.5): Schematic representation of the proposed condensation mechanism. The volume flow rate, \dot{V}_{liq} , is directed downward in the sketch. (a) The condensation is initiated with nucleation and growth at the untreated Cu surface between the micropillars. The drainage of the condensate is increased due to the nanoneedles, and the condensate film is thinner than on a flat surface. (b) The thermal conductivity of the composite layer, k_{eff} , is higher than the thermal conductivity of the pure condensate, k_{CO_2} . The composite layer is the combination of the condensate and the nanoneedles.

We attribute the increased HTC to the balance between the structured and the non-structured areas. As opposed to S19, the areas between the micropillars are not covered with a network of horizontal NN. According to the model by Ali et al. [126], flooding is less likely to occur on the S17 surface due to the larger spacing between the structures and lower density of NN. The proposed mechanism of the condensation process is that the initial condensation occurs on the flat Cu areas between the micropillars, as sketched in Figure 5.5(a). The nanostructures around the micropillars then lead to efficient drainage of the liquid CO_2 , with the mechanism reported by Oh et al. [127] – consequently, the heat transfer efficiency increases. Returning to the effect of the three competing factors 1), 2) and 3) above, the resulting the HTC is higher on S17 compared to S19 and NS. In contrast to the work by Aili et al. [40], we here show that an optimal combination of micro- and nanostructures is beneficial for heat transport in certain cases, and especially when the hierarchical nature of the surface is pronounced, such as for S17.

Even though the preferential condensation sites for the CO_2 are proposed to be on the unstructured Cu in between the micro- and nanostructures, there will still be some condensation within the nanostructures. We suggest that this condensation belongs to the wicking condensation scheme. The heat transfer by conduction through the liquid is higher than through a liquid film, as shown in Figure 5.5(b). This enhancement in heat transfer is attributed to the higher thermal conductivity of the effective film, which consists of liquid CO_2 and CuO NN [50].

5.4 Application of the results in paper II and III

The experimental results within paper II and within paper III are discussed in the two sections above and in the two papers. However, experiments have been done on untreated Cu for both articles and a comparison between the reported data in the two papers is therefore in order. This section presents the similarities and dissimilarities of the experimental results, and explain why the data are different on the same material and still valid.

As described in Chapter 3, the first version of the experimental setup was designed to observe dropwise condensation and to measure droplet contact angles. The cooling element for for achieving a surface temperature below the saturation temperature was designed with a quadratic surface and was placed in a horizontal direction and mounted to a rotational motor. We wanted to observe dropwise condensation and with the motor we could rotate the investigated surfaces to measure the angle at which the droplets start to move. The latter is a measure of the adhesion of the droplets to the surface, i.e. a measure of the wetting.

Fabrication of the micro- and nanostructured surfaces started with three quadratic Cu pieces. The geometry was based on the initial design of the heat transfer experimental setup, where the substrates were to be placed directly on the quadratic cooling element surface. When conducting heat transfer experiments on the vertically aligned cylinder, the quadratic structured and untreated Cu surfaces are therefore subject to heat loss in the perimeter of the samples. The heat that is lost in the perimeter will be equal for the four samples investigated in paper III and we assume that the comparison of the condensation heat transfer on the untreated and structured surfaces can be used to discuss the relative efficiency of the condensation heat transfer on the various structures. However, these results are to be considered rig-specific and cannot be used to develop correlations needed for equipment design.

Important to note is that the reported data in Chapter 5.3 does not include the developed heat loss function, as the data are meant for internal comparison between the four investigated substrates. The relative difference between the reported heat fluxes and HTC's are unaltered with the heat loss function and the discussion of the results in this thesis and in paper III is therefore valid.

Conclusions and further work

6.1 Summary and conclusions

Condensation heat transfer is an efficient means of transportation of heat due to the release of latent heat in the vapor. Condensation is therefore a part of several processes for thermal management, such as cooling of electronics and in refrigeration of food in supermarkets. Sometimes the condensed vapor is in itself the desired outcome of the process, e.g. when liquefying natural gas, CO_2 or H_2 for transportation purposes. Liquid requires less volume than a gas, and the liquefied state is preferential when gases are to be transported by ship over long distances. In the case of CO_2 the liquefied state requires around 77 times less volume than the gaseous state, for the same mass. Regardless of the desired outcome, condensation is an energy intensive process that requires a number of large and expensive (in cost and energy) equipment such as compressors, heat exchangers and separators. The refrigeration process has therefore been the subject for extensive research for more than a century, and process optimization is still a hot topic. Enhancing the condensation heat transfer has also been targeted by the research community. A large contributor to the heat transfer resistance during condensation is the liquid film forming on the condenser surface. The latent heat released in the vapor is transferred through the liquid film by conduction. The heat transfer resistance is therefore large due to the low thermal conductivity of most liquids. As a consequence, research is directed towards increasing the condenser area through surface structuring, reducing the thickness of the film, or removing the film all together. The latter is the case when the condensation occurs in the dropwise mode. Discrete droplets nucleate, grow and roll off the surface, leaving fresh nucleation sites for new droplet nucleation and growth. This cyclic process could be up to ten times as efficient as the conventional filmwise condensation. DWC occurs on surfaces with low surface energy or by careful structuring of a surface on the micro- and nanoscale. However, when the surface tension of the liquid in question is low, the requirements on the condenser surface become even stricter, and the fabrication could become too complex. Through the literature review conducted in this PhD, we realized that achieving DWC of CO_2 was unfeasible within the available time frame. Learning

from previous literature it seemed like it was necessary to use harmful and highly volatile chemicals, such as fluorinated isopropanol, to reduce the surface energy to a sufficient level for DWC. We therefore decided not to seek the DWC mode and rather search for ways to increase the efficiency of filmwise CO₂ condensation.

Through the work with this thesis we have reported the condensation heat transfer behavior of common materials used in the liquefaction process. The results show that there is a significant difference in the heat transfer on materials with different surface properties. The widely applied Nusselt model of FWC does not, however, include condenser surface properties. Predictions of the FWC process by the Nusselt model will therefore not result in different HTCs for different materials. Nevertheless, our results show that the HTC is affected by surface roughness and surface energy. Of the materials studied here, the smooth Cu surface is therefore the most efficient choice, while rougher Al and stainless steel are the least effective, in terms of heat transfer coefficients. Through this PhD I have shown that a revision of the Nusselt model, or developing a new model for FWC which includes the surface properties of the condenser could be a necessary next step for accurate process design.

The effect of augmented surfaces of the condenser has been the subject of extensive investigation. We wanted to study the effect of micro- and nanostructures on CO₂ condensation. We hypothesized that surface structures would increase the heat transfer, even though DWC was not induced. Two categories of structured surfaces were fabricated: 1) a surface with structures on the nanoscale, and 2) hierarchical structures, i.e surfaces with structures on both micro- and nanoscale. The structures were fabricated on Cu and the nanostructures were CuO nanoneedles. On one of the investigated surfaces the heat transfer coefficient was significantly higher than on the two others, and also compared to the flat Cu surface. The most efficient surface had a hierarchical surface structure comprised of CuO nanoneedles grown on Cu micropillars. The nanoneedles did not cover the entire surface and un-structured Cu was exposed between the micropillars. The nanoneedles had mainly grown in the horizontal direction from the base of the micropillars. The proposed condensation mechanism starts with nucleation and film growth at the exposed Cu surface, followed by efficient drainage caused by the nanostructures. The condensation that occurred within the nanostructures followed the wicking condensation regime, and an increased heat transfer is expected due to the higher thermal conductivity of the composite liquid/CuO surface, compared to the pure liquid film in conventional filmwise condensation. For the structured surfaces, it seems that there are three competing mechanisms which govern the overall heat transfer behavior. One is that the enhanced surface area increases the heat transfer. The second is that the reduced thermal conductivity of oxidized top surface on the structured material reduces the heat transfer. The third is the deterioration of the heat transfer enhancement due to surface flooding. My study has shown that the effects of these mechanisms can balance each other, especially when the density of the nanostructures is high. In this case the surface apparently behaves like an unstructured surface, in terms of overall heat transfer. More importantly, the results show that by optimizing interactions of the mechanisms, superior heat transfer behavior can be achieved.

6.2 Suggestions for further work

The above results give some indications on the potential of increasing condensation heat transfer of CO₂. However, if unlimited time was granted, the work could have included many more studies. I will therefore present some suggestions on how to continue the work of enhancing CO₂ condensation efficiency.

- **Database for condensation on different materials:** I have in this work suggested that the heat transfer on unstructured materials is governed by surface roughness and surface energy. In order to develop a new correlation between surface properties and HTC, which can be used in equipment design, an extended study with a wider range of surface energies and surface roughness must be conducted. I suggest to fabricate Cu, Al and steel surfaces with a controlled range of surface roughness, and perform heat transfer experiments on these surfaces. In this way, the governing mechanisms can be decoupled and correlations can be developed. Materials with other surface energies should also be included. Silicon (Si) is often used in the nanoscience community due to its semiconductor properties, and many fabrication techniques for micro- and nanostructures are developed for Si. This material is a natural choice for further studies. Also titanium (Ti) should be included in the database, based on its superior mechanical properties for applications requiring light-weight and robust materials.
- **Expansion of the pressure domain of the experiments:** In addition to expanding the number of studied materials, the pressure dependence of the heat transfer could be determined more thoroughly with condensation in a wider range of pressures. Especially, it is interesting to investigate elevated pressures up to the critical point of CO₂ (73.8 bar and 30.98 °C). The study of the micro- and nanostructured surfaces indicated that the heat transfer was saturated at higher pressures. This phenomena should be investigated further with smaller steps in pressure. If this plateau in HTC continues at higher pressures, process design can be optimized in terms of energy input vs heat transfer output.
- **Heat transfer at low subcooling:** One of the unsolved questions of this work is what happens with the heat transfer at very low subcooling. The Nusselt model predicts that the HTC goes to infinity as the subcooling approaches zero. This unphysical behavior could not be correct, and a thorough investigation of the condensation at low subcooling will give additional insight into the condensation mechanisms. At an atomically flat surface, the onset of condensation will occur as liquid nucleates appear evenly across the surface. For a real-life surface, with roughness caused by fabrication, the nucleation will occur at energetically favorable sites such as spikes and corners in the topography. The nucleates will grow and coalesce and eventually a liquid film will spread out on the surface. Before the entire surface is covered, there will be small ponds on the surface with dry area in between. The spread of the ponds will depend on the surface energy of the condenser. When measuring the heat transfer at this point, the data reduction techniques applied in this

work will not be applicable. The temperature will not be uniform across the surface and heat transfer will occur by both conduction through the liquid and convection and radiation from the vapor towards the dry surface.

- **Reduce the uncertainty in temperature measurements:** During the work with this PhD, I have had several challenges with the uncertainty in the thermocouple measurements. Thermocouples are very good for measuring temperatures at wide ranges in a straight forward, intuitive manner. The intrinsic uncertainty is, however, quite large, and when measuring temperature differences down to 0.1K they may not be the best choice. At least, an extensive calibration procedure is necessary, and still there might be some unfavorable noise in the results. In this work this has especially concerned the temperature measurements in the Cu cylinder for determining the heat flux. We solved the initial large scattering in the results by calibrating in a cold bath and to perform cold junction compensation, and ended up with satisfactory repeatability in the results. In future work, additional calibration of the thermocouples should be performed.
- **Continue to develop micro- and nanostructured surfaces for enhanced condensation rates:** In this work we have shown that balancing the structured and un-structured areas on a surface is beneficial for condensation heat transfer. We proposed a mechanism where the condensation rate is highest at the un-structured areas between the micropillars on the surface and that the nanostructures increase the drainage of the liquid, which together increases HTC. This mechanism should be investigated further. By fabricating surfaces with less nanoneedle density than the S17 surface and with smaller and larger un-structured areas, the effects could be quantified and an optimal design could eventually be found. The fabrication will in this case be a study in itself. The topography of the S17 and the S19 surfaces are very different, see Section 5.3, especially in terms of nanoneedle density and the size of the areas with exposed Cu. The only difference in the fabrication technique is the energy flux of the laser during photolithography, which obviously has an impact on the surface energy. A systematic study of the effect of laser beam energy flux on the subsequent growth of nanoneedles must be performed. In addition, it is interesting to determine how the size of the underlying micropillars influenced the heat transfer. Surfaces with micropillars with varying diameter, height and spacing should therefore be fabricated, followed by growth of nanoneedles with varying density. Alongside that study it is also interesting to investigate the condensation on purely microstructured surfaces, i.e. surfaces with micropillars on the Cu. Therefore, condensation heat transfer of the purely microstructured surfaces should be the focus of an individual study.
- **Expanding the experiments to other chemicals:** After spending four years to design and build an experimental setup for investigating CO₂ condensation, knowledge is built for performing similar experiments with other fluids. These could for example be other refrigerants and natural gas with various composition. Studies of the condensation heat transfer coefficient of additional chemicals will aid in developing a more robust model of filmwise condensation.

- **Proof-of-concept study of dropwise condensation of CO₂:** Finally, I have never really forgotten the desire to achieve dropwise condensation of CO₂. I believe that it is possible by sophisticated surface design and learning from work with other low surface tension chemicals such as pentane and butane. A first step could be to perform a proof-of-concept study where a SLIPS surface with fluorinated isopropanol is used as the lubricant. According to the literature on SLIPS, and the design criteria by Preston et al. [35], this chemical has the necessary properties to facilitate dropwise condensation. I have previously mentioned why this path was not taken for this PhD, but as a proof-of-concept study it could be interesting.

References

- [1] I. Snustad, I. T. Røe, A. Brunsvold, Å. Ervik, J. He, and Z. Zhang, “A review on wetting and water condensation - perspectives for CO₂ condensation”, *Advances in Colloid and Interface Science*, vol. 256, pp. 291–304, 2018. DOI: 10.1016/j.cis.2018.03.008.
- [2] I. Snustad, Å. Ervik, A. Austegard, A. Brunsvold, J. He, and Z. Zhang, “Heat transfer characteristics of CO₂ condensation on common heat exchanger materials: Method development and experimental results”, *Experimental Thermal and Fluid Science*, vol. 129, p. 110440, 2021. DOI: <https://doi.org/10.1016/j.expthermflusci.2021.110440>.
- [3] I. Snustad, L. Hollund, Å. Ervik, A. Austegard, A. Brunsvold, J. He, and Z. Zhang, “Condensation heat transfer of CO₂ on Cu based hierarchical and nanostructured surfaces”, *International Journal of Heat and Mass Transfer*, vol. 175, p. 121367, 2021. DOI: 10.1016/j.ijheatmasstransfer.2021.121367.
- [4] J. Wu, Å. Ervik, I. Snustad, S. Xiao, A. Brunsvold, J. He, and Z. Zhang, “Contact angle and condensation of a CO₂ droplet on a solid surface”, *The Journal of Physical Chemistry C*, vol. 123, no. 1, pp. 443–451, 2019. DOI: 10.1021/acs.jpcc.8b08927.
- [5] J. Wu, I. Snustad, Å. Ervik, A. Brunsvold, J. He, and Z. Zhang, “CO₂ wetting on pillar-nanostructured substrates”, *Nanotechnology*, vol. 31, no. 24, p. 245403, 2020. DOI: 10.1088/1361-6528/ab7c49.
- [6] C. v. Linde, “Process of producing low temperatures, the liquefaction of gases, and the separation of the constituents of gaseous mixtures”, US727650A.
- [7] W. Hampson, “Improvements relating to the progressive refrigeration of gases”, GB189510165A.
- [8] W. Nusselt, “Die oberflächen kondensation des wasserdampfes”, *Zeitschrift des Vereines Deutscher Ingenieure*, vol. 60, pp. 541–569, 1916.
- [9] F. P. Incropera, D. P. DeWitt, T. L. Bergman, and A. S. Lavine, *Fundamentals of Heat and Mass Transfer*, 6th. John Wiley & Sons, 2007.

- [10] E. Schmidt, W. Schurig, and W. Sellschopp, “Versuche über die kondensation von wasserdampf in film- und tropfenform”, *Technische Mechanik und Thermodynamik*, vol. 1, pp. 53–63, 2 1930. DOI: 10.1007/BF02641051.
- [11] E. J. Le Fevre and J. W. Rose, “Heat-transfer measurements during dropwise condensation of steam”, *International Journal of Heat and Mass Transfer*, vol. 7, no. 2, pp. 272–273, 1964. DOI: 10.1016/0017-9310(64)90095-x.
- [12] —, “An experimental study of heat transfer by dropwise condensation”, vol. 8, no. 8, pp. 1117–1133, 1965. DOI: 10.1016/0017-9310(65)90139-0.
- [13] J. W. Rose, “On the mechanism of dropwise condensation”, *International Journal of Heat and Mass Transfer*, vol. 10, no. 6, pp. 755–762, 1967. DOI: 10.1016/0017-9310(67)90135-4.
- [14] X. Ma, J. W. Rose, D. Xu, J. Lin, and B. Wang, “Advances in dropwise condensation heat transfer: Chinese research”, *Chemical Engineering Journal*, vol. 78, no. 2-3, pp. 87–93, 2000. DOI: 10.1016/S1385-8947(00)00155-8.
- [15] L. A. Bromley, “Effect of heat capacity of condensate”, *Industrial & Engineering Chemistry*, vol. 44, no. 12, pp. 2966–2969, 1952. DOI: 10.1021/ie50516a052.
- [16] W. M. Rohsenow, “Heat transfer and temperature distribution in laminar film condensation”, *Transactions ASME*, vol. 78, pp. 1645–1648, 1956.
- [17] B. Misra and C. F. Bonilla, “Heat transfer in the condensation of metal vapors: Mercury and sodium up to atmospheric pressure”, 1956.
- [18] E. M. Sparrow and J. L. Gregg, “A boundary-layer treatment of laminar-film condensation”, *Journal of Heat Transfer*, vol. 81, no. 1, pp. 13–18, 1959. DOI: 10.1115/1.4008118.
- [19] X. Chen, H. Ye, X. Fan, T. Ren, and G. Zhang, “A review of small heat pipes for electronics”, *Applied Thermal Engineering*, vol. 96, pp. 1–17, 2016. DOI: 10.1016/j.applthermaleng.2015.11.048.
- [20] Z. Rao and S. Wang, “A review of power battery thermal energy management”, *Renewable and Sustainable Energy Reviews*, vol. 15, no. 9, pp. 4554–4571, 2011. DOI: 10.1016/j.rser.2011.07.096.
- [21] J. B. Boreyko and C.-H. Chen, “Self-propelled dropwise condensate on superhydrophobic surfaces”, *Physical Review Letters*, vol. 103, no. 18, 2009. DOI: 10.1103/PhysRevLett.103.184501.
- [22] B. S. Sikarwar, N. K. Battoo, S. Khandekar, and K. Muralidhar, “Dropwise condensation underneath chemically textured surfaces: Simulation and experiments”, *Journal of Heat Transfer*, vol. 133, no. 2, 2010. DOI: 10.1115/1.4002396.
- [23] N. Miljkovic, R. Enright, Y. Nam, K. Lopez, N. Dou, J. Sack, and E. N. Wang, “Jumping-droplet-enhanced condensation on scalable superhydrophobic nanostructured surfaces”, *Nano Letters*, vol. 13, no. 1, pp. 179–187, 2013. DOI: 10.1021/nl303835d.

- [24] M. McCarthy, K. Gerasopoulos, S. C. Maroo, and A. J. Hart, “Materials, fabrication, and manufacturing of micro/nanostructured surfaces for phase-change heat transfer enhancement”, *Nanoscale and Microscale Thermophysical Engineering*, vol. 18, no. 3, pp. 288–310, 2014. DOI: 10.1080/15567265.2014.926436.
- [25] A. K. Kota, G. Kwon, and A. Tuteja, “The design and applications of super-omniphobic surfaces”, *NPG Asia Materials*, vol. 6, no. 7, p. 109, 2014. DOI: 10.1038/am.2014.34.
- [26] Y. Zhao, D. J. Preston, Z. Lu, L. Zhang, J. Queeney, and E. N. Wang, “Effects of millimetric geometric features on dropwise condensation under different vapor conditions”, *International Journal of Heat and Mass Transfer*, vol. 119, pp. 931–938, 2018. DOI: 10.1016/j.ijheatmasstransfer.2017.11.139.
- [27] M. Budakli, T. K. Salem, M. Arik, B. Donmez, and Y. Menceloglu, “Effect of polymer coating on vapor condensation heat transfer”, *Journal of Heat Transfer*, vol. 142, no. 4, 2020. DOI: 10.1115/1.4046300.
- [28] T.-S. Wong, S. H. Kang, S. K. Y. Tang, E. J. Smythe, B. D. Hatton, A. Grinthal, and J. Aizenberg, “Bioinspired self-repairing slippery surfaces with pressure-stable omniphobicity”, *Nature*, vol. 477, no. 7365, pp. 443–447, 2011. DOI: 10.1038/nature10447.
- [29] S. Anand, A. T. Paxson, R. Dhiman, J. D. Smith, and K. K. Varanasi, “Enhanced condensation on lubricant-impregnated nanotextured surfaces”, *ACS Nano*, vol. 6, no. 11, pp. 10 122–10 129, 2012. DOI: 10.1021/nn303867y.
- [30] R. Xiao, N. Miljkovic, R. Enright, and E. N. Wang, “Immersion condensation on oil-infused heterogeneous surfaces for enhanced heat transfer”, *Scientific Reports*, vol. 3, no. 1, 2013. DOI: 10.1038/srep01988.
- [31] X. Dai, B. B. Stogin, S. Yang, and T.-S. Wong, “Slippery wenzel state”, *ACS Nano*, vol. 9, no. 9, pp. 9260–9267, 2015. DOI: 10.1021/acsnano.5b04151.
- [32] T. Kajiya, F. Schellenberger, P. Papadopoulos, D. Vollmer, and H.-J. Butt, “3d imaging of water-drop condensation on hydrophobic and hydrophilic lubricant-impregnated surfaces”, *Scientific Reports*, vol. 6, no. 1, p. 23687, 2016. DOI: 10.1038/srep23687.
- [33] K. Chen, Y. Wu, S. Zhou, and L. Wu, “Recent development of durable and self-healing surfaces with special wettability”, *Macromolecular Rapid Communications*, vol. 37, no. 6, pp. 463–485, 2016. DOI: <https://doi.org/10.1002/marc.201500591>.
- [34] P. B. Weisensee, Y. Wang, H. Qian, D. Schultz, W. P. King, and N. Miljkovic, “Condensate droplet size distribution on lubricant-infused surfaces”, *International Journal of Heat and Mass Transfer*, vol. 109, pp. 187–199, 2017. DOI: 10.1016/j.ijheatmasstransfer.2017.01.119.
- [35] D. J. Preston, Y. Song, Z. Lu, D. S. Antao, and E. N. Wang, “Design of lubricant infused surfaces”, *ACS Applied Materials & Interfaces*, vol. 9, no. 48, pp. 42 383–42 392, 2017. DOI: 10.1021/acsmi.7b14311.

- [36] K. Rykaczewski, A. T. Paxson, M. Staymates, M. L. Walker, X. Sun, S. Anand, S. Srinivasan, G. H. McKinley, J. Chinn, J. H. J. Scott, and K. K. Varanasi, “Dropwise condensation of low surface tension fluids on omniphobic surfaces”, *Scientific Reports*, vol. 4, no. 1, 2015. DOI: 10.1038/srep04158.
- [37] D. J. Preston, Z. Lu, Y. Song, Y. Zhao, K. L. Wilke, D. S. Antao, M. Louis, and E. N. Wang, “Heat transfer enhancement during water and hydrocarbon condensation on lubricant infused surfaces”, *Scientific Reports*, vol. 8, no. 540, 2018. DOI: 10.1038/s41598-017-18955-x.
- [38] Y. Zhao, “Dropwise condensation of water and low surface tension fluids on structured surfaces”, 2018.
- [39] H.-Q. Jin and S. Wang, “Experimental study of refrigerant (r-134a) condensation heat transfer and retention behavior on paraffin-coated vertical plates and fin structures”, *Journal of Heat Transfer*, vol. 142, no. 8, 2020. DOI: 10.1115/1.4047090.
- [40] A. Aili, Q. Ge, and T. Zhang, “Effect of mini/micro/nanostructures on filmwise condensation of low-surface-tension fluids”, *Journal of Heat Transfer*, vol. 140, no. 10, p. 102402, 2018. DOI: 10.1115/1.4040143.
- [41] J. Zhang, X. Zhu, M. E. Mondejar, and F. Haglind, “A review of heat transfer enhancement techniques in plate heat exchangers”, *Renewable and Sustainable Energy Reviews*, vol. 101, pp. 305–328, 2019. DOI: 10.1016/j.rser.2018.11.017.
- [42] C. Li, Z. Wang, P.-I. Wang, Y. Peles, N. Koratkar, and G. P. Peterson, “Nanostructured copper interfaces for enhanced boiling”, *Small*, vol. 4, no. 8, pp. 1084–1088, 2008. DOI: 10.1002/smll.200700991.
- [43] D. Attinger, C. Frankiewicz, A. R. Betz, T. M. Schutzius, R. Ganguly, A. Das, C.-J. Kim, and C. M. Megaridis, “Surface engineering for phase change heat transfer: A review”, *MRS Energy & Sustainability*, vol. 1, 2014. DOI: 10.1557/mre.2014.9.
- [44] J. Cheng, A. Vandadi, and C.-L. Chen, “Condensation heat transfer on two-tier superhydrophobic surfaces”, *Applied Physics Letters*, vol. 101, no. 13, p. 131909, 2012. DOI: 10.1063/1.4756800.
- [45] J. Soontarapiromsook, O. Mahian, A. S. Dalkilic, and S. Wongwises, “Effect of surface roughness on the condensation of r-134a in vertical chevron gasketed plate heat exchangers”, *Experimental Thermal and Fluid Science*, vol. 91, pp. 54–63, 2018. DOI: 10.1016/j.expthermflusci.2017.09.015.
- [46] R. Yun, J. Heo, and Y. Kim, “Effects of surface roughness and tube materials on the filmwise condensation heat transfer coefficient at low heat transfer rates”, *International Communications in Heat and Mass Transfer*, vol. 33, no. 4, pp. 445–450, 2006. DOI: 10.1016/j.icheatmasstransfer.2006.01.009.
- [47] M. Budakli, T. K. Salem, and M. Arik, “An experimental and theoretical analysis of vapor-to-liquid phase change on microstructured surfaces”, *Applied Thermal Engineering*, vol. 178, p. 115382, 2020. DOI: 10.1016/j.applthermaleng.2020.115382.

- [48] R. Chen, M.-C. Lu, V. Srinivasan, Z. Wang, H. H. Cho, and A. Majumdar, “Nanowires for enhanced boiling heat transfer”, *Nano Letters*, vol. 9, no. 2, pp. 548–553, 2009. DOI: 10.1021/nl8026857.
- [49] R. Wen, X. Ma, Y.-C. Lee, and R. Yang, “Liquid-vapor phase-change heat transfer on functionalized nanowired surfaces and beyond”, *Joule*, vol. 2, no. 11, pp. 2307–2347, 2018. DOI: 10.1016/j.joule.2018.08.014.
- [50] D. J. Preston, K. L. Wilke, Z. Lu, S. S. Cruz, Y. Zhao, L. L. Becerra, and E. N. Wang, “Gravitationally driven wicking for enhanced condensation heat transfer”, *Langmuir*, vol. 34, no. 15, pp. 4658–4664, 2018. DOI: 10.1021/acs.langmuir.7b04203.
- [51] M. Ahlers, A. Buck-Emden, and H.-J. Bart, “Is dropwise condensation feasible? a review on surface modifications for continuous dropwise condensation and a profitability analysis”, *Journal of Advanced Research*, vol. 16, pp. 1–13, 2019. DOI: 10.1016/j.jare.2018.11.004.
- [52] J. Ma, S. Sett, H. Cha, X. Yan, and N. Miljkovic, “Recent developments, challenges, and pathways to stable dropwise condensation: A perspective”, *Applied Physics Letters*, vol. 116, no. 26, p. 260 501, 2020. DOI: 10.1063/5.0011642.
- [53] G. J. Davies and S. Zhen, “Metallic foams: Their production, properties and applications”, *Journal of Materials Science*, vol. 18, no. 7, pp. 1899–1911, 1983. DOI: 10.1007/bf00554981.
- [54] B. Metz, O. Davidson, H. D. Coninck, M. Loos, and L. Meyer, “Carbon dioxide capture and storage: IPCC special report.”, International Panel on Climate Change, 2005.
- [55] I. E. Agency, “Energy technology roadmap 2017”, in, International Energy Agency, 2017, p. 393, ISBN: 978-92-64-27597-3.
- [56] S. Budinis, S. Krevor, N. M. Dowell, N. Brandon, and A. Hawkes, “An assessment of ccs costs, barriers and potential”, *Energy Strategy Reviews*, vol. 22, pp. 61–81, 2018. DOI: 10.1016/j.esr.2018.08.003.
- [57] A. S. Bhowan and B. C. Freeman, “Analysis and status of post-combustion carbon dioxide capture technologies”, *Environmental Science & Technology*, vol. 45, no. 20, pp. 8624–8632, 2011. DOI: 10.1021/es104291d.
- [58] P. A. Webley, “Adsorption technology for CO₂ separation and capture: A perspective”, *Adsorption*, vol. 20, no. 2-3, pp. 225–231, 2014. DOI: 10.1007/s10450-014-9603-2.
- [59] E. S. Rubin, J. E. Davison, and H. J. Herzog, “The cost of CO₂ capture and storage”, *International Journal of Greenhouse Gas Control*, vol. 40, pp. 378–400, 2015. DOI: 10.1016/j.ijggc.2015.05.018.
- [60] J. Dickmeis and A. Kather, “Offgas treatment downstream the gas processing unit of a pulverised coal-fired oxyfuel power plant with polymeric membranes and pressure swing adsorption”, *Energy Procedia*, vol. 37, pp. 1301–1311, 2013. DOI: 10.1016/j.egypro.2013.06.005.

- [61] D. Zhu, J. P. Eason, and L. T. Biegler, “Energy-efficient CO₂ liquefaction for oxy-combustion power plant with ASU-CPU integration enhanced by cascaded sub-ambient energy utilization and waste heat recovery”, *International Journal of Greenhouse Gas Control*, vol. 61, pp. 124–137, 2017. DOI: 10.1016/j.ijggc.2017.03.023.
- [62] D. Berstad, R. Anantharaman, and P. Nekså, “Low-temperature CO₂ capture technologies - applications and potential”, *International Journal of Refrigeration*, vol. 36, no. 5, pp. 1403–1416, 2013. DOI: 10.1016/j.ijrefrig.2013.03.017.
- [63] C. Song, Q. Liu, S. Deng, H. Li, and Y. Kitamura, “Cryogenic-based CO₂ capture technologies: State-of-the-art developments and current challenges”, *Renewable and Sustainable Energy Reviews*, vol. 101, pp. 265–278, 2019. DOI: 10.1016/j.rser.2018.11.018.
- [64] S. Roussanaly, M. Vitvarova, R. Anantharaman, D. Berstad, B. Hagen, J. Jakobsen, V. Novotny, and G. Skaugen, “Techno-economic comparison of three technologies for pre-combustion CO₂ capture from a lignite-fired IGCC”, *Frontiers of Chemical Science and Engineering*, vol. 14, no. 3, pp. 436–452, 2020. DOI: 10.1007/s11705-019-1870-8.
- [65] R. Anantharaman, D. Berstad, and S. Roussanaly, “Techno-economic performance of a hybrid membrane - liquefaction process for post-combustion CO₂ capture”, vol. 61, pp. 1244–1247, 2014. DOI: 10.1016/j.egypro.2014.11.1068.
- [66] Z. Liao, Y. Hu, J. Wang, Y. Yang, and F. You, “Systematic design and optimization of a membrane - cryogenic hybrid system for CO₂ capture”, *ACS Sustainable Chemistry & Engineering*, vol. 7, no. 20, pp. 17186–17197, 2019. DOI: 10.1021/acssuschemeng.9b03727.
- [67] B. Ghorbani, M. Mehrpooya, and K. Shokri, “Developing an integrated structure for simultaneous generation of power and liquid CO₂ using parabolic solar collectors, solid oxide fuel cell, and post-combustion CO₂ separation unit”, *Applied Thermal Engineering*, vol. 179, p. 115687, 2020. DOI: 10.1016/j.applthermaleng.2020.115687.
- [68] A. Alabdulkarem, Y. Hwang, and R. Radermacher, “Development of CO₂ liquefaction cycles for CO₂ sequestration”, *Applied Thermal Engineering*, vol. 33-34, pp. 144–156, 2012. DOI: 10.1016/j.applthermaleng.2011.09.027.
- [69] A. Aspelund, M. J. Mølnvik, and G. De Koeijer, “Ship transport of CO₂”, vol. 84, no. 9, pp. 847–855, 2006. DOI: 10.1205/cherd.5147.
- [70] S. Roussanaly, G. Skaugen, A. Aasen, J. Jakobsen, and L. Vesely, “Techno-economic evaluation of CO₂ transport from a lignite-fired IGCC plant in the Czech Republic”, *International Journal of Greenhouse Gas Control*, vol. 65, pp. 235–250, 2017. DOI: <https://doi.org/10.1016/j.ijggc.2017.08.022>.
- [71] L. Gao, M. Fang, H. Li, and J. Hetland, “Cost analysis of CO₂ transportation: Case study in china”, *Energy Procedia*, vol. 4, pp. 5974–5981, 2011. DOI: 10.1016/j.egypro.2011.02.600.

- [72] F. Neele, R. de Kler, M. Nienoord, P. Brownsort, J. Koornneef, S. Belfroid, L. Peters, A. vanWijhe, and D. Loeve, “CO₂ transport by ship: The way forward in europe”, in *13th International Conference on Greenhouse Gas Control Technologies, GHGT-13*, vol. 114, Energy Procedia, 2017, pp. 6824–6834. DOI: 10.1016/j.egypro.2017.03.1813.
- [73] Global CCS Institute, “Fact sheet: Transporting CO₂”, Global CCS Institute, 2015.
- [74] M. J. Mazzetti, N. H. Eldrup, K. L. Anthonsen, H. A. Haugen, K. Onarheim, P. Bergmo, J. Kjarstad, F. Johnson, P. Stigson, S. R. Gislason, and N. A. Røkke, “NORDICCS CCS roadmap”, *Energy Procedia*, vol. 51, pp. 1–13, 2014. DOI: 10.1016/j.egypro.2014.07.001.
- [75] J. Pettersen, A. Hafner, G. Skaugen, and H. Rekstad, “Development of compact heat exchangers for CO₂ air-conditioning systems”, *International Journal of Refrigeration*, vol. 21, no. 3, pp. 180–193, 1998. DOI: 10.1016/S0140-7007(98)00013-9.
- [76] Y.-Y. Yan, H.-C. Lio, and T.-F. Lin, “Condensation heat transfer and pressure drop of refrigerant r-134a in a plate heat exchanger”, *International Journal of Heat and Mass Transfer*, vol. 42, no. 6, pp. 993–1006, 1999. DOI: 10.1016/S0017-9310(98)00217-8.
- [77] S. K. Fischer, “Total equivalent warming impact: A measure of the global warming impact of CFC alternatives in refrigerating equipment”, *International Journal of Refrigeration*, vol. 16, no. 6, pp. 423–428, 1993. DOI: 10.1016/0140-7007(93)90059-h.
- [78] K. M. Tsamos, Y. T. Ge, I. Santosa, S. A. Tassou, G. Bianchi, and Z. Mylona, “Energy analysis of alternative CO₂ refrigeration system configurations for retail food applications in moderate and warm climates”, *Energy Conversion and Management*, vol. 150, pp. 822–829, 2017. DOI: 10.1016/j.enconman.2017.03.020.
- [79] C. Aprea and A. Maiorino, “An experimental evaluation of the transcritical CO₂ refrigerator performances using an internal heat exchanger”, *International Journal of Refrigeration*, vol. 31, no. 6, pp. 1006–1011, 2008. DOI: <https://doi.org/10.1016/j.ijrefrig.2007.12.016>.
- [80] Z. Zhang, Z. L. Weng, T. X. Li, Z. C. Huang, X. H. Sun, Z. H. He, J. Van Es, A. Pauw, E. Laudi, and R. Battiston, “CO₂ condensation heat transfer coefficient and pressure drop in a mini-channel space condenser”, *Experimental Thermal and Fluid Science*, vol. 44, pp. 356–363, 2013. DOI: 10.1016/j.expthermflusci.2012.07.007.
- [81] S. Liu, H. Qi, V. Nian, B. Liu, B. Dai, Z. Sun, X. Li, and J. Yuan, “A new correlation for carbon dioxide boiling heat transfer coefficient outside evaporating tubes”, *Journal of Cleaner Production*, vol. 276, p. 123050, 2020. DOI: 10.1016/j.jclepro.2020.123050.
- [82] X. Huai and S. Koyama, “An experimental study of carbon dioxide condensation in mini channels”, *Journal of Thermal Science*, vol. 13, no. 4, pp. 358–365, 2004. DOI: 10.1007/s11630-004-0055-y.

- [83] C. Y. Park and P. Hrnjak, "CO₂ flow condensation heat transfer and pressure drop in multi-port microchannels at low temperatures", *International Journal of Refrigeration*, vol. 32, no. 6, pp. 1129–1139, 2009. DOI: 10.1016/j.ijrefrig.2009.01.030.
- [84] O. Iqbal and P. Bansal, "In-tube condensation heat transfer of CO₂ at low temperatures in a horizontal smooth tube", vol. 35, no. 2, pp. 270–277, 2012. DOI: 10.1016/j.ijrefrig.2011.10.015.
- [85] P. Kang, J. Heo, and R. Yun, "Condensation heat transfer characteristics of CO₂ in a horizontal smooth tube", *International Journal of Refrigeration*, vol. 36, no. 3, pp. 1090–1097, 2013. DOI: 10.1016/j.ijrefrig.2012.10.005.
- [86] C.-H. Son and H.-K. Oh, "Condensation heat transfer characteristics of carbon dioxide in a horizontal smooth tube", *Experimental Thermal and Fluid Science*, vol. 36, pp. 233–241, 2012. DOI: 10.1016/j.expthermflusci.2011.09.017.
- [87] J. Heo, H. Park, and R. Yun, "Condensation heat transfer and pressure drop characteristics of CO₂ in a microchannel", *International Journal of Refrigeration*, vol. 36, no. 6, pp. 1657–1668, 2013. DOI: 10.1016/j.ijrefrig.2013.05.008.
- [88] C. Lee, J. Yoo, J. Lee, H. Park, and S. Jeong, "Experimental investigation of CO₂ condensation process using cryogen", AIP Publishing LLC, 2014. DOI: 10.1063/1.4860830.
- [89] J. Heo and R. Yun, "Prediction of CO₂ condensation heat transfer coefficient in a tube", vol. 89, pp. 254–263, 2015. DOI: 10.1016/j.ijthermalsci.2014.11.021.
- [90] P. Li and S. Norris, "Heat transfer correlations for CO₂ flowing condensation in a tube at low temperatures", *Applied Thermal Engineering*, vol. 93, pp. 872–883, 2016. DOI: 10.1016/j.applthermaleng.2015.09.072.
- [91] P. Li, J. J. J. Chen, and S. Norris, "Flow condensation heat transfer of CO₂ in a horizontal tube at low temperatures", *Applied Thermal Engineering*, vol. 130, pp. 561–570, 2018. DOI: 10.1016/j.applthermaleng.2017.11.004.
- [92] J. R. Thome, J. El Hajal, and A. Cavallini, "Condensation in horizontal tubes, part 2: New heat transfer model based on flow regimes", *International Journal of Heat and Mass Transfer*, vol. 46, no. 18, pp. 3365–3387, 2003. DOI: [https://doi.org/10.1016/S0017-9310\(03\)00140-6](https://doi.org/10.1016/S0017-9310(03)00140-6).
- [93] W. Baik and R. Yun, "In-tube condensation heat transfer characteristics of CO₂ with n₂ at near critical pressure", *International Journal of Heat and Mass Transfer*, vol. 144, p. 118628, 2019. DOI: 10.1016/j.ijheatmasstransfer.2019.118628.
- [94] S. F. Westman, H. G. J. Stang, S. W. Løvseth, A. Austegard, I. Snustad, S. Ø. Størset, and I. S. Ertesvåg, "Vapor-liquid equilibrium data for the carbon dioxide and nitrogen (CO₂ + N₂) system at the temperatures 223, 270, 298 and 303 K and pressures up to 18 MPa", *Fluid Phase Equilibria*, vol. 409, pp. 207–241, 2016. DOI: 10.1016/j.fluid.2015.09.034.

- [95] W. Lee and R. Yun, “In-tube convective heat transfer characteristics of co 2 mixtures in a pipeline”, *International Journal of Heat and Mass Transfer*, vol. 125, pp. 350–356, 2018. DOI: 10.1016/j.ijheatmasstransfer.2018.04.121.
- [96] M.-S. Kim, K. A. L. Ada, O. K. Kwon, and C. W. Park, “A comparison of condensation heat transfer performance of MWCNT/Fe composite coatings on steel substrate”, *Journal of Mechanical Science and Technology*, vol. 28, no. 4, pp. 1589–1596, 2014. DOI: 10.1007/s12206-013-1190-8.
- [97] J. Y. Ho, X. W. Wang, and K. C. Leong, “Filmwise condensation of steam on vertical plates with novel pin fin arrays produced by selective laser melting”, *International Journal of Heat and Mass Transfer*, vol. 126, pp. 652–666, 2018. DOI: 10.1016/j.ijheatmasstransfer.2018.05.063.
- [98] “Contact angle phenomena and wetting”, in *Physics and Chemistry of Interfaces*. John Wiley & Sons, Ltd, 2003, ch. 7, pp. 118–144, ISBN: 9783527602315. DOI: <https://doi.org/10.1002/3527602313.ch7>. eprint: <https://onlinelibrary.wiley.com/doi/pdf/10.1002/3527602313.ch7>.
- [99] D. Quéré, “Wetting and roughness”, *Annual Review of Materials Research*, vol. 38, no. 1, pp. 71–99, 2008. DOI: 10.1146/annurev.matsci.38.060407.132434.
- [100] R. N. Wenzel, “Resistance of solid surfaces to wetting by water”, *Industrial & Engineering Chemistry*, vol. 28, no. 8, pp. 988–994, 1936. DOI: 10.1021/ie50320a024.
- [101] A. B. D. Cassie and S. Baxter, “Wettability of porous surfaces”, *Transactions of the Faraday Society*, vol. 40, p. 546, 1944. DOI: 10.1039/tf9444000546.
- [102] C. Dorrer and J. Rühle, “Some thoughts on superhydrophobic wetting”, *Soft Matter*, vol. 5, no. 1, pp. 51–61, 2009. DOI: 10.1039/b811945g.
- [103] C. Graham and P. Griffith, “Drop size distributions and heat transfer in dropwise condensation”, *International Journal of Heat and Mass Transfer*, vol. 16, no. 2, pp. 337–346, 1973. DOI: 10.1016/0017-9310(73)90062-8.
- [104] J. W. Rose and L. R. Glicksman, “Dropwise condensation - the distribution of drop sizes”, *International Journal of Heat and Mass Transfer*, vol. 16, no. 2, pp. 411–425, 1973. DOI: 10.1016/0017-9310(73)90068-9.
- [105] R. Bouma, F. Vercauteren, P. Van Os, E. Goetheer, D. Berstad, and R. Anantharaman, “Membrane-assisted CO₂ liquefaction: Performance modelling of CO₂ capture from flue gas in cement production”, *Energy Procedia*, vol. 114, pp. 72–80, 2017. DOI: 10.1016/j.egypro.2017.03.1149.
- [106] M. Voldsund, S. Gardarsdottir, E. De Lena, J.-F. Pérez-Calvo, A. Jamali, D. Berstad, C. Fu, M. Romano, S. Roussanaly, R. Anantharaman, H. Hoppe, D. Sutter, M. Mazzotti, M. Gazzani, G. Cinti, and K. Jordal, “Comparison of technologies for CO₂ capture from cement production - part 1: Technical evaluation”, *Energies*, vol. 12, no. 3, p. 559, 2019. DOI: 10.3390/en12030559.
- [107] Z. E. Platform, “CO₂ storage safety in the north sea: Implications of the CO₂ storage directive”, Zero Emissions Platform, 2019.

- [108] C. Lee, J. Yoo, J. Lee, H. Park, and S. Jeong, “Experimental investigation of CO₂ condensation process using cryogen”, in *AIP Conference Proceedings*, vol. 1115, 2014. DOI: 10.1063/1.4860830.
- [109] E. Bellos and C. Tzivanidis, “A theoretical comparative study of CO₂ cascade refrigeration systems”, *Applied Sciences*, vol. 9, no. 4, p. 790, 2019. DOI: 10.3390/app9040790.
- [110] E. L. Quinn, “The surface tension of liquid carbon dioxide”, *Journal of the American Chemical Society*, vol. 49, no. 11, pp. 2704–2711, 1927. DOI: 10.1021/ja01410a006.
- [111] S. I. Abu-Eishah, “Correlations for the thermal conductivity of metals as a function of temperature”, *International Journal of Thermophysics*, vol. 22, no. 6, pp. 1855–1868, 2001. DOI: 10.1023/a:1013155404019.
- [112] M. Quirk and J. Serda, *Semiconductor Manufacturing Technology*, 1st ed. Pearson, 2000, ISBN: 978-0130815200.
- [113] S. Wang, L. Feng, and L. Jiang, “One-step solution-immersion process for the fabrication of stable bionic superhydrophobic surfaces”, *Advanced Materials*, vol. 18, no. 6, pp. 767–770, 2006. DOI: 10.1002/adma.200501794.
- [114] Z. He, J. He, and Z. Zhang, “Selective growth of metallic nanostructures on microstructured copper substrate in solution”, *CrystEngComm*, vol. 17, pp. 7262–7269, 38 2015. DOI: 10.1039/C5CE01093D.
- [115] Z. He, Z. Zhang, and J. He, “CuO/Cu based superhydrophobic and self-cleaning surfaces”, *Scripta Materialia*, vol. 118, pp. 60–64, 2016. DOI: <https://doi.org/10.1016/j.scriptamat.2016.03.015>.
- [116] R. Span and W. Wagner, “A new equation of state for carbon dioxide covering the fluid region from the triple-point temperature to 1100 k at pressures up to 800 mpa”, *Journal of Physical and Chemical Reference Data*, vol. 25, no. 6, pp. 1509–1596, 1996. DOI: 10.1063/1.555991.
- [117] V. Vesovic, W. Wakeham, G. Olchowy, J. Sengers, J. Watson, and J. Millat, “The transport properties of carbon dioxide”, *Journal of Physical and Chemical Reference Data*, vol. 19, no. 3, pp. 763–808, 1990. DOI: 10.1063/1.555875.
- [118] S. H. Hoenig, S. Modak, Z. Chen, M. Kaviani, J. F. Gilchrist, and R. W. Bonner, “Role of substrate thermal conductivity and vapor pressure in drop-wise condensation”, *Applied Thermal Engineering*, vol. 178, p. 115 529, 2020. DOI: 10.1016/j.applthermaleng.2020.115529.
- [119] Z. Jian-Min, M. Fei, and X. Ke-Wei, “Calculation of the surface energy of fcc metals with modified embedded-atom method”, *Chinese Physics*, vol. 13, no. 7, pp. 1082–1090, 2004. DOI: 10.1088/1009-1963/13/7/020.
- [120] A. Kinloch, *Adhesion and Adhesives*. Springer Netherlands, 1987, ISBN: 978-0-412-27440-4. DOI: 10.1007/978-94-015-7764-9.
- [121] O. Santos, T. Nylander, R. Rosmaninho, G. Rizzo, S. Yiantsios, N. Andritsos, A. Karabelas, H. Muller-Steinhagen, L. Melo, L. Boulange-Petermann, C. Gabet, A. Braem, C. Traegaardh, and M. Paulsson, “Modified stainless steel surfaces targeted to reduce fouling – surface characterization”, *Journal of*

- Food Engineering*, vol. 64, no. 1, pp. 63–79, 2004. DOI: 10.1016/j.jfoodeng.2003.09.013.
- [122] A. Sarkar and A.-M. Kietzig, “Design of a robust superhydrophobic surface: Thermodynamic and kinetic analysis”, *Soft Matter*, vol. 11, no. 10, pp. 1998–2007, 2015. DOI: 10.1039/C4SM02787F.
- [123] T. Wu and Y. Suzuki, “Design, microfabrication and evaluation of robust high-performance superlyophobic surfaces”, *Sensors and Actuators B: Chemical*, vol. 156, no. 1, pp. 401–409, 2011. DOI: 10.1016/j.snb.2011.04.065.
- [124] C.-Y. Zhao, W.-T. Ji, P.-H. Jin, Y.-J. Zhong, and W.-Q. Tao, “The influence of surface structure and thermal conductivity of the tube on the condensation heat transfer of r134a and r404a over single horizontal enhanced tubes”, *Applied Thermal Engineering*, vol. 125, pp. 1114–1122, 2017. DOI: 10.1016/j.applthermaleng.2017.06.133.
- [125] H. M. Ali and A. Briggs, “Condensation of ethylene glycol on pin-fin tubes: Effect of circumferential pin spacing and thickness”, *Applied Thermal Engineering*, vol. 49, pp. 9–13, 2012. DOI: 10.1016/j.applthermaleng.2011.08.017.
- [126] H. M. Ali, M. Z. Qasim, and M. Ali, “Free convection condensation heat transfer of steam on horizontal square wire wrapped tubes”, *International Journal of Heat and Mass Transfer*, vol. 98, pp. 350–358, 2016. DOI: 10.1016/j.ijheatmasstransfer.2016.03.053.
- [127] J. Oh, R. Zhang, P. P. Shetty, J. A. Krogstad, P. V. Braun, and N. Miljkovic, “Thin film condensation on nanostructured surfaces”, *Advanced Functional Materials*, vol. 28, no. 16, p. 1707000, 2018. DOI: 10.1002/adfm.201707000.

Appendix **A**

Papers

A.1 Paper I

A Review on Wetting and Water Condensation - Perspectives for CO₂ Condensation

Ingrid Snustad, Ingeborg Treu Røe, Åsmund Ervik, Anders Austegard, Amy Brunsvold, Jianying He and Zhiliang Zhang.

Advances in Colloid and Interface Science, **256**, 291-304 (2018)



Contents lists available at ScienceDirect

Advances in Colloid and Interface Science

journal homepage: www.elsevier.com/locate/cis

Historical perspective

A review on wetting and water condensation - Perspectives for CO₂ condensationIngrid Snustad^{a,*}, Ingeborg T Røe^b, Amy Brunsvold^b, Åsmund Ervik^b, Jianying He^a, Zhiliang Zhang^a^a Department of Structural Engineering, Norwegian University of Science and Technology, Høgskoleringen 6, 7491 Trondheim, Norway^b SINTEF Energy Research, Norway

ARTICLE INFO

Available online 29 March 2018

Keywords:

CCS
Dropwise condensation
Nanostructured surfaces
Superhydrophobicity
Superomniphobicity

ABSTRACT

Liquefaction of vapor is a necessary, but energy intensive step in several important process industries. This review identifies possible materials and surface structures for promoting dropwise condensation, known to increase efficiency of condensation heat transfer. Research on superhydrophobic and superomniphobic surfaces promoting dropwise condensation constitutes the basis of the review. In extension of this, knowledge is extrapolated to condensation of CO₂. Global emissions of CO₂ need to be minimized in order to reduce global warming, and liquefaction of CO₂ is a necessary step in some carbon capture, transport and storage (CCS) technologies. The review is divided into three main parts: 1) An overview of recent research on superhydrophobicity and promotion of dropwise condensation of water, 2) An overview of recent research on superomniphobicity and dropwise condensation of low surface tension substances, and 3) Suggested materials and surface structures for dropwise CO₂ condensation based on the two first parts.

© 2018 Elsevier B.V. All rights reserved.

1. Introduction

Condensation of vapor is a necessary and energy consuming step in several industrial processes, such as HVAC systems [1], waste heat recovery [2], LNG production [3] and for potential CO₂ capture [4], and ship transportation of CO₂ [5]. The liquefaction of any vapor involves condensation on a surface where heat is transferred from the vapor to the surface. Increasing the heat transfer rate will therefore increase the liquefaction efficiency of the vapor. Through extensive research on condensation, it is apparent that with dropwise condensation the heat transfer rate could be increased by an order of magnitude [6–9]. Although the condensation of other gases than water have attracted more attention over the past decade [10, 11], the mechanism of dropwise condensation of water vapor is still best understood.

This review gives an overview of the research on the parameters affecting and controlling dropwise condensation of water vapor. Dropwise condensation is a cyclic process including initial nucleation, growth, and coalescence of droplets, followed by droplet removal. In this paper we focus on the properties governing the surface adhesion of droplets after nucleation and initial coalescence.

Further, we will compare these parameters with those found to control the condensation of low surface tension substances (commonly non-polar substances such as ethanol, hexadecane). Surfaces that promote dropwise condensation of low surface tension fluids will be examined and the important properties discussed. A small discussion on condensation of CO₂ is included at the end of the review. CO₂ is a very low surface tension fluid ($\approx 4 \text{ mN m}^{-1}$ at room temperature), and is interesting for both academic and environmental purposes. Liquefaction of gaseous CO₂ is an important field since improved and more energy efficient carbon capture, transport and storage (CCS) is necessary for combating anthropogenic global warming.

To fully understand the mechanisms affecting and controlling the condensation, we will first give a brief introduction to the parameters affecting the shape and morphology of static droplets on a surface.

2. Hydrophobicity, contact angles and wetting modes

Hydrophobicity, contact angles and wetting modes are underlying phenomena for dropwise condensation. A surface is labelled hydrophobic when it is repellent towards water, i.e. the contact angle (CA), θ , of water on the surface is larger than 90°. Various terms are used when surfaces are repellent towards other liquids. These are oleophobic if oil repellent, amphiphobic if repellent towards oil and water, and omniphobic if repellent towards any liquid. The

* Corresponding author.

E-mail address: ingrid.snustad@ntnu.no (I. Snustad).

same holds for -philic surfaces, which are attractive to the same compounds.

For a surface to be termed with the prefix super- (such as superhydrophobic), the surface must exhibit $\theta \geq 150^\circ$ and contact angle hysteresis (CAH) $\Delta\theta \leq 10^\circ$. CAH is defined as the difference between the receding and the advancing CA.

The -phobic and -philic terms and the super- term are used somewhat inconsequently in the literature, and often refer to the same types of surfaces. In this review, the definitions above will be used.

This section explains the above mentioned phenomena and goes through the most important equations describing the governing mechanisms.

2.1. Hydrophobicity and Young contact angle

As water droplets form on surfaces that repel water, hydrophobic surfaces have normally been utilized to achieve dropwise water condensation. The hydrophilicity and hydrophobicity of a material are characterized by the Young contact angle, θ_Y , which is the liquid-solid contact angle on a flat surface defined in Fig. 1. The relation between θ_Y and the wetting modes is shown in Fig. 2. A surface is said to be hydrophobic when $\theta_Y \geq 90^\circ$. This is, however, insufficient for sustained dropwise condensation since coalescence of droplets eventually leads to film formation. To avoid extensive coalescence, the droplet mobility must be high enough to ensure sustained self-removal of droplets from the surface. High droplet mobility results from a low contact angle hysteresis (CAH), $\Delta\theta$, defined in Fig. 3. Surfaces having $\theta_Y \geq 150^\circ$ and $\Delta\theta \leq 10^\circ$ towards water are called superhydrophobic surfaces, on which dropwise condensation is usually achievable.

2.2. Superhydrophobicity, and Cassie-Baxter and Wenzel state

While the hydrophobicity of a surface is determined by the surface chemistry, the superhydrophobicity of a surface cannot be manipulated through the surface chemistry alone. To our knowledge, there are no flat surfaces exhibiting $\theta > 120^\circ$ [13], and hence, no flat superhydrophobic surfaces. However, an apparent contact angle above 120° is attainable by introducing surface roughness. According to the Wenzel equation [14], the apparent equilibrium contact angle, θ^* , is a function of the roughness factor, $r = \frac{\text{actual surface area}}{\text{apparent surface area}}$, and the Young contact angle, θ_Y :

$$\cos \theta^* = r \cos \theta_Y. \quad (1)$$

Since $r \geq 1$, Eq. (1) shows that $\theta^* \geq \theta_Y$ for $\theta_Y \geq 90^\circ$. However, Eq. (1) is only valid for droplets where the structure under the droplet is fully wetted as illustrated in Fig. 4 (a). In the case where

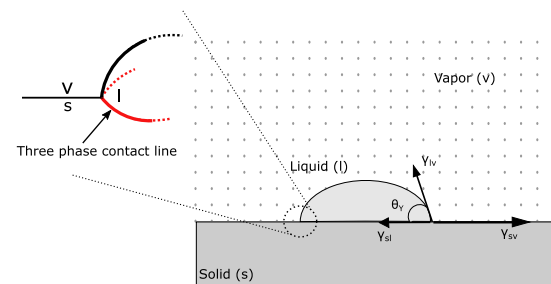


Fig. 1. Young contact angle, θ_Y , at one point on the three phase contact line (shown in inset), and the surface tensions, γ_{ij} , between the different phases.

vapor is trapped between the droplet and the surface as shown in Fig. 4 (b), the droplet is in the Cassie state¹ and the Cassie-Baxter equation is valid [15]:

$$\cos \theta^* = r_f f_s \cos \theta_Y + f_s - 1, \quad (2)$$

where $r_f = \frac{\text{actual wetted surface area}}{\text{apparent wetted solid surface area}}$ and $f_s = \frac{\text{apparent wetted surface area}}{\text{apparent solid surface area}}$, i.e. the fraction of the liquid droplet's footprint in contact with the solid, or solid fraction. In the situation where the droplet is "floating" completely on top of the surface structure, $r_f = 1$, and Eq. (2) reduces to

$$\cos \theta^* = f_s \cos \theta_Y + f_s - 1. \quad (3)$$

In the other extreme situation where the rough surface under the droplet is fully wetted, $f_s = 1$ and $r_f = r$ and Eq. (2) reduces to Eq. (1)². To achieve a contact angle above 90° on a rough surface, it is, according to the Cassie equation, necessary to have $f_s < \frac{1}{1+r_f \cos(\theta_Y)}$. In Fig. 5, contact angles for droplets with $\theta_Y = 50^\circ$ and with $r_f = 1$ with varying f_s is shown. A solid fraction less than 0.6 is sufficient to achieve non-wetting behaviour, while f_s less than 0.08 is necessary for superhydrophobicity ($\theta_{CB} > 150^\circ$).

Since droplets in the Wenzel state completely wet the surface under the droplet, the state is associated with high contact line pinning and thus low droplet mobility. The contact line is the line where vapor, liquid and solid are in contact (see Fig. 1). Because the motivation is to induce dropwise condensation, the mobile Cassie state is desirable. However, it is challenging to determine when the droplet will stabilize in the Cassie state instead of the Wenzel state since neither Eq. (1) nor Eq. (3) describes the stability of the states. The only thing we may extract from Eqs. (1) and (3) is the critical equilibrium Young contact angle, $\theta_{Y \text{ crit}}$, for which the droplet transitions from the Cassie to the Wenzel state. By equating Eqs. (1) and (3), we find $\theta_{Y \text{ crit}} \geq 90^\circ$, i.e. that the Wenzel to Cassie transition occurs above 90° . Although Eq. (3) indicates that $\theta^* > \theta_Y$ for $\theta_Y < 90^\circ$ is possible, the $\theta_{Y \text{ crit}}$ reaffirms that a thermodynamically stable Cassie state can not exist for $\theta_Y < 90^\circ$. This does not, however, mean that droplets always form in the Cassie state for $\theta_Y \geq 90^\circ$. On the contrary, the Wenzel state is often observed for $\theta_Y \geq 90^\circ$ [16, 17]. In the following, we will examine what determines the stability of the two wetting states in addition to θ_Y .

3. Impact of texture on superhydrophobicity

Not surprisingly, research has shown that the surface structure impacts the stability of the Wenzel and the Cassie state with respect to each other, as indicated by the equations above. Several studies have therefore attempted to rigorously determine the structural parameters affecting the energy states of the system. In the literature, the investigation of these parameters is divided into two scenarios; one where the droplet is deposited on the textured surface, and one where the droplets condense on the textured surface. Although it is the latter case that interests us, it is instructive to initially understand the first, and simpler case.

3.1. Design criteria for achieving static Cassie droplets

As there exists an infinite amount of possible surface geometries, the first challenge when developing a generic model for wetting

¹ From now on called the Cassie state.

² Even though we have been talking about superhydrophobicity here, it is worth to note that Eqs. (1) and (2) are valid for the apparent equilibrium contact angle of any liquid.

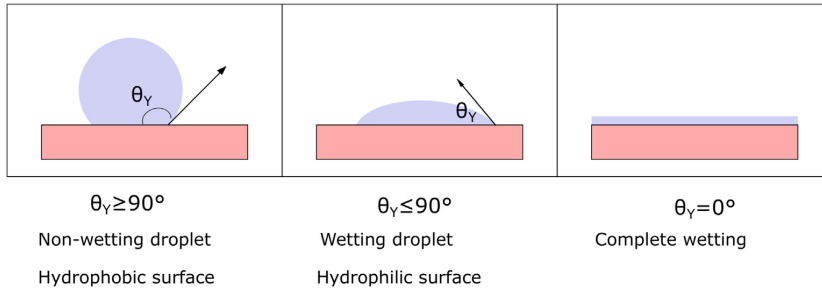


Fig. 2. Wetting modes of water on different surfaces described by the contact angle θ . Source: Figure adapted from Hiemenz and Rajagopalan [12].

states is to choose one that is fairly general, ordered, flexible and simple. One structure satisfying these criteria is the square array of square pillars with spacing b , width a , and height c . The structure is illustrated in Fig. 6.

Using this structure, Sarkar and Kietzig [19] developed a general expression for the free energy of a droplet as a function of the structure geometry, the apparent contact angle and the penetration depth of the droplet into the structure. This expression was used in the later work by Sarkar and Kietzig [18] to find the critical $\frac{b}{a}$ -ratio, $\left(\frac{b}{a}\right)_{crit}$, for a thermodynamically stable Cassie state:

$$\frac{b}{a} \leq \left(\frac{b}{a}\right)_{crit} = \sqrt{1 - \frac{4c \cos \theta_Y}{a(1 + \cos \theta_Y)}} - 1 \quad (4)$$

Increasing a or c will decrease the minimum contact angle, i.e. loosen the restriction on the surface energy for achieving a stable

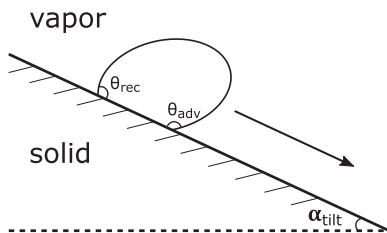
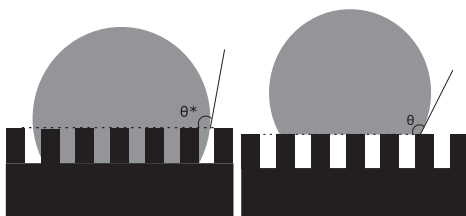


Fig. 3. Advancing, θ_{adv} , and receding, θ_{rec} , contact angles on a tilted surface with tilting angle α_{tilt} . The CAH is $\Delta\theta = \theta_{adv} - \theta_{rec}$.



(a) The Wenzel state (b) The Cassie-Baxter state

Fig. 4. Sketch of droplets in different states on a rough surface.

Cassie state, see Fig. 7. Increasing b will increase the same restriction. An increase in the pillar spacing to width ratio, b/a , will also increase the minimum CA, see Fig. 8. For achieving a droplet in the stable Cassie state, a large height, and small ratio between spacing and width is favourable. As no nominally flat surface have been

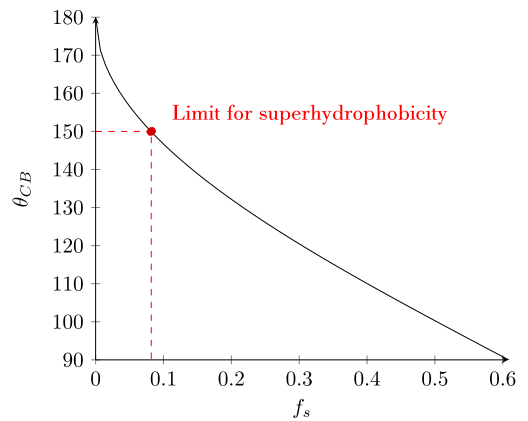


Fig. 5. Cassie contact angle, θ_{CB} in degrees, for varying solid fractions, f_s , for a Young contact angle of 50° .

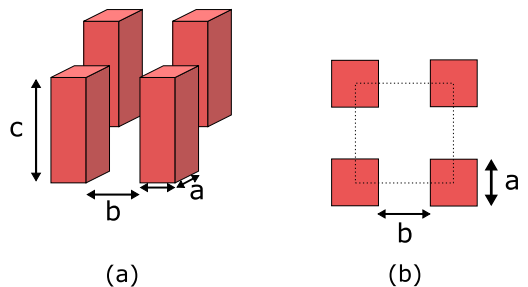


Fig. 6. The geometry of the square pillar surface: (a) 3-dimensional view showing post-width a , spacing b and height c ; (b) top view of four nearest pillars, which outline a unit. Source: Figures adapted from Sarkar and Kietzig [18].

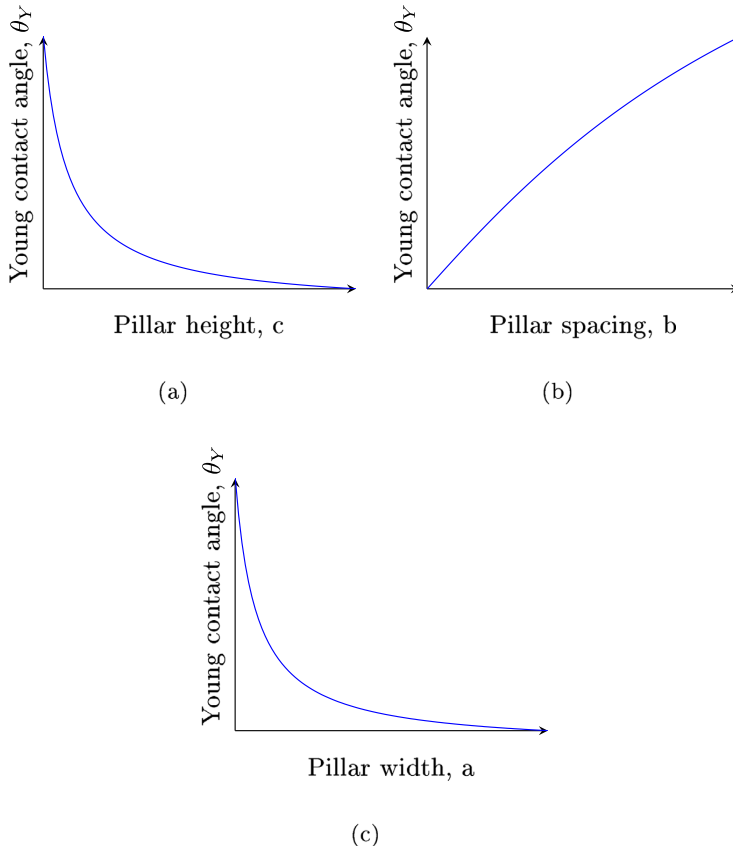


Fig. 7. Minimum Young contact angle with respect to a) pillar height, b) pillar spacing, and c) pillar width, Eq. (4). For increasing pillar height, c , and pillar width, a (the other variables kept constant), the restriction on the contact angle decreases. For increasing only pillar spacing, b , the minimum contact angle increases.

found that exhibit Young contact angle larger than 120° , Eq. (4) also determines a maximum b/a along with a restriction for c . E.g. for $b/a \approx 3.1 \Rightarrow c > 4a$, depicted as a box in Fig. 8.

Eq. (4) corresponds exactly with the criteria for stable Cassie droplets developed by Zheng et al. [20]:

$$\eta = \frac{cL}{A} \quad \left(= \frac{4c}{a} \text{ in Sarkar's notation} \right) \quad (5)$$

$$\eta \geq \eta_{crit} = -\frac{1-f_s}{f_s} \frac{(1+\cos\theta_Y)}{\cos\theta_Y}, \quad (6)$$

where L and A are the pillar perimeter ($4a$) and cross-section area (a^2), respectively, and f_s is the fraction of wet apparent solid surface area from Eq. (2). Although both models were derived from the expression of the Gibbs free energy, the procedures were slightly different. As a consequence, the two models are mutually verifying each other.

As established in the previous section, the Cassie state is not thermodynamically stable for $\theta_Y < 90^\circ$. Moreover, it may not be stable even with $\theta_Y \geq 90^\circ$. Sarkar and Kietzig therefore developed an expression for the minimum Young contact angle for a stable Cassie state:

$$\theta_Y \geq \theta_{min} = \sec^{-1} \left(\frac{\frac{4\epsilon}{a}}{1 - \left(1 + \frac{b}{a}\right)^2} - 1 \right) \quad (7)$$

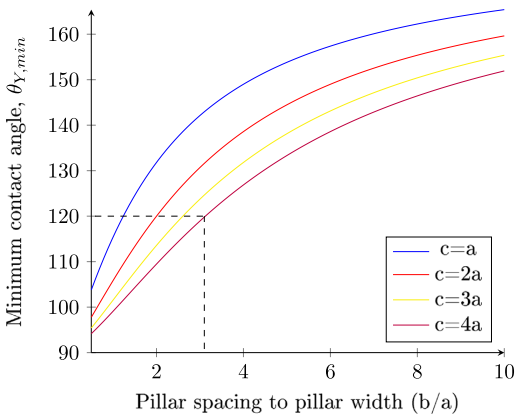


Fig. 8. Minimum Young contact angle vs pillar spacing to pillar height (b/a).

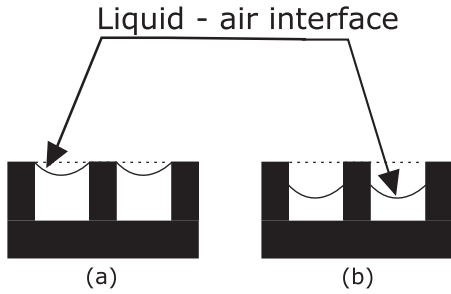


Fig. 9. Illustration of the two metastable Cassie states found by Sarkar and Kietzig [18]. The sagging state (a) and the depinned state (b).

Applying Eqs. (4) and (7) on the circular pillared structure³ fabricated by Haimov et al. [23], yield $\left(\frac{b}{a}\right)_{crit} \approx 3.7 \geq \frac{b}{a} = 2$ and $\theta_{min} \approx 99.6^\circ \leq \theta_Y \approx 110^\circ$. In other words, Sarkar and Kietzig predict this structure to promote the Cassie state. The experimental results by Haimov et al. [23] verify that the droplets indeed are in the Cassie state on this structure.

Eq. (7) shows that the θ_{min} increases with increasing $\frac{b}{a}$. As a result, the requirement on the Young contact angle soon increases above the previously mentioned “limit” that has been observed experimentally on a flat surface: $\theta_Y \approx 120^\circ$ ⁴. Nevertheless, the Cassie state has been observed on structures where the Wenzel state would have been the thermodynamically favoured state according to the previous design criteria [16, 24], suggesting that there must be a mechanism that kinetically stabilizes the Cassie state. The mechanism suggested by Sarkar and Kietzig is the energy barrier set up by one of two metastable Cassie states, the sagging and the depinned Cassie states, shown in Fig. 9. The metastable Cassie states act as energy barrier to the complete Cassie-to-Wenzel-transition.

The energy barrier induced by these metastable Cassie states have been found to depend on the structure geometry as well as the surface chemistry (in terms of θ_Y). Not surprisingly, the requirements on the relevant parameters are less strict than for the thermodynamically stable Cassie state. The requirements are summarized in Table 1.

In the above mentioned studies, the surface geometry is utilized to promote a stable or a stabilized Cassie state. Hensel et al. [25] investigated the energy barriers induced by sidewall features of the pillars in a square pillared structure (see Fig. 10) further. Using $\frac{b}{a}$ -ratios supporting the Cassie state at atmospheric pressure, they found a clear relation between the width, w , of the cavities and the breakthrough hydrostatic pressure. As the width increases, the breakthrough hydrostatic pressure decreases for the structure with smooth sidewalls. Moreover, there is an increase in the breakthrough pressure for the Cassie-to-Wenzel-transition for sidewalls with scallops, (b) in Fig. 10, compared with smooth sidewalls, (a) in Fig. 10, at equal top cavity width. The increase is caused by the change in width, from w_1 to w_2 in Fig. 10 (b), and sidewall angle as the solid-liquid contact line slides down the side wall. These experimental results match well with the analytical model that was developed.

3.2. Design criteria for condensing Cassie droplets

We now have a clear idea of how feature spacing, width and morphology impact the droplet state of a static droplet. It is of course tempting to assume that the same parameters affect the droplet state of condensing droplets. During condensation, however, the droplets may not only nucleate on the top of the surface structure, but also inside the structure. One important property in this sense is the nucleation radius of the specific vapor, a measure of the initial drop nuclei radius. If the nucleation radius is smaller than the feature spacing, nucleation may occur within the features.

Recall from the previous section that for many structures the Cassie state is kinetically stabilized by an energy barrier preventing the Cassie-to-Wenzel-transition. In the case of nucleation inside the structure, the challenge is reversed. Here the structure must promote a Wenzel-to-Cassie-transition. Although this latter case may add to the challenges associated with stabilizing a Cassie state, it is actually the desired case from a heat exchange point of view. This is because the emerging droplets explore more of the surface area during nucleation and growth in the Wenzel state, and thus increases the heat exchange, followed by easy removal after Wenzel-to-Cassie transition [26].

To investigate the difference between deposited Cassie droplets and Cassie droplets condensing on a surface, we go back to our structure comprising the square array of square pillars from Fig. 6. Enright et al. [26] investigated the water vapor condensation on this structure⁵ with different spacings and sidewall features (see Fig. 11). Condensation on two different structures similar to that shown in Fig. 11 (a) with diameter $a = 300$ nm, height $c = 6.1 \mu\text{m}$ and spacings $b_1 = 2 \mu\text{m}$ and $b_2 = 4 \mu\text{m}$ were investigated. Using Eqs. (4) and (7)⁶, we find that

$$\theta_{min b_1} \approx 114^\circ \leq \theta_Y \approx \theta_{adv} = 121.1^\circ \quad \& \quad \frac{b}{a} = 6.7 \leq \left(\frac{b}{a}\right)_{crit} \approx 8.4 \tag{8}$$

$$\theta_{min b_2} \approx 135.7^\circ \geq \theta_Y \approx \theta_{adv} = 121.1^\circ \quad \& \quad \frac{b}{a} \approx 13.3 \geq \left(\frac{b}{a}\right)_{crit} \approx 8.4 \tag{9}$$

According to Eq. (8) the surface with spacing b_1 should promote droplets in the stable Cassie state. As shown in Fig. 12 (a), the surface with spacing b_1 does indeed promote droplets in the Cassie state.

For the surface with b_2 -spacing, the calculations in Eq. (9) indicate that the Wenzel state is thermodynamically more stable than the Cassie state. In agreement with this, Fig. 12 (b) shows droplets in the Wenzel state. Hence, Sarkar and Kietzig’s mathematical predictions for the stability of static droplets are in agreement with experimental results also for condensing droplets. On the other hand, the criterion for a metastable depinned Cassie droplet given in Table 1 is also fulfilled:

$$\left(\frac{b}{a}\right)_{crit} \leq \frac{b}{a} \leq \left(\frac{b}{a}\right)_{pin} \approx 64 \tag{10}$$

Nevertheless, it is sensible that this surface supports Wenzel droplets. Due to the large spacing compared to critical nucleation

³ Circular pillars approximated as square for the occasion. $c = 10 \mu\text{m}$, $a = 1 \mu\text{m}$ and $b = 2 \mu\text{m}$. $\theta_Y \text{ dodecanethiol/Au} \approx \frac{\theta_{adv} + \theta_{rec}}{2} = \frac{112^\circ + 107^\circ}{2} \approx 110^\circ$ [21, 22].

⁴ Though some claim that secondary nanostructures count as small enough to be part of the intrinsic (flat) surface, and thus enabling $\theta_Y > 120^\circ$ [17, 18].

⁵ They used circular pillars, which again are approximated as square to fit Sarkar and Kietzig’s models.

⁶ Where we use θ_{adv} instead of θ_Y since condensing droplets are continually growing.

Table 1
Design criteria for droplets in stable and metastable Cassie states [18].

State	Geometric requirements	Material requirements
Stable Cassie	$\frac{b}{a} \leq \left(\frac{b}{a}\right)_{crit} = \sqrt{1 - \frac{4c \cos \theta_Y}{a(1 + \cos \theta_Y)}} - 1$	$\theta_Y \geq \theta_{min} = \sec^{-1} \left(\frac{4\frac{c}{a}}{1 - (\frac{b}{a})^2} - 1 \right)$
Sagging Cassie	$0.75 < \frac{c}{a} < 0.9$ & $\left(\frac{b}{a}\right)_{crit} < \frac{b}{a} < \left(\frac{b}{a}\right)_{sag} = \frac{1 + \cos \theta_Y}{\sqrt{(2\frac{c}{a})^2 - 2(1 + \cos \theta_Y)}}$	$90^\circ < \theta_Y < 105^\circ$
Depinned Cassie	$\left(\frac{b}{a}\right)_{crit} < \frac{b}{a} < \left(\frac{b}{a}\right)_{pin} = \frac{(1 + \cos \theta_Y)}{\sqrt{(2\frac{c}{a})^2 - 2(1 + \cos \theta_Y)}}$	NA

radius, typically a few nm [27], nucleation occurs all over and within the structure. Droplets nucleating and growing inside the structure have already overcome the energy barrier that the depinned state poses. Thus the droplets remain in the Wenzel state.

Moreover, Enright et al. investigated the relation between the $\frac{c}{a}$ -ratio of smooth-walled pillars with constant diameter and pitch, and the stability of the condensing Cassie droplets. They found that the depinning of contact lines stabilizing the metastable Cassie state depends on pillar height, where the stability increases with the height. Their results are therefore in agreement with Eqs. (4) and (7), which predict less strict requirements on the θ_Y and $\frac{b}{a}$ -ratio for a stable Cassie state as the $\frac{c}{a}$ -ratio increases.

Nosonovsky and Bhushan [28] also investigated the square array of cylindrical pillars with diameter $a = 5 \mu\text{m}$, height $c = 10 \mu\text{m}$ (series 1), and $a = 10 \mu\text{m}$ and $c = 14 \mu\text{m}$ (series 2). Both series

included surfaces with a range of pitches, $p (= a + b$ in Sarkar and Kietzig's notation). It was found experimentally that the critical $\frac{a}{p}$ -ratio for a Wenzel-to-Cassie transition is $\left(\frac{a}{p}\right)_{crit} = 0.51$. Only the three smallest pitches in each series exhibit $\frac{a}{p} \geq 0.51$. This is in agreement with Sarkar and Kietzig's criteria for droplets in the stable Cassie state (Eqs. (4) and (7)), which is fulfilled by the three smallest pitches in each series.

So far we have only regarded the structural geometry and chemical properties of the surfaces. However, the mechanical properties of the material may also promote or inhibit the Cassie state. Pillars fabricated of soft materials may bend as the droplets grow between the pillars. As a result the energy of the entire system increases, and flooding of the structure may become energetically favourable [29]. Consequently, the choice of material is important with regard to the intrinsic Young contact angle, but also the mechanical properties of the material. Copper and copper oxides are therefore frequently used due to their mechanical durability. Zhu et al. [30] is one of the groups that successfully fabricated clustered copper nano-needles that were able to promote a Wenzel-to-Cassie-transition. Consequently, droplets were allowed to nucleate at the base, exploring the surface area and increasing the heat transfer rate, meanwhile a continuous shedding of macrodroplets was maintained.

Although the results from the condensation experiments are not in complete agreement with the design criteria from the static droplet experiments, the trends are similar. Hence, the design criteria from static droplet studies may work as a good starting point for fabrication of surfaces for condensing droplets.

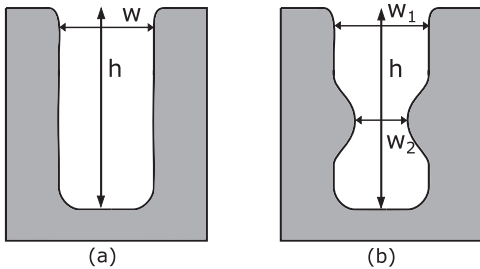


Fig. 10. The square pillar geometries without (a) and with (b) scallops, used by Hensel et al. [25].

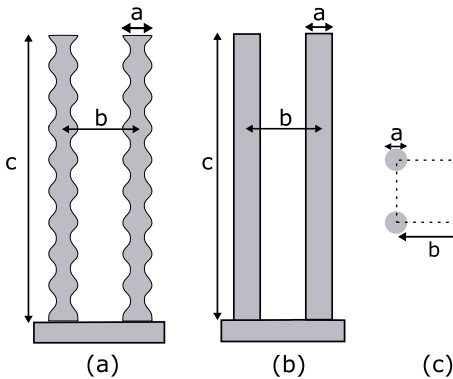


Fig. 11. Circular pillar geometries fabricated by Enright et al. [26]: (a) Si nanopillars; (b) Si micropillars; (c) top view of four nearest pillars, which outline a unit.

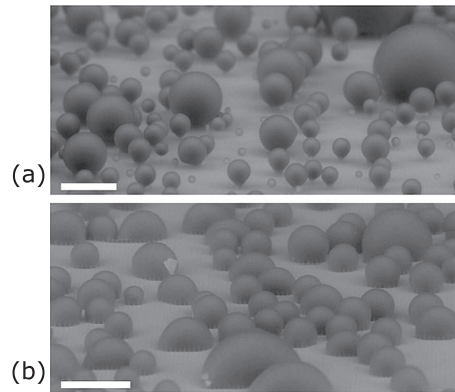


Fig. 12. Condensation on surfaces similar to structure in left pane of Fig. 11 with spacing (a) $b_1 = 2 \mu\text{m}$ and (b) $b_2 = 4 \mu\text{m}$. Surfaces exhibit formation of Cassie droplets and Wenzel droplets, respectively. Scale bars = $60 \mu\text{m}$. Source: Reprinted with permission from Enright et al. [26]. Copyright 2012 American Chemical Society.

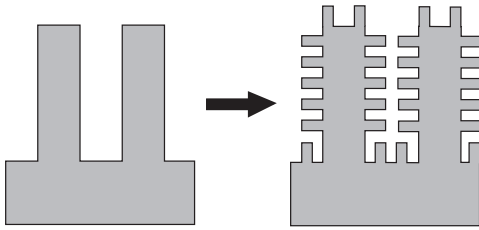


Fig. 13. Illustration of microstructure and hierarchical micro- and nanostructure.

3.3. Design of superhydrophobic surfaces for water condensation

As mentioned earlier, there is a wide range of surface structures that may promote droplets in the Cassie state. Recent research has shown that surfaces combining different structures and/or chemistries can yield high degrees of superhydrophobicity. In the following, we will therefore discuss some of these surfaces.

3.3.1. Micro- and nanostructured surfaces

Micro- and nanostructured surfaces, often named hierarchical structures in the literature, are surfaces with a combination of microstructure and a secondary nanostructure (applied on top of the microstructure as illustrated in Fig. 13).

Several groups have successfully fabricated such surfaces with a variety of materials and morphologies. CuO/Cu surfaces such as the one fabricated by He et al. [31] are promising. These surfaces have micro-sized holes in a square pattern inside which nanosized randomly oriented nanoneedles are grown. The inclusion of the nanoneedles raise the contact angle to above 150° , which means that superhydrophobicity is achieved.

For a systematic approach of investigating the role of structures on different length scales, it is suitable to look at the study by Lo et al. [16]. They investigated the water vapor condensation on micro- and nanostructured surfaces compared to plain microstructured surfaces. Two types of microstructures were used: parallel microgrooves (PMG) and cross-sectioned microgrooves (CMG). Inside the microgrooves, silicon nanowires (SiNW) were randomly and densely grown, which constitute the nanostructure of the surface. Although highly pinned Wenzel droplets are observed on the plain CMG⁷ and PMG surfaces, the hierarchical surfaces (CMG/SiNW and PMG/SiNW) both exhibit continuous shedding of droplets. This indicates that the secondary structure promotes Cassie droplets with low CAH. Interestingly though, the PMG/SiNWs exhibit a magnitude smaller cycle time (i.e. the time from nucleation to departure of a droplet) compared to CMG/SiNW. Thus, the pinning of droplets must be larger on the CMG/SiNW than the PMG/SiNW. A small cycle time is desired because it indicates a large heat and mass transfer rate [27]. On the other hand, the SiNW on a smooth surface also exhibits smaller cycle time than CMG/SiNW. Consequently, the micro- and nanostructured surface might not always yield better results.

According to classical nucleation theory (CNT), the nucleation rate on a microstructured surface (surface with micro-sized features) is higher than that on a nanostructured surface. The Gibbs free energy of formation of droplets is given by

$$\Delta G = \frac{4}{3}\pi r_e^2 \sigma_{lv} F - 4\pi \sigma_{lv} F (r_c - r_e)^2 \quad (11)$$

⁷ Note that the observations correspond to the predictions in Eqs. (4) and (7) while Nosonovsky and Bhushan's limit fail for the relevant dimensions.

where r_e is the equilibrium droplet radius, σ_{lv} the liquid-vapor surface tension, $F = 0.25(2 - 3\cos(\theta) + \cos^3(\theta))$, θ is the equilibrium contact angle, and r_c is the roughness diameter.

As seen in Fig. 14 a micro-sized roughness (cavity dimension) will increase the nucleation rate by lowering the barrier towards nucleation. In the work by Lo et al. [27] it is found that more nucleation and condensation occurs on the CMG and PMG surfaces, compared to SiNW surfaces, which supports the theoretical results.

3.3.2. Surface with hydrophilic and -phobic domains

One of the main challenges in a dropwise condensation heat exchanger is how to achieve high nucleation rates while maintaining sustainable shedding of droplets. The two processes are determined by different and opposing mechanisms. While hydrophobic surfaces promote sustainable droplet departure, they also reduce the nucleation density. There have therefore been several attempts to develop a type of hierarchical surface structure with hydrophilic and hydrophobic domains [32, 33].

Chen et al. [33] designed silicon surfaces with pyramidal structures covered by nanogras everywhere except for the lower base of the sides of the pyramids. Thus, surfaces with global superhydrophobicity, but local hydrophilicity were obtained. These surfaces were reported to exhibit sustainable dropwise condensation behaviour with enhanced droplet nucleation and droplet departure volume. In fact, the surface with the smallest spacing between the pyramids ($S = 20\mu\text{m}$) showed a 450% increase in drop self-removal volume and a 65% increase in drop number density compared to the flat surface covered with nanogras. The massive increase in droplet self-removal volume is attributed to the coalescence driven out-of-plane jumping.

The coalescence driven out-of-plane-jumping is believed to be caused by release of excess surface energy as two or more droplets coalesce. The released energy propel the resulting droplet from the surface. While this behaviour is observed on multiple surfaces with extremely low surface adhesion [30, 34, 35], the mechanism of this self-removal is not fully understood. Enright et al. [36] investigated the phenomenon further. Their study showed that this kind of self-removal is fundamentally inefficient; less than 6% of the released surface energy at coalescence was transferred to translational energy removing the droplet from the surface. As a consequence, this kind of self-removal is unlikely to occur for immobile or semi-mobile Wenzel droplets (as the adhesion energy between the droplet and

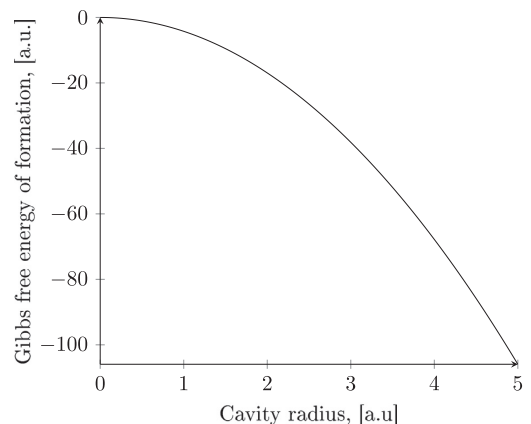


Fig. 14. Gibbs free energy of nucleation with increasing cavity dimension (Eq. (11)). The higher the dimension, the easier the formation of nuclei.

the surface is larger). Thus, the importance of promoting the formation of Cassie droplets for heat exchange applications is reinforced.

On the other hand, the results from Boreyko and Chen [9] indicate that the energy released during coalescence is higher than the Wenzel-to-Cassie-transition energy barrier. Thus the coalescence may improve the droplet mobility, even in cases where the resulting translational energy is not sufficient for complete self-removal. Moreover, the yield of the self-removal may be increased by preventing droplets from returning due to gravitational drag (for vertical surfaces) or entrainment in the vapor flow (either adjacent to the surface or towards the surface, depending on the conditions of the condensation). For example, Miljkovic et al. enhanced the yield through the use of an external electric field that prevented droplet return [37].

3.4. Coating with a low surface energy chemical

In any case of surface structuring, either on one or more length scales, it is often necessary to additionally coat the surface with a thin film of a low surface energy compound to achieve superhydrophobicity [38, 39]. Common low surface energy materials are polymers with surface functional groups, such as $-\text{CF}_2$, $-\text{CF}_2\text{H}$ and CF_3 . The fluorinated or perfluorinated materials do not influence the roughness of the surfaces, but can largely influence the surface energy and therefore the contact angle of the liquid.

3.4.1. Superhydrophobicity by liquid-infusion

So far in this paper, only surfaces with micro- and/or nanostructures have been discussed. The superhydrophobicity of these surfaces depends on the surfaces' ability to stabilize the droplets in the Cassie state. Although many of these surfaces exhibit superhydrophobicity, they may not be suitable for industrial use. In industrial applications, the surfaces will be subjected to varying conditions and various contaminants that may destabilize the Cassie state [35]. In addition, many of the surfaces are vulnerable to mechanical abrasion due to the fragile nature of the surface structures. Hence, the wetting properties may be greatly affected [11, 40]. One promising solution is to use slippery liquid- or lubricant-infused porous surfaces (SLIPS) instead. The main idea is schematically shown in Fig. 15.

The capillary forces created by the micro- or nanostructure of the underlying solid are utilized to contain a viscous lubricant within the structure. Since an excess of lubricant is applied on the solid surface, a semi-mobile, smooth top layer is created. Thus, it is the properties of the lubricant that mainly determines the wetting properties of the entire system. As opposed to a normal flat solid surface, the surface of a SLIPS can be molecularly smooth, resulting in a small friction, and hence, small CAH. The surface will therefore be "slippery" even when the surface tension of the lubricant is not small enough to attain superhydrophobicity. In addition, the semi-mobile layer introduces an additional robustness, as discussed later in this section.

Although the underlying surface of the SLIPS is less important for the surface wetting properties, it is essential for the sustained containment of the lubricant within the surface structure [40]. The

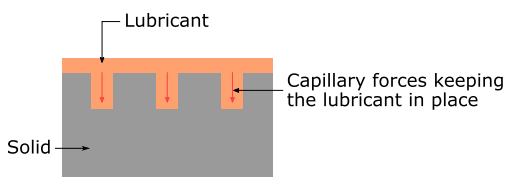


Fig. 15. A SLIPS shown schematically.

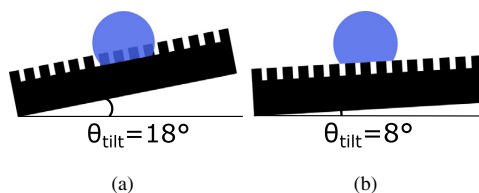


Fig. 16. Schematic of the droplets in different states on Dai et al.'s SLIPS [43]. a) Droplet in the slippery Wenzel state, b) droplet in the slippery Cassie state.

surface structure induced capillary forces are, as mentioned, important in this sense. In addition, the solid surface chemistry must be compatible with the lubricant, and reinforce the strong attraction between the underlying solid surface and the lubricant. If the attractive forces are too weak, water droplets condensing (or deposited) on the surface may displace the lubricant. Hence, the surface may lose its slippery properties [11]. Also, to further decrease probability of liquid displacement of the lubricant, the lubricant and the liquid must be immiscible.

In the scenario of low attractive capillary forces, the impact of the underlying surface chemistry was demonstrated by Kajiya et al. [41]. They showed that the water droplets may displace the lubricant during condensation and growth. Nevertheless, the surface can retain its hydrophobic state if the underlying surface is water repellent. At further growth, the droplets may detach from the underlying surface.

The increased robustness of the SLIPS arises, as mentioned, from the semi-mobile layer. While the wetting properties of a textured superhydrophobic surface are compromised beyond repair upon contamination or mechanical abrasion, the mobility of the lubricant of a SLIPS causes the surface to be self-healing [40, 42]. In addition, combinations of micro- and nanostructures can be utilized to create superhydrophobic SLIPSs that are insensitive to the wetting state of the droplet (i.e. whether it is in the Wenzel or the Cassie state). This was demonstrated in the study by Dai et al. [43]. In Fig. 16 a schematic drawing of Dai et al.'s surfaces exhibiting (a) slippery Wenzel state (sliding angle = 18°) and, (b) slippery Cassie state (sliding angle = 8°) is shown. The slippery Cassie state is caused by the superhydrophobicity of the surface, while the slippery Wenzel state occurs due to the slipperiness of the lubricant. Consequently, the surface exhibited a low CAH and high droplet departure rate even if the Cassie droplet for some reason collapsed. Thus, they created a surface that will be less vulnerable to different conditions and contaminations.

Hierarchical structures may also be utilized in SLIPSs to promote dropwise water vapor condensation. Xiao et al. [44] investigated the water condensation on a SLIPS with hydrophilic domains in the underlying surface (see Fig. 17). They observed that the lubricant layer covering the underlying pillars was thin enough for the water vapor to penetrate. Thus the vapor nucleated on the hydrophilic domains. During growth, the droplets detached from the underlying surface and attained a hydrophobic state⁸. Increased nucleation density and decreased droplet departure diameter compared to the same surface without infused lubricant was shown.

Several mechanisms can cause the failure of superhydrophobicity or the transition to filmwise condensation on SLIPS [45]. Lubricant displacement is already mentioned, which can be caused by low capillary forces between lubricant and solid, or that spreading coefficient of the lubricant on the condensate in the presence of gaseous condensate is positive [46]. Miscibility of the condensate and the

⁸ Xiao et al. claim superhydrophobicity, but although contact angle hysteresis was 3° , contact angle was only 110° .

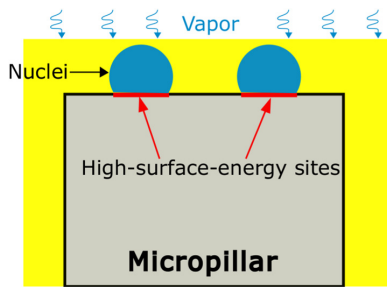


Fig. 17. SLIPS utilizing hydrophilic and -phobic domains on underlying surface for controlled nucleation.

Source: Figure adapted from Xiao et al. [44].

lubricant will cause them to mix and depletion of lubricant will gradually occur as the droplets are removed from the surface. Another failure mechanism is cloaking, for which spreading of the lubricant on the condensate is the preferred state and a thin film of lubricant will spread on the condensate droplet [47]. The removal of droplets, e.g. by gravity, will then cause removal of lubricant and with time the lubricant is consumed. Even if cloaking is avoided, there is a chance that the lubricant will not spread on the structure in the presence of the condensate and either spread only directly underneath the droplets or everywhere except underneath the droplets, causing a Wenzel state.

3.5. Challenges and future outlook

To complicate things, experimental conditions such as temperature, presence of non-condensable gases and gas flow may affect the condensation of water vapor. In addition, the mechanical and thermal properties of the solid substrates are important to consider when transferring the technology to the industry.

Most of the studies discussed in this work are performed under ideal conditions for environmental Scanning Electron Microscope. That is, low temperature, semi-vacuum and “static” conditions. This is far from industrial conditions, where higher operating temperatures, gas flow and saturated water vapor (as opposed to air or semi-vacuum) conditions are required. These conditions might introduce additional challenges to promote and maintain dropwise condensation. Increased temperatures reduce the surface energy of the water droplets and therefore, make it challenging to obtain the Cassie state [38]. The literature is, however, not conclusive on whether water vapor conditions will affect the wetting state significantly. Weisensee et al. [6] observed a finite reduction of contact angles on flat surfaces of Teflon while the remainder of the tested textured surfaces maintained their wetting states in saturated water vapor conditions, compared to water condensation in an air environment.

Torresin et al. [38] investigated water vapor condensation and heat transfer under vapor flow conditions at high operating temperatures (110°C). The high temperature caused formation of Wenzel droplets despite the fact that the surface promoted Cassie droplet formation at lower temperatures. All the same, they observed increasing heat transfer with increasing gas flow. The gas flow created a shear force that moved the initially immobile Wenzel droplets, and thus increased the heat transfer by decreasing the droplet departure radius. On the other hand, the gas flow also introduced higher wear on the surface and over time the degradation was significant. In fact, Torresin et al. found that the condensation on their superhydrophobic nanotextured surfaces went through a transition from dropwise to filmwise condensation after five days of testing. This was

caused by the degradation of the nanostructures and the deterioration of the hydrophobic monolayer from the shear stress generated by the vapor flow. After the transition the surfaces performed worse than “normal” surfaces for filmwise condensation with respect to the heat transfer. Degradation, of any kind or reason, is therefore found to be detrimental to the performance of superhydrophobic surfaces, and is still a huge unresolved issue, and therefore, poses great challenges for industrial applications.

In most of the studies discussed in preceding sections, heat transfer rates have not been measured. Instead, it is assumed and predicted by models, e.g. [48], that the heat transfer increases for dropwise condensation compared to filmwise, and also for Cassie droplet formation rather than Wenzel. On the other hand, the trapped vapor underneath the liquid droplets in the Cassie state may create additional heat transfer resistance [38], reducing the condensation rate, and it is therefore necessary to minimize this vapor volume while on the same time ensuring droplet mobility. Therefore, there are indications that the quasi-Cassie state (a metastable mix of Wenzel and Cassie) yields the highest heat transfer [49]. Aiming for surfaces promoting the pure Cassie state could therefore be a mistake.

Another solution could be not to aim for superhydrophobicity at all. Studies have shown that a slightly hydrophilic surface ($\theta \approx 78^\circ$) could promote dropwise condensation [50, 51]. In addition, high mobility of the droplets can be induced by introducing superhydrophilic trenches ($\theta \approx 0^\circ$) on the surface. The trenches can lead the droplets away from the surface and a surface for efficient nucleation, growth and drainage is possible. The heat transfer coefficient for such a surface is measured to be up to 34.4% higher than for the purely hydrophilic surface [51].

4. From superhydrophobicity to superomniphobicity

While surfaces used for water vapor condensation have been subjected to extensive research, literature on surfaces for dropwise CO₂ condensation is virtually non-existing. There is, however, an increasing amount of studies on superomniphobic surfaces⁹. These are surfaces that per definition exhibit $\theta^* \geq 150^\circ$ and $\Delta\theta \leq 10^\circ$ for any liquid. Experimentally, it is of course immensely time consuming to test the wetting properties of a surface for all possible liquids. The focus have therefore been on liquids with low surface tension, mostly organic compounds, such as ethanol, hexane and hexadecane. To understand the potential changes in surface chemistry and structure design criteria as water is replaced by CO₂, we therefore look into the similar changes as we move from superhydrophobic to superomniphobic surfaces.

Although it is tempting to assume that the surface requirements for Cassie droplet stabilization are equal for superomniphobic and -hydrophobic surfaces, dramatic reductions in liquid surface tension cause the conditions for droplet formation to change considerably. Recall from Section 2.2 that the Cassie state is always thermodynamically more unstable than the Wenzel state for $\theta_Y < 90^\circ$. As long as water is the condensate, there is a range of materials exhibiting $\theta_Y \geq 90^\circ$. Thus, with the “right” surface structure, formation of stable Cassie droplets is attainable. However, for the low surface tension condensates, the range of materials diminishes. Formation of thermodynamically stable Cassie droplets may therefore be impossible. On the other hand, from Section 3.1 we know that the surface structure can introduce energy barriers preventing Cassie-to-Wenzel transition. Even though the design criteria described in this section was developed for $\theta_Y \geq 90^\circ$, it may be possible to introduce similar

⁹ A conglomeration of different terms appear in this field; superoleophobicity, superamphiphobicity etc., rigorous definitions of these terms can be found in the introduction, Section 1.

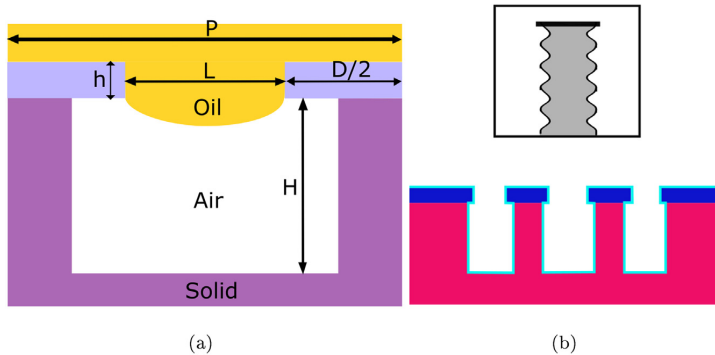


Fig. 18. (a) Illustration of the geometry of the T-shape. Figure constructed after the model by Wu and Suzuki [53]. (b) Chemistry of the T-shape shown schematically (upper). The colours describe different materials, with turquoise being 1H,1H,2H,2H-perfluoro-octyltrichlorosilane (PFOTS), red Si and blue SiO₂. Sidewall features of this T-shaped surface (lower).

Source: Figures adapted from Wu and Suzuki [53].

energy barriers for $\theta_Y < 90^\circ$. In that way, metastable Cassie droplets may be attainable.

4.1. Impact of texture on static Cassie droplet formation

As with superhydrophobic surfaces, attempts have been made to rigorously characterize the impacts of various surface features on the wetting properties of superomniphobic surfaces [52, 53].

Tuteja et al. [52] investigated the advancing and receding contact angles of liquids with a range of surface tensions on electrospun surfaces of blends of (hydrophilic) PMMA¹⁰ and (hydrophobic) fluorodecyl POSS¹¹, a polyhedral crystalline solid material. Even at low weight percent of fluorodecyl POSS (<2 wt%), high apparent advancing contact angles, $\theta_{adv}^* > 90^\circ$, with both water and low surface tension liquids were observed. Since the surfaces are hydrophilic at these wt%, indicated by $\theta_Y < 90^\circ$ on the smooth corresponding surface, we would expect $\theta_{adv}^* < \theta_{adv} < 90^\circ$ according to Eq. (1). The droplet must therefore be in a metastable Cassie state that obstruct the transition to the Wenzel state. This hypothesis was confirmed by releasing the droplets onto the surfaces from a height, where the impact energy caused a Cassie-to-Wenzel-transition and decreased θ_{adv}^* . The metastable Cassie state was observed for a range of liquid alkanes even though all the surfaces were oleophilic (wetttable for oily substances). The CAH for the low surface tension liquids were, however, large, especially for low wt% of fluorodecyl POSS.

4.1.1. Design criteria

Wu and Suzuki [53] investigated the impact of the surface texture on the introduced energy barrier for Cassie-to-Wenzel-transition further. They formulated design criteria for sustained superomniphobicity. Based on those design criteria, they showed that the T-shaped structure satisfying the following inequalities (Eq. (12)), was the most mechanically robust geometry¹².

$$R \geq \frac{\left(\frac{1}{f_s} - 1\right) D}{n \sin \theta_Y}$$

$$H \geq \frac{L}{2} \tan \frac{\theta_Y}{2} \quad (12)$$

where R is the macroscopic radius of the droplet, H and D are height and diameter of the T-shape, respectively (see Fig. 18 (a)), L is the

distance between two adjacent caps and f_s is the solid fraction from Eq. (2). Schematic diagrams of the individual micropillars and the chemistry of the T-shaped surface are shown in Fig. 18 (b).

Several geometries meeting the design criteria by Wu and Suzuki were tested for lyophobicity with water and hexadecane. Apparent contact angles, θ^* , as high as 170° for water and 167° for hexadecane were obtained for the surface shown in Fig. 18 (a). The contact angle hysteresis, $\Delta\theta$, on this surface was approximately 8° for both liquids, which confirms the superomniphobicity of the surface. Interestingly, the water and hexadecane θ^* and $\Delta\theta$ were almost the same for all the tested geometries (also those with $\theta^* < 150^\circ$), but greatly varying with solid fraction, f_s (see Eqs. (1) and (2)). This indicates that f_s dominates the wetting properties of the surface when the droplet is in the Cassie state. The role of increasing f_s for a hexadecane droplet ($\theta_Y = 50^\circ$) on Si is shown in Fig. 5. The solid fraction on the surfaces in Fig. 18 (a) is 0.08 [53], which according to Eq. (2) results a contact angle of 169° . This is in good agreement with the experimental results of 170° (water) and 167° (hexadecane).

Wu and Suzuki [53] also tested the values of $\Delta\theta$ against three existing models; the Wenzel and Cassie equations (Eqs. (1) and (2)) for advancing and receding contact angles, the linear average model by Extrand [54], and the local differential parameter model by Choi et al. [55]. While the advancing contact angles are in decent agreement with the two latter models, the receding contact angles are not predicted satisfactory for all cases with any of the models. One explanation is that the static contact angle, θ_Y , is assumed to be the same on a flat and a rough surface. However, the static contact angle may vary according to the degree of pinning on the asperities of the structures, and the predictions of contact angles are therefore not exact.

4.1.2. Micro- and nanostructured surfaces

As with water condensation, hierarchical structures featuring micro- and nanostructures have been observed to yield superomniphobicity [56]. Mazumder et al. [14] fabricated a superomniphobic surface of nanopillars (glass/SiO₂) with branching structures on top (SiO₂). Contact angles of 172° , 163° and 153° with water, oleic acid and hexadecane, respectively, were obtained. The contact angle hysteresis for the respective liquids were $<3^\circ$, $<4^\circ$ and $<6^\circ$. However, this structure is fragile and susceptible to mechanical abrasion. To improve the robustness of the surface, nanonodules were deposited instead of the branching structure. While the resistance to mechanical abrasion improved, the contact angles decreased, and became only slightly higher than those on the primary nanopillars.

¹⁰ Poly(methyl methacrylate).

¹¹ Fluorodecyl polyhedral oligomeric silsesquioxane.

¹² NB. This model is derived for droplets deposited on the surface.

Recall the criteria developed by Sarkar and Kietzig [18]. Not surprisingly, we find that the geometry of the nanopillared structure (without a secondary structure on top) does not satisfy the criteria for formation of hexadecane droplets in the stable Cassie state. Moreover, the critical value for the spacing to width ratio, $\left(\frac{b}{a}\right)_{crit}$, assumes a negative value. According to Sarkar and Kietzig's criteria (see Table 1), the metastable states for this geometry are automatically excluded too. However, experiments show that the contact angle is $\theta^* = 104 > \theta_Y$. On the other hand, the criteria for metastable (sagging) Cassie droplets are partially satisfied since $\frac{b}{a} \leq \left(\frac{b}{a}\right)_{sag}$. Although this single example surface of Mazumder et al. is not sufficient to conclude, it can be used as an indication of that the design criteria developed by Sarkar and Kietzig are applicable to superomniphobic surfaces too. In any case, they can constitute a starting point for the design of a superomniphobic surface.

4.1.3. Lowering the surface energy

As stated previously, a reduction in surface energy by coating with a low energy material such as fluorines may be necessary for superhydrophobicity. To achieve superomniphobicity, on the other hand, literature shows that this step may be crucial [57]. A variety of low surface energy materials are used in the literature, but a common feature is the small or large degree of fluorination of an organic compound. Examples are 1H,1H,2H,2H-heptadecafluorodecyl [58] and 1H,1H,2H,2H-perfluoro-octyltrichlorosilane [11, 53].

4.2. Formation of condensing Cassie droplets

As we move from liquid droplets deposited on the surface to condensation of the liquid, we face the same challenges as discussed for superhydrophobic surfaces. The major question is as follows: Will the droplets nucleating at the base of the surface structures transition to a Cassie state? This is, if possible, an even greater challenge for superomniphobic surfaces compared to superhydrophobic surfaces because we have $\theta_Y < 90^\circ$. Thus, the Wenzel state is always thermodynamically favourable. In addition, it is probable that the energy barrier for a Wenzel-to-Cassie-transition becomes even greater. Consequently, the requirements on the surfaces become even stricter.

A few attempts have been made to create superomniphobic surfaces for condensation. Rykaczewski et al. [11] tested the wetting properties during condensation of several structures including Al-SiO₂ nanotextured, polymer solution re-entrant (or overhanging) superomniphobic, Si micropost textured surfaces, and lubricant infused surfaces (SLIPS). Condensation was also tested on all the surfaces impregnated with a lubricant. The results from these experiments were mixed. In fact, the overall performance of a fluorosilane-functionalized, smooth surface¹³ was best. The impregnated surfaces were generally more likely to induce dropwise condensation than the nanotextured and superomniphobic surfaces, which both showed filmwise condensation for all or nearly all liquids.

The formation of films on the nanotextured and superomniphobic surfaces indicates that the condensates nucleate within the structure. Moreover, the structures are unable to surpass the energy barrier for a Wenzel-to-Cassie-transition. As a consequence, the liquid floods the structure. Decreasing the dimensions of the surface structure below the critical radius of nucleation may prevent nucleation within the structure. This comes, however, at the cost of increased fabrication cost and complexity.

Although the SLIPSs appear to perform better than the textured superomniphobic surfaces for dropwise condensation of liquids with low surface tension, several challenges still remain. Some of these are illustrated in the above described study by Rykaczewski et al. [11].

The condensing liquid displaced the lubricant on several occasions, and caused filmwise rather than dropwise condensation. In addition, on some of the rougher underlying structures, the lubricant layer was not thick enough to cover the structure, and instead filmwise condensation was promoted. In other words, the lubricant must exhibit good adhesion to the solid surface, while maintaining repellency towards a range of liquids. In addition, the viscosity (dependent on the temperature) and the equilibrium vapor pressure of the lubricant must be such that the lubricant is compatible with the required environment. For example, if the viscosity is too high, the lubricant may not spread homogeneously on the surface. Hence, the solid surface may be exposed to the condensate, resulting in filmwise condensation. However, if the viscosity is too low, the condensate might displace the lubricant, yielding filmwise condensation as discussed above. The latter challenge could be reduced by carefully choosing the underlying solid surface as indicated in the study by Wong et al. [40]. They observed that omniphobic underlying surfaces decrease the chance of lubricant displacement.

5. CO₂ condensation on superomniphobic surfaces

Now, we move away from the solid science and into the landscape of conjectures. If there was little literature on superomniphobicity in general, there is, as far as we know, none on surfaces promoting dropwise condensation of CO₂. As a result, an extrapolation from the knowledge attained in the former field is necessary. First, we will compare relevant chemical and physical properties of (liquid) CO₂ with the condensates from the previous sections. Subsequently, we will try to qualitatively comment on and evaluate the performance of suggested surface morphologies (from the previous sections) using CO₂ as the condensate.

5.1. Surface tension of CO₂ compared with other liquids

Table 2 shows the surface tension of various low surface tension liquids, water and CO₂. At room temperature, CO₂ has significantly lower surface tension than the other fluids, however, the surface tension of CO₂ increases dramatically as the surrounding temperature decreases. At around -50°C , the surface tension of CO₂ is comparable to the organic liquids, shown in Table 2. By assuming that surface tension is the determining factor, and that temperature has no other influence, it is possible that previous results using e.g. pentane as the test liquid [11], may be transferable to CO₂.

5.2. Candidate surfaces for promoting dropwise condensation of CO₂

In commercially available CO₂ condensers, copper and copper oxide materials are commonly used, and filmwise condensation is the default mode. To achieve dropwise condensation of CO₂, it is necessary to lower the surface energy of the copper. Functionalization of an untextured Cu surface with a fluid with low surface energy alone, is however, an unlikely path due to low durability and still too high surface energy. Nevertheless, the combination of functionalization and nano- and microscaled surface structuring has been shown to be

Table 2
Chemical and physical properties of liquid CO₂ compared to other liquids

Liquid	Surface tension $\left[\frac{\text{mN}}{\text{m}}\right]$	Temp [$^\circ\text{C}$]
CO ₂	16.54 [59]	-52.2
CO ₂	1.19 [60]	20
Hexadecane	28.12 [61]	20
Pentane	15.7 [58]	21
Hexane	18.52 [62]	20
Ethanol	22.28 [62]	20
Water	72.75 [63]	20

¹³ This is termed "oleophobic" by Rykaczewski et al. [11], but exhibit $\theta_Y < 90^\circ$.

crucial for achieving superomniphobicity [57], and is probably imperative for the case of CO₂. Regarding low surface energy chemicals, e.g. fluorinated or perfluorinated materials, it must be pointed out that the literature does not contain examples of tests done with surfaces coated with such materials in a CO₂ environment. Conduction of proper tests is therefore necessary for determining the applicability of fluorinated compounds for dropwise condensation of CO₂.

Structured surfaces already proven to yield superomniphobicity are a good starting point for achieving dropwise condensation of CO₂. The design criteria by Wu and Suzuki [53] in Eq. (12) should be fulfilled also for CO₂, and used for designing a surface that promotes CO₂ droplets in the Cassie state.

A previous review on superomniphobic surfaces pointed out the importance of a re-entrant structure for achieving superomniphobicity [57]. One such surface has been fabricated and tested by Tuteja et al. [58]. This surface has been tested for fluids with surface tension down to 15.7 mN m⁻¹ (pentane), and is therefore a candidate for the CO₂ case. Liu et al. also pointed out the importance of re-entrant surfaces [64]. For achieving droplets in the Cassie state for liquids of very low surface tension, even for fluorinated compounds (C₆F₁₄, $\gamma = 10 \text{ mN m}^{-1}$), a doubly re-entrant structure is required. However, Wu and Tuteja used fluorinated chemicals to achieve lyophobicity, and the applicability of fluorine chemicals in a CO₂ environment is unknown. In addition, the low temperature durability of the surface is unknown, and therefore an important issue to address. Also, neither of the surfaces by Wu and Suzuki, Tuteja et al. or Liu et al. are tested with condensing vapor, so the direct applicability to dropwise condensation of CO₂ is unknown. The re-entrant surfaces, both single and double, have no defence against internal condensation within the structures [64], and a Wenzel-to-Cassie transition is not expected.

On the other hand, Rykaczewski et al. [11] determined the condensation mode for seven different low surface tension fluids and water, on three different surfaces, in which one is a SLIPS [11]. Even though the contact angle towards the tested organic oils were less than 90° for all surfaces, the condensation occurred in the dropwise mode for several of the liquids. Special attention should be given to the condensation of pentane, which condensed in the dropwise mode on two of the three tested surfaces, even though the surface tension is only 15.7 mN m⁻¹. It should also be noted that perfluorohexane with a surface tension of 12 mN m⁻¹ condensed in the filmwise mode for all surfaces, which indicates a limit as to how low the surface tension can be to achieve dropwise condensation on this kind of surfaces. In any case, the flat oleophobic surfaces and the SLIPS surface fabricated in this work are candidates for dropwise condensation of CO₂.

For using SLIPS as a surface for condensation, the surface tension of CO₂ is again an issue, and the experiments have to be performed at low temperatures. The requirement for low temperature introduces yet another challenge: The ability of the surface and the infusion liquid to endure extreme conditions. Thermal compression resulting in material cracking and failure is only one example. Decomposition and/or freezing of the lubricant is another. However, low temperatures do not necessarily cause low mechanical robustness, as shown by Wang et al. [65]. They tested three different liquids for SLIPSs for anti-icing applications, and found that the superhydrophobicity was maintained, but reduced, down to -20 °C for one of the lubricants. The reduction in superhydrophobicity comes from increased pinning of water droplets on the surface, which could also be the case for CO₂ droplets. The work by Lu et al. [66] resulted in a non-wetting SLIPS against water and various liquids, such as coffee and cooking oils, also after thermal tests with liquid nitrogen (-196 °C). These results are promising for low temperature condensation of CO₂, but as for most of the results in the literature, this work is also a test of non-wetting behaviour, not for promotion of dropwise condensation. Even though superomniphobicity is necessary for

dropwise condensation, it is not the only requirement, and tests with condensing vapor must be conducted at different thermal conditions.

Generally, SLIPS are promising candidates for CO₂ condensation. However, care should be taken to choose the proper lubricant. As said above, temperature stability is important. Even more crucial is the immiscibility of the lubricant towards CO₂. If CO₂ is miscible with the lubricant it would displace the lubricant, and flood the underlying surface. Lubricants that are immiscible for low surface tension fluids can be found by utilizing the model set forth by Preston et al. [45]. For CO₂ it will not be easy to find a suitable lubricant. Liquid CO₂ is a good solvent for several oily substances that are often used as lubricants for SLIPS repelling water.

CO₂ in its supercritical form is a superior solvent and even though liquid and supercritical CO₂ does not have equal behaviour, this property will pose a challenge when condenser surfaces are coated with chemicals. This is the case both for SLIPS and for surfaces where fluorinated compounds are used for lowering the surface energy. This challenge has not been addressed previously, and work has to be done on the matter.

6. Summary and ideas for further work

Through this literature review it is shown that comprehensive design criteria for superhydrophobic surfaces have been developed, and that different sets of criteria by different research groups, are consistent. Most of the work done is applicable to static water droplets and the non-wetting behaviour of rough surfaces. Less work is conducted on condensing water droplets, and even less on condensing low surface tension liquids. Nevertheless, the previous work on superomniphobic surfaces indicate that re-entrant surfaces with structures with at least two length scales (hierarchical structures) that are coated with a low surface energy fluid such as a silane, is likely to yield superomniphobicity, i.e. non-wetting behaviour towards all liquids, including CO₂. Examples of surface designs that could be combined to give the above described surface are those by Rykaczewski et al. [11], Wu and Suzuki [53], and Tuteja et al. [52], with the basic design criteria of Sarkar and Kietzig [18] as a basis.

Even though the design criteria at hand, there are still important parameters of liquid CO₂ that is not known. One very important parameter for using the design criteria is the equilibrium contact angle of the liquid on the surface. This parameter is not known for CO₂ liquid in a CO₂ vapor environment, and a necessary starting point for future work is therefore to measure the contact angle of a CO₂ droplet on a flat surface. It is also necessary to test various low surface energy chemicals, such as fluorines, for compatibility with CO₂. The low temperature behaviour and immiscibility of candidate lubricants towards CO₂ for fabrication of SLIPS are other parameters to be tested.

Conflict of interest

None.

Acknowledgments

This publication has been produced with the support of the Research Council of Norway through the CLIMIT funding program (254813/E20).

References

- [1] Chua KJ, Chou SK, Yang WM, Yan J. Achieving better energy-efficient air conditioning – a review of technologies and strategies. *Appl Energy* 2013;104:87–104. <http://www.sciencedirect.com/science/article/pii/S030626191200743X>. <https://doi.org/10.1016/j.apenergy.2012.10.037>.

- [2] Beér JM. Combustion technology developments in power generation in response to environmental challenges. *Prog Energy Combust Sci* 2000;26(4):301–27. <http://www.sciencedirect.com/science/article/pii/S036012850000071>. [https://doi.org/10.1016/S0360-1285\(00\)00071-1](https://doi.org/10.1016/S0360-1285(00)00071-1).
- [3] Brendeng E, Hetland J. State of the art in liquefaction technologies for natural gas. In: J. Hetland T, Gochitashvili, eds. *Security of natural gas supply through transit countries*. NATO Science Series II: mathematics, physics and chemistry. vol. 149. Springer; 2004. p. 75–102. https://doi.org/10.1007/1-4020-2078-3_5.
- [4] Berstad D, Nekså P, Anantharaman R. Low-temperature CO₂ removal from natural gas. *Energy Procedia* 2012;26:41–8. 2nd Trondheim Gas Technology Conference. <http://www.sciencedirect.com/science/article/pii/S187661021201048X>. <https://doi.org/10.1016/j.egypro.2012.06.008>.
- [5] Aspelund A, Molnvik M, Koeijer GD. Ship transport of CO₂. *Chem Eng Res Des* 2006;84(9):847–55. <http://www.sciencedirect.com/science/article/pii/S0263876206729665>. <https://doi.org/10.1205/cherd.5147>.
- [6] Weisensee PB, Neelakantan NK, Suslick KS, Jacobi AM, King WP. Impact of air and water vapor environments on the hydrophobicity of surfaces. *J Colloid Interface Sci* 2015;453:177–85. <http://www.sciencedirect.com/science/article/pii/S0021979715004373>. <https://doi.org/10.1016/j.jcis.2015.04.060>.
- [7] Ma X, Rose JW, Xu D, Lin J, Wang B. Advances in dropwise condensation heat transfer: Chinese research. *Chem Eng J* 2000;78(2–3):87–93. <http://www.sciencedirect.com/science/article/pii/S1385894700001558>. [https://doi.org/10.1016/S1385-8947\(00\)00155-8](https://doi.org/10.1016/S1385-8947(00)00155-8).
- [8] Sikarwar BS, Battoo NK, Khandekar S, Muralidhar K. Dropwise condensation underneath chemically textured surfaces: simulation and experiments. *J Heat Trans* 2010;133(2):021501–021501. <https://doi.org/10.1115/1.4002396>.
- [9] Boreyko JB, Chen CH. Self-propelled dropwise condensate on superhydrophobic surfaces. *Phys Rev Lett* 2009;103(18):184501. <http://link.aps.org/doi/10.1103/PhysRevLett.103.184501>. <https://doi.org/10.1103/PhysRevLett.103.184501>.
- [10] Milonitis A, Bayer IS, Loth E. Recent advances in oil-repellent surfaces. *Int Mater Rev* 2016;61(2):101–26. <https://doi.org/10.1080/09506608.2015.1116492>.
- [11] Rykaczewski K, Paxson AT, Staymates M, Walker ML, Sun X, Anand S, et al. Dropwise condensation of low surface tension fluids on omniphobic surfaces. *Sci Rep* 2014;4: <http://www.nature.com/articles/srep04158>. <https://doi.org/10.1038/srep04158>.
- [12] Hiemenz PC, Rajagopalan R. *Principles of colloid and surface chemistry*. 3rd ed. ed., CRC Press.; 1997.
- [13] Quéré D. Wetting and roughness. *Ann Rev Mater Res* 2008;38(1):71–99. <https://doi.org/10.1146/annurev.matsci.38.060407.132434>.
- [14] Mazumder P, Jiang Y, Baker D, Carrilero A, Tulli D, Infante D, et al. Superomniphobic, transparent, and antireflection surfaces based on hierarchical nanostructures. *Nano Lett* 2014;14(8):4677–81. <https://doi.org/10.1021/nl501767j>.
- [15] Dorrer C, Rühle J. Some thoughts on superhydrophobic wetting. *Soft Matter* 2008;5(1):51–61. <http://pubs.rsc.org/en/content/articlelanding/2009/sm/b811945g>. <https://doi.org/10.1039/B811945G>.
- [16] Lo CW, Wang CC, Lu MC. Scale effect on dropwise condensation on superhydrophobic surfaces. *ACS Appl Mater Interfaces* 2014;6(16):14353–9. <https://doi.org/10.1021/am503629f>.
- [17] Kavousanakis ME, Chamakos NT, Papathanasiou AG. Connection of intrinsic wettability and surface topography with the apparent wetting behavior and adhesion properties. *J Phys Chem C* 2015;119(27):15056–66. <https://doi.org/10.1021/acs.jpcc.5b00718>.
- [18] Sarkar A, Kietzig AM. Design of a robust superhydrophobic surface: thermodynamic and kinetic analysis. *Soft Matter* 2015;11(10):1998–2007. <http://pubs.rsc.org/en/content/articlelanding/2015/sm/c4sm02787f>. <https://doi.org/10.1039/C4SM02787F>.
- [19] Sarkar A, Kietzig AM. General equation of wettability: a tool to calculate the contact angle for a rough surface. *Chem Phys Lett* 2013;574:106–11. <http://www.sciencedirect.com/science/article/pii/S0009261413005678>. <https://doi.org/10.1016/j.cplett.2013.04.055>.
- [20] Zheng QS, Yu Y, Zhao ZH. Effects of hydraulic pressure on the stability and transition of wetting modes of superhydrophobic surfaces. *Langmuir* 2005;21(26):12207–12. <https://doi.org/10.1021/la052054y>.
- [21] Drelich J, Miller JD, Good RJ. The effect of drop (bubble) size on advancing and receding contact angles for heterogeneous and rough solid surfaces as observed with sessile-drop and captive-bubble techniques. *J Colloid Interface Sci* 1996;179(1):37–50. <http://linkinghub.elsevier.com/retrieve/pii/S0021979796901861>. <https://doi.org/10.1006/jcis.1996.0186>.
- [22] Lloyd BP, Bartlett PN, Wood RJK. Wetting of surfaces made of hydrophobic cavities. *Langmuir* 2015;31(34):9325–30. <https://doi.org/10.1021/acs.langmuir.5b02107>.
- [23] Haimov B, Pechook S, TERNYAK O, Pokroy B. Shape of water-air interface beneath a drop on a superhydrophobic surface revealed: constant curvature that approaches zero. *J Phys Chem C* 2013;117(13):6658–63. <https://doi.org/10.1021/jp312650f>.
- [24] Nosonovsky M, Bhushan B. Superhydrophobic surfaces and emerging applications: non-adhesion, energy, green engineering. *Curr Opin Colloid Interface Sci* 2009;14(4):270–80. <http://www.sciencedirect.com/science/article/pii/S1539029409000399>. <https://doi.org/10.1016/j.cocis.2009.05.004>.
- [25] Hensel R, Finn A, Helbig R, Killge S, Braun HG, Werner C. In situ experiments to reveal the role of surface feature sidewalls in the Cassie-Wenzel transition. *Langmuir* 2014;30(50):15162–70. <https://doi.org/10.1021/la503601u>.
- [26] Enright R, Miljkovic N, Al-Obeidi A, Thompson CV, Wang EN. Condensation on superhydrophobic surfaces: the role of local energy barriers and structure length scale. *Langmuir* 2012;28(40):14424–32. <https://doi.org/10.1021/la302599n>.
- [27] Lo CW, Wang CC, Lu MingChang. Spatial control of heterogeneous nucleation on the superhydrophobic nanowire array. *Adv Funct Mater* 2014;24(9):1211–7. <http://onlinelibrary.wiley.com/doi/10.1002/adfm.201301984/abstract>. <https://doi.org/10.1002/adfm.201301984>.
- [28] Nosonovsky M, Bhushan B. Biomimetic superhydrophobic surfaces: multiscale approach. *Nano Lett* 2007;7(9):2633–7. <https://doi.org/10.1021/nl071023f>.
- [29] Ramchandra Narhe. Water condensation on ultrahydrophobic flexible micro pillar surface. *Europhys Lett* 2016;114(3):36002. <http://stacks.iop.org/0295-5075/114/i=3/a=36002>. <https://doi.org/10.1209/0295-5075/114/36002>.
- [30] Zhu J, Luo Y, Tian J, Li J, Gao X. Clustered ribbed-nanoneedle structured copper surfaces with high-efficiency dropwise condensation heat transfer performance. *ACS Appl Mater Interfaces* 2015;7(20):10660–5. <https://doi.org/10.1021/acsami.5b02376>.
- [31] He Z, He J, Zhang Z. Selective growth of metallic nanostructures on microstructured copper substrate in solution. *CrystEngComm* 2015;17:7262–9. <https://doi.org/10.1039/c5ce01093d>.
- [32] Anderson DM, Gupta MK, Voevodin AA, Hunter CN, Putnam SA, Tsukruk VV, et al. Using amphiphilic nanostructures to enable long-range ensemble coalescence and surface rejuvenation in dropwise condensation. *ACS Nano* 2012;6(4):3262–8. <https://doi.org/10.1021/nn300183d>.
- [33] Chen X, Wu J, Ma R, Hua M, Koratkar N, Yao S, et al. Nanogrooved micropillar architectures for continuous dropwise condensation. *Adv Funct Mater* 2011;21(24):4617–23. <http://onlinelibrary.wiley.com/doi/10.1002/adfm.201101302/abstract>. <https://doi.org/10.1002/adfm.201101302>.
- [34] Miljkovic N, Enright R, Nam Y, Lopez K, Dou N, Sack J, et al. Jumping-droplet-enhanced condensation on scalable superhydrophobic nanostructured surfaces. *Nano Lett* 2013;13(1):179–87. <https://doi.org/10.1021/nl303835d>.
- [35] Kim H, Nam Y. Condensation behaviors and resulting heat transfer performance of nano-engineered copper surfaces. *Int J Heat Mass Trans* 2016;93:286–92. <http://www.sciencedirect.com/science/article/pii/S0017931015300351>. <https://doi.org/10.1016/j.jheatmasstransfer.2015.09.079>.
- [36] Enright R, Miljkovic N, Sprittles J, Nolan K, Mitchell R, Wang EN. How coalescing droplets jump. *ACS Nano* 2014;8(10):10352–62. <https://doi.org/10.1021/nn503643m>.
- [37] Miljkovic N, Preston DJ, Enright R, Wang EN. Electric-field-enhanced condensation on superhydrophobic nanostructured surfaces. *ACS Nano* 2013;7(12):11043–54. <http://pubs.acs.org/doi/abs/10.1021/nn404707j>. <https://doi.org/10.1021/nn404707j>.
- [38] Torresin D, Tiwari MK, Del Col D, Poulikakos D. Flow condensation on copper-based nanotextured superhydrophobic surfaces. *Langmuir* 2013;29(2):840–8. <https://doi.org/10.1021/la304389s>.
- [39] He Z, Zhang Z, He J, Cuo/Cu based superhydrophobic and self-cleaning surfaces. *Scr. Mater.* 2016;118:60–4. <http://www.sciencedirect.com/science/article/pii/S1359646216300884>. <https://doi.org/10.1016/j.scriptamat.2016.03.015>.
- [40] Wong TS, Kang SH, Tang SKY, Smythe EJ, Hatton BD, Grinthal A, et al. Bioinspired self-repairing slippery surfaces with pressure-stable omniphobicity. *Nature* 2011;477(7365):443–7. <http://www.nature.com/nature/journal/v477/n7365/full/nature10447.html>. <https://doi.org/10.1038/nature10447>.
- [41] Kajiya T, Schellenberger F, Papadopoulos P, Vollmer D, Butt HJ. 3D imaging of water-drop condensation on hydrophobic and hydrophilic lubricant-impregnated surfaces. *Sci Rep* 2016;6:23687. <http://www.nature.com/articles/srep23687>. <https://doi.org/10.1038/srep23687>.
- [42] Chen K, Wu Y, Zhou S, Wu L. Recent development of durable and self-healing surfaces with special wettability. *Macromol Rapid Commun* 2016;37(6):463–85. <http://onlinelibrary.wiley.com/doi/10.1002/marc.201500591/abstract>. <https://doi.org/10.1002/marc.201500591>.
- [43] Dai X, Stogin BB, Yang S, Wong TS. Slippery Wenzel state. *ACS Nano* 2015;9(9):9260–7. <https://doi.org/10.1021/acsnano.5b04151>.
- [44] Xiao R, Miljkovic N, Enright R, Wang EN. Immersion condensation on oil-infused heterogeneous surfaces for enhanced heat transfer. *Sci Rep* 2013;3: <http://www.nature.com/articles/srep01988>. <https://doi.org/10.1038/srep01988>.
- [45] Preston DJ, Song Y, Lu Z, Antao DS, Wang EN. Design of lubricant infused surfaces. *ACS Appl Mater Interfaces* 2017;9(48):42383–92. <https://doi.org/10.1021/acsami.7b14311>.
- [46] Anand S, Paxson AT, Dhiman R, Smith JD, Varanasi KK. Enhanced condensation on lubricant-impregnated nanotextured surfaces. *ACS Nano* 2012;6(11):10122–9. <https://doi.org/10.1021/nl303867y>.
- [47] Weisensee PB, Wang Y, Hongliang Q, Schultz D, King WP, Miljkovic N. Condensate droplet size distribution on lubricant-infused surfaces. *Int J Heat Mass Trans* 2017;109:187–99. <http://www.sciencedirect.com/science/article/pii/S0017931016334925>. <https://doi.org/10.1016/j.jheatmasstransfer.2017.01.119>.
- [48] Kim S, Kim KJ. Dropwise condensation modeling suitable for superhydrophobic surfaces. *J Heat Trans* 2011;133: 081502-1 – 081502-8. <http://heattransfer.asmedigitalcollection.asme.org/article.aspx?articleid=1449979>. <https://doi.org/10.1115/1.4003742>.
- [49] Miljkovic N, Enright R, Wang EN. Effect of droplet morphology on growth dynamics and heat transfer during condensation on superhydrophobic nanostructured surfaces. *ACS Nano* 2012;6(2):1776–85. <http://pubs.acs.org/doi/abs/10.1021/nn205052a>. <https://doi.org/10.1021/nn205052a>.
- [50] Ghosh A, Beaini S, Zhang BJ, Ganguly R, Megaridis CM. Enhancing dropwise condensation through bioinspired wettability patterning. *Langmuir* 2014;30(43):13103–15. <https://doi.org/10.1021/la5028866>.

- [51] Mahapatra PS, Ghosh A, Ganguly R, Megaridis CM. Key design and operating parameters for enhancing dropwise condensation through wettability patterning. *Int J Heat Mass Trans* 2016;92:877–83. <http://www.sciencedirect.com/science/article/pii/S0017931015307158>. <https://doi.org/10.1016/j.ijheatmasstransfer.2015.08.106>.
- [52] Tuteja A, Choi W, Ma M, Mabry JM, Mazzella SA, Rutledge GC, et al. Designing superoleophobic surfaces. *Science* 2007;318(5856):1618–22. <http://science.sciencemag.org/content/318/5856/1618>. <https://doi.org/10.1126/science.1148326>.
- [53] Wu T, Suzuki Y. Design, microfabrication and evaluation of robust high-performance superomniphobic surfaces. *Sensors Actuators B Chem* 2011;156(1):401–9. <http://www.sciencedirect.com/science/article/pii/S0925400511003625>. <https://doi.org/10.1016/j.snb.2011.04.065>.
- [54] Extrand CW. Model for contact angles and hysteresis on rough and ultraphobic surfaces. *Langmuir* 2002;18(21):7991–9. <https://doi.org/10.1021/la025769z>.
- [55] Choi W, Tuteja A, Mabry JM, Cohen RE, McKinley GH. A modified Cassie–Baxter relationship to explain contact angle hysteresis and anisotropy on non-wetting textured surfaces. *J Colloid Interface Sci* 2009;339(1):208–16. <http://www.sciencedirect.com/science/article/pii/S0021979709009576>. <https://doi.org/10.1016/j.jcis.2009.07.027>.
- [56] Deng X, Mammen L, Butt HJ, Vollmer D. Candle soot as a template for a transparent robust superamphiphobic coating. *Science* 2012;335(6064):67–70. <http://science.sciencemag.org/content/335/6064/67>. <https://doi.org/10.1126/science.1207115>.
- [57] Kota AK, Kwon G, Tuteja A. The design and applications of superomniphobic surfaces. *NPG Asia Mater* 2014;6(7):e109. <http://www.nature.com/am/journal/v6/n7/full/am201434a.html>. <https://doi.org/10.1038/am.2014.34>.
- [58] Tuteja A, Choi W, Mabry JM, McKinley GH, Cohen RE. Robust omniphobic surfaces. *Proc Natl Acad Sci* 2008;105(47):18200–5. <http://www.pnas.org/content/105/47/18200.full.pdf>. <https://doi.org/10.1073/pnas.0804872105>.
- [59] Quinn EL. The surface tension of liquid carbon dioxide. *J Am Chem Soc* 1927;49(11):2704–11. <https://doi.org/10.1021/ja01410a006>.
- [60] Fronk BM, Garimella S. Condensation of carbon dioxide in microchannels. *Int J Heat Mass Trans* 2016;100:150–64. <http://www.sciencedirect.com/science/article/pii/S0017931015314162>. <https://doi.org/10.1016/j.ijheatmasstransfer.2016.03.083>.
- [61] Rolo LI, Caco AI, Queimada AJ, Marrucho IM, Coutinho JAP. Surface tension of heptane, decane, hexadecane, eicosane, and some of their binary mixtures. *Journal of Chemical & Engineering Data* 2002;47(6):1442–5. <https://doi.org/10.1021/je025536+>.
- [62] Giner B, Villares A, Martin S, Artigas H, Lafuente C. Study of the temperature dependence of surface tensions of some alkanol + hexane mixtures. *J Chem Eng Data* 2007;52(5):1904–7. <https://doi.org/10.1021/je700215z>.
- [63] Vargaftik NB, Volkov BN, Voljak LD. International tables of the surface tension of water. *J Phys Chemical Ref Data* 1983;12(3):817–20. <https://doi.org/10.1063/1.555688>.
- [64] Liu T, Kim CJ. Turning a surface superrepellent even to completely wetting liquids. *Science* 2014;346(6213):1096–100. [arXiv:http://science.sciencemag.org/content/346/6213/1096.full.pdf](http://science.sciencemag.org/content/346/6213/1096.full.pdf). <http://science.sciencemag.org/content/346/6213/1096>. <https://doi.org/10.1126/science.1254787>.
- [65] Wang N, Xiong D, Pan S, Wang K, Shi Y, Deng Y. Robust superhydrophobic coating and the anti-icing properties of its lubricants-infused-composite surface under condensing condition. *New J Chem* 2017;41:1846–53. <https://doi.org/10.1039/C6NJ02824A>.
- [66] Lu Y, He G, Carmalt CJ, Parkin IP. Synthesis and characterization of omniphobic surfaces with thermal, mechanical and chemical stability. *RSC Adv* 2016;6:106491–9. <https://doi.org/10.1039/C6RA20392B>.

A.2 Paper II

Heat transfer characteristics of CO₂ condensation on common heat exchanger materials: method development and experimental results

Ingrid Snustad, Åsmund Ervik, Anders Austegard, Amy Brunsvold, Jianying He and Zhiliang Zhang.

Experimental Thermal and Fluid Science. **129**, 110440 (2021)



Contents lists available at ScienceDirect

Experimental Thermal and Fluid Science

journal homepage: www.elsevier.com/locate/etfsHeat transfer characteristics of CO₂ condensation on common heat exchanger materials: Method development and experimental resultsIngrid Snustad^{a,*}, Åsmund Ervik^b, Anders Austegard^b, Amy Brunsvold^b, Jianying He^a, Zhiliang Zhang^a^a Faculty of Engineering, Department of Structural Engineering, Norwegian University of Science and Technology, Richard Birkelands vei 1A, 7491 Trondheim, Norway^b SINTEF Energy Research, Sem Sælands vei, 117034 Trondheim, Norway

ARTICLE INFO

Keywords:

Condensation heat transfer
 Roughness dependent heat transfer
 CO₂ liquefaction
 Surface roughness
 Nusselt model

ABSTRACT

Understanding condensation of CO₂ is essential for e.g. designing compact heat exchangers or processes involved in Carbon Capture and Storage. However, a consistent experimental campaign for condensation of CO₂ on common materials is lacking. In this work, we present an experimental method and an associated laboratory setup for measuring the heat transfer properties of CO₂ condensation on materials commonly used in heat exchangers for the liquefaction of CO₂. We have investigated the heat transfer during CO₂ condensation on copper, aluminum, stainless steel (316) to reveal the heat transfer dependency on surface properties. The experiments are conducted at three saturation pressures, 10, 15, and 20 bar and at substrate subcooling between 0 and 5K. The results show that the heat transfer coefficients decrease with increasing surface subcooling. It was also found that increasing the saturation pressure increases the heat transfer coefficient. The results indicate that surface roughness and surface energy affect the condensation heat transfer coefficient, and an increased roughness results in reduced heat transfer coefficients. The highest heat transfer coefficient is found for condensation on copper, for which the lowest surface roughness has been measured.

1. Introduction

Condensation of CO₂ occurs in several stages of industrial processes. The need for eliminating fluorine based refrigerants due to their environmental impact has, for example, opened up for CO₂ as an alternative cooling fluid in heat exchangers. The global warming potential of CO₂ is about three orders of magnitude lower than for the traditional refrigerants [1]. CO₂ has a high triple point pressure and low critical pressure, which makes it suitable for use in cooling systems. Another example is the use of CO₂ as a refrigerant in compact heat exchangers, such as in motor vehicle air-conditioning [2]. Heat exchangers with CO₂ as the refrigerant or designed for liquefaction of CO₂ are commonly made of e.g. copper (Cu), aluminum (Al) or stainless steel (steel) [2–4].

CO₂ condensation is also a pre-process for CO₂ transport during Carbon Capture and Storage (CCS). CO₂ is emitted on a large scale, and in some industries, such as cement and aluminum production, CCS is the only solution for mitigating the emissions [5]. CO₂ is mainly transported via pipeline or ship. Cost assessments of CO₂ transportation show that for long distances and/or small amounts, ship transport is the preferred

solution over pipeline. In this case, the CO₂ will be transported in the liquefied state at about -55 °C and 5–10 bar [6–10], but other options are being investigated. Reducing the energy demand of the liquefaction process will play a key role in reducing costs of ship transportation. As a result, a thorough understanding of every aspect regarding CO₂ condensation is necessary for proper process design and ultimately for reducing energy needs and costs for CO₂ condensation.

Previous studies on CO₂ condensation have focused on the flow condensation heat transfer coefficient (HTC) in various geometries, especially tubes and channels with varying diameter, from micro to macro scale [11–15]. The heat transfer properties are, in these cases, particularly affected by the flow pattern and the surface roughness internally in the channels. The well known and widely used Nusselt model for filmwise condensation on flat surfaces [16,17] is an idealized analytical model that does not include surface roughness or other substrate specific properties. For dropwise condensation heat transfer a low thermal conductivity increases the constriction resistance, thereby reducing the HTC [18]. For filmwise condensation, such material specific properties will not influence the condensation heat transfer

* Corresponding author.

E-mail address: ingrid.snustad@ntnu.no (I. Snustad).<https://doi.org/10.1016/j.expthermflusci.2021.110440>

Received 10 December 2020; Received in revised form 15 April 2021; Accepted 13 May 2021

Available online 1 June 2021

0894-1777/© 2021 The Author(s). Published by Elsevier Inc. This is an open access article under the CC BY license (<http://creativecommons.org/licenses/by/4.0/>).

resistance. Surface properties, such as roughness and surface energy, will, however, influence the heat transfer. In response to the absent studies on CO₂ condensation heat transfer on various vertical surfaces, we here report a comparison of the heat transfer performance of Al, Cu, and steel under the condensation of CO₂.

As stated above, surface roughness may play an important role in the condensation process [19], and controversial results about the effect of roughness on heat transfer have been reported. For example both Soontarapiromsook et al. [20] and Nilpueng et al. [21] observed that condensation HTC increases with surface roughness, while Yun et al. [22] came to the opposite conclusion. For this reason, we have investigated the influence of surface roughness on condensation. Modification of the surface caused by the condensation itself, may also affect the heat transfer. In particular, CO₂ adsorption on Cu has been studied in the literature, with focus on Cu as a catalyst in reactions involving CO₂, e.g. methanol synthesis [23]. Muttaqien et al. [24] concluded that CO₂ in the gaseous state does not dissociate on clean Cu at low temperatures. CO₂ in the liquid state has, however, not been studied, and the interaction between liquid CO₂ and Cu is not understood. The formation of liquid CO₂ on Cu and the effect on the HTC will be briefly discussed in this work.

Experimentally determining the HTC in CO₂ condensation is challenging, and no previous study has reported the condensation HTC of CO₂ on flat surfaces. In this study, for the first time, an experimental method that can accurately measure the static condensation HTC of CO₂ is developed. The experimental setup is built for a straightforward alternation between substrates, and systematic studies of the heat transfer on samples with a variety of surface properties and surface modifications can be performed. With the established method, the heat transfer during condensation of CO₂ on the aforementioned materials, Cu, Al, and steel, have been investigated. The condensation is studied at saturation pressures of 10 bar, 15 bar and 20 bar and surface subcooling between 0k and 5k. The surface subcooling is defined as the difference between the saturation temperature, T_{sat} , and the surface temperature, T_{surf} .

In the following, the experimental method developed especially for condensing CO₂, including the detailed setup, an overview of the piping and instrumentation diagram (P&ID), the data acquisition and reduction rules adopted, is presented first. The theoretical principles governing the development of the experimental method are documented in the Supplementary Information. In Section 3 an overall description of the three investigated materials is reported. In Section 4, the experimental results, in particular, the surface roughness dependence of the measured HTC and the unique CO₂ adsorption behavior on Cu, are elaborated. Some concluding remarks as well as topics suggested for future research to improve the experimental method and understanding of the heat transfer in CO₂ condensation are presented in Section 5.

2. Methodology

The experimental method for determining the heat transfer properties of various materials developed in this work, will be described in this section. The method is based on the theory of one-dimensional heat transfer through a Cu cylinder (Fourier theory) [25,26]. The methodology is outlined through a description of the experimental setup and an explanation of the data acquisition and reduction through a presentation of the necessary equations.

2.1. The experimental setup

The specially designed parts of the experimental setup are the pressure chamber, the cooling element and a gas delivery system for both liquid CO₂ for cooling and clean gaseous CO₂ to be condensed. In addition, the setup is equipped with a high speed camera (Phantom 9.1) for observing the point of condensation and to what extent the condensation

has developed. The design of the setup, including all tubes, pipes, valves and larger components, is presented as a P&ID, shown in Fig. 1. The descriptions of the components in the following sections should be referred to the P&ID.

2.1.1. The pressure chamber and gas delivery system

Condensation of CO₂ will never occur in an atmospheric environment. The thermodynamic triple point of CO₂ is at 5.2 bar and -56.6 °C, requiring a pressurized chamber in which the vapor will condense. The pressure level for ship transport of CO₂ will be in the same order of magnitude as the triple point [7], and the pressure chamber is therefore designed and fabricated for pressures up to 20 bar. The chamber is a stainless steel pipe (diameter = 20cm, length = 30cm) with 10 sealed holes in the pipe wall. These are included for gas inlet and outlet, cooling fluid inlet and outlet, pressure sensors, thermal measurements and a custom made electrical cable feedthrough. Swagelok couplings are used for ensuring pressure-tight inlets and outlets. The electrical cable feedthrough is a 16 mm OD tube in which wires for four T-type thermocouples (TCs) and LED lights is embedded in two component epoxy. The epoxy was fed into the tube at elevated temperature in two steps. The feedthrough was tested at 25 bar helium for which no detectable leakage was present. If additional light sources or other electrical cables are needed, an alternate feedthrough could easily be replaced with the current version. The chamber and the high speed camera are shown in Fig. 2.

The lid in the front, facing the camera, is a double flange with a sight glass embedded in the center. On the inside of the sight glass, a strip of LED light is attached around the circumference, see Fig. 3. As a result, the surface to be examined is lit from all sides during experiments.

Condensation of humid air and ice formation onto the sight glass will disturb the imaging of the condensation process. Therefore, it is necessary to reduce the dew point below the experimental temperature. For this reason, the experiments are performed at a surrounding temperature of around -10 °C and in a dry environment. The temperature is provided by lowering the pressure chamber and the camera into a freezer (Scandomestic SB 650). A hose with pressurized and dried air is inserted into the freezer through a drilled hole. The air will provide the necessary low humidity environment in the freezer. The air is dried with a Kaeser DC 4.2 air dryer. At -10 °C and 5% relative humidity, which are typical parameters of the setup, the dew point is -42 °C. The temperature inside the pressure chamber is set by the freezer temperature, so the temperature on the outside of the sight glass will be well above the dew point temperature, as required, and the see glass will be free of ice.

During operation, the chamber is filled with pressurized, gaseous CO₂. A gas delivery system consisting of a gas cylinder (Scientific CO₂, 6.0 purity, AGA) and a differential pressure controller (Alicat PCD) fills the chamber to the saturation pressure determined by the operator. According to previous reports, non-condensable gases and humidity will alter the heat transfer characteristics of the condensation [27–29]. The chamber is therefore vacuumised and flushed with CO₂ in three cycles before filling to the desired pressure. A vacuum pump is used to empty the chamber down to < 0.1mbar, between each flushing of 1 bar CO₂.

2.1.2. The cooling element

If condensation is to occur on the investigated surfaces, they must be cooled below the saturation temperature of the vapor. A stable temperature down to -55 °C is the target, for which condensation of CO₂ will occur if the pressure in the vapor is above 5.6 bar. In order to achieve the low temperatures, a small heat exchanger is designed and fabricated for cooling the investigated surfaces with a high degree of temperature stability, uniformity and control. The cooling element consists of a rectangular block of Cu where the bottom and the sides are insulated with a layer of insulation foam. Within the block there are narrow parallel channels, see Fig. 4, in which the refrigerant will flow. A CO₂ gas cylinder with a liquid riser is coupled to the cooling circuit. Initially, pressurized gaseous CO₂ flows in the circuit, followed by an increase in

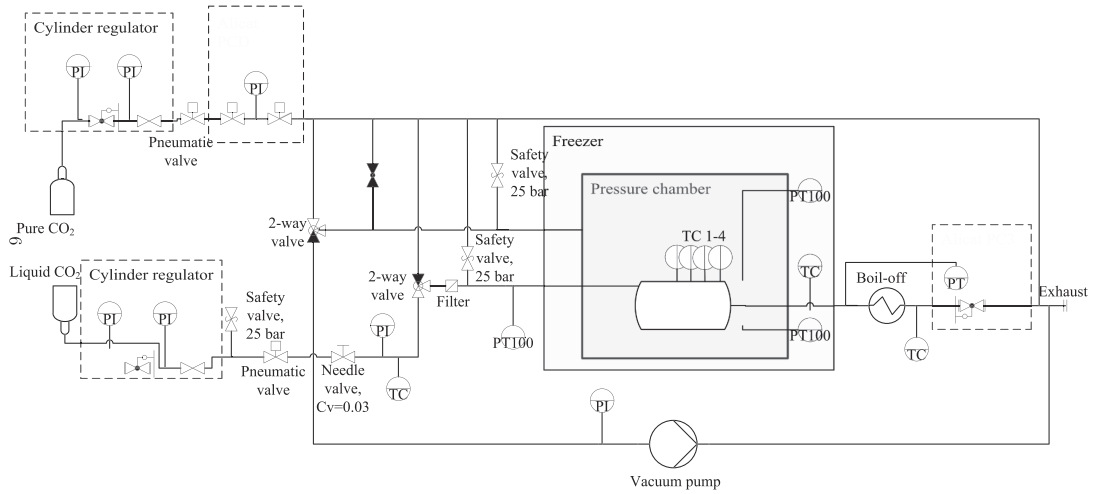


Fig. 1. Piping and Instrumentation Diagram of the experimental setup. Pure CO₂ flows into the pressure chamber with the Alicat PCD as the pressure controller. Liquid CO₂ is fed to the cooling element with the Alicat PC3 as a back pressure regulator, accurately controlling the pressure which results in a uniform temperature in the cooling element.

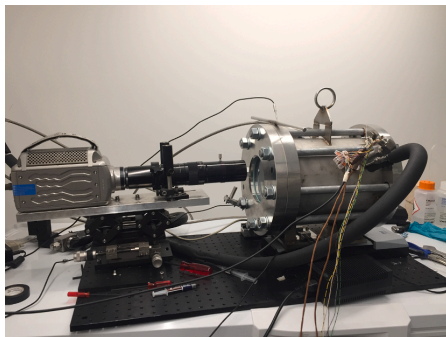


Fig. 2. The pressure chamber consists of a steel cylinder (20cm diameter) with two flanges as lids. 8 bolts keep the flanges together and two O-rings embedded in the flanges seal the chamber against leakage. A high-speed camera (Phantom 9.1) is placed in front of the chamber to monitor condensation through the sight-glass.

pressure and mass flow until they are high enough to realize two-phase flow through the heat exchanger. The pressure is set to the saturation pressure corresponding to the desired temperature, and the mass flow is adjusted with a needle valve until two-phase is obtained. The saturation pressure is varied between 6 and 20 bar, in the current design. The pressure in the circuit is controlled by a back pressure regulator (Alicat PC3). We know that two-phase flow is obtained when a TC embedded in the flow upstream the cooling element (marked TC downstream the Needle valve in the P&ID, Fig. 1) suddenly drops to the desired cooling temperature. When two-phase flow is obtained in the entire circuit, the desired temperature is observed in the TC that is embedded in the tube downstream the cooling element. Two-phase CO₂ will flow and convective boiling will occur in the channels of the cooling element. By adjusting the volumetric flow of the liquid CO₂ entering the heat exchanger, and accurately controlling the pressure drop through the cooling element, it is possible to ensure that there is two-phase flow at the outlet of the heat exchanger, and hence, that the temperature across the cooling element surface is uniform.

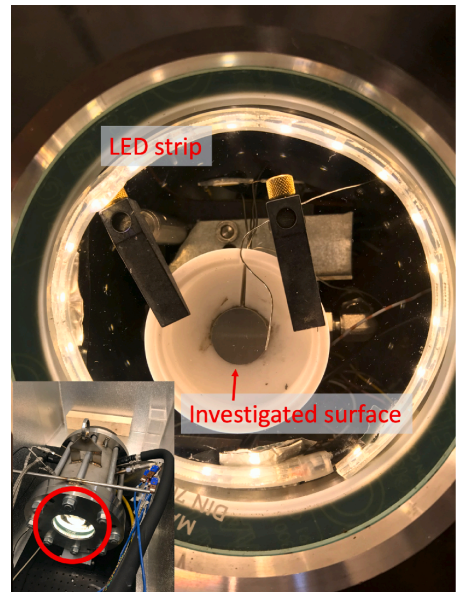


Fig. 3. View of the investigated surface through the sight glass in the lid. The red ring in the inset shows where the sight glass is located in the pressure chamber. A strip of LED light is fastened around the inner circumference of the glass and the surface is lit from all sides during experiments.

2.2. Data acquisition and reduction

The pressure and temperature measurements are collected and visualized by a LabVIEW™ program. Through the LabVIEW™ program the user can set the correct temperature of the cooling block, the desired saturation pressure and record the output from the TCs, PT100s and pressure measurements. The measurement data are reduced according to the following calculations.

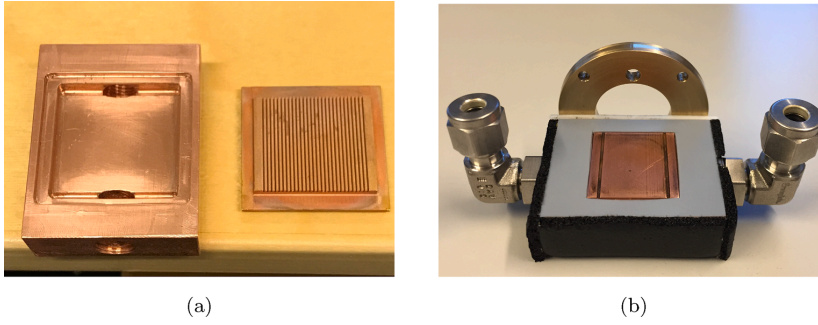


Fig. 4. (a) The interior of the cooling element, which consists of a Cu slab with narrow channels for accurate control of surface temperature. (b) The assembled cooling element with inlet and outlet for two phase flow.

$$q_{tot} = -k\nabla T \tag{1}$$

The total heat flux is calculated with the Fourier heat flux equation in Eq. (1). Here, ∇T is the temperature gradient through the Cu cylinder and k is the thermal conductivity of Cu. The temperature gradient is found by linear regression of the temperatures in the four TCs embedded in the center of the Cu cylinder. The thermocouples are of T-type and are "on site" calibrated in an icebath, i.e. the thermocouples were embedded in the Cu cylinder, and all other connections were as they were in an experiment, see Supplementary Information. Since the temperature profile is linear the gradient becomes $\nabla T = \frac{dT}{dx}$. The linearity of the gradient is confirmed by the detailed calculations included in the Supplementary Information.

The condensation heat flux is calculated by subtracting the heat flux for cooling the gas in the pressure chamber, q_{gas} , and the heat that is lost through the Teflon insulation, q_{teflon} , from the total heat flux in Eq. (1), resulting in Eq. (2).

$$q_{cond} = q_{tot} - q_{gas} - q_{teflon} \tag{2}$$

q_{gas} is calculated with Eq. (3). The gas temperature, T_{gas} , has been measured for the three investigated saturation pressures at all levels of subcooling, and an average value of q_{gas} for each pressure is used in the calculation of q_{cond} . Mm and c_p are the molar mass and heat capacity of CO₂ at the gas temperature, while A is the surface area of the investigated sample.

$$q_{gas} = c_p Mm (T_{gas} - T_{sat}) / A \tag{3}$$

$$h_c = \frac{q_{cond}}{T_{sat} - T_{surf}} \tag{4}$$

The condensation HTC, h_c , is defined by Eq. (4). The temperature in the saturated vapor adjacent to the condensate, T_{sat} , is calculated with the Span–Wagner Equation of State [30] (calculated with the NIST Webbook [31]), at the set pressure in the chamber. The surface temperature, T_{surf} , is calculated by the following procedure. First, the surface temperature of the Cu cylinder is extrapolated from the temperature measurement data. Second, using the constant heat flux, the Fourier equation (Eq. (1)) is used to calculate the gradient in the thermal interface material (TIM), which attaches the samples to the cylinder. As a result, the temperature at the interface between the TIM and the investigated material is found. Finally, the heat flux and Fourier equation is used to calculate the temperature gradient in the investigated material, with thermal conductivity, k , for the specific material. The surface temperature is calculated with the gradient in each investigated material. Fig. 5 shows an example of the temperature measurements, the linear regression and the resulting cylinder surface temperature.

The experimental data confirm that the temperature gradient

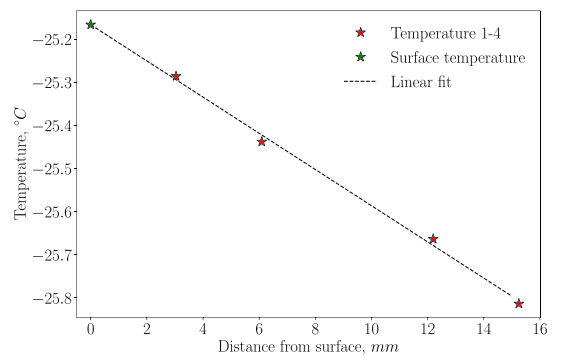


Fig. 5. Average temperatures in the four thermocouples embedded in the Cu cylinder, for one pressure and one subcooling. The linear fit provides the gradient of the temperatures, and hence the total heat flux through the cylinder. The fit also enables the calculation of the surface temperature by extrapolation, shown by the green star.

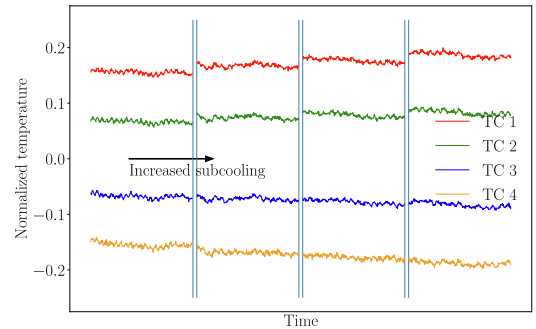


Fig. 6. Experimental measurements of the temperature in the cylinder at the position of the four embedded thermocouples, with TC 1 closest to the cooling element. The difference between TC 1 and TC 4, and hence the temperature gradient, increases for increased subcooling. The average value of the four thermocouples are subtracted in each point in order to visualize the increase of the gradient. The vertical lines divide the measurements into one area for each level of subcooling. Each vertical line represent a small jump in time (time for stable temperatures after changing subcooling).

through the cylinder increases for increasing subcooling of the surface, shown in Fig. 6. The figure includes 300 measurement points per thermocouple per level of subcooling, and four levels of subcooling. The vertical lines marks the transition between two levels of subcooling, i.e. a new temperature setpoint in the cooling element. At each vertical lines there is a time step, with the time it takes for the temperatures to stabilize.

Fig. 7 shows the scattering of the temperature measurements in the four TCs in the cylinder. The data are recorded at three different levels of subcooling (red, green and blue), and at a saturation pressure of 15 bar. The TCs are placed at approximately 3, 6, 12 and 15mm from the cylinder surface. The temperature of the fitted point for the TC at 3mm (denoted T(1) in the Figure) is subtracted from all points for a clearer comparison of the values. Each blob of red, green and blue consists of 300 measurement points and their spread in the vertical direction equals the temperature scattering for each measurement. This experimental scattering is maximum 0.03k.

2.3. Uncertainties

Table 1 presents the values of uncertainty that have been used for estimating the errors in the presented data. An uncertainty analysis has been carried out based on Gaussian error propagation, and the formulas are included in the Supplementary Information. The uncertainty in the thermocouple measurements, $TC1 - TC4$, is estimated from the relative deviation of the icebath calibration (details in Supplementary Information) and the variation in the 300 measurement points taken for each measurement, as shown in Fig. 7. The uncertainty in P_{sat} is given by the specifications of the Alicat PCD pressure sensor, and it is used to calculate the uncertainty in T_{sat} . For T_{surf} , we have estimated the uncertainty based on the uncertainty in the thickness of the thermal interface material, t_{TIM} , and the propagation of the errors in the extrapolation process. The estimated errors in heat flux, E_q , will propagate to the calculated values of HTC as well. However, as the definition of HTC includes $T_{sat} - T_{surf}$ in the denominator, the propagated errors will increase to infinity for small subcooling. The errorbars in HTC are therefore excluded in the results, Fig. 10.

3. Materials

Three materials commonly used in process equipment, especially where condensation occurs, have been investigated. These are Cu, Al, and steel. The substrates were circular discs, 2cm in diameter, which were cut from rolled plates. The thickness of Cu and steel were 0.5mm,

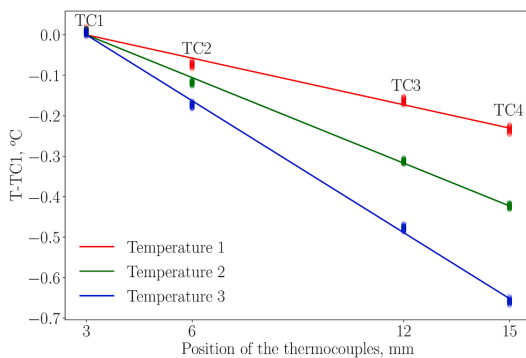


Fig. 7. Three representative temperature measurements in the four thermocouples embedded in the core of the Cu cylinder. The temperature in TC1 is subtracted from each measurement point and the positions of the thermocouples are given relative to the surface of the investigated material. The scattering of the measurements (width of the blobs) are 0.03k.

Table 1

Table with the estimated uncertainties used for calculating the overall uncertainties in heat flux and subcooling.

Parameter	Uncertainty name	Uncertainty value
TC_1, TC_2, TC_3, TC_4	E_T	$\pm 0.0337k$
P_{sat}	n/a	± 0.0875 bar
T_{sat}	$E_{T_{sat}}$	$\pm 0.2k$
t_{TIM}	$E_{t_{TIM}}$	$\pm 0.05mm$
k_{Cu}	$E_{k_{Cu}}$	$\pm 0.013\%$ [32]
k_{mat}	$E_{k_{mat}}$	$\pm 5\%$
$x_4 - x_1 = d_{1-4}$	$E_{d_{14}}$	$\pm 0.04mm$
x_1	E_{x_1}	$E_{d_{14}}/2$

while Al was 0.7mm. The surface roughness has been measured for all surfaces with a Veeco Dektak 150 Profilometer. Ten line scans, each 5µm in length, have been performed for each surface, and the results presented in Table 2 are the average values of the ten scans. The Al surface has the highest roughness, while the Cu surface is least rough, in terms of arithmetic mean average (MA) roughness and root mean square (RMS) roughness. (see Table 3).

The investigated substrates were cleaned with acetone, isopropanol and ethanol, and subsequently dried with pressurized dry air. The substrates were then attached to the Cu cylinder with a TIM (Aldrich Chemistry, Silver Conductive paste 735825). The TIM was applied in a thin uniform layer covering the entire cylinder end surface. The investigated substrate was pressed onto the surface, resulting in that the TIM spread uniformly under the investigated substrate. The thickness of the TIM has been measured to be approximately 0.15mm with an estimated error of $\pm 0.05mm$. The thickness was measured with a caliper by applying a layer of TIM on a detached circular disc with the same application technique. The Cu cylinder was fabricated in a lathe.

4. Results and discussion

4.1. Verification of setup

To ensure that no systematic error appears caused by the attachment of substrates to the Cu cylinder, we have conducted condensation experiments on the cylinder without any attached substrate. In Fig. 8 condensation heat flux obtained on the bare Cu cylinder are plotted together with the heat flux data obtained on the attached Cu substrate. The condensation heat fluxes are well within the experimental uncertainties, and as a result we conclude that the procedure of attaching the samples to the cylinder surface does not affect the heat transfer behavior. In the figure, theoretical heat flux calculated with the Nusselt model is also plotted. We see that the experimental data lies within a 15% deviation from the theoretical values. The deviation from the theoretical values is expected as the Nusselt model is idealized and does not consider surface properties of the material, vapor drag, or non-laminar flow. (see Fig. 9).

Table 2

MA and RMS roughnesses of the investigated surfaces, along with typical values for the surface energies. The surface energy for the aluminum sample is given for Al_2O_3 as an Al surface in atmospheric environment will be oxidized.

Material	MA	RMS	Peak-to-valley	Surface
	Roughness (nm)	Roughness (nm)	Roughness (nm)	Energy (mJ/m^2)
Copper	73.3	93.4	250	1650 [33]
Aluminum	513.1	722.6	2000	169 [34]
Stainless steel (316)	243.5	312.3	1000	53 [35]

Table 3
Relevant thermophysical properties of CO₂ at the two-phase line

	10 bar	15 bar	20 bar
	-40.1 °C	-28.5 °C	-19.5 °C
Liquid density, ρ_l (kgm ⁻³)	1121.8	1074.2	1034.0
Vapor density, ρ_v (kgm ⁻³)	26.2	39.2	52.8
Density difference, $\rho_l - \rho_v$ (kgm ⁻³)	1095.6	1035.0	981.2
Viscosity, μ_l (mpa s)	2.0	1.7	1.4
Latent heat, h_{fg} (kJ kg ⁻¹)	320.8	300.0	281.6
Thermal conductivity, k_l (mWm ⁻¹ K ⁻¹)	159.8	145.4	134.3
Surface tension, λ (mNm ⁻¹)	13.15	10.47	8.48

4.2. Condensation heat transfer on Cu, Al and steel surfaces

The condensation heat flux of CO₂ on Cu, Al, and steel have been measured at 10, 15, and 20 bar while varying the subcooling between 0 and 5k. The condensation heat flux increases for increasing subcooling and increased saturation pressure. The errors in heat flux and subcooling are results of the uncertainty analysis described above and in the Supplementary Information. The condensation HTC for the three saturation pressures are shown in Fig. 10, together with the results of the Nusselt model for CO₂ condensation. For each material and pressure, the condensation HTC approach a constant level for high subcooling. The constant level is reached for lower values of subcooling compared to the Nusselt model. Similar behavior has also been observed for filmwise steam condensation on modified titanium with high surface energy [36]. However, the mechanism of the phenomena is not yet described.

The Nusselt model is an analytical model of filmwise condensation on a vertical wall [16]. The Nusselt model for calculating the HTC, h_{Nu} , is

$$h_{Nu} = \frac{4}{3} \left(\frac{g \rho_l (\rho_l - \rho_v) h'_{fg} k_l^3}{4 \mu_l L (T_{sat} - T_{surf})} \right)^{1/4}, \tag{5}$$

where g is the gravitational acceleration, h'_{fg} is the latent heat modified to compensate for thermal advection effects, following the procedure of Rohsenow [37,17], ρ_l and ρ_v are the liquid and vapor density, respectively, μ_l is the dynamic viscosity of the liquid, and L is the characteristic length of the surface, which in this case is the diameter of the Cu cylinder. Nusselt theory is derived for a rectangular surface, but previous work has shown that the deviation due to a circular surface is negligible [26]. The Nusselt model also gives a value for the condensate film thickness along the height of the surface, Eq. (6), where x is the distance from the top of the surface. The resulting CO₂ film thickness along the substrate is shown in Fig. 11.

$$\delta(x) = \left(\frac{4 \mu_l k_l (T_{sat} - T_{surf}) x}{g \rho_l (\rho_l - \rho_v) h'_{fg}} \right)^{1/4} \tag{6}$$

At the bottom of the surface, and at a saturation pressure of 10 bar and subcooling of 2k, the Nusselt model predicts that the film thickness of CO₂ is 34.1 μm, see Fig. 11. In the figure a representation of the height of the roughness on Al (the roughest surface studied in this work) is shown, and it is clear that the predicted film thickness is thicker than the roughness of all three substrates. At low subcooling, the magnitudes of the film thickness and the roughness become close, and as a consequence it is expected that the experimental data will deviate from the Nusselt model. For very low subcooling, the film will become discontinuous across the surface, resulting in a non-uniform temperature distribution. The deviation between the Nusselt model and the experimental results increases significantly when the subcooling decreases to zero, which supports the claim that the roughness plays an increasingly important role in this case. In the Nusselt model the film thickness uniformly approaches zero for zero subcooling, and the HTC therefore approaches infinity. This is of course unphysical, and in experiments, an infinite HTC will never be found.

The experimental HTC values for subcooling above 1k and at saturation pressures 15 and 20 bar follow the same trend as the Nusselt model. The behavior of the HTC for low subcooling and for 10 bar subcooling is challenging to interpret at this moment and understanding the mechanism governing the condensation in these cases requires additional investigations.

4.3. Pressure dependence of condensation heat transfer

The condensation HTC is a pressure dependent quantity. According to the Nusselt model the HTC decreases with increasing pressure. The pressure dependence of the experimental HTC in this work is found opposite to that given by the Nusselt model, with increasing HTC for increasing pressure, shown in Fig. 13. One reason for this is the questionable validity of the laminar-flow assumption in Nusselt theory. The Nusselt model is only valid for laminar flow, and experiments have shown that for a Reynolds number, Re , above 20, this laminar flow assumption will not hold [38], and the flow will become wavy. The theoretical turning point between laminar and wavy flow for CO₂ at 20 bar will occur at a subcooling of 3.5k, and Re will continue to increase with increasing subcooling. With a wavy flow, the condensation HTC will increase, and the occurrence of wavy flow is therefore assumed to be part of the reason why the condensation HTC increases with pressure, in contrast to what Nusselt theory predicts. Another contribution to the opposite dependence on pressure is that a small error in calculated viscosity or thermal conductivity easily would switch the pressure

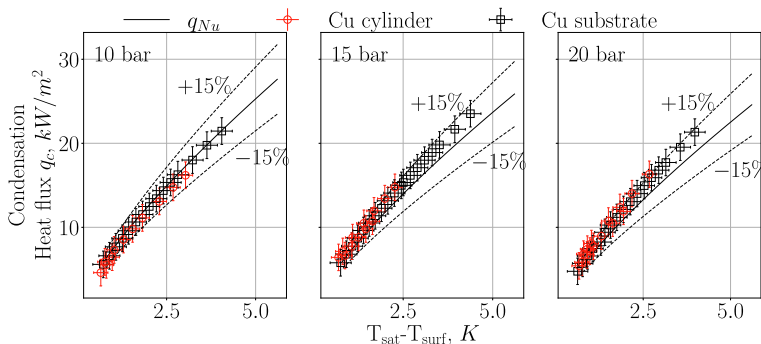


Fig. 8. Theoretical and experimental heat flux data for CO₂ condensation on the bare Cu cylinder and on the Cu substrate while attached to the cylinder with the TIM. All experimental data lies within the values of uncertainty, and within a 15% deviation from the Nusselt model.

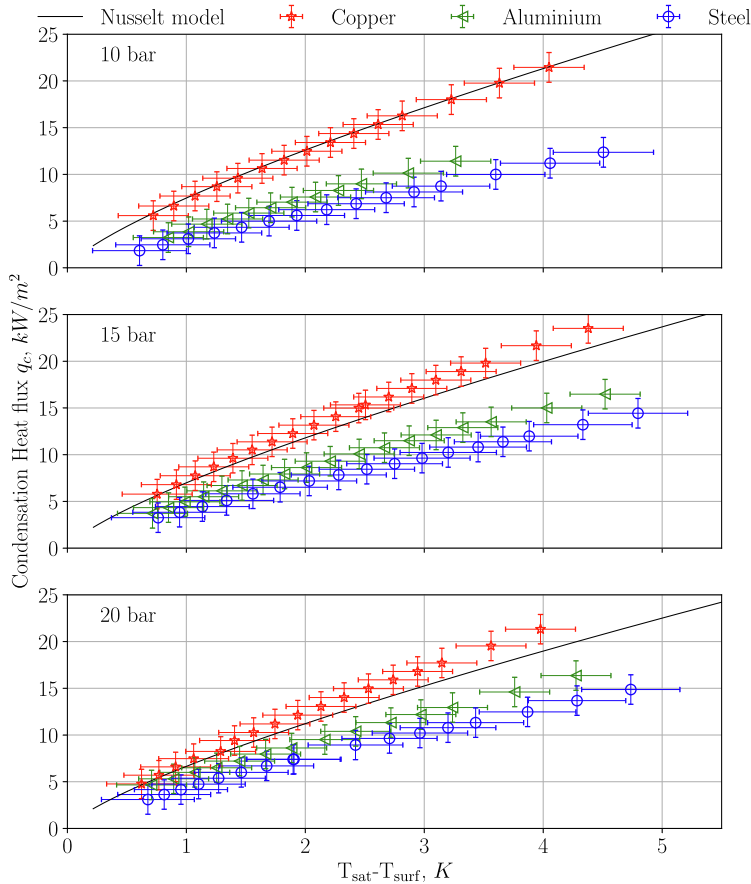


Fig. 9. Condensation heat flux for Cu, Al, and steel at 10 bar, 15 bar and 20 bar saturation pressure. The errorbars are calculated with the Gaussian error propagation shown in Supplementary Information with the uncertainty estimates in Table 1.

dependency also of the Nusselt model. The individual effects of the separate condensate properties on the HTC as modeled by Nusselt is shown in Fig. 12. We have seen that the Nusselt model does not adequately represent the heat transfer during condensation of CO₂ on the investigated samples and that the change in HTC due to pressure is smaller than the deviation between the modeled and the experimental data. The pressure dependence is not linear, and it is similar for the three substrates with a larger increase between 10 and 15 bar compared with 15 and 20 bar. The increase in HTC with pressure indicates that the film thickness is reduced for higher pressures, since the film thickness is inversely proportional to HTC. The reduction in film thickness with increased pressure may be caused by a decreased viscosity and hence a larger downward flow of the liquid due to gravity. Experimental investigation of the actual film thickness is necessary to decipher the behavior and is suggested for further work. The evolution in HTC with pressure indicates that the effects of pressure and roughness are independent.

4.4. Dependence of condenser surface properties

From the results, we see a difference in the heat flux and HTC between the three investigated samples. As stated above, the difference between steel and Al cannot be confirmed as it lies within the estimated

uncertainty. However, the condensation heat transfer on both samples are lower than on the Cu surface. According to the defined boundary condition (uniform surface temperature) the HTC will not depend on the bulk properties of the material such as thermal conductivity. However, the HTC will depend on the surface properties of the investigated material: surface roughness and surface energy.

Surface roughness has been shown to have an effect on the condensation HTC. According to Yun et al. [22], the roughness will cause an increase in the wall shear stress at the liquid-surface interface, which again results in a liquid retention on the surface and a thicker liquid film compared to on a smooth surface. A thicker film has a larger thermal resistance than a thinner film, and the HTC is therefore reduced.

As stated previously, the CO₂ film thickness may approach the same order of magnitude as the surface roughness when the subcooling is low. At a certain point, which is roughness and material dependent, the thermal resistance through the thin CO₂ film and through the roughness peaks will become similar. A simple parametric study shows that this occurs at a CO₂ thickness of 5.7 μm for the steel surface and at 1.95 μm for the Cu surface. Below these thicknesses, the temperature will no longer be uniform in the liquid-solid interface, and the values of HTC are undefined. This is reflected in the experimental data at low subcooling, where we see a large variation in the calculated HTC's.

In Fig. 14 it is shown that the theoretical liquid film thickness is

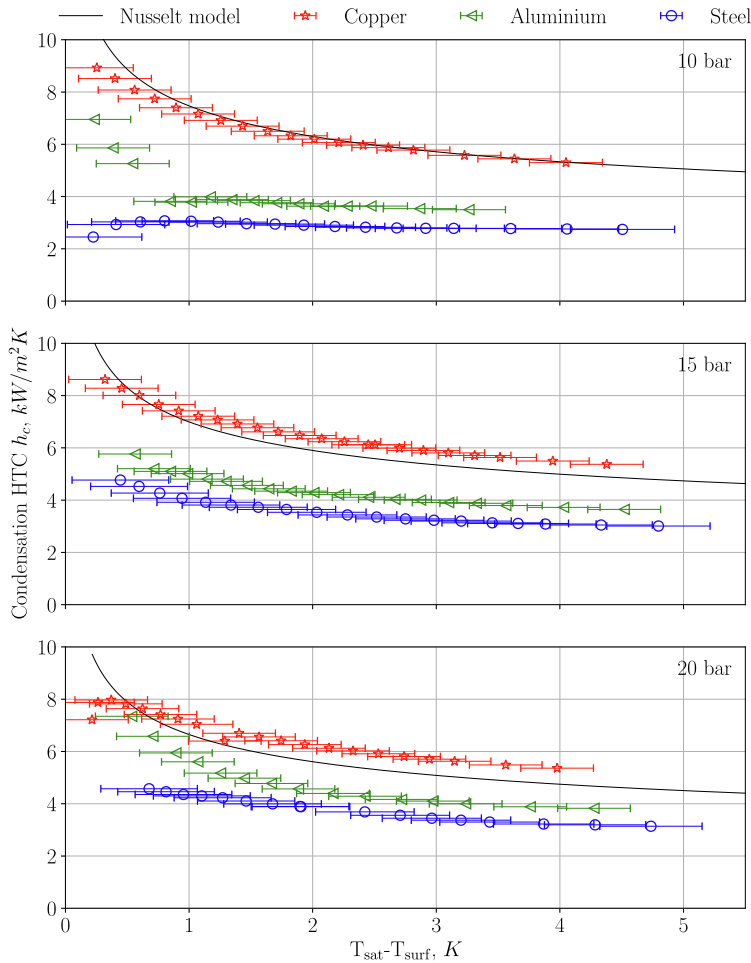


Fig. 10. Condensation HTC for Cu, Al, and steel at 10, 15 and 20 bar saturation pressure, respectively. The Nusselt models for the 15 bar and 20 bar saturation pressure are included for comparison, and a modified Nusselt model is presented.

lower for CO_2 than for water. Here, the Nusselt model is used to calculate the thickness. Assuming that the CO_2 film is thinner than a water film at the same level of surface subcooling, the effect of roughness will be more pronounced for CO_2 than for water, and we can expect larger deviations from the Nusselt model than reported for water.

Surface energy of a solid surface directly relates to the wetting properties of a liquid on the surface. A high surface energy is linked to a fully wetting surface at which a liquid spreads, while on a low surface energy solid, the liquid will form discrete droplets [39]. A material with high surface energy will, hence, adhere more strongly to a liquid than a material with low surface energy. Even though no droplets are observed in this work, it is reasonable to assume that the difference in surface energy between the samples will influence the liquid adhesion, and therefore retention on the surface. The surface energy of the materials in this work, presented in Table 2, are in three different orders of magnitude, with Cu highest and steel lowest. According to theory the Cu will adhere more to CO_2 than Al and steel and a lower HTC is therefore expected on Cu, if surface energy was the only effect. The difference in heat transfer on the three samples is therefore attributed to a combination of surface roughness and surface energy. A low surface roughness

and a high surface energy, which is the case for the Cu sample, could according to the mentioned mechanisms, result in either a higher or lower HTC depending on the relative effect of the surface properties. A quantification of the relative effect will require additional experiments on a larger set of samples with different surface energies and roughnesses to decipher. However, the results indicate that the roughness has the highest impact on the heat transfer and that a thicker liquid film due to roughness induced retention results in a lower HTC on the Al and steel samples.

4.5. CO_2 adsorption on Cu

When conducting the experiments on Cu, we observed that the experimental HTC gradually decreased for consecutive experiments at the same conditions. Fig. 15 shows the results from five repeated experiments on the same Cu sample, conducted at five different days. The difference between the highest and lowest results at subcooling of 3k is about 6kWm^{-2} . An investigation on CO_2 impact on Cu revealed that the Cu surface is altered by CO_2 due to adsorption on the surface. When creating products out of captured CO_2 , or when adsorbing CO_2 from a

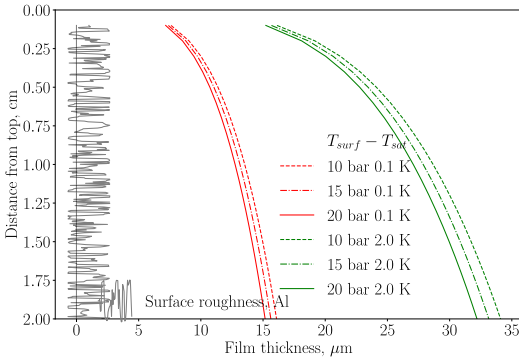


Fig. 11. The film thickness as predicted by the Nusselt model is shown for saturation pressures of 10 bar, 15 bar and 20 bar, and for 0.1k and 2.0k sub-cooling. The magnitude of the roughness on Al (the most rough surface) is represented by a random line with amplitude as the Peak-to-valley roughness = 2μm.

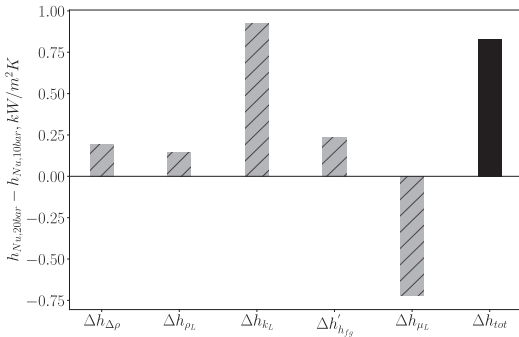


Fig. 12. The individual contributions to the change in condensate properties to the difference in h_{Nu} according to the Nusselt model. The total change in h_{Nu} when the saturation pressure is increased from 10 bar to 20 bar is shown in solid black.

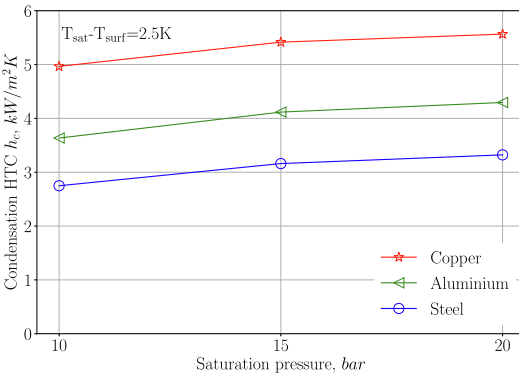


Fig. 13. Condensation HTC as a function of saturation pressure for Cu, Al, and Stainless steel at 2.5k sub-cooling.

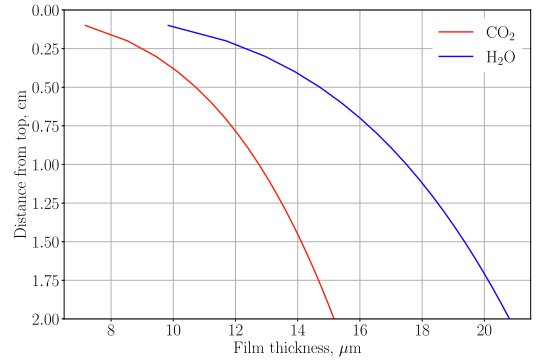


Fig. 14. The film thickness of H₂O and CO₂ on a vertical surface calculated with Nusselt theory (Eq. (6)). The subcooling is 0.1k in both cases. The average difference between the film thicknesses is 4.6μm.

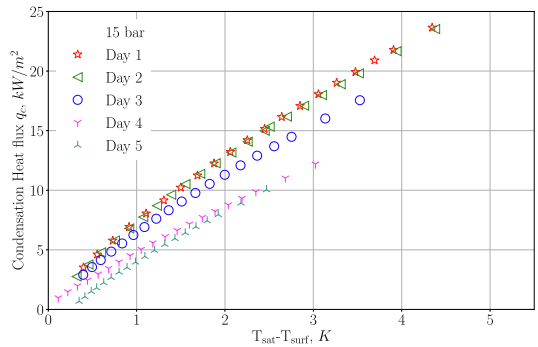


Fig. 15. Condensation heat flux for Cu at 15 bar saturation pressure, recorded at five different days, with equal settings.

gas, Cu is often used as a catalyst for CO₂ dissociation. Hence, adsorption of CO₂ on Cu is a known phenomena, and could therefore be the cause of the decrease in the heat flux results on Cu in the consecutive experiments. Previous studies have concluded that CO₂ adsorption does not occur on undisturbed flat Cu surfaces [40,41,24]. Those studies investigated gaseous CO₂ at low temperatures, and liquid CO₂ adsorption is not mentioned. The results in the present work indicate a surface modification of the Cu after several repetitions of condensation, with the decrease of heat flux. The phenomenon must be investigated further in order to depict the mechanisms and determine the degree to which the HTC is reduced. A study of the chemical composition of the surface and the amount of adsorbed CO₂ would be especially interesting, e.g. by thermal desorption spectroscopy.

5. Conclusion and outlook

In this work, an experimental method to measure the heat transfer during condensation of CO₂ on various materials is developed and validated. The main features of the associated setup are a heat transfer Cu cylinder, a two-phase flow cooling element, providing temperatures down to -55 °C, and a pressure chamber constructed for pressures between 1 and 20 bar. With the experimental method, we have measured the condensation heat transfer of CO₂, and revealed an effect of the condenser surface properties. The condensation process has been investigated at three levels of saturation pressure: 10, 15, and 20 bar. The condensation heat flux and HTC increase with pressure, which is the

opposite to the behavior of the Nusselt model. This could be caused by the properties of CO₂ and especially how the viscosity changes with pressure. The three commonly used process equipment materials, Cu, Al, and Stainless steel (316) have been investigated and the condensation HTC was presented. The results show that the heat flux and HTC are highest when condensing CO₂ on Cu, and are lowest on Al and steel. We propose that the difference is caused by the variation in surface roughness and surface energy between the three materials. A high surface roughness leads to liquid retention and therefore a higher liquid film thickness on the surface. A high liquid thickness is related to high thermal resistance and hence a low heat transfer coefficient. The surface property dependency is, however, not fully understood and a further investigation is needed. We suggest, for instance, to do a parametric study of surface roughness and surface energy separately, e.g. by fabricating a number of Cu, Al and steel surfaces with a variety of roughnesses. In such a way a correlation of the surface properties and the condensation HTC can be developed. We also suggest to investigate further the condensation heat transfer at low subcooling (below 1k) and at low saturation pressures, as the deviation between experiments and models are particularly large for these parameters. In addition, the film thickness is an important parameter for the filmwise condensation heat transfer, and the actual film thickness of the condensate as a function of saturation pressure and subcooling should be investigated further through measurements and simulations. Finally, we suggest to conduct a study on liquid CO₂ adsorption on Cu, for example by thermal desorption spectroscopy, as the results indicate that the Cu surface is altered by the CO₂ condensate.

Declaration of Competing Interest

The authors declare that they have no known competing financial interests or personal relationships that could have appeared to influence the work reported in this paper.

Acknowledgements

This publication has been produced with the support of the Research Council of Norway through the CLIMIT funding program (254813).

Appendix A. Supplementary material

Supplementary data associated with this article can be found, in the online version, at <https://doi.org/10.1016/j.exptthermflusc.2021.110440>.

References

- [1] S.K. Fischer, Total equivalent warming impact: a measure of the global warming impact of CFC alternatives in refrigerating equipment, *Int. J. Refrig* 16 (6) (1993) 423–428, [https://doi.org/10.1016/0140-7007\(93\)90059-H](https://doi.org/10.1016/0140-7007(93)90059-H).
- [2] J. Pettersen, A. Hafner, G. Skaugen, H. Rekstad, Development of compact heat exchangers for CO₂ air-conditioning systems, *Int. J. Refrig* 21 (3) (1998) 180–193, [https://doi.org/10.1016/S0140-7007\(98\)00013-9](https://doi.org/10.1016/S0140-7007(98)00013-9).
- [3] C. Aprea, A. Maiorino, An experimental evaluation of the transcritical CO₂ refrigerator performances using an internal heat exchanger, *Int. J. Refrig* 31 (6) (2008) 1006–1011, <https://doi.org/10.1016/j.ijrefrig.2007.12.016>, <http://www.sciencedirect.com/science/article/pii/S0140700708000030>.
- [4] Z.-B. Liu, Y.-L. He, Y.-F. Yang, J.-Y. Fei, Experimental study on heat transfer and pressure drop of supercritical CO₂ cooled in a large tube, *Appl. Therm. Eng.* 70 (1) (2014) 307–315, <https://doi.org/10.1016/j.applthermaleng.2014.05.024>.
- [5] I.E. Agency, Energy technology roadmap 2017, International Energy Agency (2017) 393.
- [6] A. Alabdulkarem, Y. Hwang, R. Radermacher, Development of CO₂ liquefaction cycles for CO₂ sequestration, *Appl. Therm. Eng.* 33–34 (2012) 144–156, <https://doi.org/10.1016/j.applthermaleng.2011.09.027>.
- [7] A. Aspelund, M.J. Molnkvik, G. De Koeijer, Ship transport of CO₂, *Chem. Eng. Res. Des.* 84 (9) (2006) 847–855, <https://doi.org/10.1205/cherd.5147>.
- [8] S. Roussanaly, G. Skaugen, A. Aasen, J. Jakobsen, L. Vesely, Techno-economic evaluation of CO₂ transport from a lignite-fired IGCC plant in the Czech Republic, *Int. J. Greenhouse Gas Control* 65 (2017) 235–250, <https://doi.org/10.1016/j.jggc.2017.08.022>.
- [9] L. Gao, M. Fang, H. Li, J. Hetland, Cost analysis of CO₂ transportation: Case study in China, *Energy Procedia* 4 (2011) 5974–5981, <https://doi.org/10.1016/j.egypro.2011.02.600>.
- [10] F. Neele, R. de Kler, M. Nienoord, P. Brownsort, J. Koornneef, S. Belfroid, L. Peters, A. van Wijhe, D. Loeve, CO₂ transport by ship—the way forward in Europe, in: 13th International Conference on Greenhouse Gas Control Technologies, GHGT-13, Vol. 114, *Energy Procedia*, 2017, pp. 6824–6834. doi:10.1016/j.egypro.2017.03.1813. doi: 10.1016/j.egypro.2017.03.1813.
- [11] Z. Zhang, Z.L. Weng, T.X. Li, Z.C. Huang, X.H. Sun, Z.H. He, J. Van Es, A. Pauw, E. Laudi, R. Battiston, CO₂ condensation heat transfer coefficient and pressure drop in a mini-channel space condenser, *Exp. Thermal Fluid Sci.* 44 (2013) 356–363, <https://doi.org/10.1016/j.exptthermflusc.2012.07.007>.
- [12] J. Heo, H. Park, R. Yun, Condensation heat transfer and pressure drop characteristics of CO₂ in a microchannel, *Int. J. Refrig* 36 (6) (2013) 1657–1668, <https://doi.org/10.1016/j.ijrefrig.2013.05.008>.
- [13] P. Li, S. Norris, Heat transfer correlations for CO₂ flowing condensation in a tube at low temperatures, *Appl. Therm. Eng.* 93 (2016) 872–883, <https://doi.org/10.1016/j.applthermaleng.2015.09.072>.
- [14] M.M. Shah, Prediction of heat transfer during condensation of carbon dioxide in channels, *Appl. Therm. Eng.* 93 (2016) 192–199, <https://doi.org/10.1016/j.applthermaleng.2015.09.016>.
- [15] P. Li, J.J. Chen, S. Norris, Flow condensation heat transfer of CO₂ in a horizontal tube at low temperatures, *Appl. Therm. Eng.* 130 (2018) 561–570, <https://doi.org/10.1016/j.applthermaleng.2017.11.004>.
- [16] W. Nusselt, Die oberflächen kondensation des wasserdampfes, *Zeitschrift des Vereines Deutscher Ingenieure* 60 (1916) 541–569.
- [17] F.P. Incropera, D.P. DeWitt, T.L. Bergman, A.S. Lavine, *Fundamentals of Heat and Mass Transfer*, 6th Edition, John Wiley & Sons, 2007.
- [18] S.H. Hoenig, S. Modak, Z. Chen, M. Kaviany, J.F. Gilchrist, R.W. Bonner, Role of substrate thermal conductivity and vapor pressure in dropwise condensation, *Appl. Therm. Eng.* 178 (2020) 115529, <https://doi.org/10.1016/j.applthermaleng.2020.115529>.
- [19] J. Zhang, X. Zhu, M.E. Mondejar, F. Haglind, A review of heat transfer enhancement techniques in plate heat exchangers, *Renew. Sustain. Energy Rev.* 101 (2019) 305–328, <https://doi.org/10.1016/j.rser.2018.11.017>.
- [20] J. Soontarapiromsook, O. Mahian, A.S. Dalkilic, S. Wongwises, Effect of surface roughness on the condensation of R-134a in vertical chevron gasketed plate heat exchangers, *Exp. Thermal Fluid Sci.* 91 (2018) 54–63, <https://doi.org/10.1016/j.exptthermflusc.2017.09.015>.
- [21] K. Nilpueng, S. Wongwises, Experimental study of single-phase heat transfer and pressure drop inside a plate heat exchanger with a rough surface, *Exp. Thermal Fluid Sci.* 68 (2015) 268–275, <https://doi.org/10.1016/j.exptthermflusc.2015.04.009>.
- [22] R. Yun, J. Heo, Y. Kim, Effects of surface roughness and tube materials on the filmwise condensation heat transfer coefficient at low heat transfer rates, *Int. Commun. Heat Mass Transfer* 33 (4) (2006) 445–450, <https://doi.org/10.1016/j.icheatmasstransfer.2006.01.009>.
- [23] F. Solymosi, The bonding, structure and reactions of CO₂ adsorbed on clean and promoted metal surfaces, *J. Mol. Catal.* 65 (3) (1991) 337–358, [https://doi.org/10.1016/0304-5102\(91\)85070-1](https://doi.org/10.1016/0304-5102(91)85070-1).
- [24] F. Muttaqien, Y. Hamamoto, K. Inagaki, Y. Morikawa, Dissociative adsorption of CO₂ on flat, stepped, and kinked Cu surfaces, *J. Chem. Phys.* 141 (3) (2014) 034702, <https://doi.org/10.1063/1.4887362>.
- [25] C.J. Geankoplis, *Transport Processes and Separation Process Principles*, 4th Edition, Prentice Hall, 2003.
- [26] D.J. Preston, K.L. Wilke, Z. Lu, S.S. Cruz, Y. Zhao, L.L. Becerra, E.N. Wang, Gravitationally driven wicking for enhanced condensation heat transfer, *Langmuir* 34 (15) (2018) 4658–4664, <https://doi.org/10.1021/acs.langmuir.7b04203>.
- [27] C.-Y. Wang, C.-J. Tu, Effects of non-condensable gas on laminar film condensation in a vertical tube, *Int. J. Heat Mass Transf.* 31 (11) (1988) 2339–2345, [https://doi.org/10.1016/0017-9310\(88\)90165-2](https://doi.org/10.1016/0017-9310(88)90165-2).
- [28] X.-H. Ma, X.-D. Zhou, Z. Lan, Y.-M. Li, Y. Zhang, Condensation heat transfer enhancement in the presence of non-condensable gas using the interfacial effect of dropwise condensation, *Int. J. Heat Mass Transf.* 51 (7–8) (2008) 1728–1737, <https://doi.org/10.1016/j.j.heatmasstransfer.2007.07.021>.
- [29] X.M. Wu, T. Li, Q. Li, F. Chu, Approximate equations for film condensation in the presence of non-condensable gases, *Int. Commun. Heat Mass Transf.* 85 (2017) 124–130, <https://doi.org/10.1016/j.icheatmasstransfer.2017.05.007>.
- [30] R. Span, W. Wagner, A new equation of state for carbon dioxide covering the fluid region from the triple-point temperature to 1100 K at pressures up to 800 MPa, *J. Phys. Chem. Ref. Data* 25 (6) (1996) 1509–1596, <https://doi.org/10.1063/1.555991>.
- [31] National Institute of Standards and Technology (2018). [link]. <https://webbook.nist.gov/chemistry/fluid/>.
- [32] S.I. Abu-Eishah, Correlations for the thermal conductivity of metals as a function of temperature, *Int. J. Thermophys.* 22 (6) (2001) 1855–1868, <https://doi.org/10.1023/A:1013155404019>.
- [33] Z. Jian-Min, M. Fei, X. Ke-Wei, Calculation of the surface energy of fcc metals with modified embedded-atom method, *Chin. Phys.* 13 (7) (2004) 1082–1090, <https://doi.org/10.1088/1009-1963/13/7/020>.
- [34] A. Kinloch, *Adhesion and Adhesives*, Springer Netherlands, 1987. doi:10.1007/978-94-015-7764-9.
- [35] O. Santos, T. Nylander, R. Rosmaninho, G. Rizzo, S. Yiantsios, N. Andritsos, A. Karabelas, H. Muller-Steinhagen, L. Melo, L. Boulange-Petermann, C. Gabet, A. Braem, C. Traegaardh, M. Paulsson, Modified stainless steel surfaces targeted to

- reduce fouling–surface characterization, *J. Food Eng.* 64 (1) (2004) 63–79, <https://doi.org/10.1016/j.jfoodeng.2003.09.013>.
- [36] Q. Baojin, Z. Li, X. Hong, S. Yan, Experimental study on condensation heat transfer of steam on vertical titanium plates with different surface energies, *Exp. Thermal Fluid Sci.* 35 (1) (2011) 211–218, <https://doi.org/10.1016/j.expthermflusci.2010.09.003>.
- [37] W.M. Rohsenow, Heat transfer and temperature distribution in laminar film condensation, *Transactions ASME* 78 (1956) 1645–1648.
- [38] H. Akimoto, Y. Anoda, K. Takase, H. Yoshida, H. Tamai, Condensation Heat Transfer, Springer Japan (2016) 347–359, https://doi.org/10.1007/978-4-431-55603-9_17.
- [39] J. Wu, s. Ervik, I. Snustad, S. Xiao, A. Brunsvold, J. He, Z. Zhang, Contact angle and condensation of a co2 droplet on a solid surface, *The Journal of Physical Chemistry C* 123 (1) (2019) 443–451. doi:10.1021/acs.jpcc.8b08927. doi: 10.1021/acs.jpcc.8b08927.
- [40] J. Nakamura, J.A. Rodriguez, C.T. Campbell, Does CO2 dissociatively adsorb on cu surfaces? *J. Phys.: Condens. Matter* 1 (1989) <https://doi.org/10.1088/0953-8984/SB149-SB160>.
- [41] I.A. Boenicke, W. Kirstein, F. Thieme, A study on CO2 dissociation on a stepped (332) copper surface, *Surf. Sci.* 307–309 (1994) 177–181, [https://doi.org/10.1016/0039-6028\(94\)90390-5](https://doi.org/10.1016/0039-6028(94)90390-5).

Supplementary Information

One dimensional analysis of heat transfer cylinder

Two assumptions must be true for validating the governing equations for data reduction used in this work: a) the temperature must be uniform in the radial direction, and b) the temperature profile through the Cu cylinder must be linear. Assumption a) is validated by calculating the Biot number of the teflon/Cu cylinder system. The Biot number describes the relationship between the heat transfer resistance of the body and the surface of a material, and a small Biot number ($\ll 1$) is associated with a uniform temperature in the radial direction [1]. The temperature profile in the axial direction is found by performing a one-dimensional analysis of the heat transfer through the cylinder. The results show that the temperature gradient is in fact linear along the entire cylinder length, and therefore confirms assumption b). In this section, the necessary calculations are presented.

In order to find the Biot number, one must first find the HTC of the teflon insulation. The HTC is found by performing a heat balance of the Cu/insulation network. The teflon insulation is a cylinder with a hollow core, with outer radius r_o and inner radius r_i . The cross-section for calculating the Biot number is the circular combination of the Cu and the teflon insulation. By applying Fourier's law we derive an expression for the HTC in the teflon. Q is here the heat flowing in the radial direction in the Cu/insulation, and is given by

$$Q = -k_{ins}A_{surf}\frac{dT}{dr} = -k2\pi rL\frac{dT}{dr}, \quad (1)$$

where k_{ins} is the thermal conductivity of the insulation, $A_{surf} = 2\pi rL$ is the circumferential surface area of the insulation, $\frac{dT}{dr}$ is the temperature gradient in the radial direction, and L is the length of the Cu/insulation. By integrating, we get

$$\int_{r_i}^{r_o} Q \frac{dr}{r} = -2\pi k_{ins}L \int_{T_i}^{T_o} dT \quad (2)$$

$$Q = 2\pi k_{ins}L(T_i - T_o)/\log(r_o/r_i). \quad (3)$$

The heat in the insulation is given by the insulation HTC, h_{ins} , and the temperature difference between the inner and outer wall, as

$$Q = h_{ins}2\pi r_i L(T_i - T_o). \quad (4)$$

By balancing the heat, we combine Equations (3) and (4) to obtain an expression for the h_{ins} , which is required for calculating the Biot number. The heat balance gives

$$2\pi k_{ins}L(T_i - T_o)/\log(r_o/r_i) = \pi h_{ins}r_iL(T_i - T_o) \quad (5)$$

$$\Rightarrow h_{ins} = \frac{2k_{ins}}{r_i \log(r_o/r_i)}. \quad (6)$$

In our case, the insulation is with $k_{ins} = 0.25 \text{ W m}^{-1} \text{ K}^{-1}$, $r_i = 1 \text{ cm}$ and $r_o = 3 \text{ cm}$. The calculated HTC of teflon is $45.51 \text{ W m}^{-2} \text{ K}^{-1}$.

The HTC of the outer wall of the Cu/insulation system is a series combination of the HTC of the condensation, h_{cond} , and the insulation, h_{ins} . Here, we assume a condensation HTC, h_{cond} , of $10\,000 \text{ W m}^{-2} \text{ K}^{-1}$, which is in the same order of magnitude as the experimental data. The resulting wall HTC is

$$h_{wall} = \left(\frac{1}{h_{cond}} + \frac{1}{h_{ins}} \right)^{-1} = 45.31 \text{ W m}^{-2} \text{ K}^{-1}, \quad (7)$$

giving the Biot number

$$Bi = \frac{h_{wall}r_o}{k_{Cu}} = 0.0034 \ll 1. \quad (8)$$

Hence, we can assume a uniform temperature in the cross section of the cylinder, and consequently, the cylinder can be modeled as a cylindrical fin with one-dimensional heat transfer in the axial direction.

The temperature profile through the cylinder is derived by constructing a control volume consisting of a thin slab of cross sectional area $A_{CS} = \pi r_i^2$ and width dx , see Figure 1. The heat entering the control volume is given by Fourier's law, $Q_{in} = Q_x = -k_{Cu}A_{CS}\frac{dT}{dx}$, while the heat leaving the control volume is the conductive heat plus the convective heat at the wall of the cylinder caused by condensation, $Q_{out} = Q_{cond} + Q_{conv}$. Here, $Q_{cond} = Q_{x+dx} = Q_x + \frac{d}{dx}(Q_x)dx$, where $\frac{d}{dx}(Q_x)dx = -k_{Cu}A_{CS}\frac{d^2T}{dx^2}dx$, and $Q_{conv} = h_{wall}A_{wall}(T - T_{sat})$, where $A_{wall} = 2\pi r_i dx$ is the area of the surface of the control volume and T_{sat} is the saturated vapor temperature. Filling in the expressions in the heat flux continuity equation, we get that

$$Q_{in} = Q_{out} \quad (9)$$

$$Q_x = Q_{cond} + Q_{conv} \quad (10)$$

$$Q_x = Q_x + \frac{d}{dx}(Q_x)dx + h_{wall}A_{wall}dx(T - T_{sat}) \quad (11)$$

$$0 = -k_{Cu}\pi r_i^2 \frac{dT^2}{dx^2} dx + h_{wall}2\pi r_i dx(T - T_{sat}) \quad (12)$$

$$\frac{d^2T}{dx^2} = \frac{4h_{wall}(T - T_{sat})}{k_{Cu}2r_i}. \quad (13)$$

With $\theta = T - T_{sat}$ and $m^2 = \frac{4h_{wall}}{k_{Cu}2r_i}$, we get a one-dimensional second order differential equation of the form $\frac{d^2\theta}{dx^2} - m^2\theta = 0$, which is the heat equation for

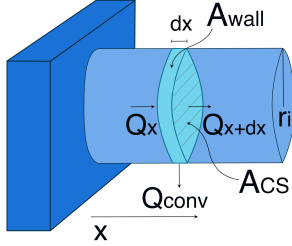


Figure 1: Model system for the one-dimensional analysis of the Cu cylinder, without insulation. The control volume is $A_{CS}dx$ and we assume pure conduction along the x-axis.

a cylindrical fin at steady state. The general solution is $\theta(x) = C_1 \exp(mx) + C_2 \exp(-mx)$. The boundary conditions are set up by the set temperature of the cooling element, $T(x = 0) = T_0$ and the fact that the heat flux at the end of the cylinder is given by the condensation heat flux at the subcooling $\theta_L = T_L - T_{sat}$:

$$\theta(0) = \theta_0 = T_0 - T_{sat} \quad (14)$$

$$q_{cond} = -k_{Cu} \frac{d\theta}{dx} = h_{cond} \theta_L \Rightarrow \frac{d\theta}{dx} = -\frac{h_{cond}}{k_{Cu}} \theta_L \quad (15)$$

T_L is the temperature at $x = L$, i.e. at the end of the cylinder.

The constants of the solution to the differential equation are

$$C_1 = \theta_0 - C_2, \quad (16)$$

$$C_2 = \frac{\theta_0}{2m \cosh(mL)} \left(2m \cosh(mL) - \frac{h_{cond} \theta_L}{k_{Cu} \theta_0} - m \exp mL \right). \quad (17)$$

The resulting temperature profile for the specific geometry and materials used in this work (Cu and teflon) is shown in Figure 2. The temperature profile is linear for the first 18 cm, shown as a vertical line in the figure. The deviation from linearity is 0.5 °C, and increasing after 18 cm. Consequently, it is safe to assume a linear temperature profile in the 4 cm long Cu cylinder in the experimental setup. Variation of the thermal conductivity of Cu along the cylinder has been neglected as the maximum deviation of heat flux caused by change in thermal conductivity in these experiments is 0.3%. The result of these calculations is that we can use Fourier's law in its simplest form to find the heat flux of the condensation experiments, which follows in the next section.

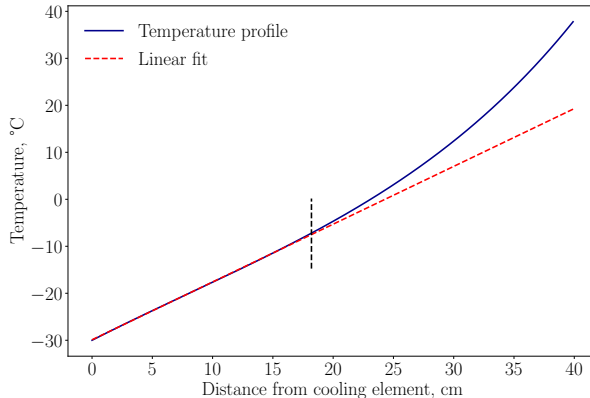


Figure 2: Temperature profile through an insulated Cu cylinder surrounded by 2 cm thick insulation, which has a thermal conductivity of $0.25 \text{ W m}^{-1} \text{ K}^{-1}$. The saturation temperature is set to -20°C and the temperature of the cooling element is -30°C . The temperature profile is linear for approximately the first 18 cm (cut-off shown as vertical line), which means that the temperature profile through the 4 cm long Cu cylinder used in this work can be assumed linear.

Icebath calibration of thermocouples

The output from thermocouples dependent strongly on the path from the acquisition point to the voltage meter, and it is important to use similar junctions and wires from the same batch in order to compare different thermocouple measurements. It is also necessary to calibrate the thermocouples with the exact connection and wire setup that will be used in the experiments in order to gain the lowest possible uncertainty and scattering in the measurements. In our case, the thermocouples were calibrated with an icebath after being embedded into the Cu cylinder, and with all connections as they were in an experiment, Figure 3. 300 consecutive datapoints were acquired for each thermocouple (2 points/second), and repeated 15 times. The average calibration value was 0.34 K with a relative standard deviation of 5.5%.

Uncertainty analysis

We have performed a uncertainty analysis based on the Gaussian propagation of errors. The total error in heat flux, E_q , is derived by starting with the one-dimensional Fourier law, Equation (18), with k being the thermal conductivity of Cu and d_{1-4} being the distance between thermocouple 1, TC_1 , and thermocouple 4, TC_4 , in the cylinder.

$$q = -k \frac{TC_4 - TC_1}{d_{1-4}} \quad (18)$$

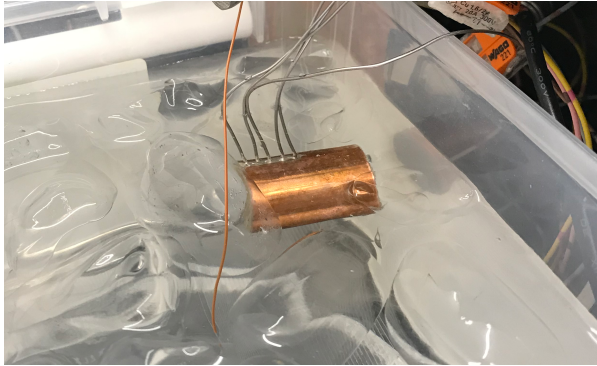


Figure 3: The Cu cylinder with the embedded thermocouples were submerged in an icebath for calibration.

The expression for the total error in heat flux, E_q , is found using the variance formula which results in Equation (19).

$$E_q = \sqrt{\left(\frac{TC_4 - TC_1}{d_{1-4}}\right)^2 E_k^2 + 2\left(\frac{k}{d_{1-4}}\right)^2 E_T^2 + \left(\frac{TC_4 - TC_1}{d_{1-4}^2}\right)^2 E_d^2} \quad (19)$$

Here, E_k is the estimated error in Cu thermal conductivity, E_T is the error in the temperature measurements, and E_d is the error in the distance between the thermocouples. We have estimated the temperature dependent thermal conductivity of Cu from the correlation presented by Abu-Eishah [2] which is given with an absolute relative error of 0.013%.

The error in temperature measurements, E_T , is estimated based on the ice-bath calibration of the thermocouples, using the standard deviation of the estimated calibration value as a constant error in the measurements. The placement of the thermocouples inside the Cu cylinder has been measured with a caliper and the error is therefore assumed to be within 0.02 mm, relating to the smallest measurable values with a caliper.

The error in subcooling is also derived with the Gaussian error distribution and the resulting formula is

$$E_{\Delta T} = \sqrt{E_{T_{sat}}^2 + E_{T_{surf}}^2} \quad (20)$$

Here, the error in the saturation temperature, $E_{T_{sat}}$, is based on the given uncertainty of the pressure controller used to control the pressure in the chamber.

The error in the surface temperature, $E_{T_{surf}}$, is calculated through a series of steps involving the extrapolation of the temperatures in the Cu cylinder and

the thermal resistance through the thermal interface material. The uncertainty in the estimated cylinder surface temperature, T_{cyl} , is derived as follows:

$$T_{cyl} = \frac{x_1}{d_{1-4}}(TC_1 - TC_4) + TC_1 \quad (21)$$

$$E_{T_{cyl}}^2 = \left(\frac{TC_1 - TC_4}{d_{1-4}} \right)^2 \left(E_{x_1}^2 + \left(\frac{x_1}{d_{1-4}} \right)^2 E_{d_{1-4}}^2 \right) + E_T^2 \left(1 + 2 \left(\frac{x_1}{d_{1-4}} \right)^2 \right) \quad (22)$$

Here, x_1 and E_{x_1} are the placement of the outermost thermocouple in the cylinder and the corresponding uncertainty, as measured with a caliper. The error in the temperature at the interface between the TIM and the sample, $E_{T_{TIM}}$, is shown in Equation (24). Here we assumed the thermal conductivity of the TIM to be certain.

$$T_{TIM} = \frac{k_{Cu} t_{TIM}}{k_{TIM} x_1} (T_{cyl} - TC_1) + T_{cyl} \quad (23)$$

$$E_{T_{TIM}}^2 = \left(\frac{1}{k_{TIM} x_1} \right)^2 \left((t_{TIM}^2 E_{k_{Cu}}^2 + k_{Cu}^2 E_{t_{TIM}}^2) (T_{cyl} - TC_1)^2 + \left(\frac{k_{Cu}}{x_1} \right)^2 E_{x_1}^2 (T_{cyl} - TC_1)^2 + k_{Cu}^2 (E_{T_{cyl}}^2 + E_T^2) \right) + E_{T_{cyl}}^2 \quad (24)$$

The calculation of the uncertainty in T_{surf} follows Equation (26).

$$T_{surf} = \frac{k_{TIM} t_{mat}}{t_{TIM} k_{mat}} \left(T_{TIM} - TC_1 - \frac{x_1}{d_{1-4}} (TC_1 - TC_4) \right) + T_{TIM} \quad (25)$$

$$E_{T_{surf}}^2 = \left(\frac{k_{TIM} t_{mat}}{t_{TIM} k_{mat}} \right)^2 \left[\left(\left(\frac{E_{t_{TIM}}}{t_{TIM}} \right)^2 + \left(\frac{E_{k_{mat}}}{k_{mat}} \right)^2 \right) \left(T_{TIM} - TC_1 - \frac{x_1}{d_{1-4}} (TC_1 - TC_4) \right)^2 + \left(E_{T_{TIM}}^2 + E_T^2 \left(1 + 2 \left(\frac{x_1}{d_{1-4}} \right)^2 \right) \right) \right] + E_{T_{TIM}}^2 \quad (26)$$

References

- [1] W. Lau, C. W. Tan, Errors in one-dimensional heat transfer analysis in straight and annular fins, *Journal of Heat Transfer* 95 (4) (1973) 549–551. doi:10.1115/1.3450110. URL <https://dx.doi.org/10.1115/1.3450110>
- [2] S. I. Abu-Eishah, Correlations for the thermal conductivity of metals as a function of temperature, *International Journal of Thermophysics* 22 (6) (2001) 1855–1868. doi:10.1023/a:1013155404019. URL <https://dx.doi.org/10.1023/A:1013155404019>

A.3 Paper III

Condensation heat transfer of CO₂ on Cu based hierarchical and nanostructured surfaces

Ingrid Snustad, Lene Hollund, Åsmund Ervik, Anders Austegard, Amy Brunsvold, Jianying He and Zhiliang Zhang.

International Journal of Heat and Mass Transfer. **175**, 121367 (2021)



Contents lists available at ScienceDirect

International Journal of Heat and Mass Transfer

journal homepage: www.elsevier.com/locate/hmt

Condensation heat transfer of CO₂ on Cu based hierarchical and nanostructured surfaces



Ingrid Snustad^{a,*}, Lene Hollund^a, Åsmund Ervik^b, Anders Austegard^b, Amy Brunsvold^b, Jianying He^a, Zhiliang Zhang^a

^aFaculty of Engineering, Department of Structural Engineering, Norwegian University of Science and Technology, Richard Birkelands vei 1A, Trondheim 7491, Norway

^bSINTEF Energy Research, Sem Sæ lands vei 11, Trondheim 7034, Norway

ARTICLE INFO

Article history:

Received 20 January 2021

Revised 26 March 2021

Accepted 11 April 2021

Keywords:

Condensation heat transfer

CO₂ liquefaction

Micro- and nanostructured surfaces

Cu based surfaces

ABSTRACT

Phase-change processes such as condensation are efficient means of heat transfer. However, condensation is also an energy-intensive process and extensive research is conducted to increase the heat transfer efficiency. Increasing the effective heat transfer area in terms of surface structures on macro or microscale is one such technique of heat transfer enhancement. In this work, we have studied micro- and nanostructured surfaces for their potentials in increasing heat transfer during condensation of CO₂. Three Cu-based surfaces on which CuO nanoneedles have been grown, have been investigated. We hypothesize three competing mechanisms govern the overall heat transfer on structured surfaces: (1) increased heat transfer area, (2) lower thermal conductivity of oxides, and (3) condensate flooding of the structures. Our study has shown that in some cases, the effect of these mechanisms can be neutralized. More importantly, the results show that superior heat transfer can be achieved by optimizing the surface structure. The best of the structured surfaces resulted in a heat transfer coefficient 66% higher than that of the unstructured surface.

© 2021 Elsevier Ltd. All rights reserved.

1. Introduction

Condensation heat transfer performance influences several industrial processes and is especially important for heat exchanger technology. CO₂ is identified as an alternative for reducing the usage of fluorine based refrigerants in heat exchangers and heat pumps due to their negative environmental impact [1–3]. CO₂ has a high triple point and low critical point, and has therefore the potential to be an efficient refrigerant [4]. Increased condensation heat transfer efficiency will reduce the energy consumption of the liquefaction process and reduce the costs of heat exchangers and heat pumps. Liquefaction of CO₂ is also a part of Carbon Capture and Storage (CCS), especially as a pre-process for ship transport [5,6]. Increased liquefaction efficiency will reduce the energy consumption and the cost of the CCS systems, which is necessary to scale up the number of CCS projects worldwide [7].

In the literature, there are several examples of studies on the increase of heat transfer efficiency by the use of micro- and nanostructures on the surface [8,9]. Hendricks et al. [10] fabricated ZnO

flower-like nanostructures on Al and Cu and reported increased critical heat flux (CHF) for both surfaces. An increased CHF is related to a higher possible operational limit, and therefore a better heat transfer performance. The same phenomenon is reported by Nam et al. [11] and by Saedi and Alemrajabi [12]. The first reported an increase in CHF at wicking structures of CuO nanostructures on top of Cu microposts and the latter reported an increase in both CHF and heat transfer coefficient (HTC) on anodized Al surfaces. In pool boiling, an increased number of nucleation sites on the structured surfaces has proven beneficial for heat transfer. For example Li et al. [13] studied nucleation boiling on Cu nanorods deposited on a Cu surface, and found that there were 30 times as many bubble nucleation sites on the structured surfaces. They also found that the nanorod surface exhibited a higher wettability towards water, which reduced the size of the bubble diameter and increases the release frequency of the bubbles. By these mechanisms the CHF, and hence the heat transfer efficiency, was increased. Chen et al. [14] reported an increased HTC for pool boiling on nanowires of both Cu and Si. The improved HTCs were caused by the increased number of bubble nucleation sites in the microscale cavities in between the nanowires. The boiling curves measured on both Cu and Si nanowires are similar to each other even though the thermal conductivity of the two materials are very

* Corresponding author.

E-mail address: ingrid.snustad@ntnu.no (I. Snustad).

different. The above results indicate that the heat transfer is dominated by the nucleation and bubble dynamics, not by the heat conduction, and the surface morphology is the determining factor.

For condensation, the number of nucleation sites have also been shown to increase on nanostructured surfaces. In the work by Boreyko and Chen, a hierarchical surface of Si micropillars covered with carbon nanotubes was investigated and the nucleation sites increased significantly along with a decrease in wettability [15]. The fabrication of the micro- and nanostructures resulted in a superhydrophobic surface on which the condensation occurred in the dropwise mode. Dropwise condensation results in HTC's up to an order of magnitude higher than the conventional filmwise condensation. On the surface by Boreyko et al., the droplets spontaneously jumped off at a droplet size much smaller than for a hydrophobic surface where the droplets are removed by gravity. On the other hand, not all superhydrophobic surfaces promotes dropwise condensation, but could actually cause a degradation of heat transfer [16]. The surface structures could in this case be flooded by the condensate, which is then strongly pinned to the surface even though the applied models predict that the surface is non-wetting. Dropwise condensation is a dynamic process and the droplets can nucleate and grow in between the structures, and consequently, be pinned to a superhydrophobic surface [8]. For this reason, superhydrophobic surfaces do not necessarily promote dropwise condensation.

Both the above mentioned studies, and others examining micro- and nanostructures for enhanced condensation heat transfer [17,18], have explored the beneficial performance of dropwise condensation. For low surface tension fluids, however, it is extremely challenging to obtain dropwise condensation as most condensates will flood the nanostructures. Aili et al. [19] studied the filmwise condensation heat transfer of a low surface tension fluid on microstructures on aluminium. They found that the heat transfer was unaffected by the microstructures. They also studied how nanostructures on a mini-fin Cu surface influenced the heat transfer performance. In this case, the heat transfer was reduced on the nanostructured surface due to solid-liquid friction, which results in a thicker condensate film on the surface. The heat transfer on a pure mini-fin Cu surface was, however, higher than on an unstructured surface, showing that increasing the effective condensation area was beneficial. The increase in heat transfer due to augmented surfaces is well-established and models describing the effect of different augmentation geometries have been developed by Ali [20] and Ali and Briggs [21]. The models include geometrical parameters in addition to the effect of the ratio between surface tension and gravity. The latter has a large impact on the flooding of the surface structures, revealing that a low surface tension fluid is less likely to flood the structures. For such fluids, a surface augmentation with small pitches between the structures would be more beneficial than for a high surface tension fluid, such as water.

Even though there are examples of studies on dropwise condensation of low surface tension fluids, no such studies exist for CO₂. Even though the refrigerant R134-a has proven to have similar flow behavior to CO₂ [22], the specific heat transfer behavior of filmwise CO₂ condensation is lacking. In previous work, using molecular dynamics simulations, we have investigated the condensation mechanism of CO₂ on Cu like surfaces [23,24]. Still, experimental studies have not yet been published for condensation of CO₂ on structured surfaces. To address this, we have in this work investigated CO₂ condensation on one untreated Cu surface and three micro- and nanostructured Cu based surfaces. The untreated surface serves as the baseline for the comparison of the heat transfer behavior of the modified surfaces. Of those, two are hierarchical in scale, with an underlying microstructure covered with nanostructures. The third substrate is purely nanostructured, with randomly oriented nanoneedles covering the entire surface. The heat

transfer performance of the four substrates are evaluated and compared. The aim of the study is to determine if and how micro- and nanostructures influence the heat transfer during filmwise condensation of a low surface tension fluid.

The main findings of the work is that the heat transfer is determined by the competing effect of nanostructures and the reduced thermal conductivity of CuO. The nanostructures induces a wicking condensation mode, which increases the heat transfer compared to filmwise mode, but the reduced thermal conductivity of CuO reduces the potential heat transfer increase and the heat transfer is therefore unaltered when the nanostructure density is high.

This paper is organized as follows. First, we describe the experimental method applied for measuring the condensation heat transfer followed by details on the fabrication of the three structured surfaces. Second, the results are presented along with a discussion of their meaning and significance. Finally, conclusions are drawn and some further work is stipulated. The results of a study of the mechanical durability of the nanostructures as a response to CO₂ condensation is included in the Supplementary Information.

2. Method and materials

The experimental method used for measuring heat flux and HTC's in this work is described in detail in our previous work [25]. A summary of the method and a description of the fabrication methods for the hierarchical and nanostructured surfaces are given in this section.

2.1. Experimental method

The experimental method relies on one dimensional heat transport through an insulated Cu cylinder, where a cooling element is attached to one end, and the investigated surface to the other. Four type K thermocouples (Omega Engineering) are embedded in the center of the cylinder to obtain the axial temperature gradient in the cylinder, which in turn is used to calculate the heat flux. The uncertainty of the thermocouples provided by the manufacturer is 1 K. To reduce the uncertainty, the thermocouples are cold junction compensated in a water cooling bath (Julabo) and calibrated on site in an ice bath. By this procedure the uncertainty is reduced and taken to be equal to the standard deviation of the measurements in the ice bath calibration, which was 0.02 K.

The cooling element attached to the Cu cylinder is a Cu block with narrow channels. Within the channels, two phase CO₂ is flowed through and evaporated, with a back-pressure regulator ensuring that the pressure inside the cooling element is the saturation pressure for the desired temperature. In this way, the CO₂ is kept at the boiling curve and two phase flow is kept throughout the cooling element. The temperature on the surface of the cooling element is thus uniform and accurately controlled by a back pressure regulator (Alicat PC3). The available temperature range is 55 to 20 °C, corresponding to a saturation pressure from 5.7 to 19.7 bar.

The investigated substrate is attached to the Cu cylinder with a thermal interface material (TIM (Aldrich Chemistry, Silver conductive paste, 735825-25G)). Prior to attachment, the baseline Cu surface is cleaned with acetone, isopropanol and ethanol (VWR, 99% reagent grade), in that order. The structured surfaces were cleaned prior to structure fabrication and kept in closed compartments to avoid deterioration of the micro- and nanostructures prior to heat transfer experiments.

The cooling element with the attached cylinder and substrates are placed in a pressure chamber consisting of a steel pipe closed off by flanges and bolts. A sight glass is embedded in one flange and a high speed camera (Phantom 9.1) is placed close to the glass for in situ observation of the condensation process. Specifically, the

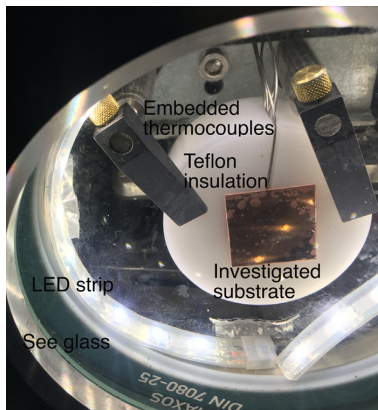


Fig. 1. Photograph of the investigated substrate as seen through the glass in the end flange of the pressure chamber. The embedded thermocouples are also seen. The Cu cylinder is enclosed in the teflon insulation and is hidden behind the substrate. A LED strip enlightening the substrate is also shown.

onset of the condensation is observed. The pressure chamber is built for pressures up to 20 bar and is filled by pure CO_2 (5.2, AGA Scientific Grade) during experiments. A pressure regulator (Alicat PCD) maintains a constant pressure in the chamber, also during condensation. The end flange with the see glass and the substrate within the chamber is shown in Fig. 1.

The temperature in the Cu cylinder is controlled, monitored and acquired with a LabView™ interface. In addition, the pressure in the chamber, the temperature of the gas and in the cooling element is controlled and monitored by the software.

2.2. Material fabrication and surface description

Four substrates have been investigated in this work: (a) an untreated Cu plate, (b) a nanostructured Cu surface, (c) and (d) micro- and nanostructured surfaces with variation in nanostructure density. All substrates were initially 0.5 mm thick quadratic (2.5×2.5 cm) Cu plates (99.9% purity, Sigma-Aldrich). The baseline Cu is untreated and has a low intrinsic roughness. The root mean square (RMS) roughness is measured in a Veeco Dektak 150 profilometer to be 73 nm.

The nanostructured surface is fabricated with an adaption of the solution immersion technique developed by He et al. [26,27]. The Cu substrate is cleaned with acetone and isopropanol, dried with nitrogen and immersed into a solution of 0.1 M ammonium persulfate and 2.5 M sodium hydroxide for 3 M. The surface is then dried at 120 °C to fully dehydrate the structures, resulting in a surface with stable CuO nanoneedles, see Fig. 2. The width of the nanoneedles is on average 175 nm and the average length is 3 μm . The nanoneedles initially grow at nucleation sites with high surface energy such as spikes and hills on the surface. Therefore, the underlying surface structure of the Cu surface is observed as lines with higher nanoneedle density. The nanostructured surface is henceforth named NS. Note here that the nanoneedles are made of the oxide corresponding to the substrate metal, i.e. CuO, a point which will prove to be important for the subsequent condensation heat transfer analysis.

For fabricating the hierarchical structures, the first step is to etch micropillars into the Cu substrate by photolithography and chemical assisted ion beam etch (CAIBE). Photolithography is a process for transferring a pattern onto a surface by exposing the surface covered in a photoreactive material (photoresist) with a laser in a predefined pattern. The photoresist hardens and works

as a mask for the following etching process. CAIBE is an etching method for physical sputtering of unprotected material on a surface. In this work, photoresist micropillars with a diameter of 10 μm were deposited onto the Cu surface. These micropillars protected the underlying Cu in the CAIBE process, and the material around the photoresist was etched. The resulting surface pattern after photolithography and CAIBE are Cu micropillars, shown in Fig. 3. The micropillars are on average 10 μm in diameter and 1 μm in height. For the two hierarchical surfaces, the exposure doses in the photolithography process were the only fabrication difference. One surface, Fig. 3(a), was exposed with a laser with 1700 mJ cm^{-2} energy flux, and the other, Fig. 3(b) was exposed with 1900 mJ cm^{-2} energy flux. This difference affect the resulting nanostructure density as described below.

Following the micropillar fabrication, the nanostructures on top of the microstructures are fabricated in the solution immersion process described above, with an immersion time of 5 M. The resulting nanoneedles are approximately 10 μm long for both surfaces. The morphology is different on the surface exposed with 1700 mJ cm^{-2} and the one exposed with 1900 mJ cm^{-2} . Henceforth the first is called S17 and the latter is called S19. The two surfaces are shown in Figs. 4 and 5, respectively. It is observed that the nanoneedles grow more uniformly on the S19 surface compared to the S17 surface. On the S17 surface, there is a large variation in the nanoneedle density across the surface and the nanoneedles grow both on the sides and on top of the micropillars. However, the nanoneedles grown on the top of the micropillars are shorter. Around the majority of the micropillars the nanoneedles have grown in the horizontal direction, normal to the micropillar circumference. At the rest of the micropillars the nanoneedles have grown in all directions causing dense clusters on the sides and top of the micropillars. On the S19 surface, the nanoneedles grow, to a large degree, only on the sides of the micropillars and with a more uniform and higher density than on S17. On the S17 surface clusters of nanoneedles are observed both on top of and in between some micropillars. The main difference in growth on S17 and S19 is caused by the robustness of the photoresist that is present at the top of the micropillars, see Fig. 3. We propose that the difference in robustness is caused by the difference in exposure dose in the photolithography step. At the S17 surface the nanoneedles occasionally grow from underneath the photoresist and the photoresist is lifted off the Cu micropillar. This can be seen in Fig. 4(b). On the S19 this behavior is not observed, and as a result, the nanoneedles only grow from the sides of the micropillar.

The topography and the appearance of the structured surfaces have been investigated with the use of a Scanning Electron Microscope (SEM, FEI Apreo). The secondary electrons were detected and a beam current of 0.2 nA and an acceleration voltage of 10 kV were applied (details on SEM theory can be found in Akhtar et al. [28]).

After preparation in a clean room, the three fabricated surfaces are carefully handled in closed boxes to ensure that the structures are not damaged before the heat transfer experiments. When the substrates are attached to the Cu cylinder in the heat transfer setup, they are handled with gloves and only touched in two corners. As the width of the substrates are higher than the diameter of the cylinder, the surface at which the condensation will occur is left untouched and the surface structures are the same under the heat transfer experiments as described in this section. To confirm the stability of the structures, SEM images were recorded both before and after the condensation experiments. The results are presented in the Supplementary Information.

2.3. Data reduction

The data acquired in the experiments are the temperatures in the four thermocouples embedded in the Cu cylinder. The heat flux

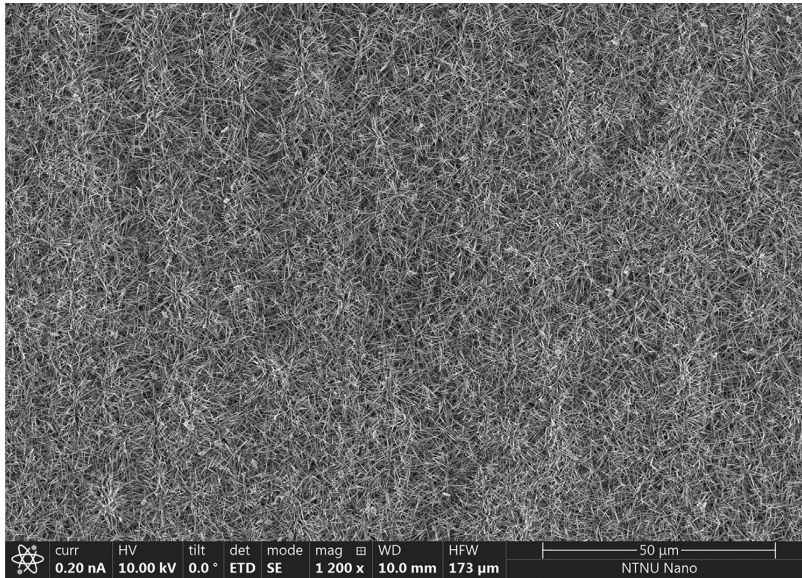


Fig. 2. Scanning Electron Microscope image of CuO nanoneedles on Cu substrate fabricated by solution immersion for 3 min. This surface is called NS.

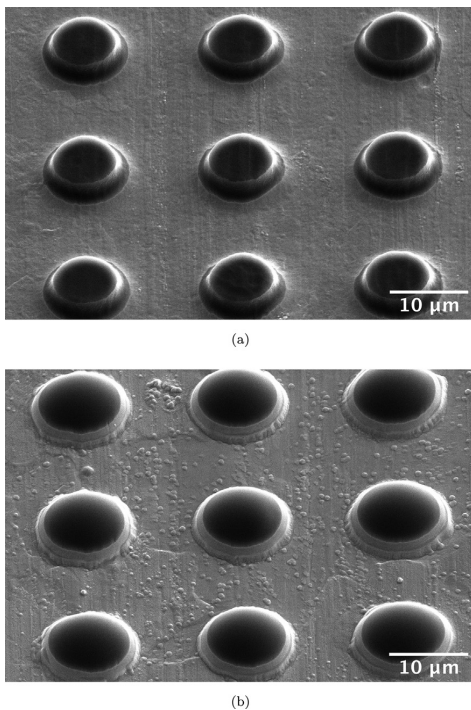


Fig. 3. Cu surface with micropillars after deposition of photoresist and 2 times etching by CAIBE. The exposure doses in the photolithography step are (a) 1700 mJ cm^{-2} (S17) and (b) 1900 mJ cm^{-2} (S19). The micropillars' height is approximately $1 \text{ }\mu\text{m}$. The width of the base of micropillars in (a) is approx. $10 \text{ }\mu\text{m}$, and in (b) the base width is approx. $13 \text{ }\mu\text{m}$. The dark color of the surfaces of the micropillars is caused by photoresist residue. In (b) some redeposited Cu is visible between the micropillars.

and the HTC's that are presented in this work are calculated with the equations in this section.

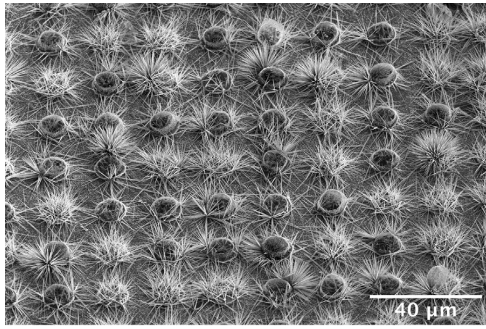
The temperature measurements are fitted with a linear equation relating the temperatures to the location of the thermocouples within the Cu cylinder. The regression gives the temperature gradient, ∇T , through the Cu cylinder and the surface temperature of the investigated substrate, T_{surf} , by extrapolation. ∇T is used to calculate the total heat flux q_{tot} through the cylinder, according to Eq. (1), where k is the thermal conductivity of Cu.

$$q_{tot} = -k\nabla T \tag{1}$$

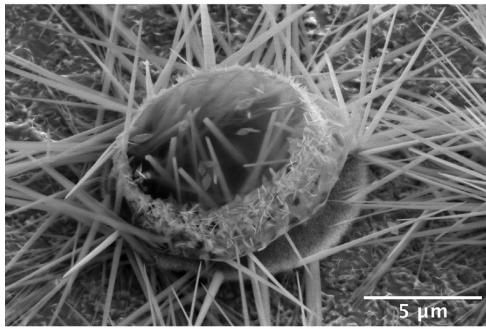
The condensation heat flux, which is the portion of the heat flux that we are interested in, is not equal to the total heat flux through the cylinder. Some heat is transported through the insulation, some goes to cooling the gas in the pressure chamber prior to condensation, and some heat is lost internally in the investigated substrate caused by the geometrical mismatch between the spherical Cu cylinder surface and the quadratic substrates. We assume that the heat loss is independent of the subcooling of the surface versus the saturation temperature. The condensation heat flux is therefore found by linearly extrapolating the heat flux data to zero subcooling, and subtracting the resulting constant value from each data series. In this way, the condensation heat flux is zero for zero subcooling, as required. Each experiment is repeated 3–6 times. The exact number is determined by the deviation in the data from experiment to experiment. After 3 experiments we evaluated the consistency in the results and determined if another series was necessary.

The condensation HTC, h_{cond} , is defined by Eq. (2), where T_{sat} is the temperature at the given saturation pressure, T_{surf} is the surface temperature, giving the subcooling of the substrate $T_{sat} - T_{surf}$. T_{sat} is found by using the Span Wagner equation of state [29] with the pressure in the chamber as input. The NIST Webbook is used for the calculation [30].

$$h_{cond} = \frac{q_{cond}}{T_{sat} - T_{surf}} \tag{2}$$

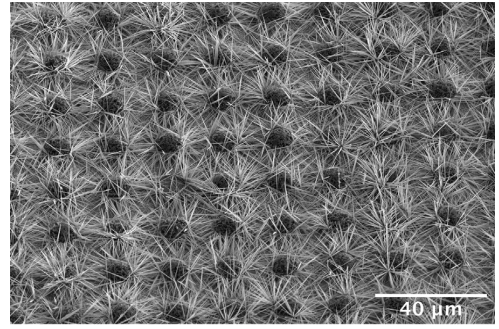


(a)

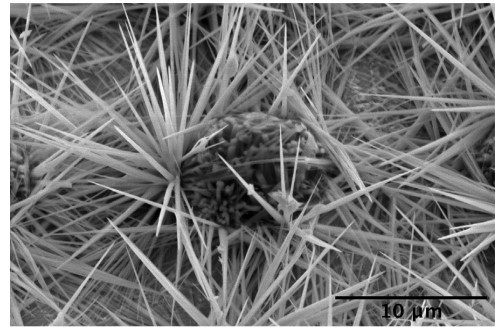


(b)

Fig. 4. SEM images of the hierarchical Cu/CuO structures for which the micro structures are fabricated with photolithography with exposure dose of 1700 mJ cm^{-2} , named S17. In (a), an overview of the surface is shown with a 1200 times magnification. In (b), one of the Cu cylinders covered in CuO flakes and nanoneedles is shown. The nanoneedles grow primarily on the top and on the sides of the microstructure, however the length of the nanoneedles are much shorter when growing on the top of the cylinder and the microscale of the Cu cylinders is intact. Smaller nanostructures, as flakes and needles, are grown at the flat surfaces between the micropillars.



(a)



(b)

Fig. 5. SEM images of the hierarchical Cu/CuO structures for which the microstructures are fabricated with photolithography with exposure dose of 1900 mJ cm^{-2} , named S19. (a) shows an overview of the surface with 1200 times magnification, where the high density of nanoneedles is evident. (b) shows one of the micro-cylinders covered in nanoneedles, 6500 times magnification. The nanoneedles grow mainly on the sides of the cylinders and in all directions partly covering the Cu surface between the cylinders with horizontal nanoneedles.

Table 1

Table with the estimated uncertainties used for calculating the overall uncertainties in heat flux and subcooling.

Parameter	Uncertainty
$TC1, TC2, TC3, TC4$	$\pm 0.0337 \text{ K}$
P_{sat}	$\pm 0.0875 \text{ bar}$
T_{sat}	$\pm 0.2 \text{ K}$
t_{TIM}	$\pm 0.05 \text{ mm}$
T_{surf}	$\pm 0-0.35 \text{ K (depending on heat flux)}$
k_{Cu}	$\pm 0.013\% [31]$
$x4 - x1$	$\pm 0.04 \text{ mm}$

2.4. Uncertainty analysis

An uncertainty analysis based on the propagation of errors have been performed. The resulting expression for the total error in heat flux, E_q , is presented in Eq. (3), and the total error in subcooling is shown in Eq. (4). The values used for calculating the errors are shown in Table 1.

$$E_q = \sqrt{\left(\frac{T_4 - T_1}{d_{1-4}}\right)^2 E_k^2 + 2\left(\frac{k}{d_{1-4}}\right)^2 E_T^2 + \left(\frac{T_4 - T_1}{d_{1-4}^2}\right)^2 E_d^2} \quad (3)$$

$$E_{\Delta T} = \sqrt{E_{T_{sat}}^2 + E_{T_{surf}}^2} \quad (4)$$

Here, E_k is the estimated error in Cu thermal conductivity, E_T is the error in the temperature measurements, and E_d is the error in the distance between the thermocouples.

The error in temperature measurements, E_T , is estimated based on the icebath calibration of the thermocouples, using the standard deviation of the estimated calibration value as a constant error in the measurements. We have estimated the temperature dependent thermal conductivity of Cu from the correlation presented by Abu-Eishah [31]. The placement of the thermocouples inside the Cu cylinder has been measured with a caliper and the error is therefore assumed to be within 0.02 mm, relating to the smallest measurable values with a caliper. The error in the saturation temperature, $E_{T_{sat}}$, is based on the given uncertainty of the pressure controller used to control the pressure in the chamber. The error in the surface temperature, $E_{T_{surf}}$, is calculated from the uncertainty in the thickness of the thermal interface material, t_{TIM} .

3. Results

Fig. 6 shows the temperature measurements in the four thermocouples embedded in the Cu cylinder during condensation experiments on the flat Cu at 15 bar. T1 is situated closest to the cylinder surface and T4 is closest to the cooling element. The temperature gradient gradually increases with decreasing temperature in the cylinder. The jumps in time are the time it takes for a new stable temperature level to be reached. The stable temperatures are

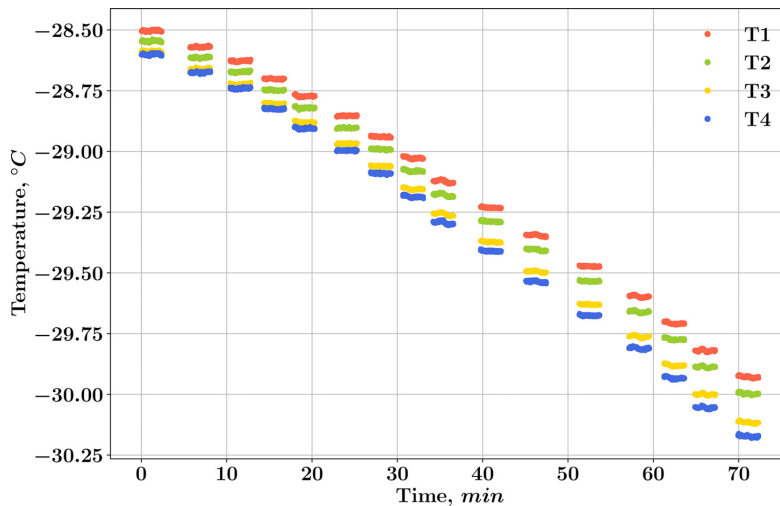


Fig. 6. Temperature measurements in the cylinder during the condensation of CO₂ on flat Cu when varying the surface temperature at 15 bar. T1–T4 are the thermocouples embedded in the cylinder, with T1 closest to the cooling element and T4 closest to the investigated surface. The jumps in time are the time it takes for a new temperature level to stabilize. Each temperature is kept for 180s.

recorded for 3 min for each level of subcooling, and the resulting average temperature gradient is used to calculate the heat flux through the cylinder with Eq. (1).

The condensation heat flux of CO₂ on Cu, S17, S19, and NS as functions of subcooling are shown in Fig. 7, with chamber pressures of 10, 15, and 20 bar. For all saturation pressures, the CO₂ condensation heat flux on the S17 substrate is significantly higher than on the three other substrates. The heat flux is within the error estimate for Cu, S19 and NS, and no significant difference between the heat transfer behavior on these surfaces is observed. For all surfaces and pressures the heat flux increases with increasing subcooling between surface and saturated gas, as expected.

The condensation HTC calculated from the heat flux data in Fig. 7 with Eq. (2), are shown in Fig. 8. For subcooling above 1K, the condensation HTC is nearly independent of subcooling on all substrates. There is a slight decrease in the condensation HTC on S17 for increasing subcooling at saturation pressures of 15 and 20 bar, while for 10 bar the HTC is approximately constant for all levels of subcooling. The condensation HTC is significantly higher on S17 compared to the other surfaces. At maximum deviation, the HTC is 66% higher on S17 than the flat Cu, S19 and NS surfaces. This occurs for 20 bar saturation pressure and approximately 1 K subcooling.

Along with the much higher values of condensation HTC on S17, the pressure dependence is also more pronounced for this surface, as shown in Fig. 9. The increase in HTC is 30% when increasing the saturation pressure from 10 to 15 bar, while it is 10% for S19, the structure with the smallest pressure dependence. When increasing the pressure from 15 to 20 bar, the HTC on Cu, S17 and S19 increases with between 1.6 and 4.2%. The HTC on the NS substrate decreases with 2.2% between 15 and 20 bar.

4. Discussion

Condensation heat transfer is a complex process and the exact physical mechanisms of the condensation on nanostructured and hierarchical structures can not be proved at this moment. Nevertheless, there are results from literature that can be looked at for an indication of the heat transfer behavior on the four substrates. As seen in the results, the HTC and the heat flux on the unstruc-

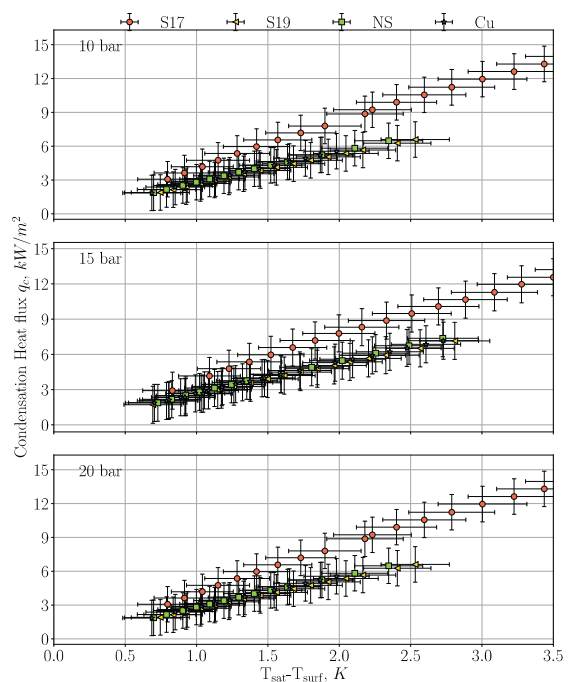


Fig. 7. Condensation heat flux data for the four investigated substrates at 10, 15, and 20 bar. Each data point is the average of repeated experiments and the errors bars are the results of the uncertainty analysis.

tured Cu, the S19 and the NS surfaces are within the uncertainty range of each other, and therefore considered equal. This is an intriguing result, and we suggest that this is caused by three competing effects: (1) lower thermal conductivity of CuO compared with Cu, (2) increase in surface area due to the nanostructures and (3) flooding of the nanostructures. An oxidized metallic surface

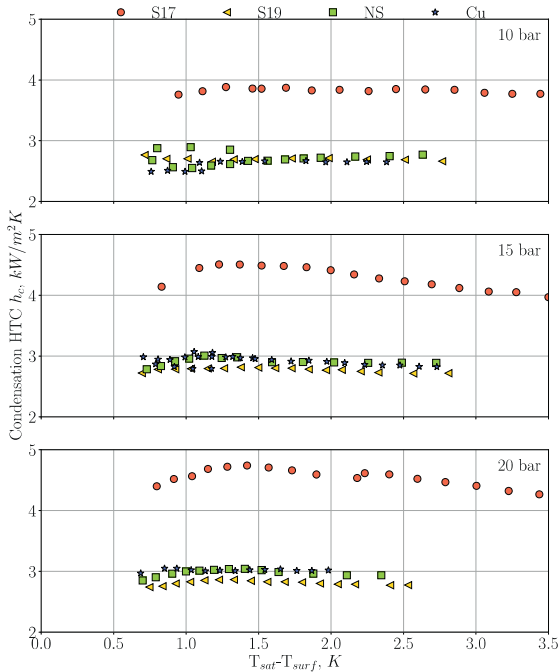


Fig. 8. Condensation HTC for Cu, S17, S19 and NS at saturation pressure of 10 bar, 15 bar, and 20 bar. Refer to Fig. 7 for uncertainty of experiments.

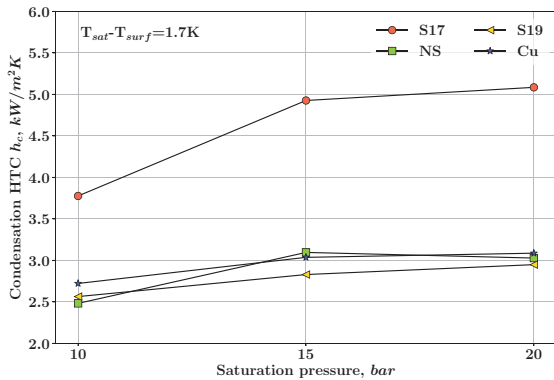


Fig. 9. The condensation HTC as a function of saturation pressure for the four investigated materials: flat Cu, S17, S19 and NS. The subcooling is 1.7 K in all cases.

generally has a lower thermal conductivity than the pure metal. This is indeed the case for Cu and CuO, for which the thermal conductivity decreases from typical values of $400 \text{ Wm}^{-1} \text{ K}^{-1}$ to $33 \text{ Wm}^{-1} \text{ K}^{-1}$ for the oxidized metal [32]. If the thermal conductivity alone would have been the determining factor, as in Hoenig et al. [33], the HTC should have been lower on the structured surfaces. It is therefore apparent that the surface structures increase the heat transfer in such a way that they balance the decrease in thermal conductivity caused by the oxidation. An increase in heat transfer due to surface structures is attributed to the increased heat transfer area. This is well-known for augmented surfaces such as fins on tubes [34] and pin-fins on tubes [35]. However, if the spacing between the surface structures is small, the heat trans-

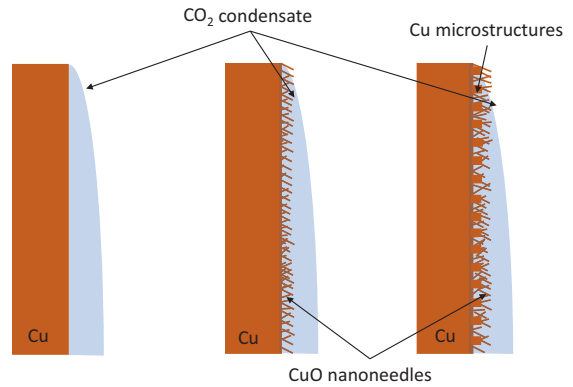


Fig. 10. Sketch of the flooding of the high density nanostructured surfaces, S17 and NS.

fer increase due to augmented surface area can be counteracted by surface flooding. Ali et al. [36] showed that by lowering the spacing between the surface structures, the effect of increased heat transfer area is balanced by a heat transfer reduction caused by flooding. On both the S19 and the NS surfaces the nanoneedle density is high and the entire structures on the surfaces are therefore likely completely flooded during condensation. The resulting HTCs are within the uncertainty range of each other and indistinguishable from the HTCs on the unstructured Cu. The increase in heat transfer caused by the higher area on the surfaces are hence completely balanced by flooding and the low thermal conductivity of the CuO nanoneedles. As a consequence, the heat transfer the S19, NS and untreated Cu resembles conventional filmwise condensation on flat surfaces as elucidated in Fig. 10. The film thickness on the S19 and NS surfaces are higher than on the bare Cu surface due to liquid retention in the flooded areas, but the increase in heat transfer area balances the increased thermal resistance through the film.

The S17 surface clearly exhibits a different thermal behavior than the other surfaces. The heat flux and the HTC are significantly higher for this surface. The lower nanoneedle density increases the hierarchical nature of the surface, and reduces the likelihood of complete flooding. The surface area between the micropillars is not filled with nanoneedles, as on the S19 surface, and the flat area is beneficial for the heat transfer. The proposed condensation mechanism is that the nucleation and spreading of the condensate film occurs on the non-structured areas between the micropillars and that the nanoneedles and the micropillars reduce the film thickness. The unstructured areas between the micropillars are not completely flat, and spikes and grooves are available nucleation sites. The reduced film thickness is a result of a more efficient drainage of the CO_2 liquid along the space between the micro- and nanostructures, compared to the pinned liquid on the S19 and NS surfaces. Efficient drainage will lead to a thinner CO_2 liquid film, which again increases the HTC.

According to the model by Ali et al. [36], flooding is less likely to occur on the S17 surface due to the larger spacing between the structures. Returning to the effect of the three competing factors 1), 2) and 3) above, where the latter was related to flooding, the resulting the HTC is higher on S17 compared to S19 and NS. In contrast to the work by Aili et al. [19], we here show that an optimal combination of micro- and nanostructures is beneficial for heat transport in certain cases, and especially when the hierarchical nature of the surface is pronounced, such as for S17.

The influence of pressure on the heat transfer is highest for the NS and the S17 surface, which both show a high increase in the HTC between 10 and 15 bar, see Fig. 9. The S17 surface also exhibit a slight increase in HTC when reaching 20 bar saturation pressure, while the HTC on the NS structure decreases between 15 and 20 bar saturation pressure. According to Preston et al. flooding of the nanostructures will occur in wicking condensation at high values of subcooling due to the high amount of condensate as the subcooling is increased [37]. When increasing the saturation pressure, on the other hand, the condensate film thickness decreases and the HTC increases. Flooding is therefore not the likely explanation of the apparent saturation of the HTC. The plateau in the HTC is therefore explained by the fluid properties of CO₂ and how these are altered with pressure. Especially, the viscosity is decreased with increasing pressure and the result could be a higher downward flow rate of the liquid. This would again lead to a thinner liquid film and an increased heat transfer. One could imagine that the liquid flow down the surface deteriorates the nanostructures, and that this could influence the pressure dependence of the heat transfer. The nanoneedles could be bent or broken and flushed down along with the condensate. We have, however, investigated the surfaces before and after condensation, and find that both the micropillars and nanoneedles are intact after repeated condensation experiments. Details can be found in Supplementary Information.

5. Conclusions and outlook

We have in this work experimentally investigated the heat transfer behavior of Cu based surfaces during the condensation of CO₂. Three different micro- and nanostructured surfaces have been fabricated and compared in terms of heat flux and heat transfer coefficient during the condensation. The surfaces are (1) a purely nanostructured surface where CuO nanoneedles are grown on a Cu substrate, (2) a hierarchical surface with Cu micropillars underneath CuO nanoneedles with high density, and (3) a surface similar to the second, but where the nanoneedles are much less dense. We have shown that when the right balance between structured and unstructured surface area is found, the outcome is an increase in the condensation heat transfer. On surfaces with a high density of CuO nanoneedles, the reduced heat transfer due to lower thermal conductivity of the oxidized surface and increased heat transfer due to the higher effective surface area neutralize each other. The HTCs are therefore similar on the purely nanostructured surface, the micro- and nanostructured surface with high nanostructure density, and the flat untreated surface. However, when the density of the nanostructures is lower, such that the true hierarchical nature of the surface is more pronounced, the HTC is increased with maximum 66% compared to the untreated surface. The work show that surface structures have a potential of increasing condensation heat transfer of CO₂ if designed and fabricated properly. The optimal design criteria have yet to be developed, but the path of hierarchical surfaces is very promising and should be followed in future work.

Declaration of Competing Interest

Authors declare that they have no conflict of interest.

CRedit authorship contribution statement

Ingrid Snustad: Conceptualization, Methodology, Software, Validation, Formal analysis, Investigation, Data curation, Writing - original draft, Writing - review & editing, Visualization. **Lene Hollund:** Validation, Investigation, Data curation, Writing - review & editing. **Åsmund Ervik:** Conceptualization, Methodology, Software,

Validation, Formal analysis, Writing - review & editing, Supervision. **Anders Austegard:** Methodology, Formal analysis, Writing - review & editing. **Amy Brunsvold:** Conceptualization, Methodology, Writing - review & editing, Supervision. **Jianying He:** Writing - review & editing, Supervision. **Zhiliang Zhang:** Conceptualization, Methodology, Formal analysis, Writing - review & editing.

Acknowledgments

This publication has been produced with the support of the Research Council of Norway through the CLIMIT funding program (254813), and through the Norwegian Micro- and Nano-Fabrication Facility, NorFab (245963/F50).

Supplementary material

Supplementary material associated with this article can be found, in the online version, at [10.1016/j.ijheatmasstransfer.2021.121367](https://doi.org/10.1016/j.ijheatmasstransfer.2021.121367)

References

- [1] S.K. Fischer, Total equivalent warming impact: a measure of the global warming impact of CFC alternatives in refrigerating equipment, *Int. J. Refrig.* 16 (6) (1993) 423–428, doi:[10.1016/0140-7007\(93\)90059-h](https://doi.org/10.1016/0140-7007(93)90059-h).
- [2] K.M. Tsamos, Y.T. Ge, I. Santosa, S.A. Tassou, G. Bianchi, Z. Mylona, Energy analysis of alternative CO₂ refrigeration system configurations for retail food applications in moderate and warm climates, *Energy Convers. Manag.* 150 (2017) 822–829, doi:[10.1016/j.enconman.2017.03.020](https://doi.org/10.1016/j.enconman.2017.03.020).
- [3] S. Liu, H. Qi, V. Nian, B. Liu, B. Dai, Z. Sun, X. Li, J. Yuan, A new correlation for carbon dioxide boiling heat transfer coefficient outside evaporating tubes, *J. Clean. Prod.* 276 (2020) 123050, doi:[10.1016/j.jclepro.2020.123050](https://doi.org/10.1016/j.jclepro.2020.123050).
- [4] B. Dai, H. Qi, S. Liu, M. Ma, Z. Zhong, H. Li, M. Song, Z. Sun, Evaluation of transcritical CO₂ heat pump system integrated with mechanical subcooling by utilizing energy, exergy and economic methodologies for residential heating, *Energy Convers. Manag.* 192 (2019) 202–220, doi:[10.1016/j.enconman.2019.03.094](https://doi.org/10.1016/j.enconman.2019.03.094).
- [5] A. Aspelund, K. Jordal, Gas conditioning - the interface between CO₂ capture and transport, *Int. J. Greenhouse Gas Control* 1 (3) (2007) 343–354, doi:[10.1016/S1750-5836\(07\)00040-0](https://doi.org/10.1016/S1750-5836(07)00040-0).
- [6] F. Neele, R. de Kler, M. Nienoord, P. Brownsort, J. Koornneef, S. Belfroid, L. PETERS, A. vanWijhe, D. Loeve, CO₂ transport by ship: the way forward in Europe, in: 13th International Conference on Greenhouse Gas Control Technologies, GHGT-13, T14, Energy Procedia, 2017, pp. 6824–6834, doi:[10.1016/j.egypro.2017.03.183](https://doi.org/10.1016/j.egypro.2017.03.183).
- [7] E.S. Rubin, J.E. Davison, H.J. Herzog, The cost of CO₂ capture and storage, *Int. J. Greenhouse Gas Control* 40 (2015) 378–400, doi:[10.1016/j.ijggc.2015.05.018](https://doi.org/10.1016/j.ijggc.2015.05.018).
- [8] I. Snustad, I.T. Røe, A. Brunsvold, Å. Ervik, J. He, Z. Zhang, A review on wetting and water condensation - perspectives for CO₂ condensation, *Adv. Colloid Interface Sci.* 256 (2018) 291–304, doi:[10.1016/j.cis.2018.03.008](https://doi.org/10.1016/j.cis.2018.03.008).
- [9] D. Attinger, C. Frankiewicz, A.R. Betz, T.M. Schutzius, R. Ganguly, A. Das, C.-J. Kim, C.M. Megaridis, Surface engineering for phase change heat transfer: a review, *MRS Energy Sustain.* 1 (2014), doi:[10.1557/mre.2014.9](https://doi.org/10.1557/mre.2014.9).
- [10] T.J. Hendricks, S. Krishnan, C. Choi, C.-H. Chang, B. Paul, Enhancement of pool-boiling heat transfer using nanostructured surfaces on aluminum and copper, *Int. J. Heat Mass Transf.* 53 (15–16) (2010) 3357–3365, doi:[10.1016/j.ijheatmasstransfer.2010.02.025](https://doi.org/10.1016/j.ijheatmasstransfer.2010.02.025).
- [11] Y. Nam, S. Sharratt, G. Cha, Y.S. Ju, Characterization and modeling of the heat transfer performance of nanostructured Cu micropost wicks, *J. Heat Transf.* 133 (10) (2011) 101502, doi:[10.1115/1.4004168](https://doi.org/10.1115/1.4004168).
- [12] D. Saeidi, A.A. Alemrajabi, Experimental investigation of pool boiling heat transfer and critical heat flux of nanostructured surfaces, *Int. J. Heat Mass Transf.* 60 (2013) 440–449, doi:[10.1016/j.ijheatmasstransfer.2013.01.016](https://doi.org/10.1016/j.ijheatmasstransfer.2013.01.016).
- [13] C. Li, Z. Wang, P.-I. Wang, Y. Peles, N. Koratkar, G.P. Peterson, Nanostructured copper interfaces for enhanced boiling, *Small* 4 (8) (2008) 1084–1088, doi:[10.1002/sml.200700991](https://doi.org/10.1002/sml.200700991).
- [14] R. Chen, M.-C. Lu, V. Srinivasan, Z. Wang, H.H. Cho, A. Majumdar, Nanowires for enhanced boiling heat transfer, *Nano Lett.* 9 (2) (2009) 548–553, doi:[10.1021/nl8026857](https://doi.org/10.1021/nl8026857).
- [15] J.B. Boreyko, C.-H. Chen, Self-propelled dropwise condensate on superhydrophobic surfaces, *Phys. Rev. Lett.* 103 (18) (2009), doi:[10.1103/PhysRevLett.103.184501](https://doi.org/10.1103/PhysRevLett.103.184501).
- [16] J. Cheng, A. Vandadi, C.-L. Chen, Condensation heat transfer on two-tier superhydrophobic surfaces, *Appl. Phys. Lett.* 101 (13) (2012) 131909, doi:[10.1063/1.4756800](https://doi.org/10.1063/1.4756800).
- [17] R. Wen, X. Ma, Y.-C. Lee, R. Yang, Liquid-vapor phase-change heat transfer on functionalized nanowired surfaces and beyond, *Joule* 2 (11) (2018) 2307–2347, doi:[10.1016/j.joule.2018.08.014](https://doi.org/10.1016/j.joule.2018.08.014).
- [18] J. Ma, S. Sett, H. Cha, X. Yan, N. Miljkovic, Recent developments, challenges, and pathways to stable dropwise condensation: a perspective, *Appl. Phys. Lett.* 116 (26) (2020) 260501, doi:[10.1063/5.0011642](https://doi.org/10.1063/5.0011642).

- [19] A. Aili, Q. Ge, T. Zhang, Effect of Mini/Micro/Nanostructures on Film-wise Condensation of Low-Surface-Tension Fluids, *J. Heat Transf.* 140 (10) (2018) 102402, doi:[10.1115/1.4040143](https://doi.org/10.1115/1.4040143), https://asmedigitalcollection.asme.org/heattransfer/article-pdf/140/10/102402/6219575/ht_140_10_102402.pdf
- [20] H.M. Ali, An analytical model for prediction of condensate flooding on horizontal pin-fin tubes, *Int. J. Heat Mass Transf.* 106 (2017) 1120–1124, doi:[10.1016/j.ijheatmasstransfer.2016.10.088](https://doi.org/10.1016/j.ijheatmasstransfer.2016.10.088).
- [21] H.M. Ali, A. Briggs, A semi-empirical model for free-convection condensation on horizontal pin-fin tubes, *Int. J. Heat Mass Transf.* 81 (2015) 157–166, doi:[10.1016/j.ijheatmasstransfer.2014.10.008](https://doi.org/10.1016/j.ijheatmasstransfer.2014.10.008).
- [22] A.T. Wijayanta, T. Miyazaki, S. Koyama, Refrigerant distribution in horizontal headers with downward minichannel-branching conduits; experiment, empirical correlation and two-phase flow pattern map, *Exp. Therm. Fluid Sci.* 81 (2017) 430–444, doi:[10.1016/j.expthermflusci.2016.09.011](https://doi.org/10.1016/j.expthermflusci.2016.09.011).
- [23] J. Wu, Å. Ervik, I. Snustad, S. Xiao, A. Brunsvold, J. He, Z. Zhang, Contact angle and condensation of a CO₂ droplet on a solid surface, *J. Phys. Chem. C* 123 (1) (2019) 443–451, doi:[10.1021/acs.jpcc.8b08927](https://doi.org/10.1021/acs.jpcc.8b08927).
- [24] J. Wu, I. Snustad, Å. Ervik, A. Brunsvold, J. He, Z. Zhang, CO₂ wetting on pillar-nanostructured substrates, *Nanotechnology* 31 (24) (2020) 245403, doi:[10.1088/1361-6528/ab7c49](https://doi.org/10.1088/1361-6528/ab7c49).
- [25] I. Snustad, Å. Ervik, A. Austegard, A. Brunsvold, J. He, Z. Zhang, Heat transfer characteristics of CO₂ condensation on common heat exchanger materials: method development and experimental results, 2021. Under Review.
- [26] Z. He, J. He, Z. Zhang, Selective growth of metallic nanostructures on microstructured copper substrate in solution, *CrystEngComm* 17 (2015) 7262–7269, doi:[10.1039/C5CE01093D](https://doi.org/10.1039/C5CE01093D).
- [27] Z. He, Z. Zhang, J. He, CuO/Cu based superhydrophobic and self-cleaning surfaces, *Scr. Mater.* 118 (2016) 60–64, doi:[10.1016/j.scriptamat.2016.03.015](https://doi.org/10.1016/j.scriptamat.2016.03.015), <http://www.sciencedirect.com/science/article/pii/S1359646216300884>
- [28] K. Akhtar, S.A. Khan, S.B. Khan, A.M. Asiri, Scanning electron microscopy: principle and applications in nanomaterials characterization, in: *Handbook of Materials Characterization*, Springer International Publishing, 2018, pp. 113–145, doi:[10.1007/978-3-319-92955-2_4](https://doi.org/10.1007/978-3-319-92955-2_4).
- [29] R. Span, W. Wagner, A new equation of state for carbon dioxide covering the fluid region from the triple-point temperature to 1100 K at pressures up to 800 MPa, *J. Phys. Chem. Ref. Data* 25 (6) (1996) 1509–1596, doi:[10.1063/1.555991](https://doi.org/10.1063/1.555991).
- [30] National Institute of Standards and Technology, 2018, <https://webbook.nist.gov/chemistry/fluid/>.
- [31] S.I. Abu-Eishah, Correlations for the thermal conductivity of metals as a function of temperature, *Int. J. Thermophys.* 22 (6) (2001) 1855–1868, doi:[10.1023/a:1013155404019](https://doi.org/10.1023/a:1013155404019).
- [32] M. Liu, M. Lin, C. Wang, Enhancements of thermal conductivities with Cu, CuO, and carbon nanotube nanofluids and application of MWNT/water nanofluid on a water chiller system, *Nanoscale Res. Lett.* 6 (1) (2011) 297, doi:[10.1186/1556-276x-6-297](https://doi.org/10.1186/1556-276x-6-297).
- [33] S.H. Hoenig, S. Modak, Z. Chen, M. Kaviani, J.F. Gilchrist, R.W. Bonner, Role of substrate thermal conductivity and vapor pressure in dropwise condensation, *Appl. Therm. Eng.* 178 (2020) 115529, doi:[10.1016/j.applthermaleng.2020.115529](https://doi.org/10.1016/j.applthermaleng.2020.115529).
- [34] C.-Y. Zhao, W.-T. Ji, P.-H. Jin, Y.-J. Zhong, W.-Q. Tao, The influence of surface structure and thermal conductivity of the tube on the condensation heat transfer of R134A and R404A over single horizontal enhanced tubes, *Appl. Therm. Eng.* 125 (2017) 1114–1122, doi:[10.1016/j.applthermaleng.2017.06.133](https://doi.org/10.1016/j.applthermaleng.2017.06.133).
- [35] H.M. Ali, A. Briggs, Condensation of ethylene glycol on pin-fin tubes: effect of circumferential pin spacing and thickness, *Appl. Therm. Eng.* 49 (2012) 9–13, doi:[10.1016/j.applthermaleng.2011.08.017](https://doi.org/10.1016/j.applthermaleng.2011.08.017).
- [36] H.M. Ali, M.Z. Qasim, M. Ali, Free convection condensation heat transfer of steam on horizontal square wire wrapped tubes, *Int. J. Heat Mass Transf.* 98 (2016) 350–358, doi:[10.1016/j.ijheatmasstransfer.2016.03.053](https://doi.org/10.1016/j.ijheatmasstransfer.2016.03.053).
- [37] D.J. Preston, K.L. Wilke, Z. Lu, S.S. Cruz, Y. Zhao, L.L. Becerra, E.N. Wang, Gravitationally driven wicking for enhanced condensation heat transfer, *Langmuir* 34 (15) (2018) 4658–4664, doi:[10.1021/acs.langmuir.7b04203](https://doi.org/10.1021/acs.langmuir.7b04203).

Supplementary Information

Mechanical stability

We have conducted a small study to investigate the mechanical abrasion of the nanostructures caused by the low temperature, the elevated pressures or the condensation itself. The hypothesis was that the nanostructures could withstand the pressure, the temperatures and the flow of liquid CO₂. To investigate this we imaged the surfaces in a SEM before and after conducting the condensation experiments. The images show that the nanostructures are intact after condensation, and that no noticeable alteration of the surfaces could be detected. SEM images recorded before and after the condensation experiments are shown in Figure 1.

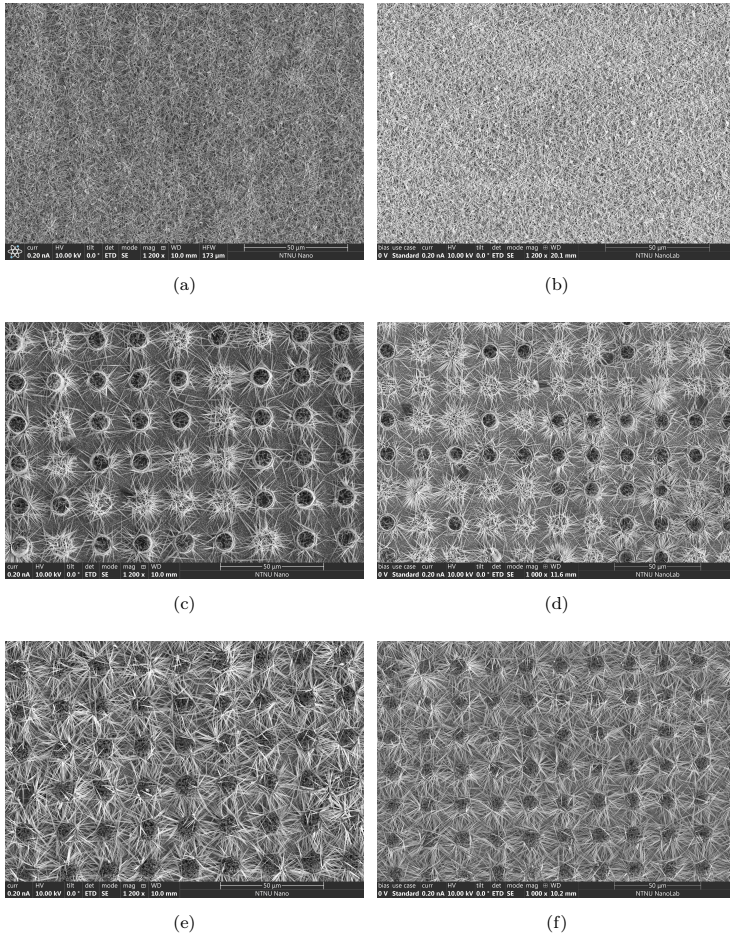


Figure 1: SEM images of the three structured surfaces that have been fabricated and investigated in this work. The left column ((a), (c), and (e)) are images recorded before condensation and the right column ((b), (d) and (f)) are recorded after the condensation. (a) and (b) are images of the NS surface, (c) and (d) of the S17 surface and (e) and (f) of the S19 surface. The different appearance of the images in the right and left column is solely due to the difference in contrast and brightness settings of the SEM.

Appendix **B**

Publication list

**Department of Structural Engineering
Norwegian University of Science and Technology (NTNU)**

**DEPARTMENT OF STRUCTURAL ENGINEERING
NORWEGIAN UNIVERSITY OF SCIENCE AND TECHNOLOGY**

N-7491 TRONDHEIM, NORWAY
Telephone: +47 73 59 47 00

"Reliability Analysis of Structural Systems using Nonlinear Finite Element Methods",

C. A. Holm, 1990:23, ISBN 82-7119-178-0.

"Uniform Stratified Flow Interaction with a Submerged Horizontal Cylinder",

Ø. Arntsen, 1990:32, ISBN 82-7119-188-8.

"Large Displacement Analysis of Flexible and Rigid Systems Considering Displacement-Dependent Loads and Nonlinear Constraints",

K. M. Mathisen, 1990:33, ISBN 82-7119-189-6.

"Solid Mechanics and Material Models including Large Deformations",

E. Levold, 1990:56, ISBN 82-7119-214-0, ISSN 0802-3271.

"Inelastic Deformation Capacity of Flexurally-Loaded Aluminium Alloy Structures",

T. Welo, 1990:62, ISBN 82-7119-220-5, ISSN 0802-3271.

"Visualization of Results from Mechanical Engineering Analysis",

K. Aarnes, 1990:63, ISBN 82-7119-221-3, ISSN 0802-3271.

"Object-Oriented Product Modeling for Structural Design",

S. I. Dale, 1991:6, ISBN 82-7119-258-2, ISSN 0802-3271.

"Parallel Techniques for Solving Finite Element Problems on Transputer Networks",

T. H. Hansen, 1991:19, ISBN 82-7119-273-6, ISSN 0802-3271.

"Statistical Description and Estimation of Ocean Drift Ice Environments",

R. Korsnes, 1991:24, ISBN 82-7119-278-7, ISSN 0802-3271.

"Properties of concrete related to fatigue damage: with emphasis on high strength concrete",

G. Petkovic, 1991:35, ISBN 82-7119-290-6, ISSN 0802-3271.

"Turbidity Current Modelling",

B. Brørs, 1991:38, ISBN 82-7119-293-0, ISSN 0802-3271.

"Zero-Slump Concrete: Rheology, Degree of Compaction and Strength. Effects of Fillers as Part Cement-Replacement",

C. Sørensen, 1992:8, ISBN 82-7119-357-0, ISSN 0802-3271.

"Nonlinear Analysis of Reinforced Concrete Structures Exposed to Transient Loading",

K. V. Høiseth, 1992:15, ISBN 82-7119-364-3, ISSN 0802-3271.

"Finite Element Formulations and Solution Algorithms for Buckling and Collapse

- Analysis of Thin Shells",
R. O. Bjærnum, 1992:30, ISBN 82-7119-380-5, ISSN 0802-3271.
- "Response Statistics of Nonlinear Dynamic Systems",
J. M. Johnsen, 1992:42, ISBN 82-7119-393-7, ISSN 0802-3271.
- "Digital Models in Engineering. A Study on why and how engineers build and operate digital models for decision support",
J. Høyte, 1992:75, ISBN 82-7119-429-1, ISSN 0802-3271.
- "Sparse Solution of Finite Element Equations",
A. C. Damhaug, 1992:76, ISBN 82-7119-430-5, ISSN 0802-3271.
- "Some Aspects of Floating Ice Related to Sea Surface Operations in the Barents Sea",
S. Løset, 1992:95, ISBN 82-7119-452-6, ISSN 0802-3271.
- "Modelling of Cyclic Plasticity with Application to Steel and Aluminium Structures",
O. S. Hopperstad, 1993:7, ISBN 82-7119-461-5, ISSN 0802-3271.
- "The Free Formulation: Linear Theory and Extensions with Applications to Tetrahedral Elements with Rotational Freedoms",
G. Skeie, 1993:17, ISBN 82-7119-472-0, ISSN 0802-3271.
- "Høyfast betongs motstand mot piggdekkslitasje. Analyse av resultater fra prøving i Veisliter'n",
T. Tveter, 1993:62, ISBN 82-7119-522-0, ISSN 0802-3271.
- "A Nonlinear Finite Element Based on Free Formulation Theory for Analysis of Sandwich Structures",
O. Aamlid, 1993:72, ISBN 82-7119-534-4, ISSN 0802-3271.
- "The Effect of Curing Temperature and Silica Fume on Chloride Migration and Pore Structure of High Strength Concrete",
C. J. Hauck, 1993:90, ISBN 82-7119-553-0, ISSN 0802-3271.
- "Failure of Concrete under Compressive Strain Gradients",
G. Markeset, 1993:110, ISBN 82-7119-575-1, ISSN 0802-3271.
- "An experimental study of internal tidal amphidromes in Vestfjorden",
J. H. Nilsen, 1994:39, ISBN 82-7119-640-5, ISSN 0802-3271.
- "Structural analysis of oil wells with emphasis on conductor design",
H. Larsen, 1994:46, ISBN 82-7119-648-0, ISSN 0802-3271.
- "Adaptive methods for non-linear finite element analysis of shell structures",
K. M. Okstad, 1994:66, ISBN 82-7119-670-7, ISSN 0802-3271.
- "On constitutive modelling in nonlinear analysis of concrete structures",
O. Fyrileiv, 1994:115, ISBN 82-7119-725-8, ISSN 0802-3271.

"Fluctuating wind load and response of a line-like engineering structure with emphasis on motion-induced wind forces",

J. Bogunovic Jakobsen, 1995:62, ISBN 82-7119-809-2, ISSN 0802-3271.

"An experimental study of beam-columns subjected to combined torsion, bending and axial actions",

A. Aalberg, 1995:66, ISBN 82-7119-813-0, ISSN 0802-3271.

"Scaling and cracking in unsealed freeze/thaw testing of Portland cement and silica fume concretes",

S. Jacobsen, 1995:101, ISBN 82-7119-851-3, ISSN 0802-3271.

"Damping of water waves by submerged vegetation. A case study of laminaria hyperborea",

A. M. Dubi, 1995:108, ISBN 82-7119-859-9, ISSN 0802-3271.

"The dynamics of a slope current in the Barents Sea",

Sheng Li, 1995:109, ISBN 82-7119-860-2, ISSN 0802-3271.

"Modellering av delmaterialenes betydning for betongens konsistens",

Ernst Mørtzell, 1996:12, ISBN 82-7119-894-7, ISSN 0802-3271.

"Bending of thin-walled aluminium extrusions",

Birgit Søvik Opheim, 1996:60, ISBN 82-7119-947-1, ISSN 0802-3271.

"Material modelling of aluminium for crashworthiness analysis",

Torodd Berstad, 1996:89, ISBN 82-7119-980-3, ISSN 0802-3271.

"Estimation of structural parameters from response measurements on submerged floating tunnels",

Rolf Magne Larssen, 1996:119, ISBN 82-471-0014-2, ISSN 0802-3271.

"Numerical modelling of plain and reinforced concrete by damage mechanics",

Mario A. Polanco-Loria, 1997:20, ISBN 82-471-0049-5, ISSN 0802-3271.

"Nonlinear random vibrations - numerical analysis by path integration methods",

Vibeke Moe, 1997:26, ISBN 82-471-0056-8, ISSN 0802-3271.

"Numerical prediction of vortex-induced vibration by the finite element method",

Joar Martin Dalheim, 1997:63, ISBN 82-471-0096-7, ISSN 0802-3271.

"Time domain calculations of buffeting response for wind sensitive structures",

Ketil Aas-Jakobsen, 1997:148, ISBN 82-471-0189-0, ISSN 0802-3271.

"A numerical study of flow about fixed and flexibly mounted circular cylinders",

Trond Stokka Meling, 1998:48, ISBN 82-471-0244-7, ISSN 0802-3271.

"Estimation of chloride penetration into concrete bridges in coastal areas",

Per Egil Steen, 1998:89, ISBN 82-471-0290-0, ISSN 0802-3271.

"Stress-resultant material models for reinforced concrete plates and shells",

Jan Arve Øverli, 1998:95, ISBN 82-471-0297-8, ISSN 0802-3271.

"Chloride binding in concrete. Effect of surrounding environment and concrete composition",

Claus Kenneth Larsen, 1998:101, ISBN 82-471-0337-0, ISSN 0802-3271.

"Rotational capacity of aluminium alloy beams",

Lars A. Moen, 1999:1, ISBN 82-471-0365-6, ISSN 0802-3271.

"Stretch Bending of Aluminium Extrusions",

Arild H. Clausen, 1999:29, ISBN 82-471-0396-6, ISSN 0802-3271.

"Aluminium and Steel Beams under Concentrated Loading",

Tore Tryland, 1999:30, ISBN 82-471-0397-4, ISSN 0802-3271.

"Engineering Models of Elastoplasticity and Fracture for Aluminium Alloys",

Odd-Geir Lademo, 1999:39, ISBN 82-471-0406-7, ISSN 0802-3271.

"Kapasitet og duktilitet av dybelforbindelser i trekonstruksjoner",

Jan Siem, 1999:46, ISBN 82-471-0414-8, ISSN 0802-3271.

"Etablering av distribuert ingeniørarbeid; Teknologiske og organisatoriske erfaringer fra en norsk ingeniørbedrift",

Lars Line, 1999:52, ISBN 82-471-0420-2, ISSN 0802-3271.

"Estimation of Earthquake-Induced Response",

Símon Ólafsson, 1999:73, ISBN 82-471-0443-1, ISSN 0802-3271.

"Coastal Concrete Bridges: Moisture State, Chloride Permeability and Aging Effects",

Ragnhild Holen Relling, 1999:74, ISBN 82-471-0445-8, ISSN 0802-3271.

"Capacity Assessment of Titanium Pipes Subjected to Bending and External Pressure",

Arve Bjørset, 1999:100, ISBN 82-471-0473-3, ISSN 0802-3271.

"Validation of Numerical Collapse Behaviour of Thin-Walled Corrugated Panels",

Håvar Ilstad, 1999:101, ISBN 82-471-0474-1, ISSN 0802-3271.

"Strength and Ductility of Welded Structures in Aluminium Alloys",

Mirosław Matusiak, 1999:113, ISBN 82-471-0487-3, ISSN 0802-3271.

"Thermal Dilation and Autogenous Deformation as Driving Forces to Self-Induced Stresses in High Performance Concrete",

Øyvind Bjøntegaard, 1999:121, ISBN 82-7984-002-8, ISSN 0802-3271.

"Some Aspects of Ski Base Sliding Friction and Ski Base Structure",

Dag Anders Moldestad, 1999:137, ISBN 82-7984-019-2, ISSN 0802-3271.

"Electrode reactions and corrosion resistance for steel in mortar and concrete",

Roy Antonsen, 2000:10, ISBN 82-7984-030-3, ISSN 0802-3271.

"Hydro-Physical Conditions in Kelp Forests and the Effect on Wave Damping and Dune Erosion. A case study on Laminaria Hyperborea",
Stig Magnar Løvås, 2000:28, ISBN 82-7984-050-8, ISSN 0802-3271.

"Random Vibration and the Path Integral Method",
Christian Skaug, 2000:39, ISBN 82-7984-061-3, ISSN 0802-3271.

"Buckling and geometrical nonlinear beam-type analyses of timber structures",
Trond Even Eggen, 2000:56, ISBN 82-7984-081-8, ISSN 0802-3271.

"Structural Crashworthiness of Aluminium Foam-Based Components",
Arve Grønsund Hanssen, 2000:76, ISBN 82-7984-102-4, ISSN 0809-103X.

"Measurements and simulations of the consolidation in first-year sea ice ridges, and some aspects of mechanical behaviour",
Knut V. Høyland, 2000:94, ISBN 82-7984-121-0, ISSN 0809-103X.

"Kinematics in Regular and Irregular Waves based on a Lagrangian Formulation",
Svein Helge Gjøsund, 2000:86, ISBN 82-7984-112-1, ISSN 0809-103X.

"Self-Induced Cracking Problems in Hardening Concrete Structures",
Daniela Bosnjak, 2000:121, ISBN 82-7984-151-2, ISSN 0809-103X.

"Ballistic Penetration and Perforation of Steel Plates",
Tore Børvik, 2000:124, ISBN 82-7984-154-7, ISSN 0809-103X.

"Freeze-Thaw resistance of Concrete. Effect of: Curing Conditions, Moisture Exchange and Materials",
Terje Finnerup Rønning, 2001:14, ISBN 82-7984-165-2, ISSN 0809-103X

"Structural behaviour of post tensioned concrete structures. Flat slab. Slabs on ground",
Steinar Trygstad, 2001:52, ISBN 82-471-5314-9, ISSN 0809-103X.

"Slipforming of Vertical Concrete Structures. Friction between concrete and slipform panel",
Kjell Tore Fosså, 2001:61, ISBN 82-471-5325-4, ISSN 0809-103X.

"Some numerical methods for the simulation of laminar and turbulent incompressible flows",
Jens Holmen, 2002:6, ISBN 82-471-5396-3, ISSN 0809-103X.

"Improved Fatigue Performance of Threaded Drillstring Connections by Cold Rolling",
Steinar Kristoffersen, 2002:11, ISBN: 82-421-5402-1, ISSN 0809-103X.

"Deformations in Concrete Cantilever Bridges: Observations and Theoretical Modelling",
Peter F. Takács, 2002:23, ISBN 82-471-5415-3, ISSN 0809-103X.

"Stiffened aluminium plates subjected to impact loading",

Hilde Giæver Hildrum, 2002:69, ISBN 82-471-5467-6, ISSN 0809-103X.

"Full- and model scale study of wind effects on a medium-rise building in a built up area",

Jónas Thór Snæbjörnsson, 2002:95, ISBN82-471-5495-1, ISSN 0809-103X.

"Evaluation of Concepts for Loading of Hydrocarbons in Ice-infested water",

Arnor Jensen, 2002:114, ISBN 82-417-5506-0, ISSN 0809-103X.

"Numerical and Physical Modelling of Oil Spreading in Broken Ice",

Janne K. Økland Gjøsteen, 2002:130, ISBN 82-471-5523-0, ISSN 0809-103X.

"Diagnosis and protection of corroding steel in concrete",

Franz Pruckner, 20002:140, ISBN 82-471-5555-4, ISSN 0809-103X.

"Tensile and Compressive Creep of Young Concrete: Testing and Modelling",

Dawood Atrushi, 2003:17, ISBN 82-471-5565-6, ISSN 0809-103X.

"Rheology of Particle Suspensions. Fresh Concrete, Mortar and Cement Paste with Various Types of Lignosulfonates",

Jon Elvar Wallevik, 2003:18, ISBN 82-471-5566-4, ISSN 0809-103X.

"Oblique Loading of Aluminium Crash Components",

Aase Reyes, 2003:15, ISBN 82-471-5562-1, ISSN 0809-103X.

"Utilization of Ethiopian Natural Pozzolans",

Surafel Ketema Desta, 2003:26, ISBN 82-471-5574-5, ISSN:0809-103X.

"Behaviour and strength prediction of reinforced concrete structures with discontinuity regions",

Helge Brå, 2004:11, ISBN 82-471-6222-9, ISSN 1503-8181.

"High-strength steel plates subjected to projectile impact. An experimental and numerical study",

Sumita Dey, 2004:38, ISBN 82-471-6282-2 (printed version), ISBN 82-471-6281-4 (electronic version), ISSN 1503-8181.

"Alkali-reactive and inert fillers in concrete. Rheology of fresh mixtures and expansive reactions,"

Bård M. Pedersen, 2004:92, ISBN 82-471-6401-9 (printed version), ISBN 82-471-6400-0 (electronic version), ISSN 1503-8181.

"On the Shear Capacity of Steel Girders with Large Web Openings",

Nils Christian Hagen, 2005:9 ISBN 82-471-6878-2 (printed version), ISBN 82-471-6877-4 (electronic version), ISSN 1503-8181.

"Behaviour of aluminium extrusions subjected to axial loading",

Østen Jensen, 2005:7, ISBN 82-471-6873-1 (printed version), ISBN 82-471-6872-3 (electronic version), ISSN 1503-8181.

"Thermal Aspects of corrosion of Steel in Concrete",

Jan-Magnus Østvik, 2005:5, ISBN 82-471-6869-3 (printed version), ISBN 82-471-6868 (electronic version), ISSN 1503-8181.

"Mechanical and adaptive behaviour of bone in relation to hip replacement. A study of bone remodelling and bone grafting.",
Sébastien Muller, 2005:34, ISBN 82-471-6933-9 (printed version), ISBN 82-471-6932-0 (electronic version), ISSN 1503-8181.

"Analysis of geometrical nonlinearities with applications to timber structures",
Lars Wollebæk, 2005:74, ISBN 82-471-7050-5 (printed version), ISBN 82-471-7019-1 (electronic version), ISSN 1503-8181.

"Pedestrian induced lateral vibrations of slender footbridges",
Anders Rönnquist, 2005:102, ISBN 82-471-7082-5 (printed version), ISBN 82-471-7081-7 (electronic version), ISSN 1503-8181.

"Initial Strength Development of Fly Ash and Limestone Blended Cements at Various Temperatures Predicted by Ultrasonic Pulse Velocity",
Tom Ivar Fredvik, 2005:112, ISBN 82-471-7105-8 (printed version), ISBN 82-471-7103-1 (electronic version), ISSN 1503-8181.

"Behaviour and modelling of thin-walled cast components",
Cato Dørum, 2005:128, ISBN 82-471-7140-6 (printed version), ISBN 82-471-7139-2 (electronic version), ISSN 1503-8181.

"Behaviour and modelling of selfpiercing riveted connections",
Raffaele Porcaro, 2005:165, ISBN 82-471-7219-4 (printed version), ISBN 82-471-7218-6 (electronic version), ISSN 1503-8181.

"Behaviour and Modelling of Aluminium Plates subjected to Compressive Load",
Lars Rønning, 2005:154, ISBN 82-471-7169-1 (printed version), ISBN 82-471-7195-3 (electronic version), ISSN 1503-8181.

"Bumper beam-longitudinal system subjected to offset impact loading",
Satyanarayana Kokkula, 2005:193, ISBN 82-471-7280-1 (printed version), ISBN 82-471-7279-8 (electronic version), ISSN 1503-8181.

"Control of Chloride Penetration into Concrete Structures at Early Age",
Guofei Liu, 2006:46, ISBN 82-471-7838-9 (printed version), ISBN 82-471-7837-0 (electronic version), ISSN 1503-8181.

"Modelling of Welded Thin-Walled Aluminium Structures",
Ting Wang, 2006:78, ISBN 82-471-7907-5 (printed version), ISBN 82-471-7906-7 (electronic version), ISSN 1503-8181.

"Time-variant reliability of dynamic systems by importance sampling and probabilistic analysis of ice loads",
Anna Ivanova Olsen, 2006:139, ISBN 82-471-8041-3 (printed version), ISBN 82-471-8040-5 (electronic version), ISSN 1503-8181.

"Fatigue life prediction of an aluminium alloy automotive component using finite element analysis of surface topography",
Sigmund Kyrre Ås, 2006:25, ISBN 82-471-7791-9 (printed version), ISBN 82-471-7791-9 (electronic version), ISSN 1503-8181.

"Constitutive models of elastoplasticity and fracture for aluminium alloys under strain path change",
Dasharatha Achani, 2006:76, ISBN 82-471-7903-2 (printed version), ISBN 82-471-7902-4 (electronic version), ISSN 1503-8181.

"Simulations of 2D dynamic brittle fracture by the Element-free Galerkin method and linear fracture mechanics",
Tommy Karlsson, 2006:125, ISBN 82-471-8011-1 (printed version), ISBN 82-471-8010-3 (electronic version), ISSN 1503-8181.

"Penetration and Perforation of Granite Targets by Hard Projectiles",
Chong Chiang Seah, 2006:188, ISBN 82-471-8150-9 (printed version), ISBN 82-471-8149-5 (electronic version), ISSN 1503-8181.

"Deformations, strain capacity and cracking of concrete in plastic and early hardening phases",
Tor Arne Hammer, 2007:234, ISBN 978-82-471-5191-4 (printed version), ISBN 978-82-471-5207-2 (electronic version), ISSN 1503-8181.

"Crashworthiness of dual-phase high-strength steel: Material and Component behaviour",
Venkatapathi Tarigopula, 2007:230, ISBN 82-471-5076-4 (printed version), ISBN 82-471-5093-1 (electronic version), ISSN 1503-8181.

"Fibre reinforcement in load carrying concrete structures",
Åse Lyslo Døssland, 2008:50, ISBN 978-82-471-6910-0 (printed version), ISBN 978-82-471-6924-7 (electronic version), ISSN 1503-8181.

"Low-velocity penetration of aluminium plates",
Frode Grytten, 2008:46, ISBN 978-82-471-6826-4 (printed version), ISBN 978-82-471-6843-1 (electronic version), ISSN 1503-8181.

"Robustness studies of structures subjected to large deformations",
Ørjan Fyllingen, 2008:24, ISBN 978-82-471-6339-9 (printed version), ISBN 978-82-471-6342-9 (electronic version), ISSN 1503-8181.

"Constitutive modelling of morsellised bone",
Knut Birger Lunde, 2008:92, ISBN 978-82-471-7829-4 (printed version), ISBN 978-82-471-7832-4 (electronic version), ISSN 1503-8181.

"Experimental Investigations of Wind Loading on a Suspension Bridge Girder",
Bjørn Isaksen, 2008:131, ISBN 978-82-471-8656-5 (printed version), ISBN 978-82-471-8673-2 (electronic version), ISSN 1503-8181.

"Cracking Risk of Concrete Structures in The Hardening Phase",

Guomin Ji, 2008:198, ISBN 978-82-471-1079-9 (printed version), ISBN 978-82-471-1080-5 (electronic version), ISSN 1503-8181.

"Modelling and numerical analysis of the porcine and human mitral apparatus",
Victorien Emile Prot, 2008:249, ISBN 978-82-471-1192-5 (printed version), ISBN 978-82-471-1193-2 (electronic version), ISSN 1503-8181.

"Strength analysis of net structures",
Heidi Moe, 2009:48, ISBN 978-82-471-1468-1 (printed version), ISBN 978-82-471-1469-8 (electronic version), ISSN 1503-8181.

"Numerical analysis of ductile fracture in surface cracked shells",
Espen Berg, 2009:80, ISBN 978-82-471-1537-4 (printed version), ISBN 978-82-471-1538-1 (electronic version), ISSN 1503-8181.

"Subject specific finite element analysis of bone for evaluation of the healing of a leg lengthening and evaluation of femoral stem design",
Sune Hansborg Pettersen, 2009:99, ISBN 978-82-471-1579-4 (printed version), ISBN 978-82-471-1580-0 (electronic version), ISSN 1503-8181.

"Evaluation of fracture parameters for notched multi-layered structures",
Lingyun Shang, 2009:137, ISBN 978-82-471-1662-3 (printed version), ISBN 978-82-471-1663-0 (electronic version), ISSN 1503-8181.

"Modelling of Dynamic Material Behaviour and Fracture of Aluminium Alloys for Structural Applications",
Yan Chen, 2009:69, ISBN 978-82-471-1515-2 (printed version), ISBN 978-82-471-1516-9 (electronic version), ISSN 1503-8181.

"Nanomechanics of polymer and composite particles",
Jianying He 2009:213, ISBN 978-82-471-1828-3 (printed version), ISBN 978-82-471-1829-0 (electronic version), ISSN 1503-8181.

"Mechanical properties of clear wood from Norway spruce",
Kristian Berbom Dahl 2009:250, ISBN 978-82-471-1911-2 (printed version) ISBN 978-82-471-1912-9 (electronic version), ISSN 1503-8181.

"Modeling of the degradation of TiB₂ mechanical properties by residual stresses and liquid Al penetration along grain boundaries",
Micol Pezzotta 2009:254, ISBN 978-82-471-1923-5 (printed version) ISBN 978-82-471-1924-2 (electronic version) ISSN 1503-8181.

"Effect of welding residual stress on fracture",
Xiabo Ren 2010:77, ISBN 978-82-471-2115-3 (printed version) ISBN 978-82-471-2116-0 (electronic version), ISSN 1503-8181.

"Pan-based carbon fiber as anode material in cathodic protection system for concrete structures",
Mahdi Chini 2010:122, ISBN 978-82-471-2210-5 (printed version) ISBN 978-82-471-2213-6 (electronic version), ISSN 1503-8181.

"Structural Behaviour of deteriorated and retrofitted concrete structures",
Irina Vasilijeva Sæther 2010:171, ISBN 978-82-471-2315-7 (printed version) ISBN 978-82-471-2316-4 (electronic version) ISSN 1503-8181.

"Prediction of local snow loads on roofs",
Vivian Meløysund 2010:247, ISBN 978-82-471-2490-1 (printed version) ISBN 978-82-471-2491-8 (electronic version) ISSN 1503-8181.

"Behaviour and modelling of polymers for crash applications",
Virgile Delhayé 2010:251, ISBN 978-82-471-2501-4 (printed version) ISBN 978-82-471-2502-1 (electronic version) ISSN 1503-8181.

"Blended cement with reduced CO₂ emission - Utilizing the Fly Ash-Limestone Synergy",
Klaartje De Weerd 2011:32, ISBN 978-82-471-2584-7 (printed version) ISBN 978-82-471-2584-4 (electronic version) ISSN 1503-8181.

"Chloride induced reinforcement corrosion in concrete. Concept of critical chloride content - methods and mechanisms",
Ueli Angst 2011:113, ISBN 978-82-471-2769-9 (printed version) ISBN 978-82-471-2763-6 (electronic version) ISSN 1503-8181.

"A thermo- electric- mechanical study of the carbon anode and contact interface for energy savings in the production of aluminium",
Dag Herman Andersen 2011:157, ISBN 978-82-471-2859-6 (printed version) ISBN 978-82-471-2860-2 (electronic version) ISSN 1503-8181.

"Structural Capacity of Anchorage Ties in Masonry Veneer Walls Subjected to Earthquake. The implications of Eurocode 8 and Eurocode 6 on a typical Norwegian veneer wall",
Ahmed Mohamed Yousry Hamed 2011:181, ISBN 978-82-471-2911-1 (printed version) ISBN 978-82-471-2912-8 (electronic ver.) ISSN 1503-8181.

"Work-hardening behaviour in age-hardenable Al-Zn-Mg(-Cu) alloys",
Ida Westermann , 2011:247, ISBN 978-82-471-3056-8 (printed ver.) ISBN 978-82-471-3057-5 (electronic ver.) ISSN 1503-8181.

"Behaviour and modelling of selfpiercing riveted connections using aluminium rivets",
Nguyen-Hieu Hoang, 2011:266, ISBN 978-82-471-3097-1 (printed ver.) ISBN 978-82-471-3099-5 (electronic ver.) ISSN 1503-8181.

"Fibre reinforced concrete",
Sindre Sandbakk, 2011:297, ISBN 978-82-471-3167-1 (printed ver.) ISBN 978-82-471-3168-8 (electronic ver) ISSN 1503:8181.

"Dynamic behaviour of cable-supported bridges subjected to strong natural wind",
Ole Andre Øiseth, 2011:315, ISBN 978-82-471-3209-8 (printed ver.) ISBN 978-82-471-3210-4 (electronic ver.) ISSN 1503-8181.

"Constitutive modeling of solar-grade silicon materials",
Julien Cochard, 2011:307, ISBN 978-82-471-3189-3 (printed ver.) ISBN 978-82-471-3190-9 (electronic ver.) ISSN 1503-8181.

"Constitutive behavior and fracture of shape memory alloys",
Jim Stian Olsen, 2012:57, ISBN 978-82-471-3382-8 (printed ver.) ISBN 978-82-471-3383-5 (electronic ver.) ISSN 1503-8181.

"Field measurements in mechanical testing using close-range photogrammetry and digital image analysis",
Egil Fagerholt, 2012:95, ISBN 978-82-471-3466-5 (printed ver.) ISBN 978-82-471-3467-2 (electronic ver.) ISSN 1503-8181.

"Towards a better understanding of the ultimate behaviour of lightweight aggregate concrete in compression and bending",
Håvard Nedrelid, 2012:123, ISBN 978-82-471-3527-3 (printed ver.) ISBN 978-82-471-3528-0 (electronic ver.) ISSN 1503-8181.

"Numerical simulations of blood flow in the left side of the heart",
Sigrid Kaarstad Dahl, 2012:135, ISBN 978-82-471-3553-2 (printed ver.) ISBN 978-82-471-3555-6 (electronic ver.) ISSN 1503-8181.

"Moisture induced stresses in glulam",
Vanessa Angst-Nicollier, 2012:139, ISBN 978-82-471-3562-4 (printed ver.) ISBN 978-82-471-3563-1 (electronic ver.) ISSN 1503-8181.

"Biomechanical aspects of distraction osteogenesis",
Valentina La Russa, 2012:250, ISBN 978-82-471-3807-6 (printed ver.) ISBN 978-82-471-3808-3 (electronic ver.) ISSN 1503-8181.

"Ductile fracture in dual-phase steel. Theoretical, experimental and numerical study",
Gaute Gruben, 2012:257, ISBN 978-82-471-3822-9 (printed ver.) ISBN 978-82-471-3823-6 (electronic ver.) ISSN 1503-8181.

"Damping in Timber Structures",
Nathalie Labonnote, 2012:263, ISBN 978-82-471-3836-6 (printed ver.) ISBN 978-82-471-3837-3 (electronic ver.) ISSN 1503-8181.

"Biomechanical modeling of fetal veins: The umbilical vein and ductus venosus bifurcation",
Paul Roger Leinan, 2012:299, ISBN 978-82-471-3915-8 (printed ver.) ISBN 978-82-471-3916-5 (electronic ver.) ISSN 1503-8181.

"Large-Deformation behaviour of thermoplastics at various stress states",
Anne Serine Ognedal, 2012:298, ISBN 978-82-471-3913-4 (printed ver.) ISBN 978-82-471-3914-1 (electronic ver.) ISSN 1503-8181.

"Hardening accelerator for fly ash blended cement",
Kien Dinh Hoang, 2012:366, ISBN 978-82-471-4063-5 (printed ver.) ISBN 978-82-

471-4064-2 (electronic ver.) ISSN 1503-8181.

"From molecular structure to mechanical properties",
Jianyang Wu, 2013:186, ISBN 978-82-471-4485-5 (printed ver.) ISBN 978-82-471-4486-2 (electronic ver.) ISSN 1503-8181.

"Experimental and numerical study of hybrid concrete structures",
Linn Grepstad Nes, 2013:259, ISBN 978-82-471-4644-6 (printed ver.) ISBN 978-82-471-4645-3 (electronic ver.) ISSN 1503-8181.

"Mechanics of ultra-thin multi crystalline silicon wafers",
Saber Saffar, 2013:199, ISBN 978-82-471-4511-1 (printed ver.) ISBN 978-82-471-4513-5 (electronic ver.) ISSN 1503-8181.

"Through process modelling of welded aluminium structures",
Anizahyati Alisibramulisi, 2013:325, ISBN 978-82-471-4788-7 (printed ver.) ISBN 978-82-471-4789-4 (electronic ver.) ISSN 1503-8181.

"Combined blast and fragment loading on steel plates",
Knut Gaarder Rakvåg, 2013:361, ISBN 978-82-471-4872-3 (printed ver.) ISBN 978-82-4873-0 (electronic ver.) ISSN 1503-8181.

"Characterization and modelling of the anisotropic behaviour of high-strength aluminium alloy",
Marion Fourmeau, 2014:37, ISBN 978-82-326-0008-3 (printed ver.) ISBN 978-82-326-0009-0 (electronic ver.) ISSN 1503-8181.

"Behaviour of threaded steel fasteners at elevated deformation rates",
Henning Fransplass, 2014:65, ISBN 978-82-326-0054-0 (printed ver.) ISBN 978-82-326-0055-7 (electronic ver.) ISSN 1503-8181.

"Sedimentation and Bleeding",
Ya Peng, 2014:89, ISBN 978-82-326-0102-8 (printed ver.) ISBN 978-82-326-0103-5 (electronic ver.) ISSN 1503-8181.

"Impact against X65 offshore pipelines",
Martin Kristoffersen, 2014:362, ISBN 978-82-326-0636-8 (printed ver.) ISBN 978-82-326-0637-5 (electronic ver.) ISSN 1503-8181.

"Formability of aluminium alloy subjected to prestrain by rolling",
Dmitry Vysochinskiy, 2014:363, ISBN 978-82-326-0638-2 (printed ver.) ISBN 978-82-326-0639-9 (electronic ver.) ISSN 1503-8181.

"Experimental and Numerical Study of Yielding, Work- Hardening and Anisotropy in Textured AA6xxx Alloys Using Crystal Plasticity Models",
Mikhail Khadyko, 2015:28, ISBN 978-82-326-0724-2 (printed ver.) ISBN 978-82-326-0725-9 (electronic ver.) ISSN 1503-8181.

"Behaviour and Modelling of AA6xxx Aluminium Alloys Under a Wide Range of Temperatures and Strain Rates",

Vincent Vilamosa, 2015:63, ISBN 978-82-326-0786-0 (printed ver.) ISBN 978-82-326-0787-7 (electronic ver.) ISSN 1503-8181.

"A Probabilistic Approach in Failure Modelling of Aluminium High Pressure Die-Castings",
Octavian Knoll, 2015:137, ISBN 978-82-326-0930-7 (printed ver.) ISBN 978-82-326-0931-4 (electronic ver.) ISSN 1503-8181.

"Ice Abrasion on Marine Concrete Structures",
Egil Møen, 2015:189, ISBN 978-82-326-1034-1 (printed ver.) ISBN 978-82-326-1035-8 (electronic ver.) ISSN 1503-8181.

"Fibre Orientation in Steel-Fibre-Reinforced Concrete",
Giedrius Zirgulis, 2015:229, ISBN 978-82-326-1114-0 (printed ver.) ISBN 978-82-326-1115-7 (electronic ver.) ISSN 1503-8181.

"Effect of spatial variation and possible interference of localised corrosion on the residual capacity of a reinforced concrete beam",
Mohammad Mahdi Kioumars, 2015:282, ISBN 978-82-326-1220-8 (printed ver.) ISBN 978-82-1221-5 (electronic ver.) ISSN 1503-8181.

"The role of concrete resistivity in chloride-induced macro-cell corrosion",
Karla Horbostel, 2015:324, ISBN 978-82-326-1304-5 (printed ver.) ISBN 978-82-326-1305-2 (electronic ver.) ISSN 1503-8181.

"Flowable fibre-reinforced concrete for structural applications",
Elena Vidal Sarmiento, 2015:335, ISBN 978-82-326-1324-3 (printed ver.) ISBN 978-82-326-1325-0 (electronic ver.) ISSN 1503-8181.

"Development of crushed sand for concrete production with microproportioning",
Rolands Cepuritis, 2016:19, ISBN 978-82-326-1382-3 (printed ver.) ISBN 978-82-326-1383-0 (electronic ver.) ISSN 1503-8181.

"Withdrawal properties of threaded rods embedded in glued-laminated timber elements",
Haris Stamatopoulos, 2016:48, ISBN 978-82-326-1436-3 (printed ver.) ISBN 978-82-326-1437-0 (electronic ver.) ISSN 1503-8181.

"An Experimental and numerical study of thermoplastics at large deformation",
Marius Andersen, 2016:191, ISBN 978-82-326-1720-3 (printed ver.) ISBN 978-82-326-1721-0 (electronic ver.) ISSN 1503-8181.

"Modeling and Simulation of Ballistic Impact",
Jens Kristian Holmen, 2016:240, ISBN 978-82-326-1818-7 (printed ver.) ISBN 978-82-326-1819-4 (electronic ver.) ISSN 1503-8181.

"Early age crack assessment of concrete structures",
Anja B. Estensen Klausen, 2016:256, ISBN 978-82-326-1850-7 (printed ver.) ISBN 978-82-326-1851-4 (electronic ver.) ISSN 1503-8181.

- "Uncertainty quantification and sensitivity analysis for cardiovascular models",
Vinzeng Gregor Eck, 2016:234, ISBN 978-82-326-1806-4 (printed ver.) ISBN 978-82-326-1807-1 (electronic ver.) ISSN 1503-8181.
- "Dynamic behaviour of existing and new railway catenary systems under Norwegian conditions",
Petter Røe Nåvik, 2016:298, ISBN 978-82-326-1935-1 (printed ver.) ISBN 978-82-326-1934-4 (electronic ver.) ISSN 1503-8181.
- "Mechanical behaviour of particle-filled elastomers at various temperatures",
Arne Ilseeng, 2016-295, ISBN978-82-326-1928-3 (printed ver.) ISBN 978-82-326-1929-0 (electronic ver.) ISSN 1503-8181.
- "Nanotechnology for Anti-Icing Application",
Zhiwei He, 2016:348, ISBN 978-82-326-2038-8 (printed ver.) ISBN 978-82-326-2019-5 (electronic ver.) ISSN 1503-8181.
- "Conduction Mechanisms in Conductive Adhesives with Metal-Coated Polymer Spheres",
Sigurd Rolland Pettersen, 2016:349, ISBN 978-326-2040-1 (printed ver.) ISBN 978-82-326-2041-8 (electronic ver.) ISSN 1503-8181.
- "The interaction between calcium lignosulfonate and cement",
Alessia Colombo, 2017:20, ISBN 978-82-326-2122-4 (printed ver.) ISBN 978-82-326-2123-1 (electronic ver.) ISSN 1503-8181.
- "Behaviour and Modelling of Flexible Structures Subjected to Blast Loading",
Vegard Aune, 2017:101, ISBN 978-82-326-2274-0 (printed ver.) ISBN 978-82-326-2275-7 (electronic ver.) ISSN 1503-8181.
- "Behaviour of steel connections under quasi-static and impact loading",
Erik Løhre Grimsmo, 2017:159, ISBN 978-82-326-2390-7 (printed ver.) ISBN 978-82-326-2391-4 (electronic ver.) ISSN 1503-8181.
- "An experimental and numerical study of cortical bone at the macro and Nano-scale",
Masoud Ramenzanzadehkoldeh,, 2017:208, ISBN 978-82-326-2488-1 (printed ver.) ISBN 978-82-326-2489-8 (electronic ver.) ISSN 1503-8181.
- "Optoelectrical Properties of a Novel Organic Semiconductor: 6,13-Dichloropentacene",
Mao Wang, 2017:130, ISBN 978-82-326-2332-7 (printed ver.) ISBN 978-82-326-2333-4 (electronic ver.) ISSN 1503-8181.
- "Core-shell structured microgels and their behavior at oil and water interface",
Yi Gong, 2017:182, ISBN 978-82-326-2436-2 (printed. ver.) ISBN 978-82-326-2437-9 (electronic ver.) ISSN 1503-8181.
- "Aspects of design of reinforced concrete structures using nonlinear finite element analyses",
Morten Engen, 2017:149, ISBN 978-82-326-2370-9 (printed ver.) ISBN 978-82-326-

2371-6 (electronic ver.) ISSN 1503-8181.

"Numerical studies on ductile failure of aluminium alloys",
Lars Edvard Dæhli, 2017:284, ISBN 978-82-326-2636-6 (printed ver.) ISBN 978-82-326-2637-3 (electronic ver.) ISSN 1503-8181.

"Modelling and Assessment of Hydrogen Embrittlement in Steels and Nickel Alloys",
Haiyang Yu, 2017:278, ISBN 978-82-326-2624-3 (printed. ver.) ISBN 978-82-326-2625-0 (electronic ver.) ISSN 1503-8181.

"Network arch timber bridges with light timber deck on transverse crossbeams",
Anna Weronika Ostrycharczyk, 2017:318, ISBN 978-82-326-2704-2 (printed ver.) ISBN 978-82-326-2705-9 (electronic ver.) ISSN 1503-8181.

"Splicing of Large Glued Laminated Timber Elements by Use of Long Threaded Rods",
Martin Cepelka, 2017:320, ISBN 978-82-326-2708-0 (printed ver.) ISBN 978-82-326-2709-7 (electronic ver.) ISSN 1503-8181.

"Thermomechanical behaviour of semi-crystalline polymers: experiments, modelling and simulation",
Joakim Johnsen, 2017:317, ISBN 978-82-326-2702-8 (printed ver.) ISBN 978-82-326-2703-5 (electronic ver.) ISSN 1503-8181.

"Small-Scale Plasticity under Hydrogen Environment",
Kai Zhao, 2017:356, ISBN 978-82-326-2782-0 (printed ver.) ISBN 978-82-326-2783-7 (electronic er.) ISSN 1503-8181.

"Risk and Reliability Based Calibration of Structural Design Codes",
Michele Baravalle, 2017:342, ISBN 978-82-326-2752-3 (printed ver.) ISBN 978-82-326-2753-0 (electronic ver.) ISSN 1503-8181.

"Dynamic behaviour of floating bridges exposed to wave excitation",
Knut Andreas Kvåle, 2017:365, ISBN 978-82-326-2800-1 (printed ver.) ISBN 978-82-326-2801-8 (electronic ver.) ISSN 1503-8181.

"Dolomite calcined clay composite cement - hydration and durability",
Alisa Lydia Machner, 2018:39, ISBN 978-82-326-2872-8 (printed ver.) ISBN 978-82-326-2873-5 (electronic ver.) ISSN 1503-8181.

"Modelling of the self-excited forces for bridge decks subjected to random motions: an experimental study",
Bartosz Siedziako, 2018:52, ISBN 978-82-326-2896-4 (printed ver.) ISBN 978-82-326-2897-1 (electronic ver.) ISSN 1503-8181.

"A probabilistic-based methodology for evaluation of timber facade constructions",
Klodian Gradeci, 2018:69, ISBN 978-82-326-2928-2 (printed ver.) ISBN 978-82-326-2929-9 (electronic ver.) ISSN 1503-8181.

"Behaviour and modelling of flow-drill screw connections",

Johan Kolstø Sønstabø, 2018:73, ISBN 978-82-326-2936-7 (printed ver.) ISBN 978-82-326-2937-4 (electronic ver.) ISSN 1503-8181.

"Full-scale investigation of the effects of wind turbulence characteristics on dynamic behavior of long-span cable-supported bridges in complex terrain",
Aksel Fenerci, 2018:100, ISBN 9978-82-326-2990-9 (printed ver.) ISBN 978-82-326-2991-6 (electronic ver.) ISSN 1503-8181.

"Modeling and simulation of the soft palate for improved understanding of the obstructive sleep apnea syndrome",
Hongliang Liu, 2018:101, ISBN 978-82-326-2992-3 (printed ver.) ISBN 978-82-326-2993-0 (electronic ver.) ISSN 1503-8181.

"Long-term extreme response analysis of cable-supported bridges with floating pylons subjected to wind and wave loads",
Yuwang Xu, 2018:229, ISBN 978-82-326-3248-0 (printed ver.) ISBN 978-82-326-3249-7 (electronic ver.) ISSN 1503-8181.

"Reinforcement corrosion in carbonated fly ash concrete",
Andres Belda Revert, 2018:230, ISBN 978-82-326-3250-3 (printed ver.) ISBN 978-82-326-3251-0 (electronic ver.) ISSN 1503-8181.

"Direct finite element method for nonlinear earthquake analysis of concrete dams including dam-water-foundation rock interaction",
Arnkjell Løkke, 2018:252, ISBN 978-82-326-3294-7 (printed ver.) ISBN 978-82-326-3295-4 (electronic ver.) ISSN 1503-8181.

"Electromechanical characterization of metal-coated polymer spheres for conductive adhesives",
Molly Strimbeck Bazilchuk, 2018:295, ISBN 978-82-326-3380-7 (printed. ver.) ISBN 978-82-326-3381-4 (electrical ver.) ISSN 1503-8181.

"Determining the tensile properties of Arctic materials and modelling their effects on fracture",
Shengwen Tu, 2018:269, ISBN 978-82-326-3328-9 (printed ver.) ISBN 978-82-326-3329-6 (electronic ver.) ISSN 1503-8181.

"Atomistic Insight into Transportation of Nanofluid in Ultra-confined Channel",
Xiao Wang, 2018:334, ISBN978-82-326-3456-9 (printed ver.) ISBN 978-82-326-3457-6 (electronic ver.) ISSN 1503-8181.

"An experimental and numerical study of the mechanical behaviour of short glass-fibre reinforced thermoplastics",
Jens Petter Henrik Holmstrøm, 2019:79, ISBN 978-82-326-3760-7 (printed ver.) ISBN 978-82-326-3761-4 (electronic ver.) ISSN 1503-8181.

"Uncertainty quantification and sensitivity analysis informed modeling of physical systems",
Jacob Sturdy, 2019:115, ISBN 978-82-326-3828-4 (printed ver.) ISBN 978-82-326-3829-1 (electric ver.) ISSN 1503-8181.

"Load model of historic traffic for fatigue life estimation of Norwegian railway bridges",

Gunnstein T. Frøseth, 2019:73, ISBN 978-82-326-3748-5 (printed ver.) ISBN 978-82-326-3749-2 (electronic ver.) ISSN 1503-8181.

"Force identification and response estimation in floating and suspension bridges using measured dynamic response",

Øyvind Wiig Petersen, 2019:88, ISBN 978-82-326-3778-2 (printed ver.) ISBN 978-82-326-3779-9 (electronic ver.) ISSN 1503-8181.

"Consistent crack width calculation methods for reinforced concrete elements subjected to 1D and 2D stress states",

Reignard Tan, 2019:147, ISBN 978-82-326-3892-5 (printed ver.) ISBN 978-82-326-3893-2 (electronic ver.) ISSN 1503-8181.

"Nonlinear static and dynamic isogeometric analysis of slender spatial and beam type structures",

Siv Bente Raknes, 2019:181, ISBN 978-82-326-3958-8 (printed ver.) ISBN 978-82-326-3959-5 (electronic ver.) ISSN 1503-8181.

"Experimental study of concrete-ice abrasion and concrete surface topography modification",

Guzel Shamsutdinova, 2019:182, ISBN 978-82-326-3960-1 (printed ver.) ISBN 978-82-326-3961-8 (electronic ver.) ISSN 1503-8181.

"Wind forces on bridge decks using state-of-the art FSI methods",

Tore Andreas Helgedagsrud, 2019:180, ISBN 978-82-326-3956-4 (printed ver.) ISBN 978-82-326-3957-1 (electronic ver.) ISSN 1503-8181.

"Numerical Study on Ductile-to-Brittle Transition of Steel and its Behavior under Residual Stresses",

Yang Li, 2019:227, ISBN 978-82-326-4050-8 (printed ver.) ISBN 978-82-326-4051-5 (electronic ver.) ISSN 1503-8181.

"Micromechanical modelling of ductile fracture in aluminium alloys",

Bjørn Håkon Frødal, 2019:253, ISBN 978-82-326-4102-4 (printed ver.) ISBN 978-82-326-4103-1 (electronic ver.) ISSN 1503-8181.

"Monolithic and laminated glass under extreme loading: Experiments, modelling and simulations",

Karoline Osnes, 2019:304, ISBN 978-82-326-4204-5 (printed ver.) ISBN 978-82-326-4205-2 (electronic ver.) ISSN 1503-8181.

"Plastic flow and fracture of isotropic and anisotropic 6000-series aluminium alloys: Experiments and numerical simulations",

Susanne Thomesen, 2019:312, ISBN 978-82-326-4220-5 (printed ver.), ISBN 978-82-326-4221-2 (electronic ver.) ISSN 1503-8181

"Stress-laminated timber decks in bridges",

Francesco Mirko Massaro, 2019:346, ISBN 978-82-326-4288-5 (printed ver.), ISBN

978-82-326-4289-2 (electronic ver.) ISSN 1503-8181

"Connections between steel and aluminium using adhesive bonding combined with self-piercing riveting: Testing, modelling and analysis",
Matthias Reil, 2019:319, ISBN 978-82-326-4234-2 (printed ver.), ISBN 978-82-326-4235-9 (electronic ver.) ISSN 1503-8181

"Designing Polymeric Icephobic Materials",
Yizhi Zhuo, 2019:345, ISBN 978-82-326-4286-1 (printed ver.), ISBN 978-82-326-4287-8 (electronic ver.) ISSN 1503-8181

"Fundamental Mechanisms of Ice Adhesion",
Rønneberg, Sigrid 2020:87, ISBN 978-82-326-4527-8 (printed version) ISBN 978-82-326-4524-5 (electronic version) ISSN 1503-8181

"Mechanical modeling of the polymeric coating on a subsea pipeline",
Vestrum, Ole 2020:105, ISBN 978-82-326-4562-6 (printed version) ISBN 978-82-4563-3 (electronic version) ISSN 1503-8181

"Conceptual form-finding in structural engineering",
Marcin Luczkowski 2020

"Self-assembled superstructures of magnetic nanoparticles: advanced nanofabrication and enhanced mechanical properties",
Verner Håkonsen 2020:271, ISBN 978-82-326-4890-0 (printed version) ISBN 978-82-326-4891-7 (electronic version) ISSN 1503-8181

"Micromechanical modelling of fracture in ductile alloys with applications to high-strength steel",
Sondre Bergo 2020:313, ISBN 978-82-326-4974-7 (printed version) ISBN 978-82-326-4975-4 (electronic version) ISSN 1503-8181

"Fracture in wood of Norway spruce - Experimental and numerical study",
Katarzyna Ostapska 2020:314, ISBN 978-82-326-4976-1 (printed version) ISBN 978-82-326-4977-8 (electronic version) ISSN 1503-8181

"Dynamic anti-icing surfaces (DAIS)",
Feng Wang 2020:330 ISBN 978-82-326-5006-4 (printed version) ISBN 978-82-326-5007-1 (electronic version) ISSN 1503-8181

"Multiaxial Fatigue analysis of offshore mooring chains, considering the effects of residual stresses and corrosion pits",
Ershad P. Zarandi 2020:337 ISBN 978-82-326-5020-0 (printed version) ISBN 978-82-326-5021-7 (electronic version) ISSN 1503-8181

"Production and documentation of frost durable high-volume fly ash concrete: air entrainment, cracking and scaling in performance testing",
Andrei Shpak 2020:366 ISBN 978-82-326-5078-1 (printed version) ISBN 978-82-326-5079-8 (electronic version) ISSN 1503-8181